Novel Structures and Unusual Reactivity Powered by Tautomerism and Electron Delocalization in Salicylimines

by

Seyed Hessam Moosavi Mehr

BSc., Sharif University of Technology, 2009

A THESIS SUBMITTED IN PARTIAL FULFILLMENT OF
THE REQUIREMENTS FOR THE DEGREE OF

DOCTOR OF PHILOSOPHY

in

The Faculty of Graduate and Postdoctoral Studies

(Chemistry)

THE UNIVERSITY OF BRITISH COLUMBIA
(Vancouver)

August 2017

Abstract

A family of tris(salicylaldimine) (TSAN) analogues was prepared by condensation of 2,4,6-triformylphloroglucinol (TFP) and various nitrogen-containing bases. Characterization of these compounds by ^{1}H NMR spectroscopy and single-crystal X-ray diffraction (SCXRD) revealed that some of them adopt the previously unknown enol-imine tautomeric form. Experimental data and *ab initio* modelling were used to establish which factors govern the keto-enamine/enol-imine tautomeric equilibrium, culminating in a simple structural model of TSAN behaviour. According to this model, π electron-withdrawing X groups in the NH_2X starting material stabilize the keto-enamine tautomeric form, whereas σ electron withdrawing X, *e.g.* electronegative heteroatoms, lead to the enol-imine form.

The same tautomeric equilibrium has also been leveraged in a family of hydroxysalicylaldehyde Schiff bases to bring about facile exchange of specific aromatic C*H* hydrogen atoms when these compounds are dissolved in CD_3OD or D_2O under ambient conditions. The mechanism of this surprising isotopic exchange reaction has been investigated experimentally using ^{1}H NMR kinetic experiments on these Schiff bases and a number of control compounds as well as *ab initio* modelling. Both sources point to the involvement of the minor keto-enamine tautomeric form of the salicylimines, which facilitates electrophilic aromatic substitution of hydrogen with deuterium by stabilizing the sp^3-hybridized Wheland intermediate formed in the course of the reaction.

The impact of the keto-enamine tautomeric form on the electronic structure of TSANs has been studied in isolation by preparing a TSAN permanently “locked” in keto-enamine connectivity. This was achieved by replacing the labile proton present in regular TSANs with a non-labile

methyl group. The resulting compound assumes the expected keto-enamine structure; however, a large degree of strain is introduced since coplanarity of the peripheral enamine arms with the central ring, required for electronic coupling between the two, results in steric repulsion between the methyl groups and the carbonyl oxygen atoms. The central ring of the product is consequently highly contorted.

The unsatisfactory preparation of many of the salicylaldehyde precursors to the SANs above has been improved through a mild and efficient procedure using formamidine acetate and acetic anhydride. This method allows one to install up to three formyl group on various phenolic substrates without the harsh conditions encountered with common formylation techniques such as the Vilsmeier–Haack reaction.

Lay Summary

The common picture of a chemical bond includes a pair of electrons shared between adjacent atoms. More generally, though, electrons in a molecule can be shared between any number of atoms in a phenomenon called *electron delocalization*. Electron delocalization has a deep impact on our daily lives, underlying the red colour of tomatoes, the conductivity of metals, and the function of many enzymes in our bodies. Similarly, we associate most molecules with a fixed skeleton whereas the connectivity of atoms in certain molecules can undergo rapid back-and-forth change in a phenomenon known as *tautomerism*.

In this thesis, we demonstrate the power of electron delocalization and tautomerism by showing examples where they add surprising new behaviour to ordinary-looking organic molecules. Ideally, other chemists can use this information to design more effective drugs and catalysts.

Preface

The entirety of the work described in this thesis was carried out under the supervision of Prof. Mark J. MacLachlan. Mass spectroscopy data were collected by Marshall Llapawa, Derek Smith, and Marco Yeung in the Mass Spectrometry facility at the University of British Columbia. Unless otherwise mentioned, I set up all *ab initio* calculations and ran them on software and hardware provided by the Western Canada Research Grid, *Westgrid*.

Chapter 2: Single-crystal X-ray diffraction data were obtained by Dr. Brian O. Patrick, Dr. Nicholas G. White, and Veronica Carta. Dr. Paul Xia of UBC Chemistry Facility carried out the ^{13}C {^{1}H, ^{19}F} NMR experiment on compound **2.6** using machine time kindly allocated to him by the NMR facility at Simon Fraser University.

Chapter 3: A version of this chapter has been published: S. H. M. Mehr, K. Fukuyama, S. Bishop, F. Lelj and M. J. MacLachlan, *J. Org. Chem.*, **2015**, *80*, 5144–5150. *Ab initio* calculations in this chapter were obtained by Prof. Francesco Lelj. at the Università degli Studi della Basilicata. Dr. Katsuya Fukuyama and I jointly prepared compound **3.3** and derivatives thereof. Stephanie Bishop (BSc., UBC Chemistry) prepared and characterized compounds **3.5** and **3.6**. I performed all other experiments and wrote the manuscript with input from Prof. MacLachlan and Prof. Lelj.

Chapter 4: A version of this chapter has been published: S. H. M. Mehr, B. O. Patrick and M. J. MacLachlan, *Org. Lett.*, **2016**, *18*, 1840–1843. Single-crystal X-ray diffraction data were obtained by Dr. Brian O. Patrick. I performed all other experiments and wrote the manuscript with input from Prof. MacLachlan.

Chapter 5: A version of this chapter has been published: S. H. M. Mehr, H. Depmeier, K. Fukuyama, M. Maghami and M. J. MacLachlan, *Org. Biomol. Chem.*, **2017**, *15*, 581–583.

Mahboubeh Maghami and I jointly worked on early incarnations of the procedure. Dr. Katsuya Fukuyama and I worked on early protocols using formamidine acetate. Hannah Depmeier and I jointly optimized the reaction conditions and characterized the various reaction products. Hannah Depmeier and I wrote the manuscript with input from Prof. MacLachlan.

Table of Contents

List of Tables

List of Figures

List of Symbols and Abbreviations

Ac	acetyl
acac	acetylacetonato
AIM	atoms in molecules
ASE	aromatic stabilization energy
Bn	benzyl ($CH_2C_6H_5$)
Bu	butyl
Bz	benzoyl ($C(O)C_6H_5$)
CC	coupled cluster calculation
COSY	correlation spectroscopy
DBU	1,8-diazabicyclo(5.4.0)undec-7-ene
DCM	dichloromethane
DFT	density functional theory
DMF	*N*,*N*-dimethylformamide
DMSO	dimethylsulfoxide
equiv	equivalent(s)
ESI	electrospray ionization
Et	ethyl
FA	formamidine acetate
GIAO	Gauge-Including Atomic Orbitals
HMBC	heteronuclear multiple bond correlation spectroscopy
HRMS	high resolution mass spectrometry

HSQC	heteronuclear single quantum correlation spectroscopy
*i*Pr	isopropyl
IR	infrared
$J^n_{X–Y}$	n-bond scalar coupling constant between X and Y
MALDI	matrix-assisted laser desorption/ionization
Me	methyl
MP	Møller-Plesset perturbation theory
MS	mass spectrometry
NMR	nuclear magnetic resonance
OAc	acetate
PA	proton affinity
Ph	phenyl (C_6H_5)
r.t.	room temperature
SAN	salicylaldimine
SCXRD	single-crystal X-ray diffraction
T_1	longitudinal relaxation time constant
*t*Bu	tertiary butyl
TFP	2,4,6-triformylphloroglucinol
THF	tetrahydrofuran
TOF	time of flight
TSAN	tris(salicylaldimine)
UDEFT	uniform driven equilibrium Fourier transform
UV-vis	ultraviolet-visible

δ	chemical shift in ppm
δ^+ / δ^-	partial positive/negative charge

Acknowledgements

First and foremost, I would like to thank my parents, whose continued support has allowed me to pursue my lifelong dream of becoming a scientist. I am eternally grateful to my father for introducing me to chemistry — I still remember the sparkles from his glycerol–$KMnO_4$ demo — and to my mother for the unconditional love and the countless sacrifices she has made to ensure that my brother and I receive a good education.

I owe much of my chemical education to my good friend in high school, Arash Nazeri, and our early morning chemistry chats everyday before class. In addition, I have to thank my fantastic chemistry teachers at the Allameh Helli High School in Tehran, M. Bahraini, S. Shahparvizi, B. Graili, S. S. Safavi, M. Pourjavid, M. Moeini, M. Rezapour, M. Karimi and the late S. Keshavarz and O. Farahkhah for putting up with my endless questions and constant shenanigans in the chemistry lab.

My undergraduate education was in electrical engineering and I would have had no hope of becoming a chemist were it not for my supervisor, Prof. Mark MacLachlan, who took a risk by generously taking me on, fresh out of engineering school. During my time in his lab, Mark has been a mentor and role model and my biggest source of inspiration and encouragement. I will be forever indebted to him for giving me the freedom to follow my curiosity while helping me stay on track with publications and graduation. His fast but painstaking edits of our manuscripts and my thesis have been extremely helpful. Thanks for all the excellent advice and discussions; thank you for believing in me, Mark!

My years as a PhD student have been well-spent among the wonderful people in the MacLachlan and Wolf labs. I would like to thank Brian, Zhengyu, Angela, Kevin, Renee, and

Clement for helping me get up to speed when I was new to the lab. Brian's ideas and advice have always been immensely helpful — thank you Brian! The cheerful company of my lab-mates past and present, Veronica, Andrea, Debbie, Guillaume, Mo, Miguel, Ryan, Lev (and Brittany), Susan, Michael, Maik, Lina, Joel, Vitor, Erlantz, Taku, Becky, Francesco, Thanh, Duane, and Dr. Nick has helped me get through some of the tougher days.

I have had the great fortune of collaborating with some brilliant computational chemists, in particular Prof. Francesco Lelj, a gentle and knowledgeable mentor who has always treated me like a son, and my former teacher and long-time friend, Dr. Cina Foroutan-Nejad, who has been an inspiration since my high school days. I am also grateful to my other collaborators: Marcus Farnfield, Jason Yang, Dr. Katsuya Fukuyama, Stephanie Bishop, Kasumi Nakamura, Hiroya Oshima, Mahboubeh Maghami, and Hannah Depmeier.

This work would have been impossible without the help of research staff at the UBC Department of Chemistry. Thanks to Paul, and Maria for educating me about NMR, patiently helping me troubleshoot my experiments, and forgiving my silly mistakes. The NMR lab will always be my second home thanks to you! Thanks as well to Yun, Marshall, Derek, and Marco in the MS lab. Emily and Felix (and Sophia) at the SIF not only helped with science but shared my various obsessions (milk tea, sourdough baking, dim sum, biking) — thank you for that! For X-ray data, I am grateful to Dr. Brian Patrick and Anita Lam, as well as MacLachlan group members Veronica and Dr. Nick.

I would like to thank NSERC and UBC for generously funding my studies, allowing me to focus my attention on research as opposed to financing my stay in Vancouver. I am also grateful to *Westgrid*, the Western Canada Research Grid (especially Roman Baranowski and Grigory Shamov) for more than 20,000 CPU-hours of calculations.

Last but not least, I would like to thank all my friends for our good times together and their emotional support, especially during the past few months. Sorry I haven't been much fun lately! Thank you, Gabriele, Ehsan, Atena, Ostad, Khorshid, Sara, Nariman, Kaveh, Omar, Hamid, Sepideh, Jason, Angeli, and Katherine.

To my loving parents.

Chapter 1

Introduction

This thesis describes a series of experiments in designing organic building blocks with novel and, in some cases, surprising structure and reactivity by taking advantage of tautomerism and electron delocalization. Some of the ideas explored here have parallels in the related field of supramolecular chemistry: whereas supramolecular chemistry achieves the same goal by leveraging non-covalent interactions between molecules, we focus on individual molecules, aiming to discover patterns of atomic arrangement and electronic structure that can lead to unprecedented chemical behaviour.

Like many other good ideas in chemistry, it can be argued that supramolecular chemistry was inspired by nature,[1,2] critically including the weak interactions at the active sites of biomacromolecules that recognize, bind and enhance the reactivity of their guests.[3] At the other extreme lies classical coordination chemistry which, though not as directly, can also be seen to resemble natural systems in its detailed attention to the electronic environment of a single metal centre. What we propose here, rather than a departure from these two ideas, is to imitate nature on an intermediate length scale: a scale that is amenable to accurate *ab initio* analysis owing to its tractable size, and perfectly suited to reasoning using the simple and time-tested tools of structural chemistry.

The ideal length scale referred to above often coincides with the dimensions of enzyme cofactors: small molecules with precise, well-conserved[4] structures that are at the center of many critical biological pathways, Figure 1.1. Examining the reactivity of these and other cofactors has

revealed that they often take advantage of two familiar chemical phenomena: electron delocalization and tautomerism,[5] both of which we shall aim to leverage in order to achieve the goals set forth above.

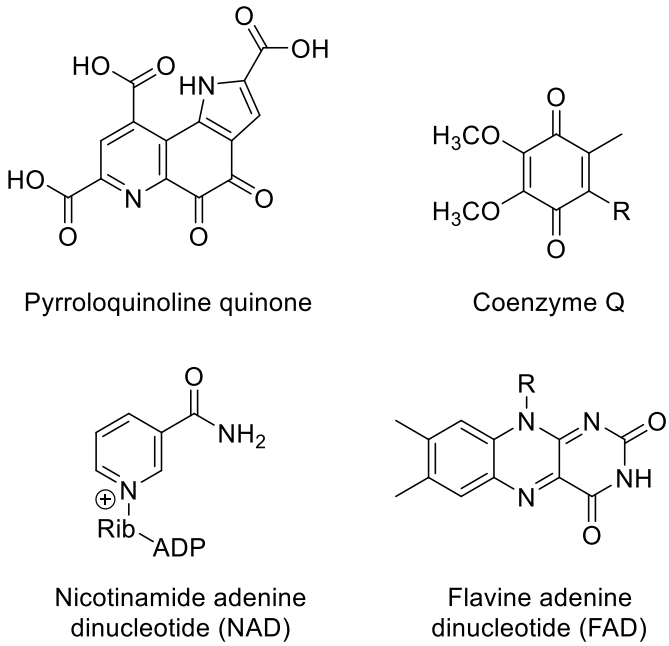

Figure 1.1. Examples of enzyme cofactors involved in catalyzing biological redox reactions.

1.1 Electron Delocalization

Instead of having of a formal definition in mind, working chemists often learn and think about electron delocalization through example systems (butadiene, benzene, α,β-unsturated carbonyl compounds) where a more flexible picture of bonding than a static sharing of an electron pair between two atoms needs to be invoked to account for observed structure and reactivity. Typically, these are molecules where a number of parallel *p* orbitals overlap side-on, causing a "spreading" effect where, *e.g.* what is formally described as the oxygen lone pair in phenol can profoundly affect reactivity in the remote *para* position by exerting a signficant presence there. Electron delocalization has been invoked to rationalize such diverse phenomena as the unique structure and reactivity of the benzene molecule,[6] the acidity of α hydrogens in carbonyl compounds,[7] the C–N

bond rotation barrier in amides,[8] and elongation of ligand bonds in coordination compounds in the presence of back-bonding.[9]

Although now a textbook concept and recognized by chemists for more than a century,[10] the exact nature and impact of electron delocalization in organic compounds is still debated.[7] This is remarkable given the proliferation of accurate quantum chemical calculations. Discussions of this type still aid chemists in constructing and re-adjusting their mental models of structure and reactivity. For instance, the relative contributions of π resonance stabilization versus the inductive effect to the acidity of carboxylic acids and enols (relative to that of regular alcohols) has seen much discussion.[11]

Several models have been developed to study electron delocalization. The most simple and widespread among these is the use of resonance structures: snapshots of extrema in electron distribution, termed resonance contributors, which are depicted as discrete Lewis structures. This simple model postulates that the actual electronic structure is an average of the various contributors, each contributing proportionally to its projected stability. Recent developments in quantum chemistry have placed this useful concept on firm theoretical foundations.[12]

Since the formulation of this picture, *ab initio* computational chemistry methods have progressed to the point where the electronic structure of a molecule can be routinely described in an accurate manner by assigning electrons to an array of whole-molecule wavefunctions, commonly termed *molecular orbitals*. These techniques have the advantage of, describing chemical systems using a simple mathematical model and sound physical theory with well-defined scope and assumptions/limitations.

Given its merits, one might hope that the *ab initio* picture be able to provide a straightforward description of electron delocalization that is easily reconcileable with the simple pen and paper model used by chemists. In practice, doing so is complicated by the fact that quantum chemical molecular orbitals *all* seems to extend throughout the molecule, apprently robbing conjugated π systems of their special status. What is it, then, that sets benzene and cyclohexane apart? Why is one easily described using as discrete two-atom σ bonds while the other cannot be understood without summoning the concept of a delocalized electron cloud?

Mathematically, it has been noted that the constituent single-electron wavefunctions of the Slater determinant describing a many-electron system can be combined using a unitary transformation without affecting the energy and properties of said determinant.[13] One can thus choose the unitary transformation to produce one-electron orbitals that are maximally localized, giving rise to localized molecular orbitals (LMOs). Depending on the mathematical criterion of locality, different localization schemes have been proposed, some of which can faithfully reproduce the familiar σ and π bonds used intuitively in chemistry.[14–17] A common feature of these methods is the ability to recover electron delocalization, namely in terms of LMOs that have signficant contributions from three or more atoms.

An alternative approach has to do with *resonance* and how chemists still find themselves reaching for this familiar concept in spite of the numerous advances in electronic structure theory.[18] In this case, the desire to reconcile *ab initio* methods with the intuitive resonance-based picture of electron delocalization in valence bond theory has led to the development of other pictures, *e.g.* generalized valence bond (GVB) and valence bond self-consistent field (VBSCF).[11,12,19] Briefly, this is achieved by associating each resonance structure with a *configuration* (*i.e.* Slater determinant) in the total electronic wavefunction of the molecule, Figure 1.2.

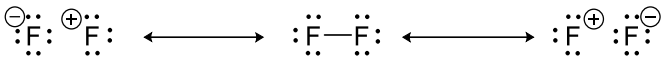

$$\psi = \alpha_{ionic1}\psi_{ionic1} + \alpha_{covalent}\psi_{covalent} + \alpha_{ionic2}\psi_{ionic2}$$

Figure 1.2. Generalized valence bond (GVB) picture of bonding in the F_2 molecule.

Ultimately, it is difficult to precisely identify what electron delocalization in the chemical sense *is*. More tangible answers might be within reach, however, if electron delocalization is measured as a response property, *i.e.* molecular response to an external perturbation is used to gauge the degree of electron delocalization. For instance, it has been shown that strong electron delocalization correlates with large molecular polarizability.[20] We shall encounter an application of this method in Chapter 2, where the calculated diamagnetic ring current in response to incident magnetic field is used to measure the degree of aromatic electron delocalization across a family of compounds.

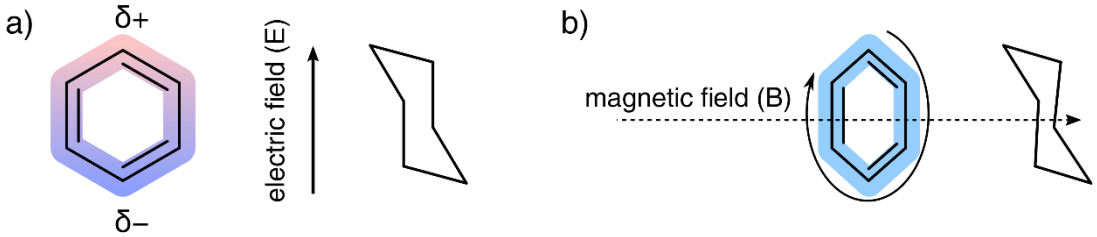

Figure 1.3. Enhanced polarizability as an electric field response property of molecules with extensive electron delocalization (a). Induced diamagnetic ring current in response to incident magnetic field as a magnetic marker of aromaticity.

1.1.1 Electron Delocalization in Nature and Synthetic Chemistry

As with other chemical effects, living systems have evolved to take advantage of electron delocalization, particularly in the context of catalysis. For example, the enzyme cofactor thiamine pyrophosphate (TPP, a derivative of vitamin B_1) facilitates decarboxylation reactions in all living organism through the mechanism shown in Figure 1.4.[21–23]

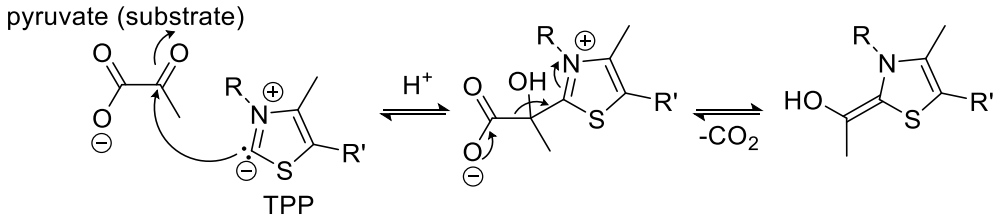

Figure 1.4. Partial mechanism for decarboxylation of pyruvate by the enzyme pyruvate dehydrogenase showing the action of cofactor thiamine pyrophosphate (TPP).

As the above example illustrates, precisely controlled electron delocalization, or lack thereof, underlies the effectiveness of TPP. Thus, enough electron delocalization is needed to stabilize the formally carbonanionic TPP ylide, but too much delocalization would deactivate the ylide towards nucleophilic attack on pyruvate in the first step. Similarly, in the second step, electron delocalization accommodates the negative charge left by the departing CO_2 molecule, stabilizing the transition state.

In a more familiar example, ascorbic acid (vitamin C) can protect organisms against radical chain reactions thanks to its ability to undergo one-electron oxidation to a radical stabilized by electron delocalization, Figure 1.5a.[24,25] Likewise, the ubiquity of coenzyme A in biological systems has been linked to the more facile cleavage of the C–S bond in thioesters relative to that of the C–O bond in the more common oxoesters due to more extensive electron delocalization in the latter, Figure 1.5b.[26]

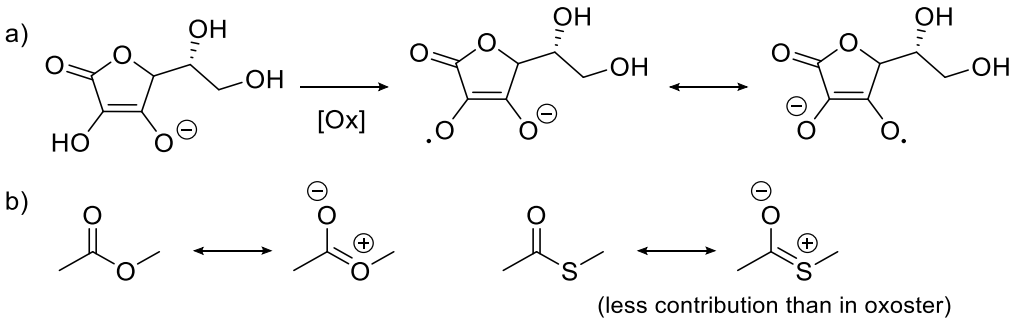

Figure 1.5. (a) One-electron oxidation of ascorbate to a delocalization-stabilized radical anion. (b) Comparison of electron delocalization between an oxyester and a thioester.

As in natural systems, electron delocalization is an invaluable tool in synthetic and materials chemistry. For instance, the stability of aryl trifluoroborates, critical to their application as ^{18}F PET imaging agents, shows acute dependence on the presence and position of electron donating or withdrawing groups on the aryl portion, Figure 1.6a.[27] Interestingly, electron donating groups in the *para* position produce a much larger acceleration than the same substituents in the *ortho* position. This can be attributed to the steric repulsion between the fluorine atoms and the *ortho* substituent when the $–BF_2$ moiety is coplanar with the aryl group to maximize electron delocalization, Figure 1.6b.[28] Chapter 4 examines a similar situation where more extensive electron delocalization is only possible at the cost of significant strain due to steric crowding.

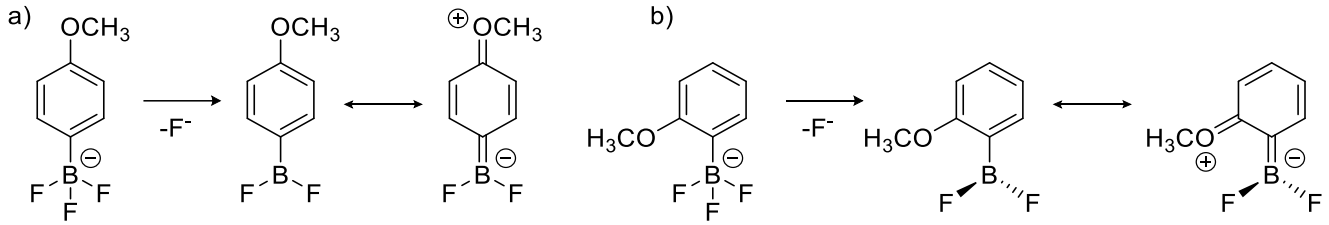

Figure 1.6. (a) Acceleration of aryl trifluoroborate hydrolysis by electron donating groups in the *para* position. (b) Limited electron delocalization in an *ortho*-substituted aryl trifluoroborate due to unfavourable steric interactions.

1.2 Tautomerism

Since the material in the following chapters frequently makes use of tautomerism, it is worthwhile at this point to revisit this textbook concept. Tautomerism is most commonly encountered in organic chemistry, where it underlies the interconversion of the keto and enol forms of carbonyl compounds, Figure 1.7a. This form of tautomerism is invaluable because of its contributions to the reactivity of these compounds, allowing both the oxygen and α carbon atoms

to act as nucleophile/base under different conditions. The example reaction in Figure 1.7b shows the versatility of this property.

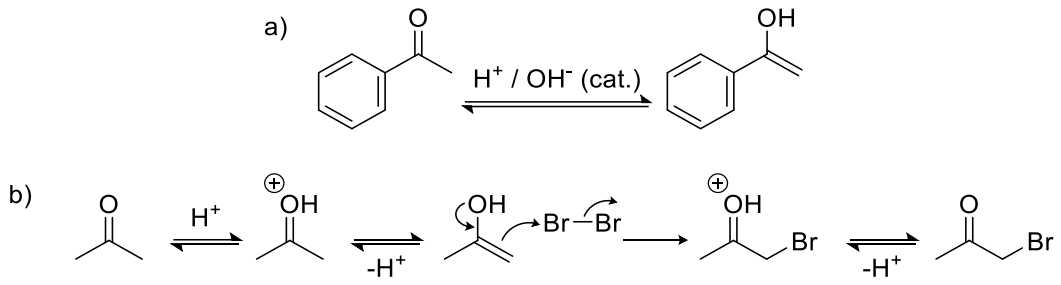

Figure 1.7. (a) Keto–enol tautomerism of acetophenone catalyzed by acid or base. (b) Bromination of acetone through its enol tautomer.

More generally, tautomerism is defined by IUPAC as a fast equilibrium whereby a group G (most commonly hydrogen) moves along a conjugated system as G^+, termed *electrofuge*, or G^-, termed nucleofuge,* Figure 1.8.[29] Although this definition might appear to overlap with that of a sigmatropic shift, tautomerism is a distinct concept as it does not constrain the mechanism by which the transfer occurs, merely specifying the initial and final connectivities.

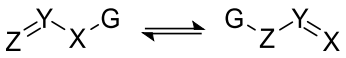

Figure 1.8. Tautomeric migration of group G along the X-Y=Z conjugated system.

As mentioned before, a common example of tautomerism is that between the keto and enol forms of carbonyl compounds. Tautomeric equilibria of this type are often mediated by solvent and acid or base, and are very slow in their absence. In contrast, certain systems, *e.g.* 2-pyridone, can undergo facile tautomerism by associating in solution as hydrogen-bonded dimers, Figure 1.9a.[30,31] In yet other systems, interconversion of tautomers can occur in an intramolecular fashion, *e.g.* Figure 1.9b. The structure of the various tautomers in these systems is reminiscent of

* Proton (H^+) or hydride (H^-), respectively, in the case of migrating hydrogen atoms.

resonance contributors except with atomic rearrangement. Naturally, fast interconversion is possible irrespective of solvent or catalyst in this case. This latter category of tautomeric equilibrium is attractive because it essentially allows the molecule to display two often contrasting characters, as explained in the next section.

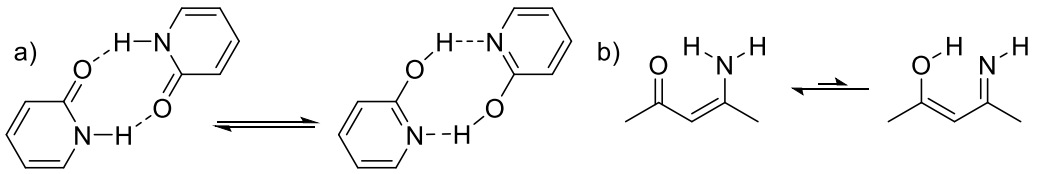

Figure 1.9. Tautomeric interconversion facilitated by dimerization. (b) Fast intramolecular tautomeric equilibrium.

The migrating group need not be proton or hydride. This is commonly seen in *ring–chain* tautomerism, illustrated in Figure 1.10a, where movement of the migrating group, often a nucleofuge, leads to ring formation.[6] Finally, it is worth mentioning that certain types of molecular interconversion are commonly termed tautomerism even though they do not satisfy the definition above.[*] For instance, rapid bond formation/breaking of the type shown in Figure 1.10b is called *valence tautomerism* by IUPAC,[32] yet does not feature the atom migration that distinguishes true tautomeric equilibria. This phenomenon is not exclusive to organic molecules; the manganese–porphyrinoid coordination compound in Figure 1.10c can exhibit valence tautomerism in the presence of the Lewis acidic Zn^{2+} cation.[33]

[*] Indeed, common cases of ring tautomerism (such as the ones shown in Figure 1.10a) do not conform to the IUPAC definition, either.

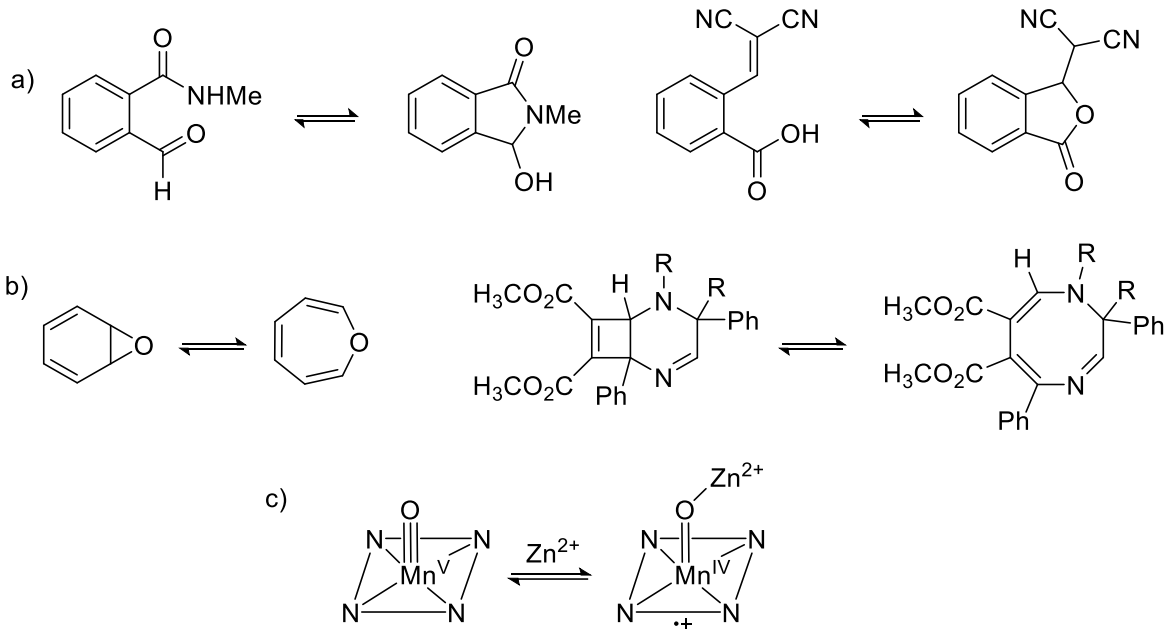

Figure 1.10. (a) Examples of ring–chain tautomerism.[6,34,35] (b, c) Examples of valence tautomerism in organic[36] and inorganic systems, respectively.

Since different tautomers have distinct sturctures and reactivities, the apparent properties of a given compound can be dramatically affected by factors influencing the position of the tautomeric equilibrium or the rate of equilibration. This problem is explored for a family of aromatic Schiff bases in Chapter 2, where the structural factors influencing the dominant tautomeric form are probed.

1.3 Tautomerism and Electron Delocalization

Separate discussion of electron delocalization and tautomerism might imply that they are independent. In reality, however, the two are intricately connected:[37,38] rearrangement of atoms during tautomeric interconversion can affect the relative contribution of the various resonance structures, thereby skewing electron distribution (as seen in Chapter 3); likewise, perturbations in electron distribution can lead to a change in the relative stability of different tautomers of a

molecule (as seen in Chapter 2).[39] The interplay between tautomerism and electron delocalization has been reviewed by Raczyńska *et al*.[40]

The mutual influence of electron delocalization and tautomerism has been extensively studied in the case of acetylacetone and other molecules with RC(=X)–CH=C(YH)R′ (X, Y = O/NH) connectivity, which are noted for the formation of unusually strong hydrogen bonds.[41,42] Furthermore, it is found that within this category of organic compounds, more even delocalization of electrons leads to stronger hydrogen bonds, Figure 1.11a. This has led to formulation of the *PA rule*, which states that the X–H···Y hydrogen bond is strongest when X and Y have the same proton affinity (PA)[*] values. Interestingly, Plusiak and Solà have noted that the equivalent interaction in salicylaldehydes leads to reduction of various markers of aromaticity, since it requires that the aromatic π sextet be localized, Figure 1.11b.[43]

[*] pK_a values for XH and YH can be used for comparison of the proton affinities of X and Y.

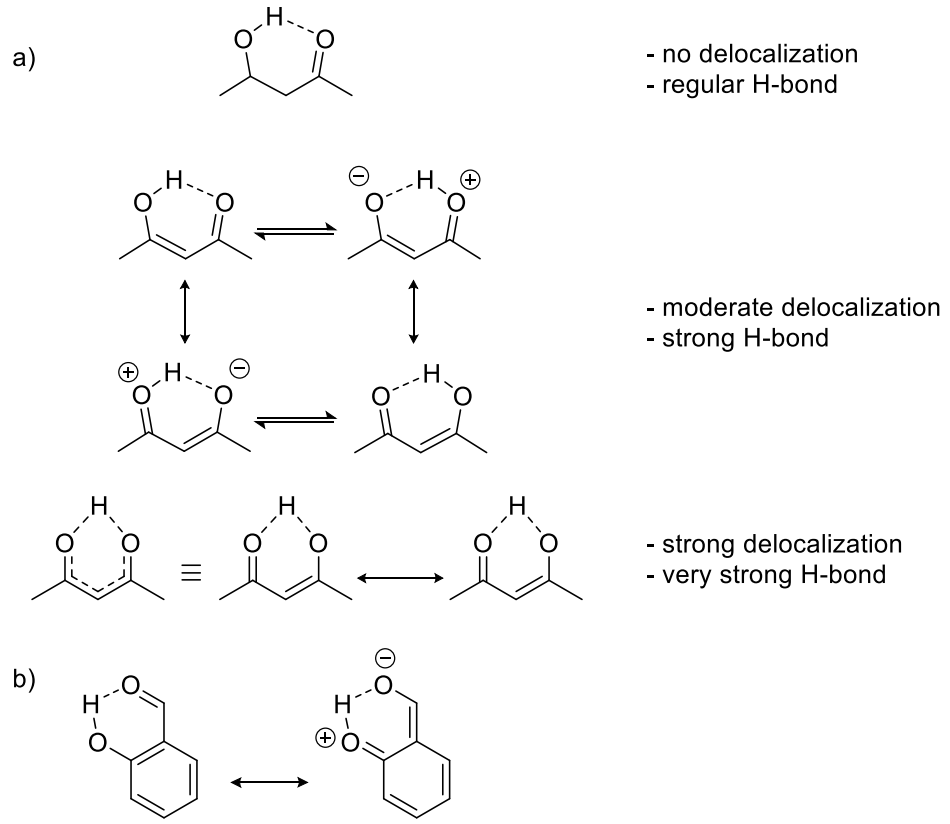

Figure 1.11. (a) Regular hydrogen bond and tautomeric equilibrium in the absence of strong electronic coupling. (b) Strong, resonance-assisted hydrogen bond with extensive electronic coupling.

From the practical point of view, tautomerism is useful in the context of electron delocalization because small rearrangements in molecular structure can alter the relative stabilities of the various modes of electron delocalization for a molecule, as demonstrated in the case of acetone in Figure 1.7b. The tandem movement of atoms and redistribution of electrons in tautomeric interconversions can thus furnish low-energy pathways for chemical reactions. Electronic coupling, on the other hand, provides a means of communication between remote atoms, potentially allowing a single molecule to expose both acidic and basic termini at the same time. For instance, the mutarotation of glucose and aminolysis of esters are both accelerated by 2-pyridone due to the interactions depicted in Figure 1.12.[44–47] This form of acceleration is not simply due to the presence of hydrogen bonding groups on 2-pyridone. Indeed, the acceleration is much

smaller when 2-pyridone is replaced with a compound without electronic coupling between the O and N termini, such as 2-hydroxypiperidine. Analogous activity has been observed with benzoic acid, pyrazole, and 1,2,4-triazole, all of which can exhibit delocalization-coupled tautomeric activity.[48] One source of inspiration in our work is to leverage similar tautomeric interconversions to activate molecules toward otherwise extraordinary reactivity.

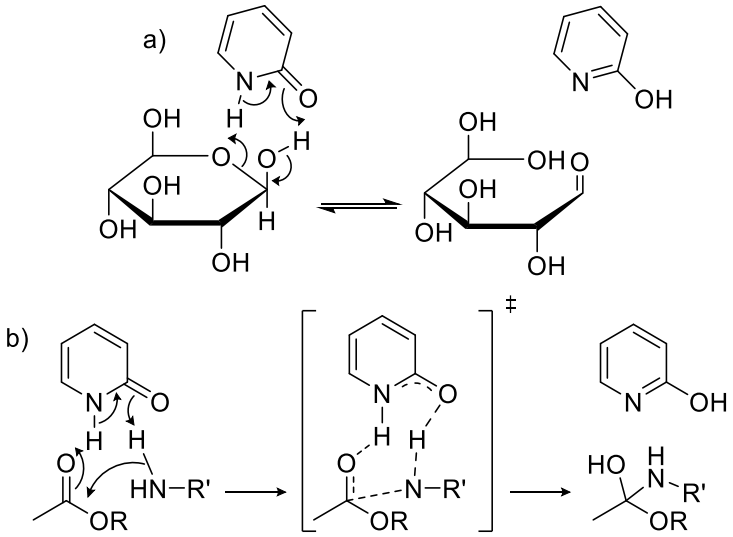

Figure 1.12. Partial mechanism for 2-pyridone catalyzed mutarotation of glucose (a) and ester aminolysis (b).

1.4 Salicylimines

Salicylaldimines (SANs) and salicylketimines are *o*-hydroxy Schiff bases of aromatic aldehydes and ketones, respectively. Known collectively as *salicylimines*, these compounds are best known for their ubiquity in coordination chemistry as the salen and salphen chelating ligands, Figure 1.13a. Owing to the labile nature of the acidic –OH proton, salicylimines can undergo fast intramolecular tautomeric interconversion between two tautomeric forms: enol-imine and keto-enamine, Figure 1.13b. In both tautomers, π electron delocalization pathways connect the oxygen and nitrogen termini through the aromatic system, making salicylimines ideal for the tandem study

of tautomerism and electron delocalization. The rich tautomeric and electron delocalization properties of salicylimines is the focus of this thesis.

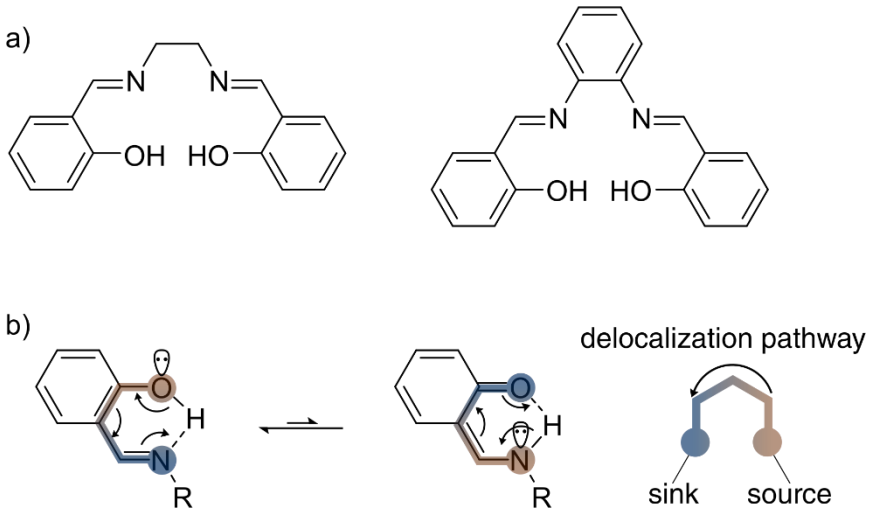

Figure 1.13. (a) Representative salen (left) and salphen (right) ligands. (b) Enol-imine/keto-enamine tautomerism in a SAN.

Salicylimines can be prepared in a straightforward fashion from the direct condensation of primary amines with the parent aldehyde or ketone. While ketones typically require heating, catalyst, or both to react with amines, the condensation reaction with aldehydes has a low activation barrier and is therefore often reversible at room temperature. The reversible nature of SAN formation has been exploited by us and others to create self-assembled macromolecules, examples of which are shown in Figure 1.14.[49–53]

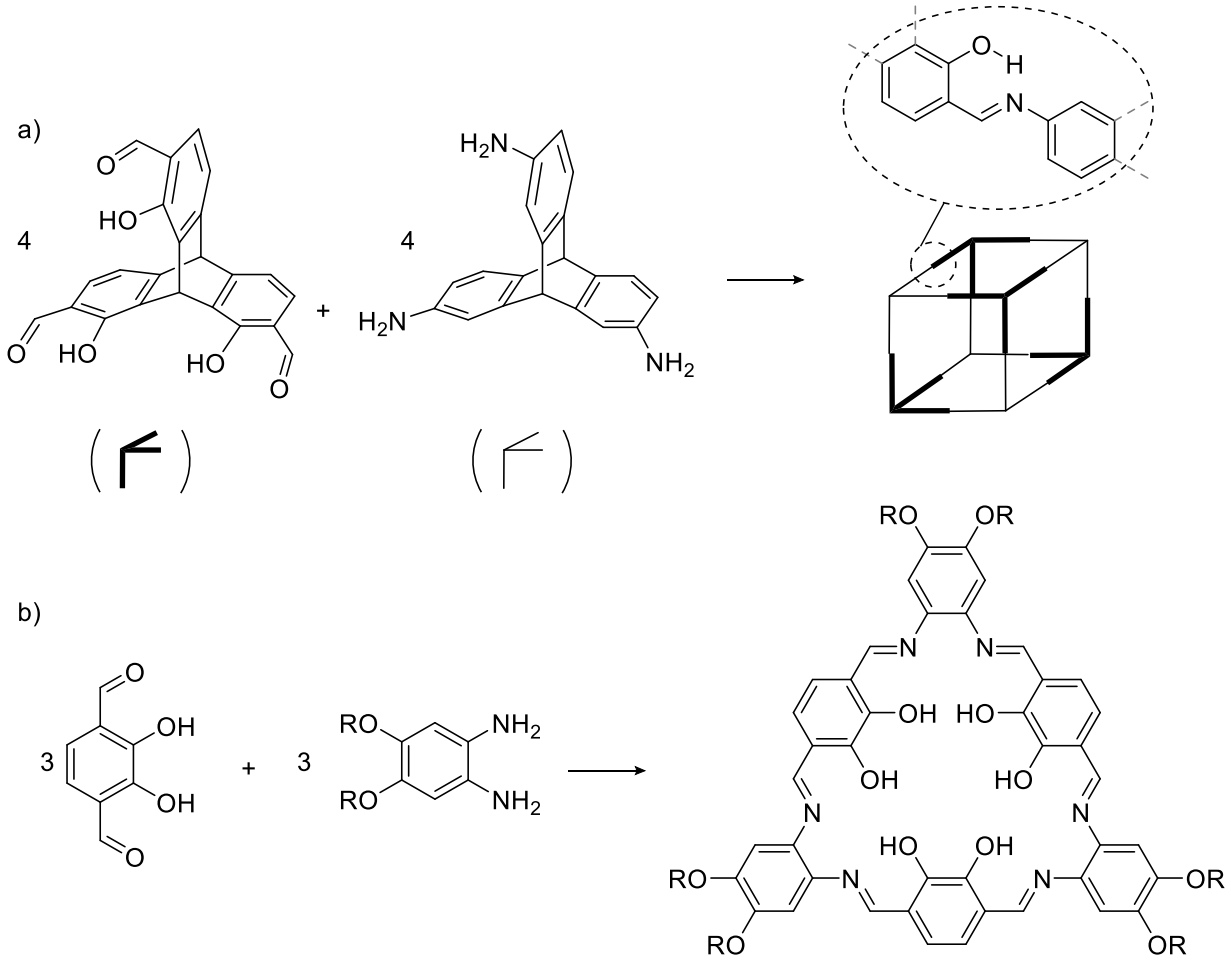

Figure 1.14. (a) Self-assembled cube held together by 12 SAN linkages.[52] (b) Self-assembled Schiff base macrocycle.[54]

Salicylimines are not only of interest in the laboratory; there is plenty of inspiration to draw from the tautomeric chemistry of salicylimines found in biological systems. The extremely versatile coenzyme pyridoxal phosphate (PLP, vitamin B_6, Figure 1.15a) is involved in at least 145 enzymatic reactions, almost all of which involve the SAN formed by condensation of PLP with an amine function in its various substrates.[55] Figure 1.15b shows an amino acid racemization

reaction,* for instance, where electron delocalization between the PLP pyridinium and the newly formed SAN stabilizes the negative charge from deprotonation of the amino acid backbone.[56,57]

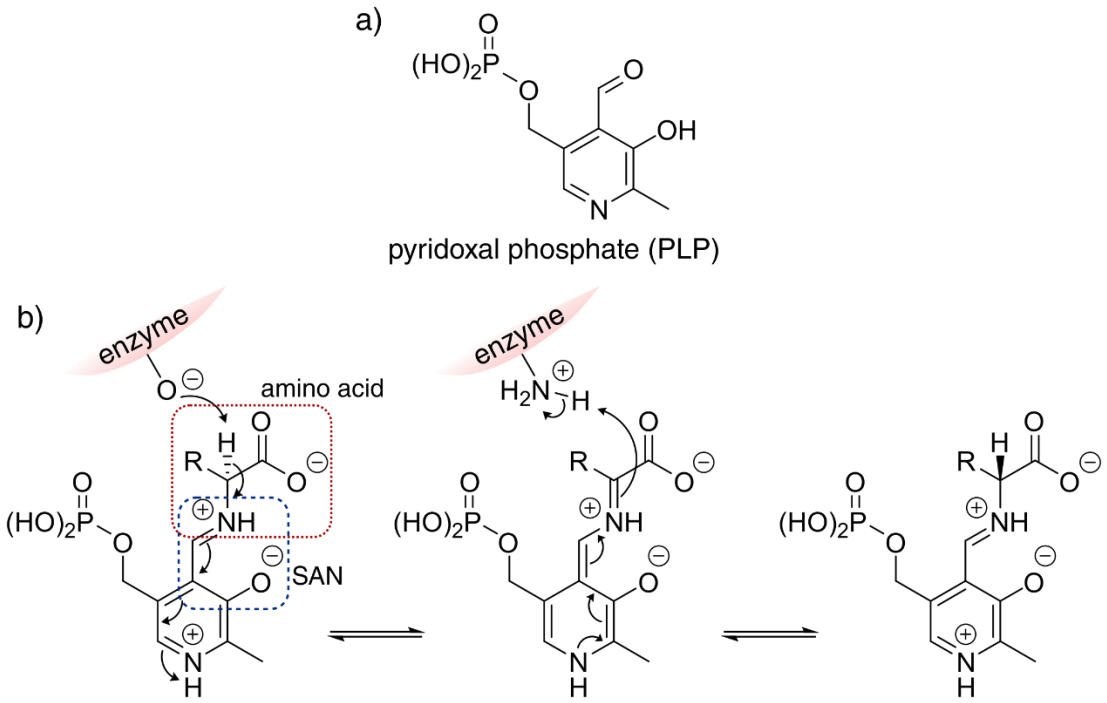

Figure 1.15. (a) Enzyme cofactor pyridoxal phosphate (PLP). (b) Enzymatic amino acid racemization catalyzed by PLP.

The example above is a reminder of the familiar observation that electron delocalization can act to disperse any destabilizing charge accumulation during reactions. From the point of view of functionality, enzyme cofactors like PLP can be compared to transition metal catalysts as they can bring about more flexibility in bond formation and cleavage. As we shall see in the following chapters, the combination of electron delocalization and tautomerism in synthetic salicylimines can be exploited to similar effect.

* To be fair, one must also take into account substrate/coenzyme interactions with the enzyme manifold acting as base, then acid in the first two steps of the above mechanism.

A large part of our interest in salicylimines is due to the interplay between tautomerism and competing modes of electron delocalization in these compounds. Specifically, electron delocalization can occur around the aromatic ring or in the peripheral enol-imine/keto-enamine moieties. As expected, the position of the labile hydrogen atom (enol-imine vs. keto-enamine) has a profound effect on the relative contribution of these competing delocalization modes, Figure 1.16.

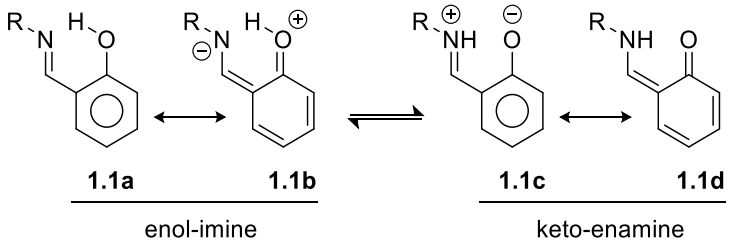

Figure 1.16. Resonance contributors for the enol-imine and keto-enamine tautomeric forms of a SAN.

Of the four structures in Figure 1.16, **1.1b** and **1.1c** are zwitterionic contributors, with separated positive and negative formal charges. To avoid charge separation, one would expect the canonical aromatic structure **1.1a** and the quinoidal structure **1.1d** to be the major contributors to the enol-imine and keto-enamine tautomers, respectively. Experimental and *ab initio* results presented in the following chapters generally support this simple assessment, although any of the four structures can become representative depending on the specific SAN and conditions under study. For instance, Ogawa and coworkers found that the enol-imine form of compound **1.2**, Figure 1.17, dominated in solution, while the keto-enamine tautomer was prevalent otherwise. Interestingly, this keto-enamine structure is best described as a zwitterion (like **1.1c**) in the crystalline state and as having exocyclic double bonds (like **1.1d)** in the gas phase.[58,59]

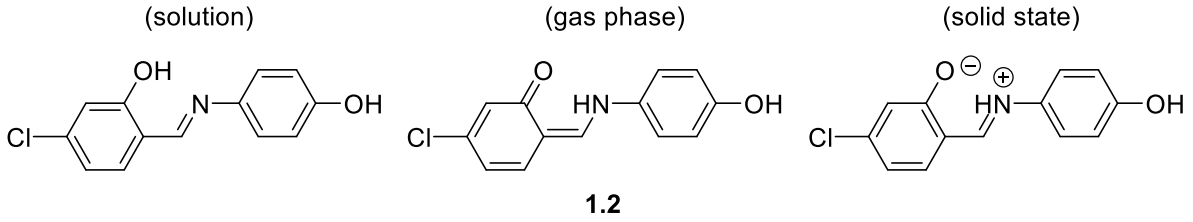

Figure 1.17. Dominant tautomers/resonance contributors for compound **1.2** under various conditions.

The presence of alternative modes of electron delocalization in SANs can be synthetically useful. For instance, as demonstrated in Chapters 2–4, the keto-enamine tautomeric form allows electrophilic aromatic substitution (EAS) reactions to proceed more easily. In other words, the sp^3-hybridized Wheland complex formed during EAS is stabilized in these compounds since electron delocalization can be offloaded to the peripheral keto-enamine arms, Figure 1.18. We make use of this property in Chapter 3 to bring about H/D exchange at specific aromatic positions under very mild conditions. Similar tautomeric activation of aromatic systems has the potential to bring the versatility of enolate/enamine chemistry (*e.g.* aldol-, Stork-type reactions) to aromatic systems.

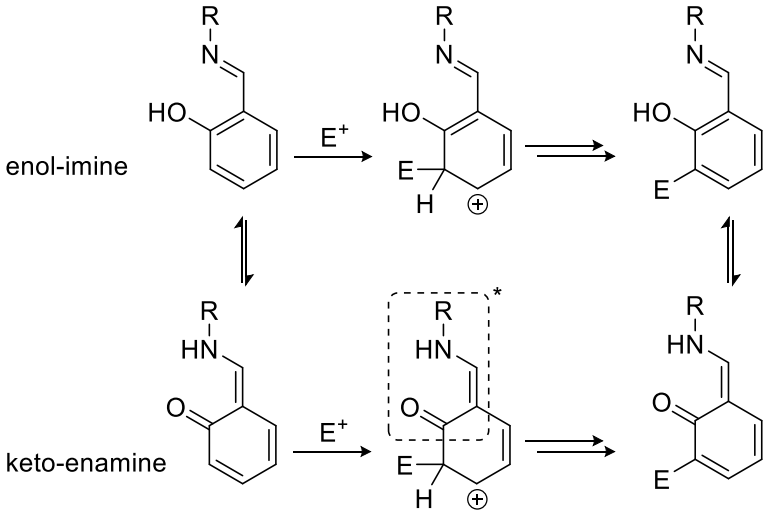

Figure 1.18. Electrophilic aromatic substitution reaction of a TSAN substrate (*: electron delocalization in keto-enamine periphery undisturbed by formation of Wheland complex).

In 2003 the MacLachlan group reported the first example of a tris(salicylaldimine), also known as TSAN.[49] TSANs are conveniently prepared by direct condensation of primary amines with 2,4,6-triformylphloroglucinol* (TFP), Figure 1.19. They are notable for their unusual robustness and strong intramolecular hydrogen bonds. Since their discovery, TSANs have seen rapid uptake in the fields of supramolecular and materials chemistry. Among other applications, they have seen use as building blocks in covalent organic frameworks and molecular capsules.[60–67]

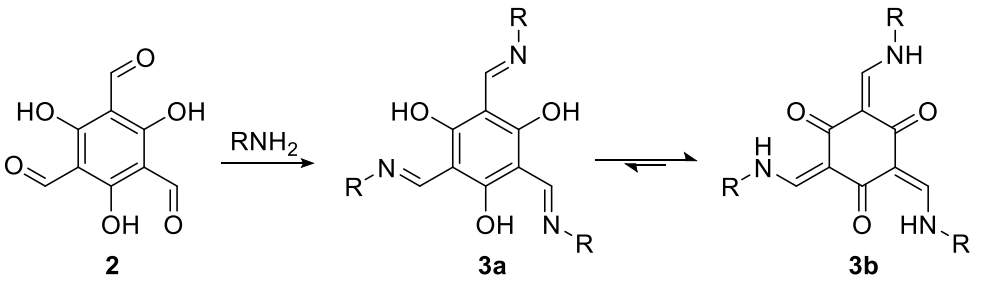

Figure 1.19. Preparation of a TSAN from TFP and a primary amine.

Unlike simple SANs, TSANs have a strong preference for the keto-enamine tautomeric form both in solution and in the solid state, a well-known property with various implications for their applications. Chapter 2 tackles the rather unexplored question of why the keto-enamine form of these compouds is more stable and introduces surprising examples of enol-imine TSAN analogues.

1.5 Tautomerism versus Resonance in SANs

Tautomeric interconversion in SANs is notable since it requires relatively little atomic motion. Indeed, the only skeletal changes during the process is the electrofuge movement of a hydrogen atom between the oxygen and nitrogen atoms. Whereas this movement is very facile thanks to the labile nature of the migrating proton, we were also interested in what would happen if a non-labile

* IUPAC name: 2,4,6-trihydroxybenzenetricarbaldehyde.

group is used instead of the hydrogen atom. Is the extensive degree of electron delocalization seen in SANs predicated on the labile character of the H atom? To answer this question, in Chapter 4 we prepare a TSAN analogue where the exchanging proton is replaced with a methyl group attached to the nitrogen atom. This has the consquence of locking the structure in keto-enamine-like connectivity, Figure 1.20.

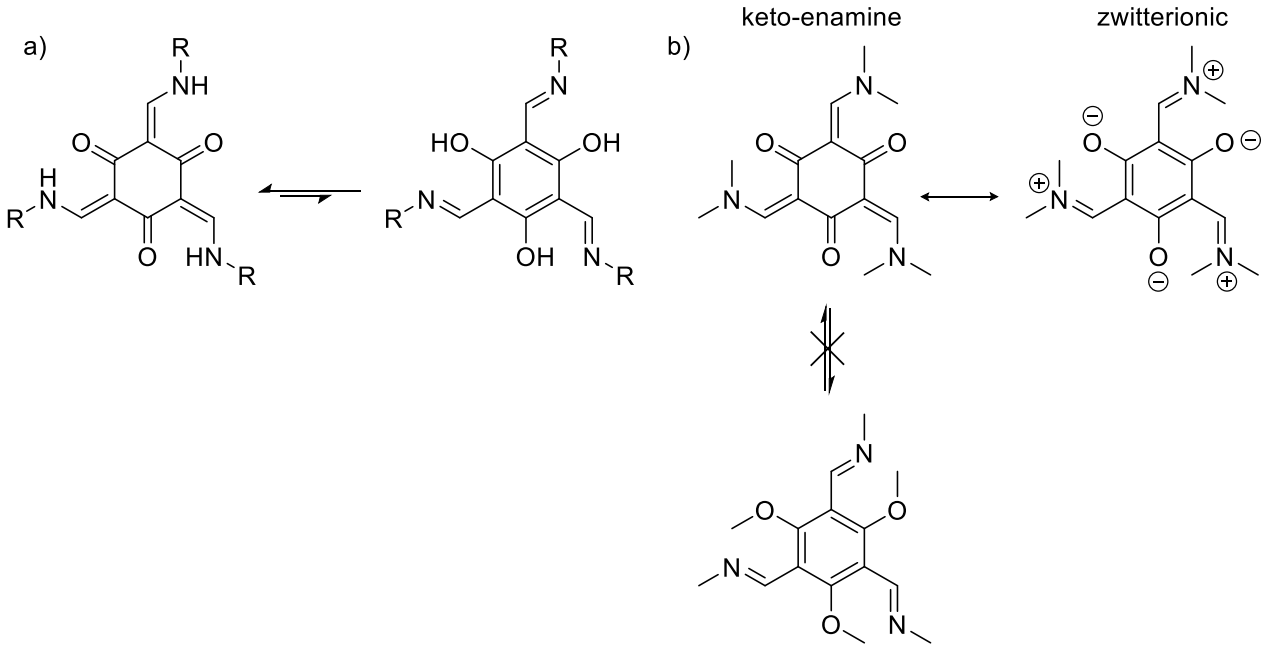

Figure 1.20. (a) Tautomeric interconversion in a regular TSAN. (b) Resonance in a TSAN "locked" in keto-enamine connectivity.

Nevertheless, extensive electron delocalization between the enamine arms and ring keto moieties causes the enamine arms to become approximately coplanar with the central ring. This occurs in spite of the steric repulsion between the carbonyl oxygen atoms and the enamine methyl groups (since they are much larger than the NH/OH hydrogen atom in a regular TSAN). As a result, the molecule adapts an unusual contorted shape in order to relieve the strain.

1.6 Efficient Methods of Salicylaldehyde Synthesis

Aromatic aldehydes are important precursors to the compounds studied in this thesis. In particular, aromatic compounds containing multiple *o*-hydroxy formyl moities are used in the formation of SANs. Though a variety of methods for formylation of aromatic compounds exist, examples of which are shown in Figure 1.21, we found them inefficient when it comes to multiple formylation of our electron-rich substrates (*e.g.* phenols, resorcinols).

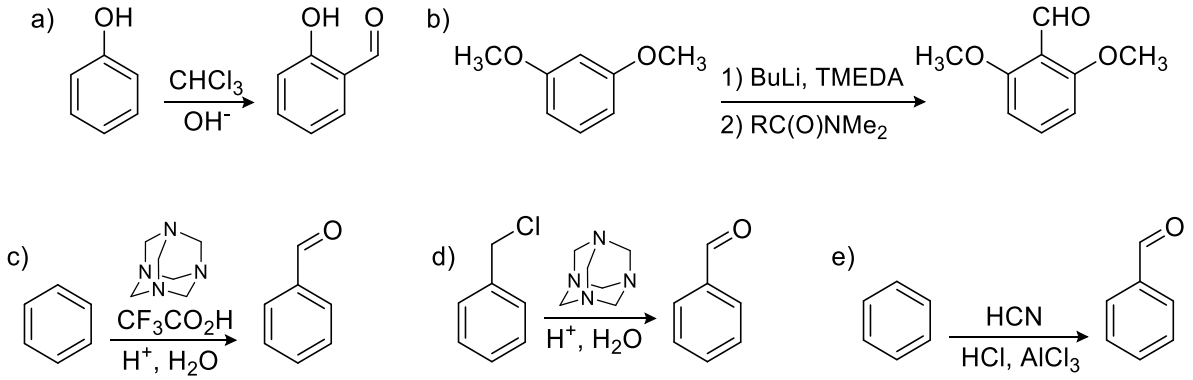

Figure 1.21. Examples of aromatic formylation reactions. (a) Reimer-Tieman reaction.[68,69] (b) Metallation and quenching.[70] (c) Duff reaction.[71] (d) Sommelet reaction.[72] (e) Gattermann reaction.[73]

Chapter 5 addresses this problem by adapting a protocol originally proposed for the monoformylation of anilines to multiple formylation of phenols. Interestingly, similar electron delocalization phenomena as those studied in the previous chapters are key to devising an efficient formylation protocol for these substrates.

Taken together, I hope that the material in the following chapters serves to illustrate the opportunities accessible by careful tuning of electron delocalization and the relative stabilities of competing tautomeric forms. Although most model systems studied here are discrete organic compounds, it is straightforward to envision applications in materials chemistry, as indicated by

the soaring number of publications on salicylaldimine-based covalent organic frameworks (COFs), or coordination chemistry, particularly in the design of non-innocent ligands for catalysis.

Chapter 2

Tautomeric Behaviour in TSANs: Understanding the Driving Forces

The material discussed in this chapter developed naturally in the course of designing Schiff base precursors to large hydrogen-bonded networks. The counter-intuitive tautomeric behaviour of these Schiff bases prompted us to look more closely at the factors governing the tautomeric equilibrium and devise a simple structural model to explain it. The various stages are presented here in the original chronological order to better convey the exciting and open-ended nature of this project. The discussion culminates in the question of whether the driving forces involved can be tapped into in order to bring about extraordinary reactivity.

2.1 Introduction

Schiff bases of 2,4,6-triformylphloroglucinol (TFP), also known as tris(salicylaldimines) (TSANs), are stable compounds that are easily prepared from the condensation of TFP and primary amines, Figure 2.1. In addition to being robust trivalent linking units, TSANs are ideal model systems for the study of tautomerism and electron delocalization, since their structure allows them to switch between two readily interconvertible tautomeric forms.

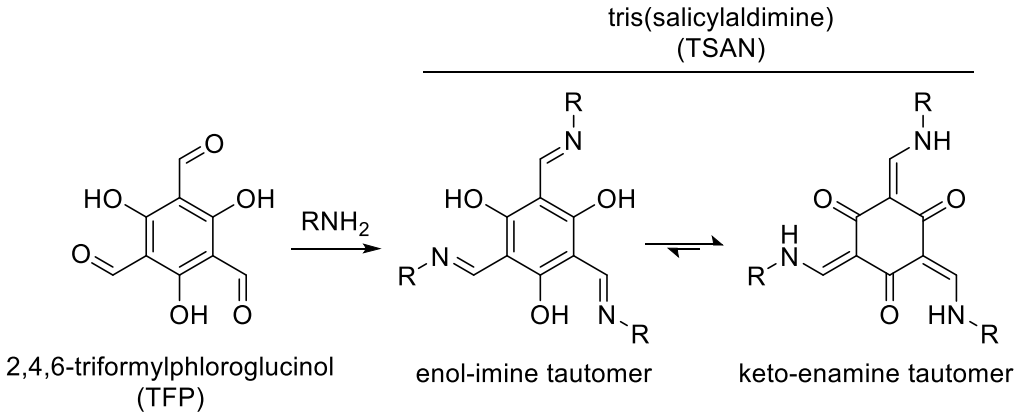

Figure 2.1. Preparation of TSAN from direct condensation of TFP and primary amine RNH_2.

2.1.1 Early Examples and Current Applications of TSANs

Virtually no work was published on TSANs prior to 2003. Given their straightforward synthesis from TFP, Figure 2.1, the lack of work on these compounds can be attributed to the difficult preparation of TFP itself. Indeed, before 2003, the only published route to TFP was an inefficient seven-step procedure.[74] The initial report of TSANs included a simple one-step preparation of TFP, which paved the way for wider adoption of TSANs by various researchers. The efficient preparation of TFP and similar compounds is the subject of Chapter 5.

Since this first report, TSANs have enjoyed continuous attention thanks to their stability, triple connectivity, and their straightforward self-assembly in solution. A survey of the literature reveals more than 120 papers and patents using TSANs as a stable linking motif in a variety of macromolecules and supramolecular systems.[63,75–77]

2.1.2 Structure and Hydrogen Bonding in Keto-Enamine TSANs

In their initial report on TSANs, the authors noted the unusually complicated ^{1}H NMR spectrum of TSANs (Figure 2.2 shows an example). This spectrum shows couplings between the downfield H-bonding protons and the CH protons on the sidechains. Additionally, both signals appear in groups of four. These observations indicate that the molecule adopts a predominantly keto-enamine structure in solution, where the exocyclic C–CH bonds have sufficient double bond character to allow the symmetric and asymmetric forms of the compound to be distinguished at room temperature.

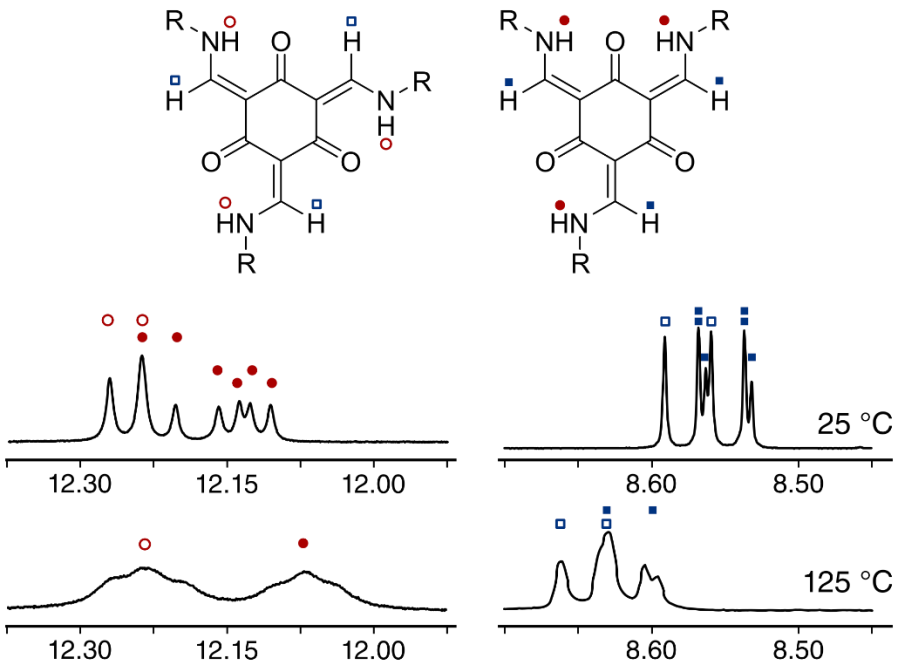

Figure 2.2. ^{1}H NMR spectrum of a TSAN showing the prevalence of the keto-enamine tautomer and geometric isomerism even at 125 °C (DMSO-d_6, 400 MHz, R = Ac).

Crystallographic characterization of TSANs are consistent with the above description. Figure 2.3 shows the structure of a typical keto-enamine TSAN derived from single-crystal X-ray diffraction (SCXRD) data,[78] comparing the observed interatomic distances to various reference bond lengths. Thus, CH–N and ring C–C bonds are best described as single, whereas C–O and C–CH bonds have more double-bond character. These assignments are in line with the description of TSANs as *heteroradialenes*: cyclic molecules with exocyclic double bonds. Closer investigation of heteroradialene character in a strained keto-enamine TSANs is the focus of Chapter 4.

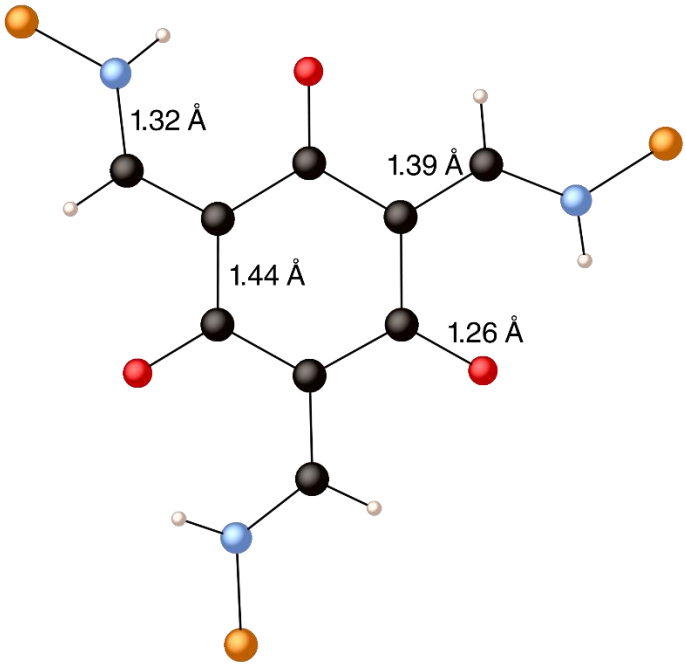

Reference bond lengths

C—C	1.46 – 1.52 Å
C=C	1.30 – 1.34 Å
C⋯C	(C_6H_6) 1.397 Å
C—N	1.38 – 1.48 Å
C=N	1.21 – 1.31 Å
C—O	1.34 – 1.45 Å
C=O	1.16 – 1.23 Å

Figure 2.3. Bond lengths (molecular average) for a typical keto-enamine TSAN based on SCXRD data (left) and experimental bond length ranges for various atom connectivities (right). Structure truncated (orange atoms = CH(*i*-Pr)CH_2OH).[78]

2.1.3 Geometric Isomerism in TSANs

NMR spectra of keto-enamine TSANs often show comparable amounts of C_{3h} and C_s isomer, suggesting that the two should have very similar stabilities. Indeed, calculating the energies of the optimized geometries for the C_{3h}- and C_s-symmetric isomers of the model compound shown in Figure 2.4 reveals a small energy difference of only 1.0 kcal/mol. The bottom spectrum in Figure 2.2 shows that interconversion between the symmetric and asymmetric forms is slow, even at 125 °C, confirming that the two are genuine geometric isomers rather than mere conformers.

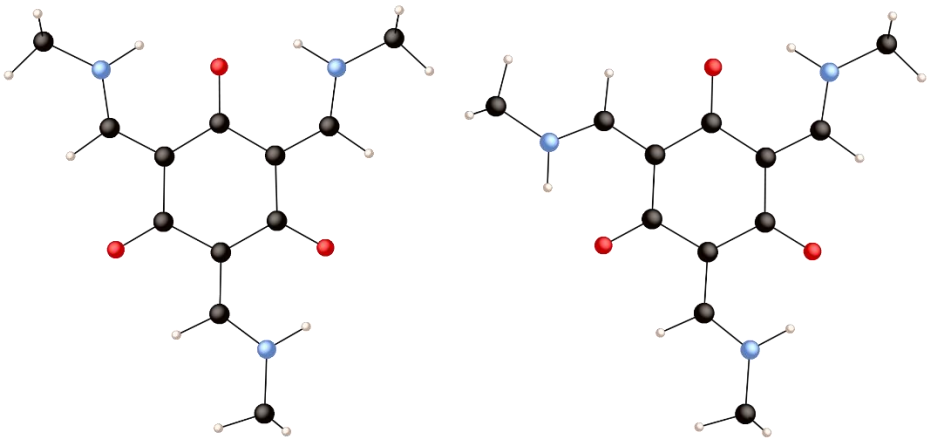

Figure 2.4. Optimized geometries for the C_{3h} and C_s geometric isomers of a model keto-enamine TSAN (B3LYP/Def2TZVPP).

It is worth mentioning that although this type of geometric isomerism could find use in a number of applications (*e.g.* optical switching, mechanochemistry), it can be a major impediment to preparing TSAN-based macromolecules. This is due to the large number of possible geometrical isomers when multiple TSAN units are present in the same molecule. For instance, Figure 2.5 shows an incomplete list of geometric isomers for a macromolecule incorporating four TSAN units in a triangular arrangement (the complete list would contain many more). Due to the similar stabilities of these configurations, one would expect them to form in roughly equal amounts, making isolation of a single configuration extremely challenging.

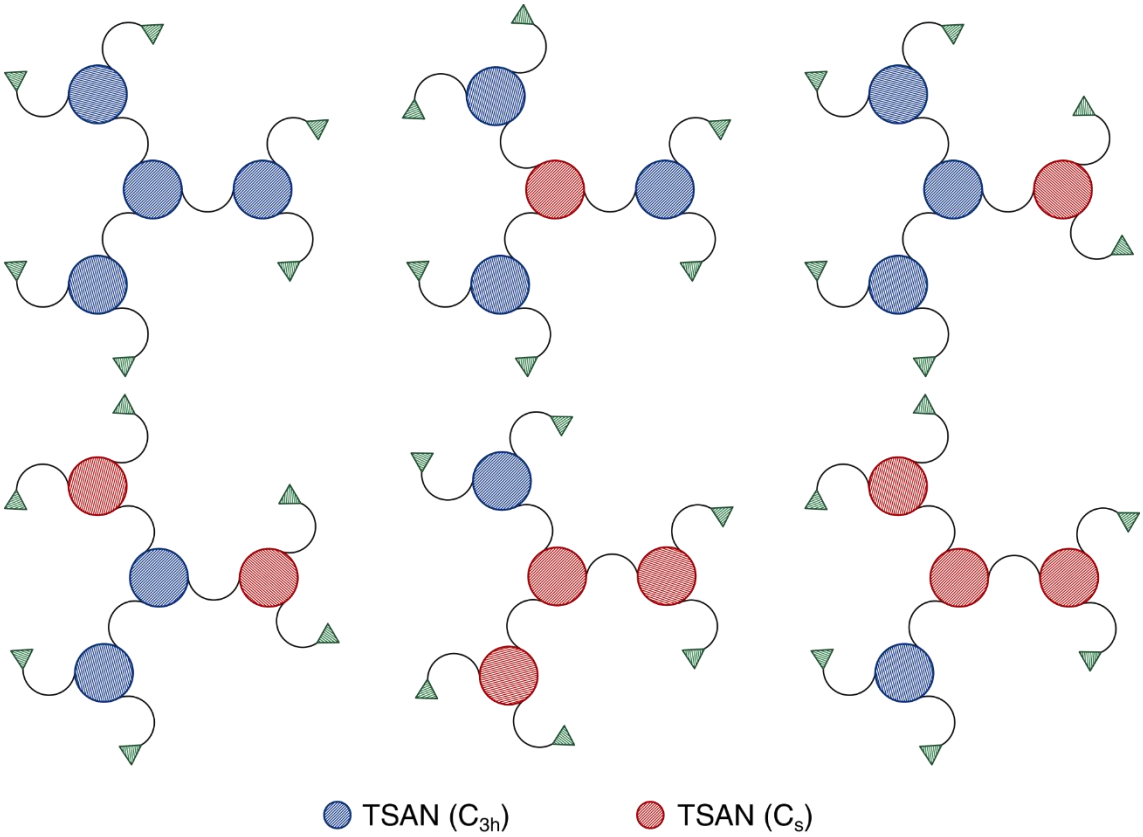

Figure 2.5. Partial list of possible configurations for a molecule incorporating four TSAN moieties.

2.2 H-Bonding TSANs

The material in this chapter has its roots in a research proposal on networks of tiled, strongly hydrogen-bonding TSANs prepared from small hydrogen-bonding amines, Figure 2.6. Since each molecule of **2.1** has three available H-bond donors (in the form of the exterior NH hydrogens) and three available H-bond acceptors (in the form of the dangling oxygen lone pair), it was hypothesized that molecules of **2.1** would self assemble into large two-dimensional sheets held together by these intermolecular hydrogen bonds.

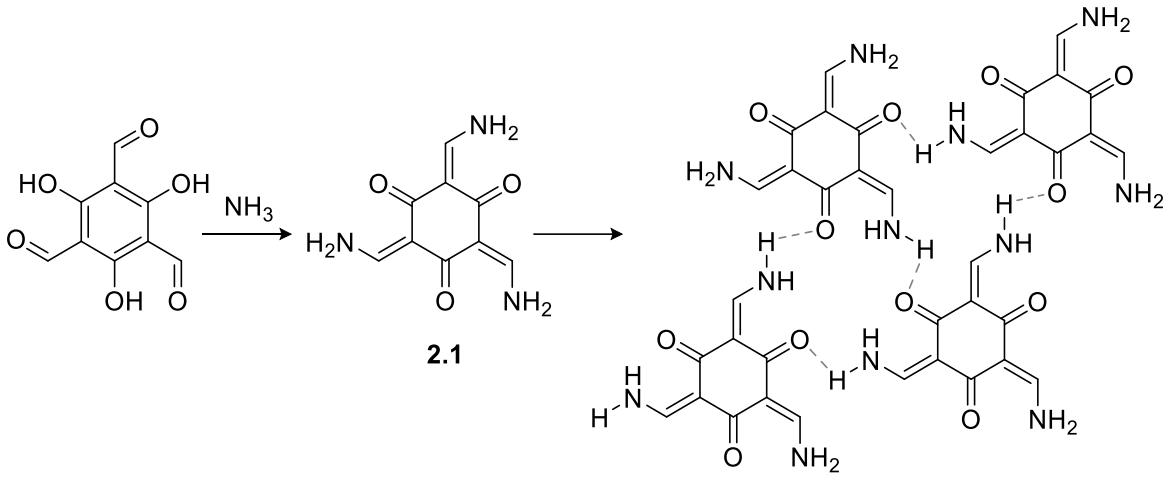

Figure 2.6. Hydrogen-bonded network of TFP-ammonia Schiff base 2.1.

The preparation of **2.1** is straightforward: TFP is combined directly with aqueous ammonia or ammonia gas is bubbled into a suspension/solution in a suitable solvent (such as methanol). The reaction with aqueous ammonia gives an orange solution, from which an orange-brown powder gradually precipitates. On a few occasions, purple crystals also appeared at this stage. SCXRD data for these crystals show the asymmetric species shown in Figure 2.7.

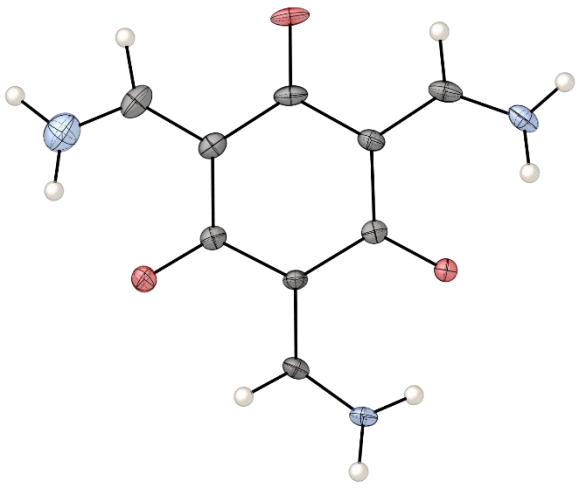

Figure 2.7. Thermal ellipsoid diagram (50%) for the asymmetric geometric isomer of **2.1** as determined by SCXRD.

As expected, the lack of rotational symmetry in this molecule precludes the formation of the tiled hydrogen-bonded sheets that we had hoped to obtain with its putative C_{3h}-symmetric counterpart. Instead, the herringbone packing in Figure 2.8 is seen. Presumably, the powder portion of the precipitate contains the desired symmetric form of the compound. Unfortunately, we were never able to obtain single crystals of C_{3h}-symmetric **2.1**.

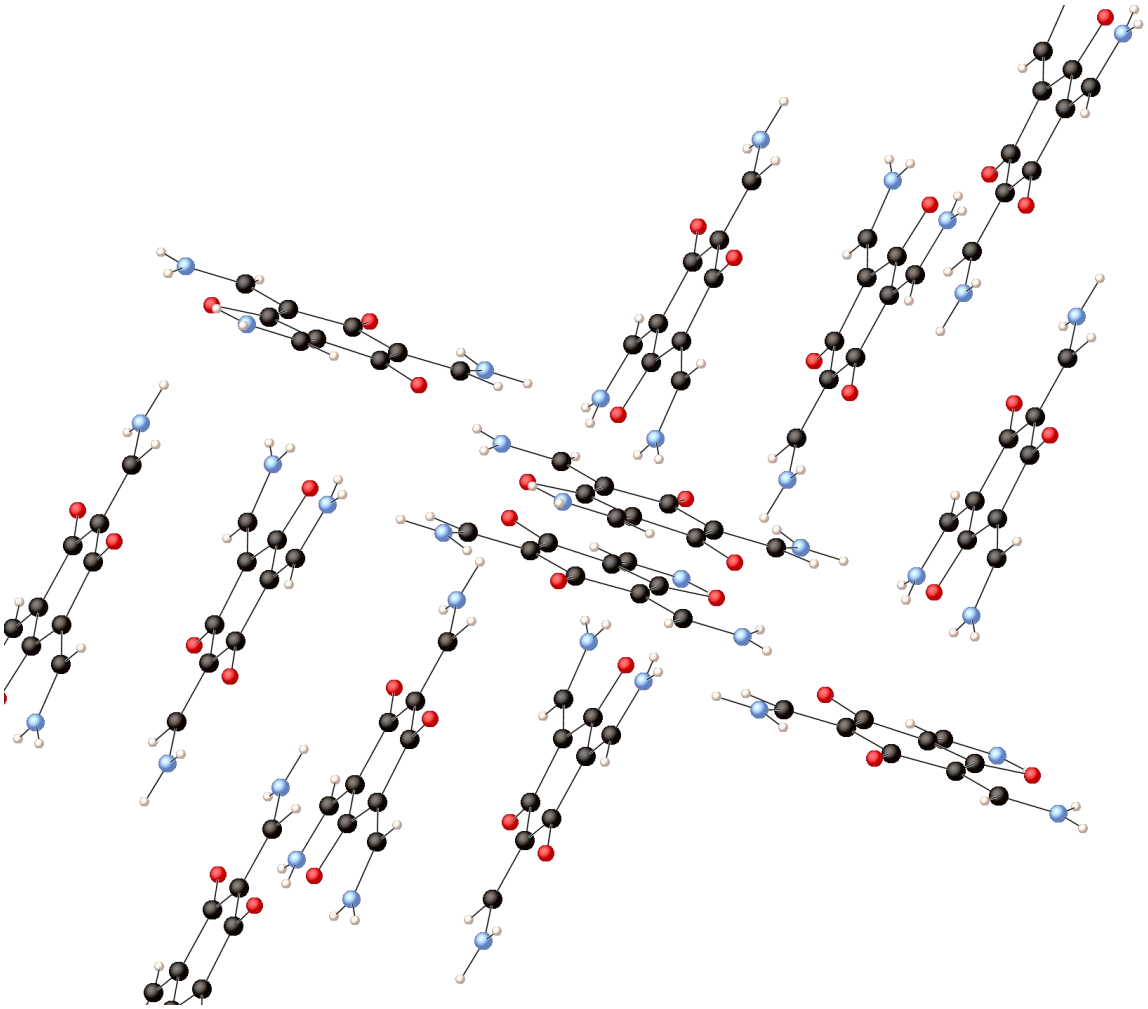

Figure 2.8. Section of the crystal packing from the SCXRD of **2.1**.

Further characterization of **2.1** was complicated by its unusual aggregation behavior. For instance, once precipitated from solution, the compound cannot be re-dissolved in water or any

other solvent.[*] This is consistent with the strong and highly specific interactions between molecules of **2.1** and has been shown in similar planar molecules with strong intermolecular interactions.[79] We were able to confirm that the elemental composition of this insoluble powder is consistent with the species observed by SCXRD. Interestingly, this Schiff base is extraordinarily stable toward hydrolysis: suspensions of **2.1** survive boiling in 9 M H_2SO_4 for 30 min. While keto-enamine TSANs have been noted for their robustness toward hydrolysis,[49] this degree of resilience is unprecedented and most likely due to strong hydrogen bonding between molecules of **2.1**.

We have since found a workaround to the problem of aggregation, which has allowed us to properly characterize **2.1** in solution. In this solvent-free route, TFP is combined with a large excess of ammonium carbonate at 80 °C, essentially combining TFP with ammonia produced *in situ* from the decomposition of ammonium carbonate. We suspect that symmetric **2.1** does not find the opportunity to aggregate under these solvent-free conditions, given the product is readily soluble in polar organic solvents. Figure 2.9a shows the COSY NMR spectrum of **2.1** prepared in this fashion (Figure 2.9b goes further to show that the CH resonances for the C_{3h} and C_s symmetric forms can be individually assigned in CD_3OH). Scalar coupling between the CH and both NH_2 protons in Figure 2.9b confirms the keto-enamine structure. Note the similarity of this spectrum to that of the keto-enamine in Figure 2.2.

[*] Solvents attempted: water, CH_2Cl_2, $CHCl_3$, EtOH, MeOH, acetone, toluene, benzonitrile, acetonitrile, DMF, DMSO, formamide.

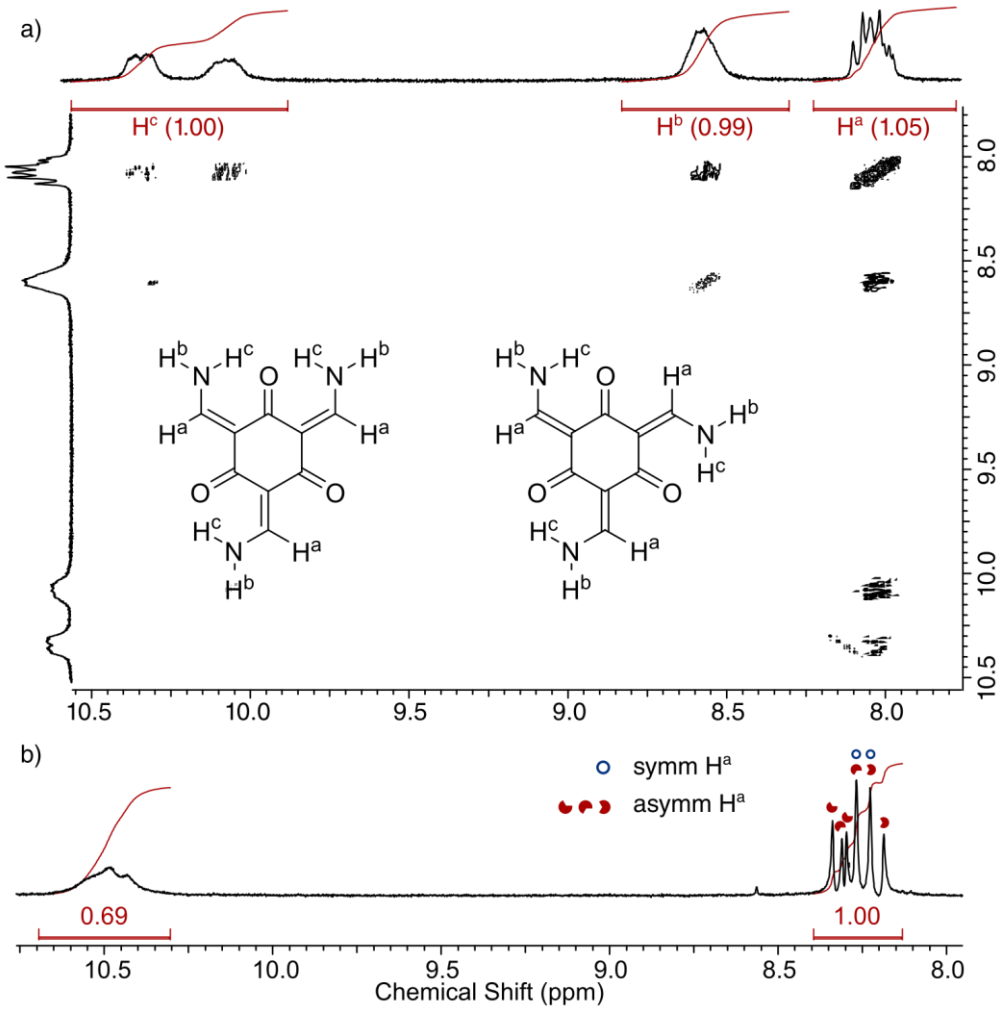

Figure 2.9. (a) COSY NMR spectrum of **2.1** (300 MHz, 25 °C, DMSO-d_6).* (b) ^{1}H NMR spectrum of **2.1** in CD_3OH.†

2.3 TFP–Hydrazine TSAN

Given the challenging crystallization behaviour of **2.1**, we decided to use the condensation reaction between TFP and hydrazine to synthesize **2.2**, which we hoped would form similar hydrogen-bonded structures, Figure 2.10. Our primary motivation in choosing hydrazine was to improve solubility by allowing less specific hydrogen-bonding interactions, *i.e.* interactions where

* Pulse program used: COSY45GPQF (Bruker notation): Quantum-filtered 45° COSY with gradient pulses.

† The W5 variant of the WATERGATE[222] series of solvent suppression pulse sequences was used to supress the CD_3OH proton signal. The resonances around 10.5 ppm were also somewhat affected as a result.

solvent can be competitive with nearby Schiff base molecules. In addition, it was hoped that the free NH_2 functionality in **2.2** would enable further functionalization or self-assembly of the condensation product.

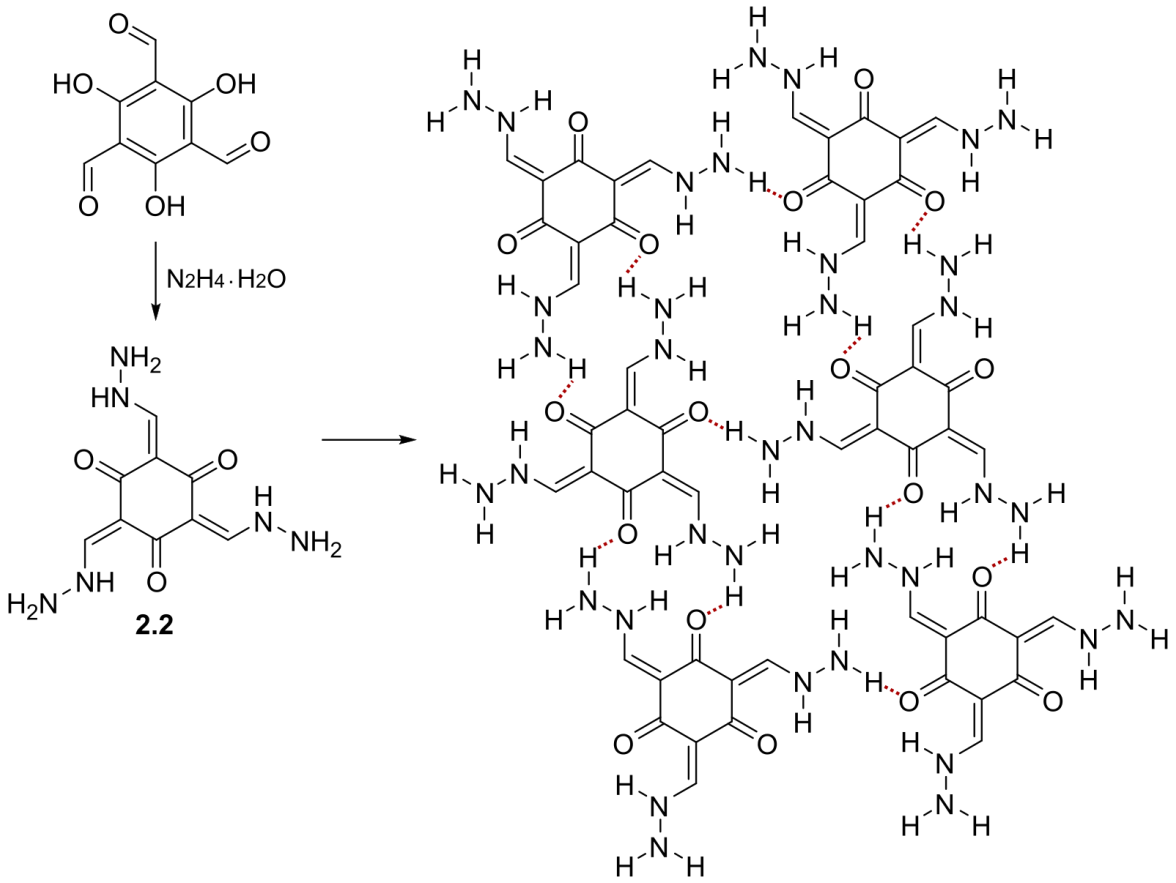

Figure 2.10. Putative hydrogen-bonded network of TFP-hydrazine Schiff base **2.2** (intermolecular hydrogen bonds shown in red).

A common complication in the study of hydrazones derived from aldehydes is their spontaneous condensation to form azines, Figure 2.11a. This form of condensation is especially troubling in the case of **2.2**, Figure 2.11b, since the product tends to precipitate as a dark red mass that is presumably a partially-formed covalent network linked by the azine moieties, Figure 2.11c.

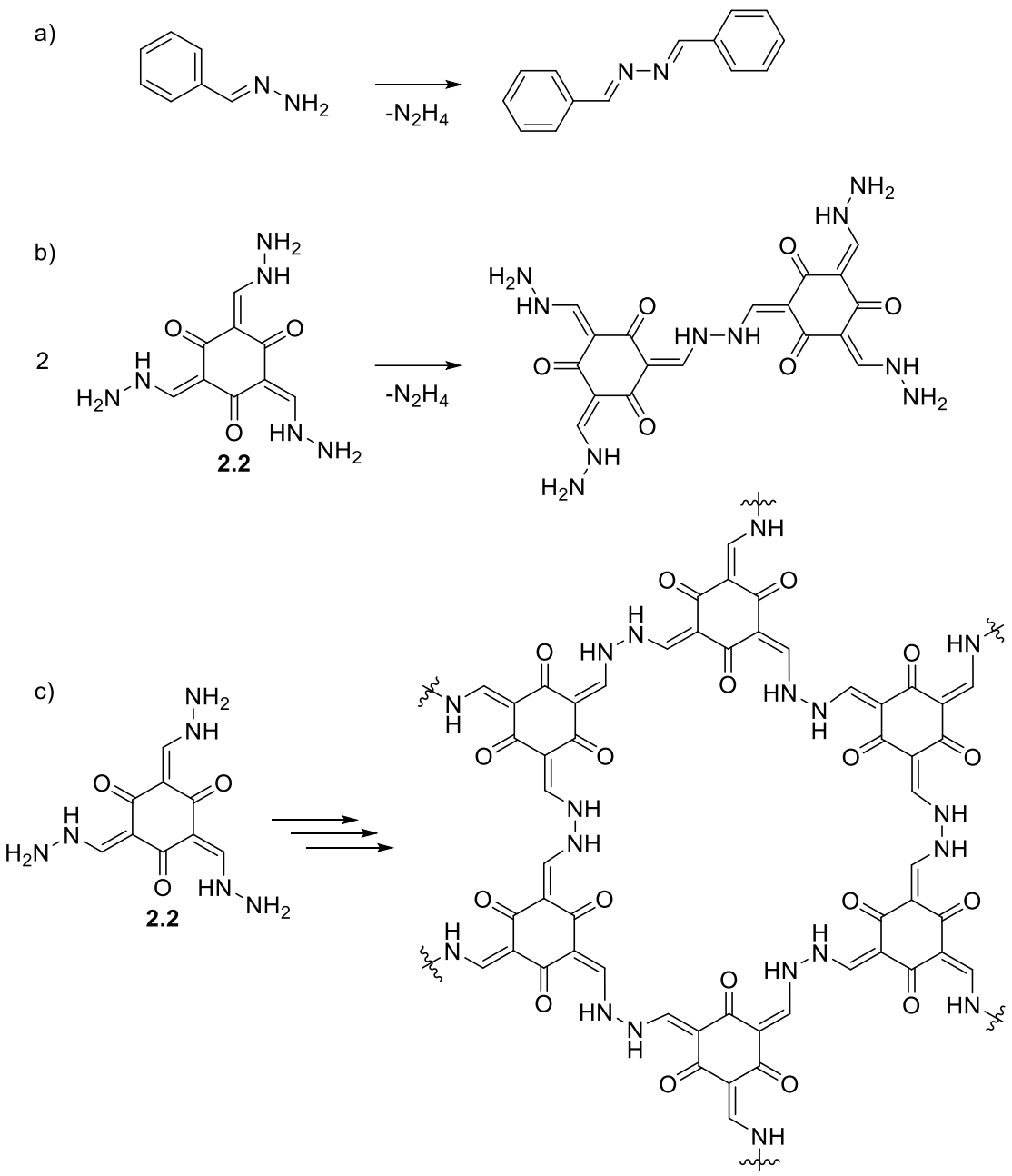

Figure 2.11. (a) Spontaneous condensation of benzaldehyde hydrazone to benzaldehyde azine. (b) Condensation of **2.2**. (c) Formation of insoluble polyazine structure by repeated condensation of **2.2**.

It was not possible to obtain pure **2.2** by reacting TFP and hydrazine at stoichiometries close to the theoretical 3:1 hydrazine:TFP ratio. Instead, an insoluble red to purple powder was obtained. Critically, we observed that excess hydrazine hydrate and TFP react to form a cloudy orange

solution that, upon heating or removal of excess hydrazine under high vacuum, was converted to the insoluble product. This led us to separate the orange precipitate formed upon combining a large excess of cold hydrazine hydrate and TFP, quickly washing away excess hydrazine with ethanol and drying the residue under a stream of N_2. This orange powder proved to be pure **2.2**.

Compound is **2.2** is stable as a dry powder if stored at -20 °C. At room temperature, it slowly turns into the insoluble red-brown powder described above over the course of several months. The condensation process is faster in solution: a solution of **2.2** will, upon standing in DMSO for two weeks, separate into a red gel and clear supernatant. This gel fails to disperse in DCM, EtOH, MeOH, acetone, DMF, and DMSO and is left unchanged by hot 6M HCl solution, but can be de-swelled by exchanging DMSO solvent with acetone. This step alone produces no change in the appearance of the gel; however, evaporating the trapped acetone under air yielded dark red flakes. These flakes can be analyzed by MALDI-TOF MS, Figure 2.12, showing fragments that suggest the formation of a structure like the putative azine network in Figure 2.11c.

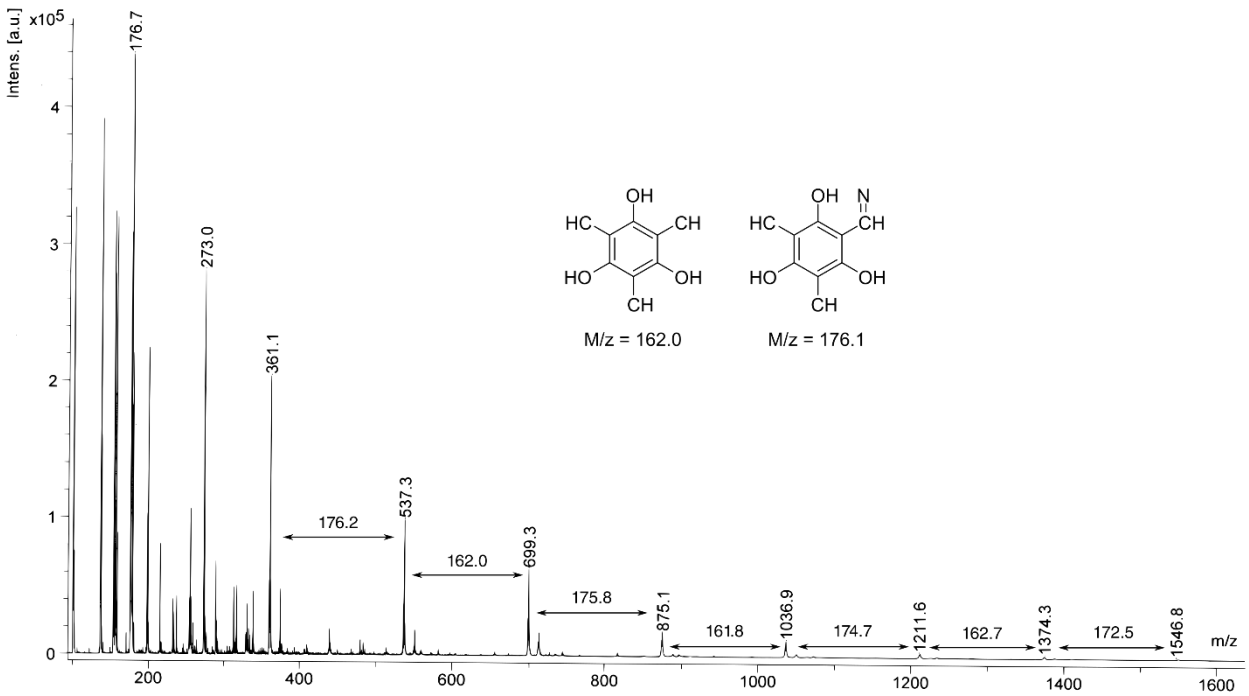

Figure 2.12. MALDI-TOF mass spectrum of gel from condensation of **2.2** after solvent exchange and evaporation of acetone solvent (2,5-dihyroxybenzoic acid matrix).

After much experimentation, single crystals of **2.2** were obtained by adding chloroform to a solution of the compound in DMSO. As in the case of **2.1**, SCXRD data for these orange needles suggests that **2.2** packs in a herringbone arrangement rather than the hydrogen-bonded sheets that we had anticipated. Interestingly, two disorder components are present in the crystal, the dominant one being the familiar keto-enamine TSAN shown in Figure 2.13.

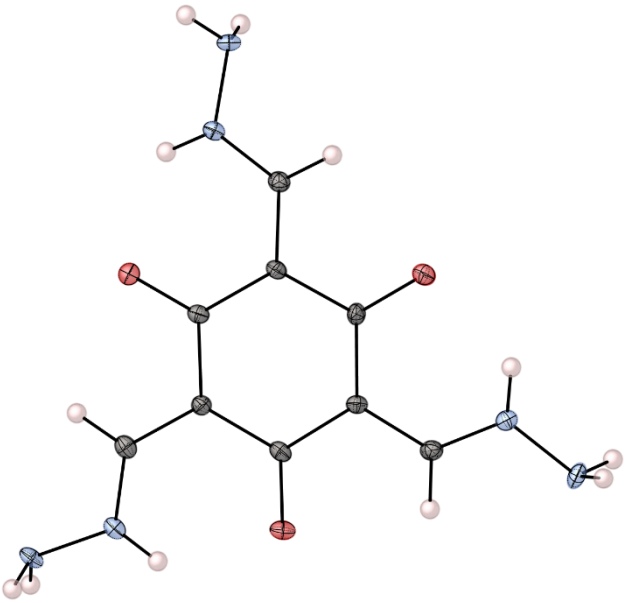

Figure 2.13. Thermal ellipsoid diagram (50%) for the major component of **2.2** determined by SCXRD.

It was determined that the keto-enamine component above has *ca.* 92% percent site occupancy. We were surprised to find that the weak diffraction from the remaining 8% revealed the enol-imine structure in Figure 2.14 since, at the time, enol-imine TSANs were unknown.

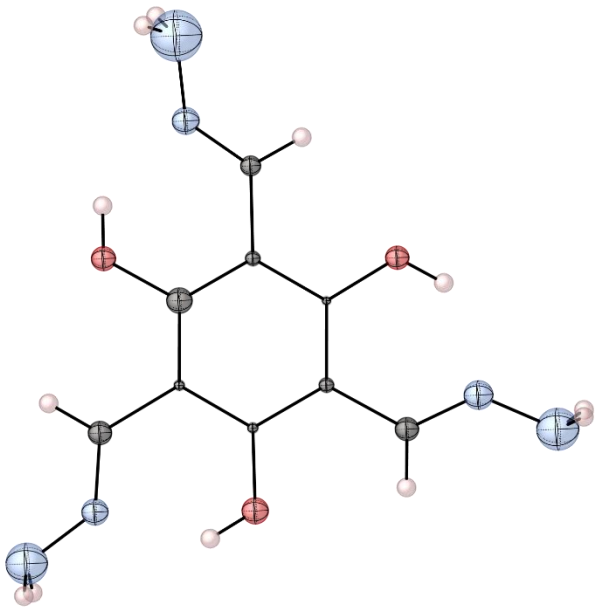

Figure 2.14. Thermal ellipsoid diagram (50%) for the minor component of **2.2** determined by SCXRD.

The unusual tautomeric behaviour of **2.2** is not confined to the solid state. Figure 2.15 shows the ^{1}H NMR spectrum of this compound in DMSO-d_6, which similarly suggests that distinct keto-enamine and enol-imine components co-exist in solution.

Since interconversion between the two tautomers has to be slow on the NMR timescale for them to be distinguishable, we predict that the keto-enamine form must adopt the asymmetric geometry shown in Figure 2.15 because asymmetric keto-enamine **2.2** cannot be converted to the [symmetric] enol-imine form through a simple intramolecular hydrogen shift. This is explained in more detail in the following sections. Based on the NMR spectrum in Figure 2.15, we conclude that the enol-imine form is more stable in solution but that some of **2.2** can be trapped in the kinetically stable asymmetric form.

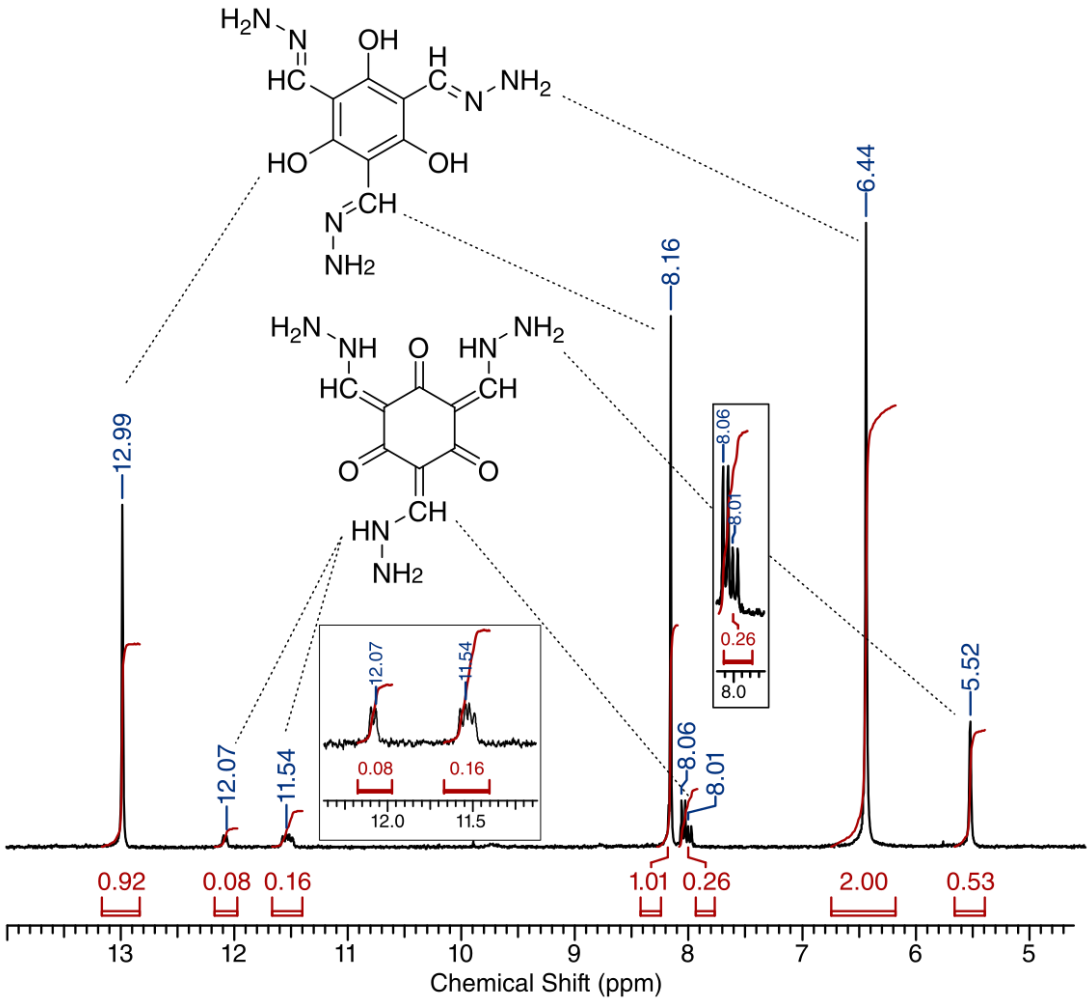

Figure 2.15. ^{1}H NMR spectrum of 2.2 (300 MHz., DMSO-*d*$_6$, 25 °C).

2.4 TFP–Hydroxylamine TSAN

Another TSAN analogue **2.3**, which is the product of the condensation reaction between TFP and hydroxylamine, was prepared with the goal of improving solubility and post-synthesis functionalization, Figure 2.6. Owing to hydroxylamine's tendency to decompose explosively, it was only allowed to form transiently during the reaction by combining hydroxylamine hydrochloride, TFP, and potassium carbonate in methanol solvent, Figure 2.16.

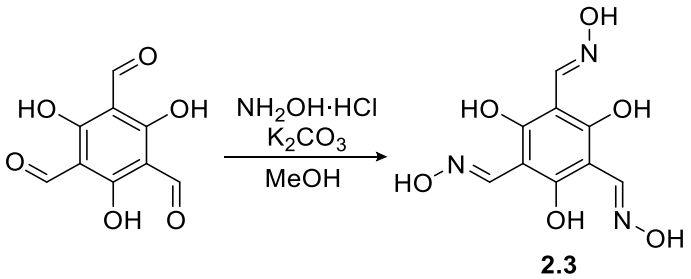

Figure 2.16. Preparation of enol-imine TSAN analogue **2.3**.

Compound **2.3** is unequivocally an enol imine both in solution (by ^{1}H NMR, Figure 2.18) and in the solid state. Figure 2.17 shows the structure of this compound determined by SCXRD where, interestingly, ring C–C distances are very close to those of benzene (1.40 Å).

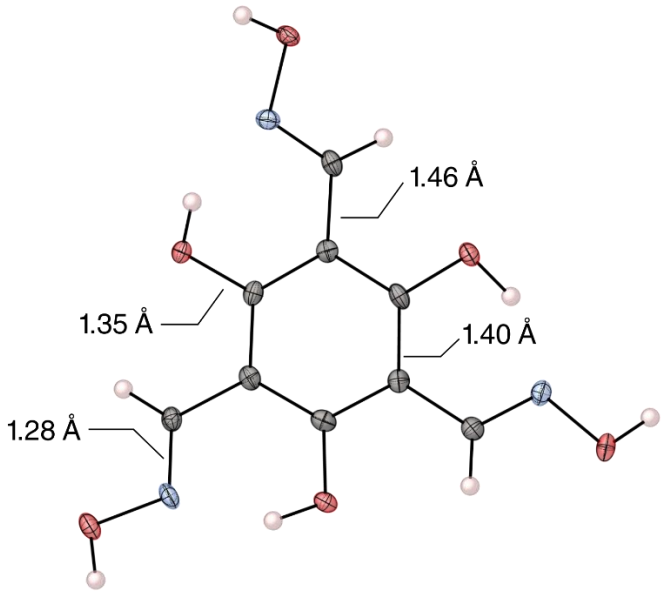

Figure 2.17. Thermal ellipsoid diagram (50%) of compound **2.3** as determined by SCXRD.

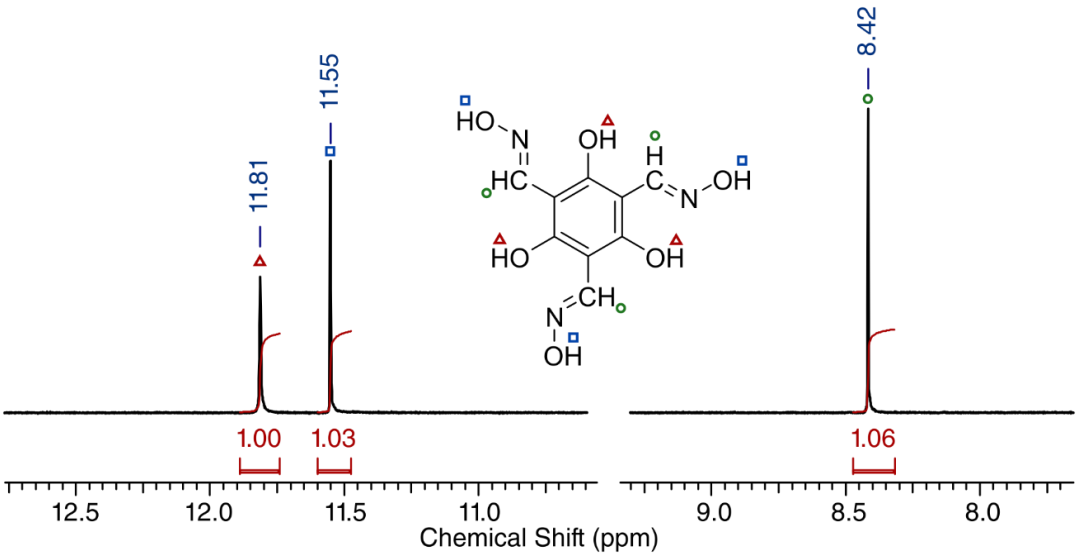

Figure 2.18. ^{1}H NMR spectrum of **2.3** (400 MHz, DMSO-d_6, 25 °C).

2.5 Interlude: The Impact of Tautomeric State on Molecular Properties

At this point, it is worthwhile to take a closer look at how the unusual enol-imine tautomeric state of **2.2** and **2.3** affects their properties. Specifically, we look at how the different hydrogen-bonding pattern in these compounds leads to their unique threefold-symmetric geometry. The impact on aromaticity is also briefly explored.

2.5.1 Geometric Isomerism

The prevalence of the enol-imine tautomer in **2.2** and **2.3** has the additional consequence of drastically altering hydrogen bonding in these compounds. Whereas the symmetric and asymmetric geometric isomers of a keto-enamine TSAN both represent stable hydrogen bonding configurations, symmetric to asymmetric conversion in enol-imine TSANs results in the breaking of a hydrogen bond, Figure 2.19. This could explain the absence of the asymmetric form in the ^{1}H NMR spectrum of **2.2** and **2.3**.

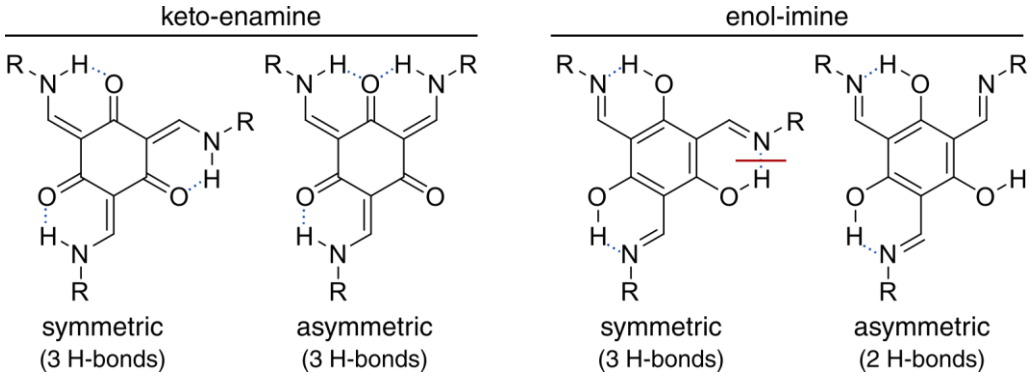

Figure 2.19. Comparison of hydrogen bonding patterns between the symmetric and asymmetric forms of keto-enamine (left) and enol-imine (right) TSANs.

To put the above argument in more quantitative terms, we undertook a simple *ab initio* experiment where we simulate the rotation of one C–CH arm in the keto-enamine and enol-imine tautomer of both **2.2** and **2.3**. Here, the dihedral angle corresponding to one of the C–CH bonds was varied between 0–180°, 0° representing the symmetric (C_{3h}) and 180° the non-symmetric (C_s) molecule.* Figure 2.20 shows the results, where the gray curves indicate that breaking a hydrogen bond in the enol-imine form of both compounds is associated with an energetic cost of *ca.* 15 kcal/mol. Furthermore, for enol-imines, the asymmetric (C_s) geometry represents a local maximum in the plots, signifying that the molecule can never be trapped in its asymmetric form. This is consistent with the results of our variable-temperature ^{1}H NMR experiments on enol-imine TSAN analogues (Section 2.6).

* Section 2.10 gives a more complete description of the *ab initio* component of our work on these compounds.

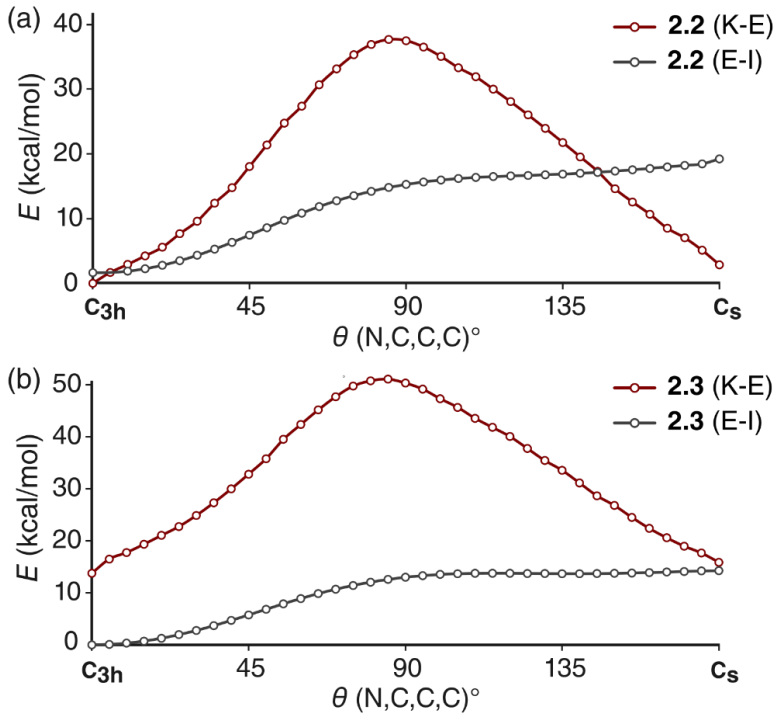

Figure 2.20. Dihedral scan of energy for **2.2** (a) and **2.3** (b) in their keto-enamine (red trace) and enol-imine (gray trace) forms.

Another interesting observation in Figure 2.20 is the large bond rotation barrier for the keto-enamines, which is *ca.* 20 kcal/mol more than what is required for the breaking of a hydrogen bond. This is yet another indication of double C–CH bond character in keto-enamines.* To summarize, the absence of geometric isomerism in enol-imine TSANs is explained by the fact that the asymmetric form is both kinetically unstable (thanks to relatively free sidearm rotation) and thermodynamically unstable (thanks to the lower π character of the exocyclic C–CH bonds) with respect to conversion to the C_{3h}-symmetric form.

2.5.2 Impact on Aromaticity and Magnetic Properties

Diamagnetic ring currents are a hallmark feature of aromatic compounds and have been used alongside geometric and thermodynamic observables as a reliable indicator of aromatic electron

* In comparison the barrier ($\Delta H^{\ddagger}$) to rotation of the internal C–C bond in butane is less than 4 kcal/mol.[223]

delocalization. While accurate *ab initio* methods exist for calculating diamagnetic current distribution in space, there are several competing interpretations of this as ring current intensity. Section 2.10.2 gives a brief overview of the state of the art and the methods that we used.

Figure 2.21 compares the calculated induced diamagnetic ring current between a keto-enamine TSAN* and **2.3**. Aside from the drastic reduction of ring current in the keto-enamine form, it is illustrative that the majority of the remaining current passes through the keto-enamine arms as opposed to the central ring.

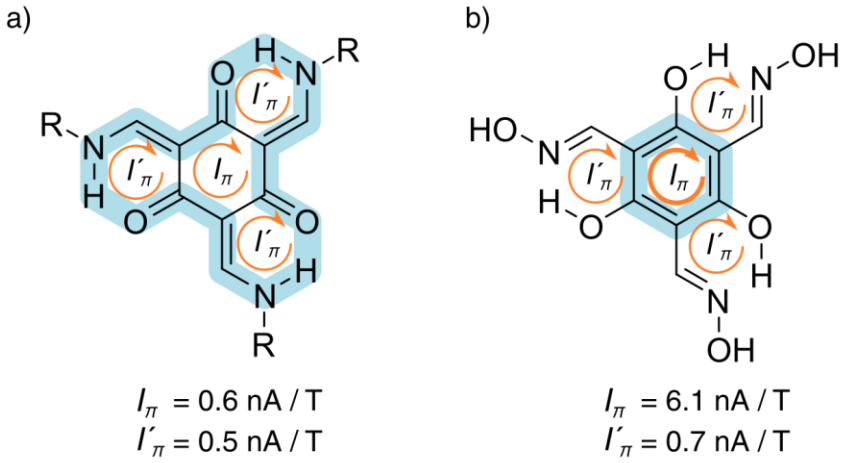

Figure 2.21. Comparison of induced diamagnetic ring current for a keto-enamine (a) and an enol-imine (b) TSAN (R = Ac). Calculation methods are described in Section 2.10.2.

Another textbook marker of aromaticity in rings is the absence of bond length alternation. Instead of having alternating short and long bonds as the individual Kekulé structures would suggest, aromatic rings are characterized by relatively constant C–C bond lengths of *ca.* 1.39 Å (for six-membered rings). This has motivated the definition of the harmonic oscillator model of aromaticity (HOMA), a geometric indicator of aromatic character that expresses the degree of bond length homogeneity in a cyclic molecule.[80] Defined as $1 - 42.95\ \Sigma_i\ (d_i - 1.388)^2$, HOMA has

* Compound **2.7** in particular, to be encountered in Section 2.7.

been formulated such that benzene itself has the highest possible value of 1. Comparing C–C bond lengths around the central ring between keto-enamine and enol-imine TSANs reveals a large degree of deviation from benzene in the former (in the form of long-short alternation, HOMA = −0.65) while the latter closely matches benzene (with essentially no variation in length, HOMA = 0.89), Figure 2.22. The alternating long and short bonds in keto-enamines could be attributed to the strong intramolecular hydrogen bonds pulling the otherwise widely separated ring carbon atoms closer.

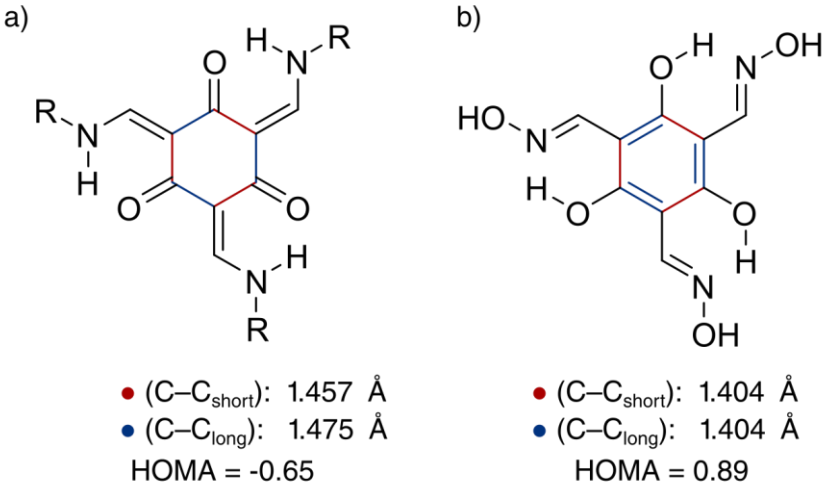

Figure 2.22. Comparison of bond length alternation in the central ring between a keto-enamine (a) and enol-imine (b) TSAN (R = Ac).

2.6 Extended Enol-Imine TSAN Analogues

As expected, analogues of **2.2** and **2.3** extended with organic substituents can be accessed in a straightforward fashion, Figure 2.23. Thus, compounds **2.4** and **2.5** are trivial to prepare by direct condensation of TFP with the respective hydrazide (in case of **2.4**) or *O*-hydroxylamine (in case of **2.5**).

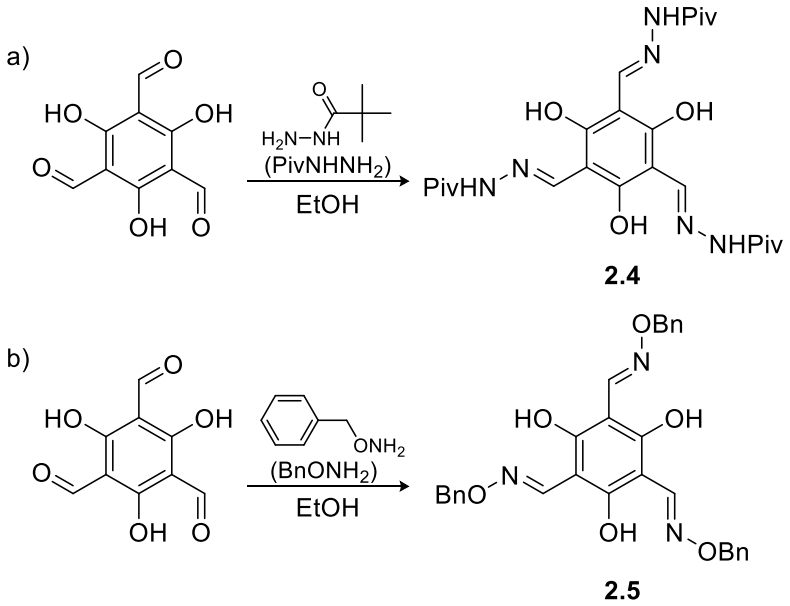

Figure 2.23. Preparation of analogues of **2.2** (**2.4**, a) and **2.3** (**2.5**, b) extended with organic substituents (Piv = $C(O)(CH_3)_3$, Bn = CH_2Ph).

Like **2.3**, both **2.4** and **2.5** adopt the enol-imine tautomeric form in solution. The ^{1}H NMR spectrum of each shows two simple uncoupled singlets (for the CH and OH resonances, respectively). In the case of **2.5** we were able to confirm that the simple ^{1}H NMR spectrum is due to a symmetric enol-imine structure in solution as opposed to fast rotation about the exocyclic C–CH bonds. This was achieved through variable-temperature ^{1}H NMR spectroscopy. Specifically, the same simple spectrum is obtained even at −91 °C, Figure 2.24, which invalidates the hypothesis that fast bond rotation is the factor at play. This is in line with the lack of geometric isomerism in enol-imine TSANs described in the previous section.

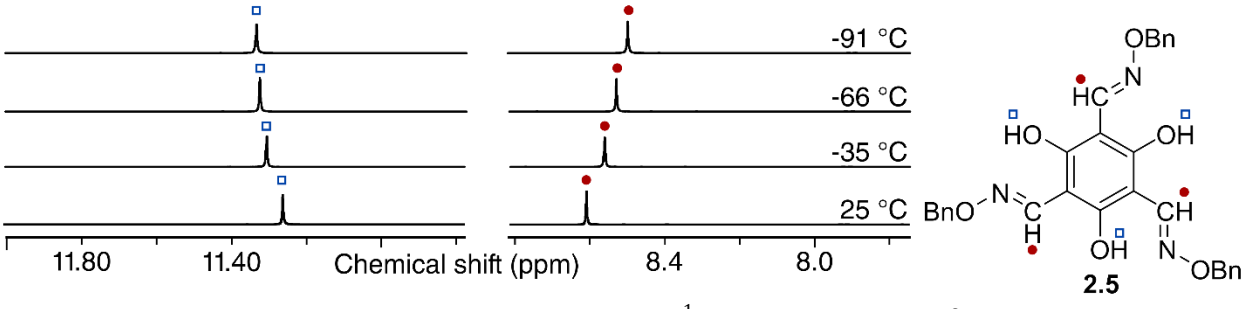

Figure 2.24. Variable-temperature ^{1}H NMR spectrum of **2.5**.

In the solid state as well, both **2.4** and **2.5** adopt the enol-imine tautomeric form. No site occupancy corresponding to the keto-enamine (as in the case of **2.2**) was found for either, Figure 2.25.

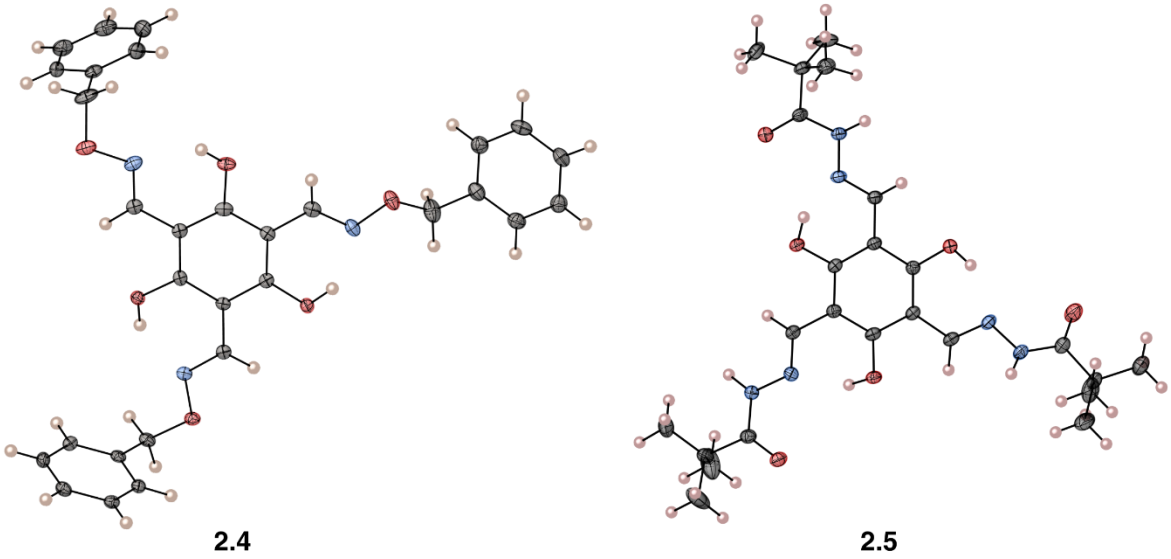

Figure 2.25. Thermal ellipsoid diagram (50%) for **2.4** and **2.5**.

At the time of their discovery, **2.2**–**2.5** were the only TSAN derivatives to exist as enol-imines to the best of our knowledge. Crystal structures of enol-imine TSANs, including that of **2.3** have since been published by others.[81,82]

2.7 Unexpected Keto-Enamine Character in Similar TSANs

The evidence so far suggests that the low basicity of the nitrogen atom in hydrazine is responsible for the predominance of the enol-imine tautomeric form in **2.2**–**2.5**. Our subsequent experiments with other weak bases revealed this hypothesis to be incomplete. For instance, the formal condensation products of TFP with the very weak bases pentafluoroaniline and acetamide (**2.6** and **2.7**, Figure 2.26) show ^{1}H NMR spectra typical of keto-enamine TSANs.

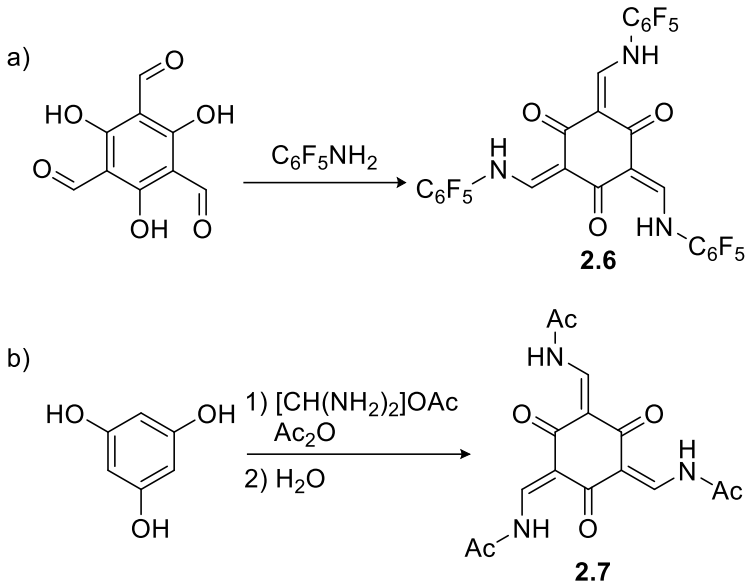

Figure 2.26. Preparation of **2.6** and **2.7**.

Note that **2.7** was not prepared by direct condensation of TFP and acetamide. Rather, it was obtained as an intermediate in the formylation of phloroglucinol using formamidine acetate, discussed in Chapter 5.

As with previous examples, SCXRD data for **2.6** and **2.7** are consistent with their solution characterization as keto-enamine TSANs, Figure 2.27. To our surprise, we found that among the TSANs reported by us and others, **2.7** exhibits the highest degree of keto-enamine character in terms of bond lengths, Table 2.1. This clearly challenges our simplistic hypothesis of nitrogen basicity as the sole determinant of tautomeric state.

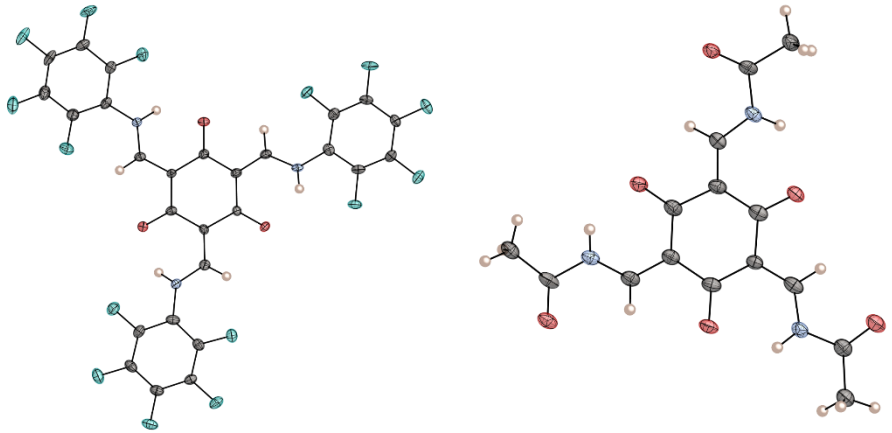

2.6 **2.7**

Figure 2.27. Thermal ellipsoid diagram (50%) for **2.6** and **2.7** as determined by SCXRD.

Table 2.1. Experimental and calculated properties for various TSANs (TFP + X–NH_2).

	X	pK_b (X–NH_2)	Major tautomer			Bond lengths (SCXRD/calculated)			
			SCXRD[a]	NMR (solvent)[a]	*Ab Initio* ($E_{K\text{-}E} - E_{E\text{-}I}$)[b]	C_{Ar}–C_{Ar}[c]	C_{Ar}–O	C_{Ar}–CH	CH–N
2.2	NH_2	5.90[83]	K-E	E-I (DMSO-d_6)	E-I (0.2)	1.446–1.453/ 1.454–1.462	1.263/ 1.251	1.392/ 1.383	1.311/ 1.324
2.3	OH	8.03[83]	E-I	E-I (DMSO-d_6)	E-I (14.6)	1.404/ 1.409	1.355/ 1.337	1.455/ 1.448	1.277/ 1.281
2.4	NHPiv	10.76[84d]	E-I	E-I (DMSO-d_6)	E-I (6.1)	1.406–1.409/ 1.409	1.343/ 1.339	1.448/ 1.446	1.285/ 1.288
2.5	OCH_2Ph	9.40[85e]	E-I	E-I ($CDCl_3$)	—	1.403–1.408/ 1.410	1.344/ 1.337	1.452/ 1.448	1.280/ 1.282
2.6	C_6F_5	> 12[86f]	K-E	K-E (toluene-d_8)	K-E (-7.0)	1.455–1.462/ 1.457–1.465	1.256/ 1.247	1.373/ 1.379	1.343/ 1.344
2.7	Ac	15.1[86]	K-E	K-E (DMSO-d_6)	K-E (-27.9)	1.457–1.475/ 1.462–1.472	1.248/ 1.240	1.364/ 1.372	1.335/ 1.343

(a) For major tautomer reported (K–E = keto-enamine; E–I = enol-imine). (b) Energies in kcal/mol. (c) All bond lengths in Å. Ranges for C–C bonds indicate long–short alternation. (d) Value for acetyl hydrazide. (e) Value for CH_3ONH_2. (f) Based on pK_b = 11.95 for 2,4-dichloroaniline.

2.8 A Structural Model of Tautomeric Preference

Figure 2.28 summarises the variation of dominant tautomeric state for Schiff bases of TFP and X–NH_2 across a range of X–NH_2 pK_b values. Inspection of the pK_b values and associated tautomeric form shows no clear connection between the two. Indeed, 3,5-dimethylaniline ($ArNH_2$) and $PhCH_2ONH_2$, in spite of having similar pK_b values, form Schiff bases with opposite tautomeric preference.

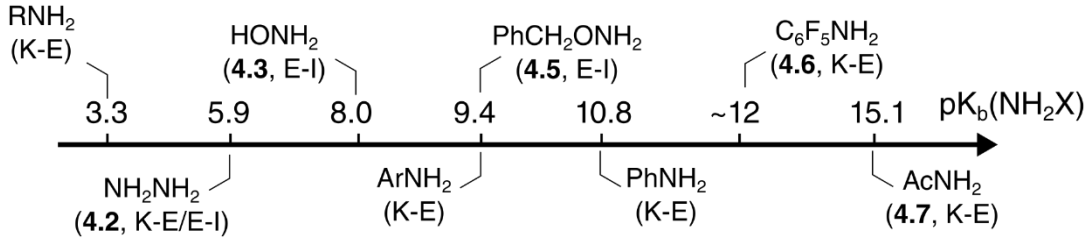

Figure 2.28 Preferred tautomeric state of TFP–NH_2X as a function of base dissociation constant, $pK_b(NH_2X)$ in water. Dominant tautomeric form for TFP–RNH_2[78] and TFP–$ArNH_2$[49] taken from the literature. Approximate pK_b values reported for $PhCH_2NH_2$ and $C_6F_5NH_2$.

Figure 2.29 illustrates the intuition behind this initial hypothesis. Our expectation was that more basic X–NH_2 bases would favor the keto-enamine tautomer, since the tautomeric equilibrium can be seen as a competition between the O and N atoms for the labile proton.

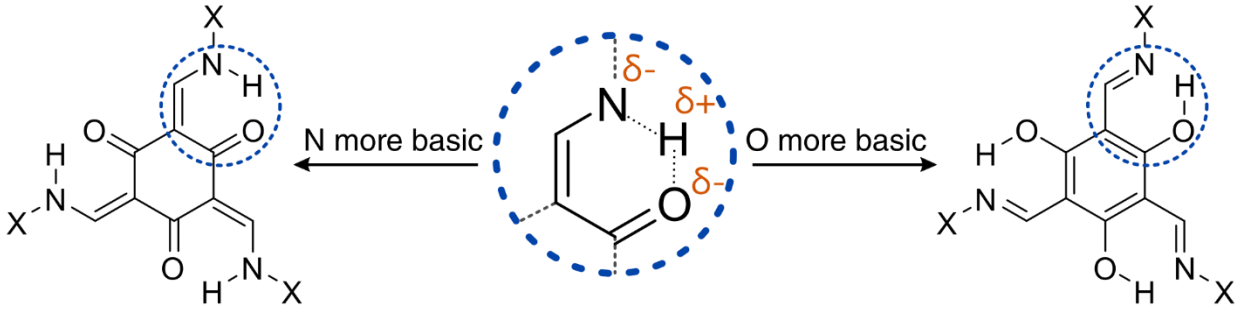

Figure 2.29 Depiction of the keto-enamine/enol-imine equilibrium as an acid-base competition.

In light of these observations (especially the extraordinary keto-enamine character of **2.7**), we can revise our hypothesis by better qualifying nitrogen basicity. Looking more closely at the keto-

enamine moiety in Figure 2.30a, it is easy to see that the inductive effect of an electronegative X substituent would lead to partial positive charge on the hydrogen atom, while the relatively unaffected nitrogen lone pair is free to delocalize into the keto oxygen atom, making it more basic. The combination of these factors encourages the migration of the proton to form the enol-imine tautomer.

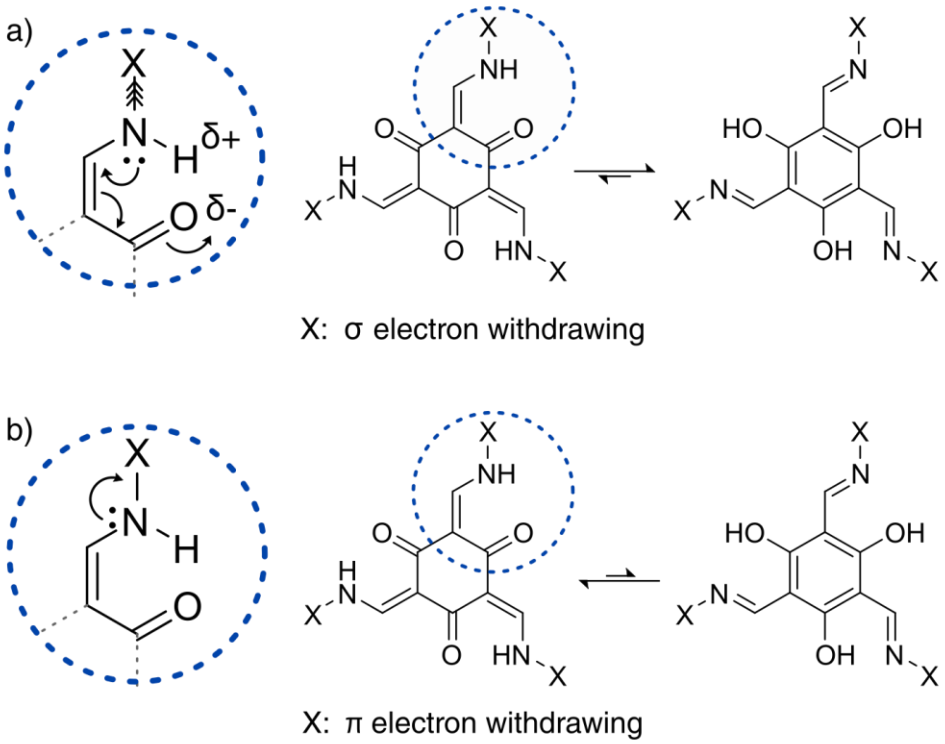

Figure 2.30. A more comprehensive model of tautomeric behaviour in TSANs. (a) Destabilization of the keto-enamine form when X is strictly σ electron withdrawing. (b) Stabilization of the keto-enamine form when X is strictly π electron withdrawing.

Figure 2.30b shows the converse situation where the nitrogen lone pair is delocalized into the X group (as one would find with X = Ac, Ph) without the X being especially electronegative, *i.e.* not electron withdrawing through the σ skeleton. In this case, very little partial negative charge develops in the oxygen atom, and the keto C=O maintains its carbonyl-like nature.

Conceptually, this new model gives a coherent picture for the observed tautomeric tendencies across **2.2**–**2.7**. For instance, condensation of TFP and anilines leads to keto-enamine TSANs thanks to the ability of the phenyl group to efficiently delocalize the lone pair electron density of the enamine nitrogen atom. Thus, these compounds are keto-enamines despite the fact that anilines are very weakly basic.

Finally, pentafluoroaniline represents a special case where the inductive effect of the fluorine atoms makes the C_6F_5 group both σ and π electron withdrawing, Figure 2.31. This is in line with the observation of a small (10%) degree of enol-imine tautomerization of **2.6** in the solid state.

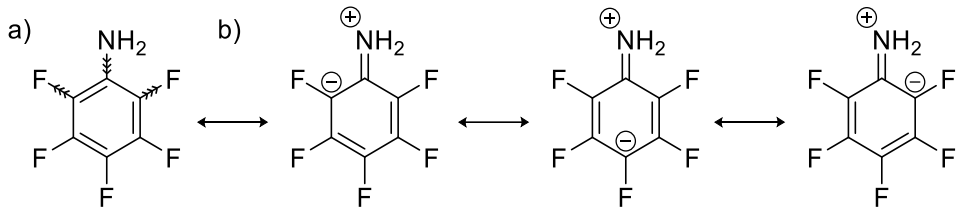

Figure 2.31. Inductive (a) and resonance (b) electron withdrawing action of the C_6F_5 group in pentafluoroaniline.

2.8.1 Ab Initio Validation of Model

Chemical pictures such as the above are challenging to test using quantum chemical techniques, since these *ab initio* techniques have no inherent notion of atoms or bonds. The need to reconcile the strictly observable-based minimal description of *ab initio* quantum mechanics with these chemically useful notions has led to development of various competing interpretations. For example, partial charges can be assigned to atoms following the Mulliken[87], Löwdin,[88,89] or Natural Population Analysis (NPA)[90] interpretations.[91]

For the purpose of testing the predictions of our model, we chose to use the theory of atoms in molecules (AIM). Briefly, AIM separates space into atomic basins separated by stationary points of electron density. Connected together, these points form surfaces that partition the system into

the quantum mechanical equivalent of a closed system in thermodynamics. Qualitatively, each partition contains the nucleus of one of the constituent atoms along with the space around it that "belongs" to that particular atom. Physical observables, *e.g.* energy or charge, can then be unambiguously assigned to each partition and interpreted as corresponding to the atom inside.

Charge delocalization can be studied in a straightforward fashion within the framework of AIM: each one-electron wavefunctions making up the Slater determinant is assigned to an atomic basin and the vestigial probability density crossing over to other basins is counted as electron delocalization. We can therefore test our hypothesis by examining whether more extensive N → O electron delocalization in the keto-enamine tautomer of a given TSAN implies preference for the enol-imine form.

Figure 2.32 shows the plot of tautomeric preference $(E_{K\text{-}E} - E_{E\text{-}I})$[*] versus AIM N → O electron delocalization calculated for a range of TSANs, including some that we have studied experimentally in this chapter. We find a strong correlation between N → O electron delocalization and preference for the enol-imine tautomer, in agreement with our hypothesis. While the complete picture is bound to be more nuanced,[†] these results support our simple model, which can now be applied as a useful rule of thumb to predict the preferred tautomeric state of new TSANs.

[*] Positive values correspond to the enol-imine tautomer being preferred.
[†] Incorporating for instance, the σ electron withdrawing character of X in X–NH_2.

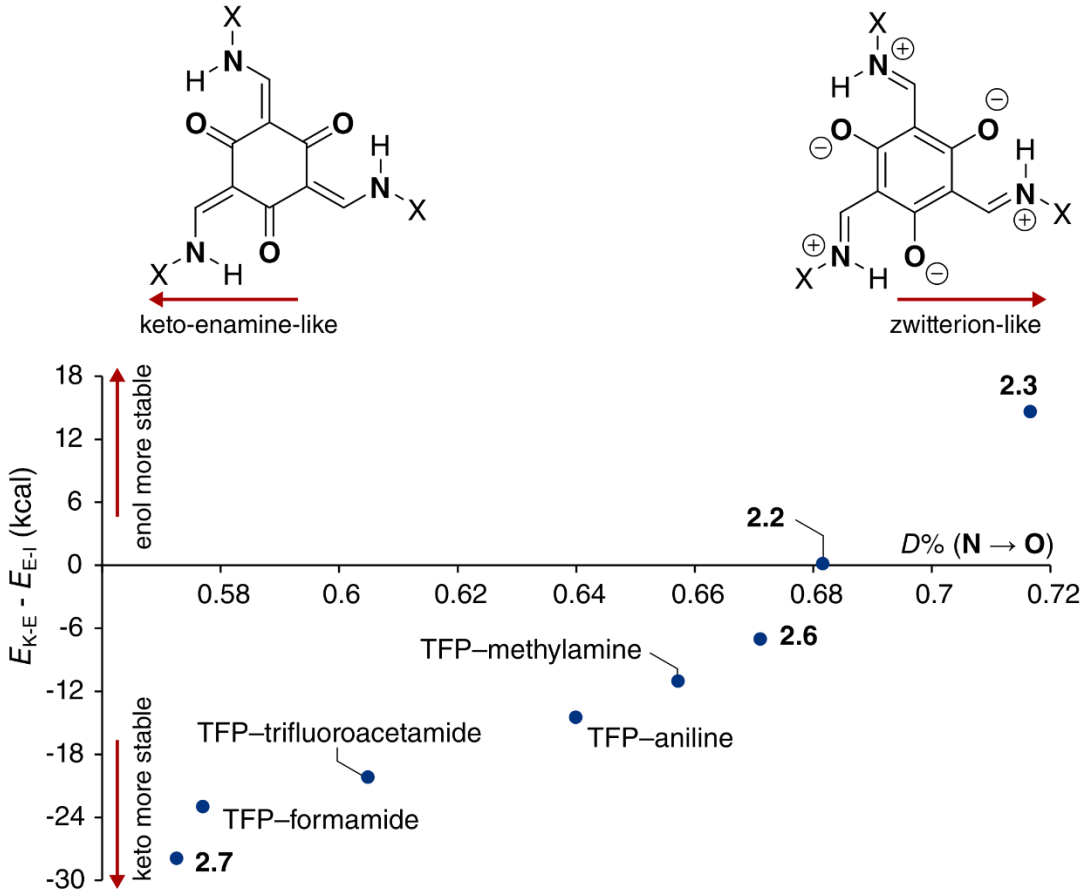

Figure 2.32. Plot of tautomeric preference (keto-enamine vs enol-imine stability) as a function of calculated N → O electron delocalization, *D*% (N → O), in the keto-enamine structure (B3LYP/Def2TZVPP, AIMAll).

2.9 Conclusions and Future Work

In this chapter, several new TSANs were prepared and characterized with the initial goal of using them as building blocks for self-assembled hydrogen-bonded sheets. To better understand the unusual tautomeric behaviour of these compounds, their experimental characterization was supplemented by *ab initio* calculations aimed at elucidating the effect of electron delocalization on their preference for one or the other tautomeric form.

In a nutshell, the initially counterintuitive position of the tautomeric equilibrium for compounds like **2.2**–**2.7** can be rationalized using the resonance–equilibrium picture of Figure

Figure 1.16: larger contribution of the zwitterionic **1.1c** structure drives the equilibrium towards the enol-imine form (**1.1a**, specifically) while the other zwitterionic structure **1.1b** (especially revalent in the case of **4.6** and **4.7**) is suspected to move the equilibrium in favour of the keto-enamine form (**1.1d**, specifically).

What determines whether a given TSAN is a keto-enamine versus enol-imine has been a longstanding question for us and a necessary step toward "designer tautomers": molecules that exhibit a precise, application-defined degree of preference for one or the other form. While, technically, this preference could already be calculated using *ab initio* methods, having a simple structural model as a guide is invaluable in facilitating the design process.

2.9.1 The Tautomeric Chemistry of Pyridines

Competition between tautomers with peripheral versus central (aromatic) electron delocalization schemes is not limited to TSANs; 2-pyridone famously exhibits a similar form of interconversion between its lactam and lactim tautomers, Figure 2.33a. More interestingly, there are examples in the literature of deprotonation of carbon atoms α to a pyridine unit (technically imine–enamine tautomerism), *e.g.* Figure 2.33b.[92] Tautomerizations of this type are possible due in part to the lower aromatic stabilization energy of pyridine compared to that of benzene.[93]

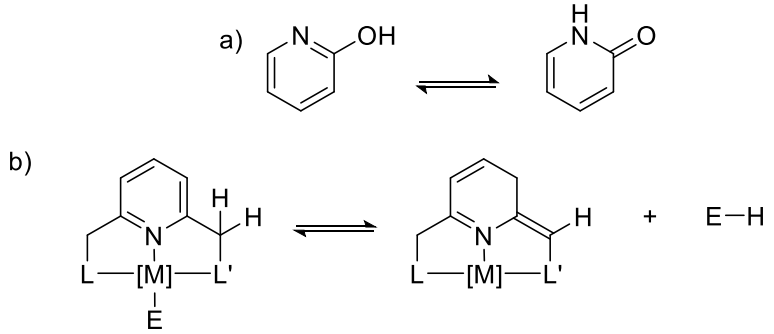

Figure 2.33. (a) Tautomerism interconversion between 2-hydroyxpyridine and 2-pyridone. (b) Pyridine pincer ligand showing non-innocent tautomeric behaviour.

One can imagine that methylenedihydropyridine products of the type shown in Figure 2.34 could be further stabilized with more extensive delocalization of the resulting negative charge as shown, for instance, in Figure 2.34a. Indeed, Ogawa and coworkers have been exploited this in the design of a macrocycle, Figure 2.34b, described as having labile H atoms.[94]

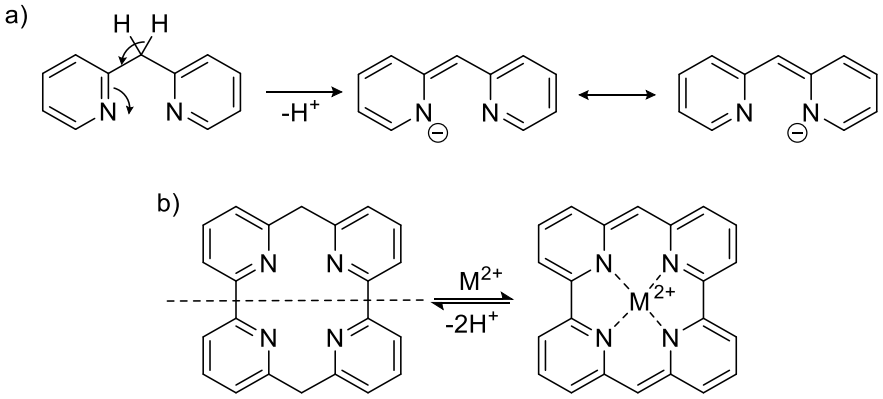

Figure 2.34. (a) Possible scheme for stabilization of an α deprotonated pyridine. (b) Macrocycle designed around the same principle.

Following this design, various interesting motifs can be envisioned. In each case, we take advantage of the enhanced basicity of the nitrogen atoms in the deprotonated form, Figure 2.35.

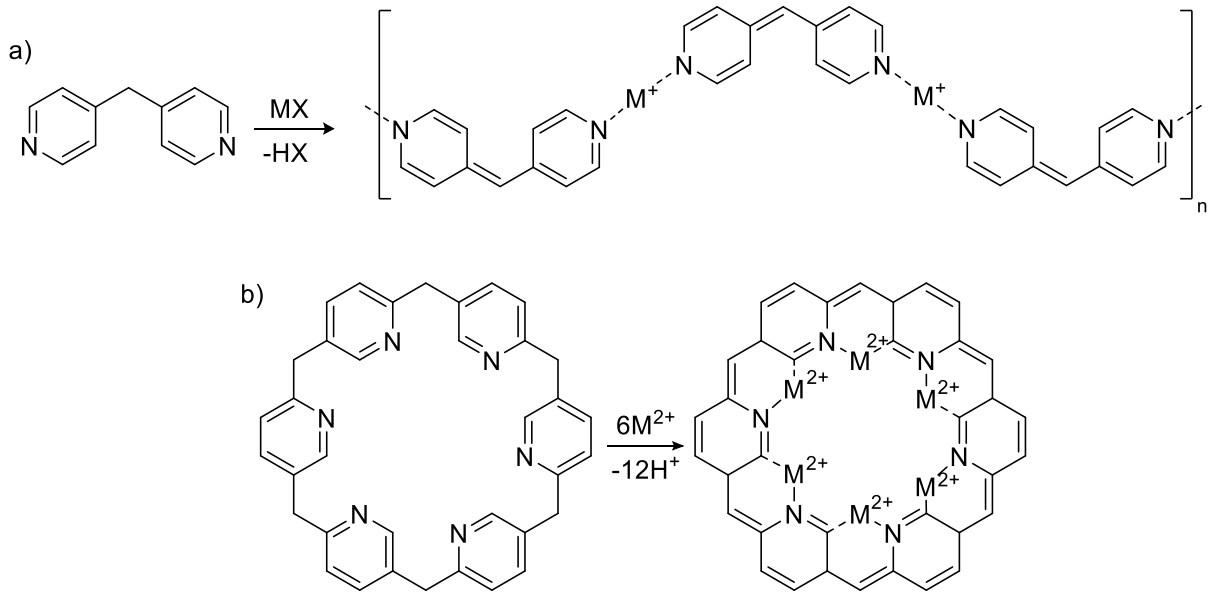

Figure 2.35. Polymer (a) and macrocycle (b) designed based on imine–enamine tautomerism in pyridines.

2.10 Ab Initio Details

Calculations in this chapter were performed at the B3LYP/Def2TZVPP[95] level of theory with no attempt to model solvent effects.* The Gaussian 09 (revision D)[96] suite of programs was used throughout, except for AIM calculations where the AIMAll[97] code was used with the Gaussian wavefunction as input.

2.10.1 Geometry Optimization and Dihedral Scan

For each of **2.2**–**2.7**, initial atomic coordinates for the dominant tautomer were taken from SCXRD data and subjected to geometry optimization using the B3LYP functional and progressively more elaborate basis sets (typically 6-31G+(d,p) → Def2TZVP → Def2TZVPP). At each stage, vibrational analysis was performed on the optimized structure to guard against imaginary frequencies, *i.e.* to reject any potential saddle points.

Rather than relying on SCXRD data, the structures for any minor/unobserved tautomers were derived computationally. In each case, the optimized structure of the dominant tautomer was mutated by manually moving the labile protons to the requisite locations (N*H*, O → N, O*H* or vice versa), followed by the same geometry optimization procedure described above. Structures for all minor tautomers were obtained in this fashion without any convergence issues. Using a similar methodology, we were also able to derive the optimized geometries of the asymmetric keto-enamine TSANs. Specifically, the $C_{Ar}C_{Ar}$–CN dihedral angle for one of the enamine arms was changed by 180° to arrive at the asymmetric TSAN molecule.

The type calculation producing the dihedral scan plots shown in Figure 2.20 entails varying one molecular coordinate, here the $NC^1C^2C^3$ dihedral angle in Figure 2.36, by a small amount (5°

* Chapter 3 gives a more detailed treatment of the techniques and conventions used throughout for calculations.

in this case) and relaxing all other molecular coordinates (bond lengths, angles, and dihedral angles) to their lowest energy values while the dihedral angle in question is held fixed. The above modification–optimization steps can be repeating with further [dihedral angle] increments in order to cover the range of interest. This process is an example of *constrained geometry optimization calculation* (sometimes termed relaxed dihedral scan in this particular case) and is widely available in *ab initio* electronic structure software.

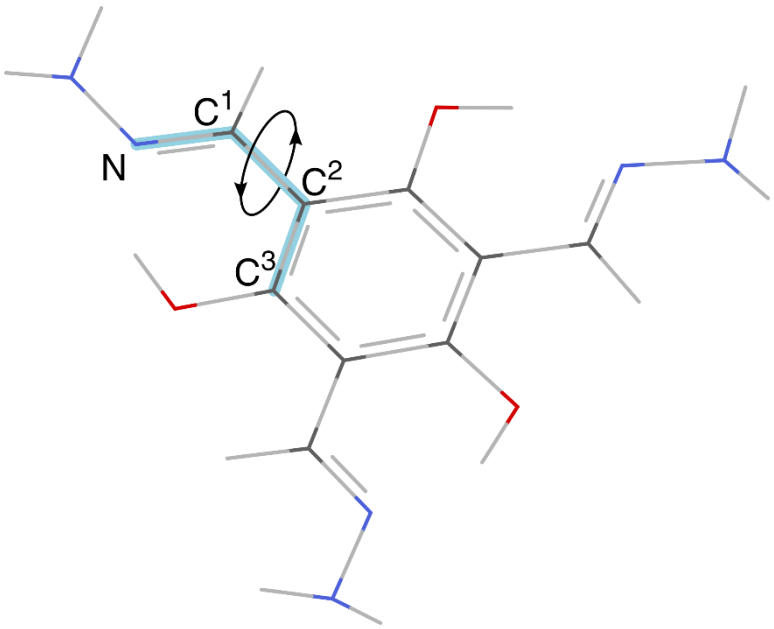

Figure 2.36. Simplified representation of the relaxed dihedral scan experiment wherein the $NC^1C^2C^3$ dihedral angle is fixed at 5° increments, while other molecular coordinates are allowed to relax using the usual geometry optimization procedures.

2.10.2 Aromatic Ring Currents

A widely used magnetic marker of aromaticity is nucleus-independent chemical shift (NICS), popularized by Schleyer,[98,99] which attributes the intensity of magnetic shielding to diamagnetic ring currents. NICS is thus conveniently calculated as the value of the magnetic shielding tensor at various points in space — different versions of NICS exist depending on the component of shielding tensor measured and the exact point of measurement. A more intuitive (and less arbitrary)

definition relies on partitioning of space into atomic basins using the theory of atoms in molecules (AIM), and calculating the diamagnetic current crossing the boundary surfaces between adjacent ring carbon atoms. It should be noted that in both cases, the *ab initio* calculation uses a method termed Gauge-Independent Atomic Orbitals (GIAO)[100,101] to calculate the electronic response to incident magnetic field.

2.11 Experimental

2.11.1 Procedures and Characterization Data

Preparation of 2,4,6-tris(aminomethylene)cyclohexane-1,3,5-trione (TFP–ammonia Schiff base, 2.1)

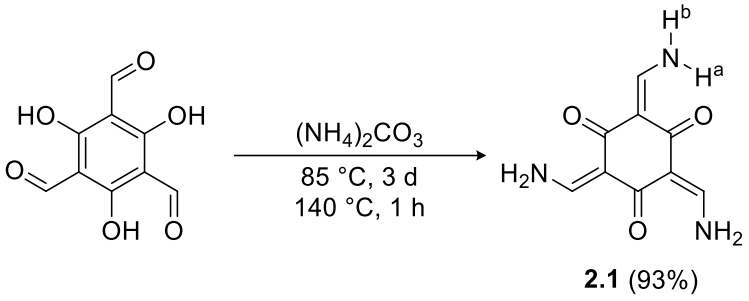

2.1 (93%)

TFP (150 mg, 0.714 mmol, 1 eq) and ammonium carbonate (2.00 g, 20.8 mmol, 30 eq) were ground together into a fine orange-rose powder. This powder was transferred to a small Schlenk tube, which was sealed and heated at 85 °C for three days. Following this, the tube was opened to air and the contents heated up to 140 °C for 1 h to remove any leftover ammonium carbonate, leaving 138 mg (0.667 mmol, 93%) of yellow-brown product.

Data for 2.1: ^{1}H NMR (400 MHz, DMSO-d_6) δ 10.32, 10.05 (m, br, 1H; NH^{a}), 8.57 (m, br, 1H; NH^{b}), 8.05 (m, 1H; CHN) ppm. ^{13}C {^{1}H} NMR (100 MHz, DMSO-d_6, 25 °C) δ 188.4 (CO), 185.0

(CO),* 181.9 (CO), 156.2 (CH), 155.8 (CH), 155.6 (CH), 155.1 (CH), 105.0 (*C*CH), 104.9 (*C*CH), 104.7 (*C*CH), 104.4 (*C*CH) ppm. IR (soluble form) ν = 3268 (br), 3118 (br), 1532 (br), 1429, 1298, 1092, 962, 838, 738, 671, 484, 444, 405 cm^{-1}. IR (insoluble form) ν = 3199 (br), 1733, 1597, 1541, 1430, 1364, 1340, 1269, 1207, 1160, 1032, 900, 832, 789, 609, 513, 463 cm^{-1}. HRMS (ESI/TOF-Q) *m/z*: [**2.1** + H]$^+$ Calcd for $C_9H_{10}N_3O_3$ 208.0722; Found 208.0724. Elemental analysis: Calcd. for $C_9H_9N_3O_3$ C: 52.17%, H: 4.38%, N: 20.28%; Found C: 52.51%, H: 4.68%, N: 18.65%.

Preparation of tris(N-salicylidenehydrazine) (TFP–hydrazine Schiff base, 2.2):

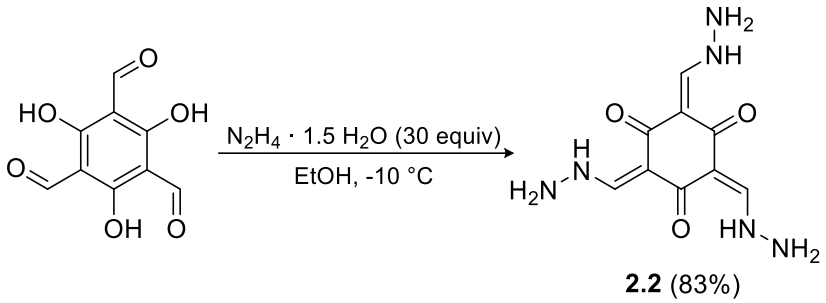

2.2 (83%)

Hydrazine hydrate ($N_2H_4{\cdot}1.5H_2O$, 2.0 mL, 2.0 g, 35 mmol, 73 equiv.) was added to a suspension of TFP (100 mg, 0.476 mmol, 1 equiv.) in ethanol (10 mL) chilled in a dry ice-ethylene glycol bath at -10 °C. After 3 min, ethanol (10 mL) and ethyl acetate (30 mL) were added. The resulting yellow suspension was filtered immediately and washed with ethanol, ethyl acetate, and DCM, giving the product as a yellow powder (98.4 mg, 0.390 mmol, 82%). Single crystals were obtained by quick addition of chloroform (3 mL) to a DMSO solution (1 mL) of **2.2**.

Data for 2.2: m.p. (decomposes slowly at r.t. and above); ^{1}H NMR (400 MHz, DMSO-d_6) major tautomer (**2.2$_{E\text{-}I}$**, 80%): δ=12.99 (s, 3H; OH), 8.16 (s, 3H; CH), 6.44 (s, 6H; NH_2) ppm, minor tautomer (**2.2$_{K\text{-}E}$**, 20%): δ=12.07 (d, ^3J(H,H)=11 Hz, 1H; NH), 11.56 (d, ^3J(H,H)=12 Hz, 1H; NH),

* Based on the relative intensity of ^{13}C peaks as well as HMBC coupling patterns, it appears that two of the CO resonances have very close frequencies, hence the missing CO resonance here.

11.50 (d, ^{3}J(H,H)=12 Hz, 1H; NH), 8.06 (d, ^{3}J(H,H)=11 Hz, 2H; CH), 8.01 (d, ^{3}J(H,H)=12 Hz, 1H; CH), 5.52 (s, 6H; NH_2) ppm; ^{13}C {^{1}H} NMR (100 MHz, DMSO-d_6): δ=162.7 (COH), 143.0 (CHN), 100.1 (*C*CH) ppm; IR (neat): ν = 3342, 3299, 3141, 1650, 1557, 1519, 1444, 1323, 1270, 1210, 1099, 1006, 963, 819, 755, 734, 699, 595, 513 cm^{-1}; UV/Vis (DMSO): λ_{max} (ε)=305 (5.5×10^4) nm (mol^{-1} L cm^{-1}); HRMS (ESI/TOF-Q) *m/z*: [**2.2** + H]$^+$ Calcd for $C_9H_{13}N_6O_3$ 253.1049; Found 253.1048.

Preparation of tris(N-salicylidenehydroxylamine) (TFP–hydroxylamine Schiff base, 2.3):

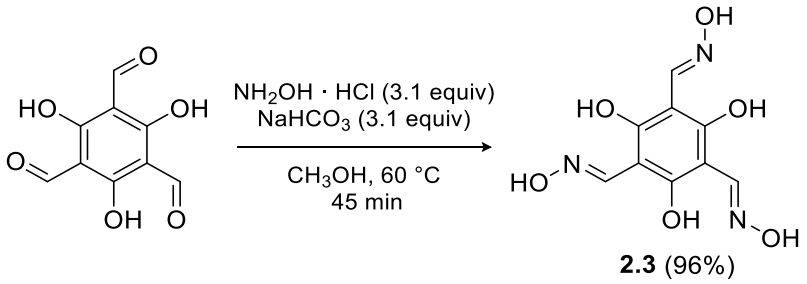

2.3 (96%)

A suspension of TFP (50.0 mg, 0.238 mmol, 1 equiv.), hydroxylamine hydrochloride (53.0 mg, 0.763 mmol, 3.2 equiv.), and $NaHCO_3$ (64.0 mg, 0.762 mmol, 3.2 equiv.) was stirred in methanol (10 mL, 60 °C, 45 min). Solvent was removed under reduced pressure and the product extracted with into THF-DCM (50:50, 20 mL). The residue obtained from evaporating this solution was washed with hot $CHCl_3$, affording the product (58.0 mg, 0.227 mmol, 96%) as a tan powder. Slow evaporation of a CH_3OH-CH_2Cl_2-hexanes solution yielded single crystals of **2.3**.

Data for 2.3: m.p. > 150 °C (decomposes); ^{1}H NMR (300 MHz, DMSO-d_6, 25 °C): δ=11.81 (s, br, 3H; COH), 11.56 ppm (s, 3H; NOH), 8.42 ppm (s, 3H; CH); ^{13}C {^{1}H} NMR (75 MHz, DMSO-d_6, 25°C): δ=158.6 (COH), 146.1 (CHN), 98.2 ppm (*C*CH); IR (neat): ν = 3508, 3416, 3255, 1628, 1602, 1454, 1405, 1322, 1277, 1244, 1142, 1012, 999, 961, 937, 768, 719, 689, 622 cm^{-1}; UV/Vis

(DCM): λ^{max} (ε)=278 nm (6.1 × 10^4 mol^{-1} L cm^{-1}); HRMS (ESI/TOF-Q) *m/z*: [**2.3** + H]$^+$ Calcd for $C_9H_{10}N_3O_6$ 256.0570; Found 256.0575.

Preparation of tris(N-salicylidenepivaloyl hydrazide) (TFP–pivaloyl hydrazide, 2.4):

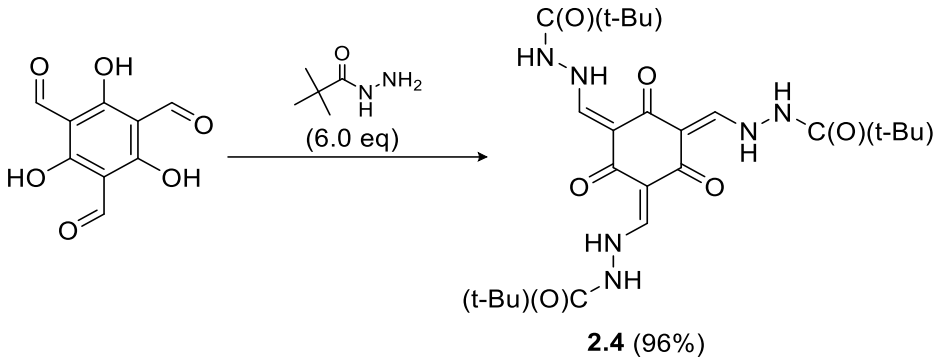

2.4 (96%)

TFP (50.0 mg, 0.238 mmol, 1 equiv.) and pivaloyl hydrazide (166 mg, 1.43 mmol, 6.0 equiv.) were combined in ethanol (5 mL) in a small glass bomb, giving a clear pale yellow solution that turned into a thick slurry. The bomb was sealed and heated at 100 °C for 2 h. Once the solution returned to room temperature, the pale yellow precipitate was collected by filtration, washed with methanol, and air dried, affording the product as a bright yellow powder (115 mg, 0.228 mmol, 96%). Single crystals were obtained by slowly cooling down a solution of **2.4** in hot 2-propanol.

Data for 2.4: m.p. > 250 °C (decomposes); ^{1}H NMR (400 MHz, DMSO-d_6, 25 °C): δ=13.84 (s, 3H; NH), 11.28 (s, 3H; NH), 8.81 (s, 3H; CH), 1.21 (s, 27H; CH_3) ppm; ^{13}C {^{1}H} NMR (100 MHz, DMSO-d_6, 25°C): δ=173.8 (CONH), 162.0 (COH), 144.8 (CHN), 99.3 (*C*CH), 38.1 (*C*(CH_3)$_3$), 27.5 (CH_3) ppm; IR (neat): ν = 3233, 2965, 1627, 1537, 1479, 1398, 1368, 1329, 1283, 1199, 1002, 919, 812, 781, 484 cm^{-1}; UV/Vis (EtOH): λ^{max} (ε)=319 nm (8.3 × 10^4 mol^{-1} L cm^{-1}); HRMS (ESI/TOF-Q) *m/z*: [**2.4** + H]$^+$ Calcd for $C_{24}H_{37}N_6O_6$ 505.2775; Found 505.2781.

Preparation of tris(N-salicyclidene(O-benzylhydroxylamine)) (2.5):

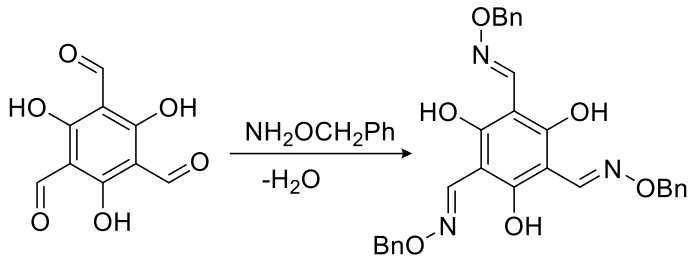

2.5 (40%)

TFP (199.0 mg, 0.947 mmol, 1 equiv.) and O-benzylhydroxylamine (350.0 mg, 2.84 mmol, 3 equiv.) were combined in ethanol (4.0 mL) and stirred at 55 °C for 4 h. Evaporation of solvent under reduced pressure gave 431 mg of crude product, which was purified by flash column chromatography on silica gel using 1:2 CH_2Cl_2:hexanes as eluent. The first fraction collected (R_f = 0.37, 1:2 CH_2Cl_2:hexanes) was evaporated to give the product as a tan solid (200.3 mg, 0.381 mmol, 40%). Slow evaporation of a CH_2Cl_2-hexanes solution gave single crystals of **2.5**.

Data for 2.5: m.p. 134–138 °C; ^{1}H NMR (400 MHz, CD_2Cl_2): δ=11.26 (s, 3H; OH), 8.61 (s, 3H; CHN), 7.44–7.34 (m, 15H, Ar), 5.17 (s, 6H; CH_2) ppm; ^{13}C NMR (100 MHz, CD_2Cl_2): δ=160.0 (COH), 147.1 (CHN), 136.9 (*C*CH), 128.50 (Ar), 128.46 (Ar), 128.2 (Ar), 97.9 (*C*CH_2), 76.6 (CH_2) ppm; IR (neat): ν =2929, 1632, 1481, 1467, 1455, 1360, 1306, 1211, 1165, 1027, 998, 957, 933, 921, 740, 694, 635, 580, 511, 422 cm^{-1}; UV/Vis (DCM): λ_{max} (ε)=290 nm (5.0×10^4 mol^{-1} L cm^{-1}); HRMS (ESI/TOF-Q) *m/z*: [**2.5** - H]$^-$ Calcd for $C_{30}H_{26}N_3O_6$ 524.1822; Found 524.1828.

Preparation of tris(N-salicylidenepentafluoroaniline) (TFP–pentafluoroaniline Schiff base, 2.6):

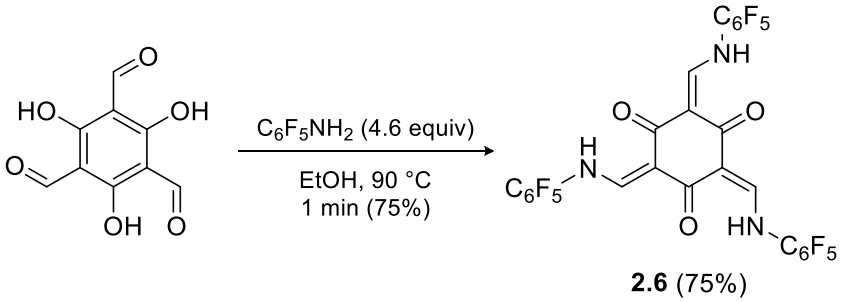

2.6 (75%)

Pentafluoroaniline (100 mg, 0.564 mmol, 4.6 equiv) and TFP (24.8 mg, 0.118 mmol) were combined in ethanol (2 mL) and heated in a sealed Schlenk tube at 90 °C for 1 min, causing a bright yellow solid to precipitate. Filtration and washing with ethanol yields the product (63.3 mg, 75%).

Data for 2.6: m.p. > 250 °C (decomposes); ^{1}H NMR (500 MHz, toluene-d_8, 80 °C): δ=13.66 (d, ^{3}J(H,H)=12 Hz; NH_{symm}), 13.44 (d, ^{3}J(H,H)=12 Hz; NH_{asymm}), 12.70 (d, ^{3}J(H,H)=12 Hz; NH_{asymm}), 12.59 (d, ^{3}J(H,H)=11 Hz; NH_{asymm}), 8.75 (d, ^{3}J(H,H)=13 Hz; CH_{asymm}), 8.68 (d, ^{3}J(H,H)=12 Hz; CH_{symm}), 8.64 (d, ^{3}J(H,H)=13 Hz; CH_{asymm}) ppm; $^{13}C\{^{1}H,^{19}F\}$ NMR (125 MHz, toluene-d_8, 80 °C): δ=186.0 (CO), 154.2 (CHN), 140.8 (CF), 139.0 (CF), 138.9 (CF), 116.3 (CNH), 109.5 (*C*CH) ppm; ^{19}F NMR (100 MHz, toluene-d_8, 80°C): δ=-153.6 (d, ^{3}J(F,F)=22 Hz, *o*-CF_{symm}), -153.79 (d, ^{3}J(F,F)=22 Hz, *o*-CF_{asymm}), -153.83 (d, ^{3}J(F,F)=22 Hz, *o*-CF_{asymm}), -160.6 (t, ^{3}J(F,F)=21 Hz; *p*-CF_{asymm}), -160.7 (t, ^{3}J(F,F)=22 Hz; *p*-CF_{asymm}), -160.8 (t, ^{3}J(F,F)=21 Hz; *p*-CF_{symm}), -161.1 (t, ^{3}J(F,F)=22 Hz; *p*-CF_{asymm}), -162.1 ppm (td ^{3}J(F,F)=21 Hz, ^{5}J(F,F)=5 Hz; *m*-CF_{asymm}); -162.2 ppm (td ^{3}J(F,F)=22 Hz, ^{5}J(F,F)=5 Hz; *m*-CF_{asymm}); -162.3 (td ^{3}J(F,F)=22 Hz, ^{5}J(F,F)=5 Hz; *m*-CF_{symm}); -162.4 ppm (td ^{3}J(F,F)=22 Hz, ^{5}J(F,F)=5 Hz; *m*-CF_{asymm}) ppm; IR (neat): ν =3093, 1598, 1564, 1514, 1478, 1429, 1345, 1266, 995, 958, 864, 661, 576, 514, 437 cm^{-1}; UV/Vis (DCM): λ^{max} (ε)=389 (8.5×10^4), 316 (4.5×10^4), 230 nm (1.9×10^4 mol^{-1} L cm^{-1}); HRMS (ESI/TOF-Q) *m/z*: [**2.6** + H]$^{+}$ Calcd for $C_{27}H_7N_3O_3F_{15}$ 706.0248; Found 706.0253.

Tris(N-salicylideneacetamide) (TFP–acetamide Schiff base, 2.7): [*]

[*] The following procedure constitutes the first step of the formylation reaction converting phloroglucinol to TFP, the preparation of which is explored in Chapter 5.

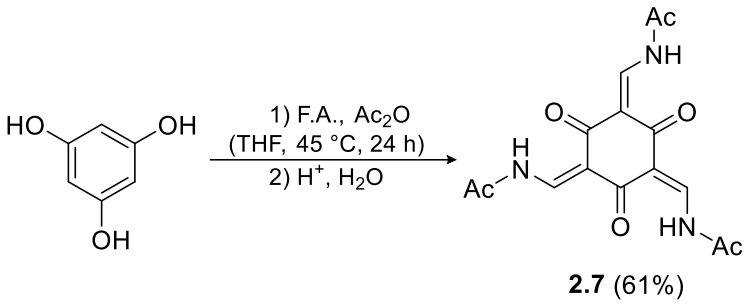

2.7 (61%)

Formamidine acetate (8.25 g, 79.4 mmol, 5.0 equiv) and phloroglucinol (2.00 g, 15.9 mmol, 1.0 equiv) were combined in THF (200 mL) at 45 °C, in a round-bottom flask. After stirring for 15 min, acetic anhydride (14.7 mL, 159 mmol, 10.0 equiv) was added, the flask was subsequently capped and the reaction allowed to proceed for 1 d. The reaction was worked up by evaporating THF solvent, leftover acetic anhydride and acetic acid under reduced pressure at 50 °C, followed by stirring in HCl (150 mL, 0.02 M) at 50 °C for 2 h. Suction filtration of the resulting light orange-salmon coloured suspension and washing with water gave pure **2.7** (3.27 g, 9.82 mmol, 61%).

Data for 2.7: m.p. > 233 °C (decomposes); ^{1}H NMR (400 MHz, $CDCl_3$, 25 °C): δ=12.63 (d, ^{3}J(H,H)=12 Hz, 3H; NH), 8.78 (d, ^{3}J(H,H)=12 Hz, 3H; CH), 2.37 (s, 9H; CH_3) ppm; ^{13}C NMR (100 MHz, $CDCl_3$, 25 °C): δ=186.1 (*C*OCH_3), 169.3 (*C*O), 147.8 (CHN), 110.8 (*C*CH), 24.1 (CH_3) ppm; IR (neat): $\tilde{\nu}$=3190, 2929, 1737, 1607, 1557, 1456, 1368, 1338, 1265, 1207, 1169, 1034, 984, 892, 827, 787, 641, 589, 512, 461 cm^{-1}; UV/Vis (DCM): λ^{max} (ε)=371 (5.6×10^4), 360 (5.8×10^4), 291 nm (4.4×10^4 mol^{-1} L cm^{-1}); HRMS (ESI/TOF-Q) *m/z*: [**2.7** + Na]$^+$ Calcd for $C_{15}H_{15}N_3O_6Na$ 356.0859; Found 356.0859.

Chapter 3

Tautomeric Acceleration of Aromatic H/D Exchange

3.1 Introduction

Isotopic labeling, making molecules with specific isotopes of the constituent elements at one or more positions, has served as a powerful diagnostic tool since the earliest days of modern chemistry. An early example is Konrad Bloch's elucidation of the mechanism for cholesterol biosynthesis using ^{14}C-labeled acetic acid as carbon source,[102–105] a discovery that earned him and F. F. K. Lynen the 1964 Nobel Prize in Physiology or Medicine.

Hydrogen, the lightest element on the periodic table occurs in nature as one of three isotopes. Of these, the heaviest, tritium (^{3}T), is unstable with a half life of 12 years while protium (^{1}H) and deuterium (^{2}D) are stable. Protium makes up the vast majority of the planet's supply of hydrogen, with deuterium accounting for only 156 parts per million of hydrogen atoms in ocean water.

Both ^{1}H and ^{2}D have atomic number Z = 1 (*i.e.* only one proton in the nucleus). They therefore have very similar chemical properties, differing primarily in the vibrational energy of the bonds that they form. A bond between atoms A and B can be modelled as a spring with force constant *k* connecting to two particles with masses m_A and m_B, respectively. In this model system, the vibration energy is $E_n = (n + 1/2)\hbar\omega$ (with $n = 0, 1, 2, ...$) where $\omega = \sqrt{k/\mu}$ and μ, the reduced mass, is defined as $\frac{m_A m_B}{m_A + m_B}$. The reduced mass is roughly twice as large for a typical X–D versus X–H bond (X being a second-row element or heavier), translating to the vibrational energy, E_n, being ≈ 40% smaller for X–D bonds at a given *n*.

The smaller E_n of X–D bonds has two useful consequences. First, it makes deuterium labelling ideal for vibrational studies, thanks to the pronounced difference in infrared absorption frequencies for X–H bonds upon deuterium substitution. Second, since X–H and X–D have different energies in their vibration ground states (E_0, also known as the zero-point energy), more energy must be supplied to break a X–D bond. This gives rise to the phenomenon known as the kinetic isotope effect, where the rate of a reaction is reduced by replacing an element with one of its heavier isotopes. Among stable nuclides across the periodic table, the kinetic isotope effect is by far most dramatic for the $^1H/^2D$ pair.*

The discovery of the kinetic isotope effect not only amplified the diagnostic value of deuterium labeling, it allowed the technique to evolve from a mere structural probe to a method for tuning reactivity. This is used to great effect in synthetic chemicals, especially pharmaceuticals, where it is used to slow down the deactivation and removal of drug molecules by enzymatic breakdown, thereby enhancing their bioavailability.[106–108]

Although deuterium has a low natural abundance, ocean water can be deuterium enriched to give D_2O (heavy water) relatively inexpensively. Figure 3.1 illustrates the Girdler sulfide process, a common method for deuterium enrichment that relies on the temperature dependence of the deuterium exchange equilibrium between water and H_2S.

* $^1H/^3T$ would give a more pronounced isotope effect, but tritium is not a stable nuclide.

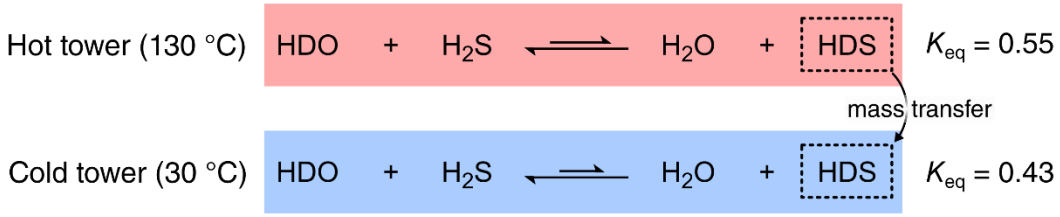

Figure 3.1. The Girdler sulfide process for deuterium enrichment of ocean water to D_2O. The equilibrium constant K_{eq} for deuterium transfer from HDO to H_2S is larger in the hot tower than in the cold tower, allowing a net transfer of deuterium from the hot to the cold tower through the mass transfer of HDS between the two. As a result, water in the hot tower, replenished from the ocean, is deuterium-depleted while the cold water is deuterium enriched.

Other methods for D_2O production include electrolysis and distillation of water or liquid H_2.[109] While these processes are generally energy-intensive, D_2O is still far less expensive than other commercially available isotopically enriched compounds, *e.g.* $^{15}NH_4Cl$, $^{13}CO_2$.

Being a spin ±1 nucleus, deuterium also has the advantage of being NMR-active. Deuterium's small gyromagnetic ratio (ca. 15% that of proton) means it is less sensitive than proton, and its quadrupole moment leads to line broadening;[86] however this quadrupole moment is sufficiently small that deuterium NMR can still be used to confirm labeling at the desired position in a molecule by comparison with the proton chemical shift at the same position. The combination of deuterium-labelling and NMR has been instrumental in numerous discoveries in structural biology.[110–113]

3.2 Deuterium Labeling by H/D Exchange

In contrast to ^{13}C, ^{15}N, and ^{17}O labeled compounds, which often need to be synthesized from scratch, deuterated molecules can often be prepared by exchanging hydrogen atoms in a molecule with deuterium. In many cases, this is thanks to the relative ease with which hydrogen atoms can be removed from a molecule under basic conditions. Figure 3.2 shows an example from the

literature where an organic molecule is deuterium labeled by removal of a proton using strong base. The resulting carbanion can be quenched with D_2O to give deuterium labeling at the acidic site.[114]

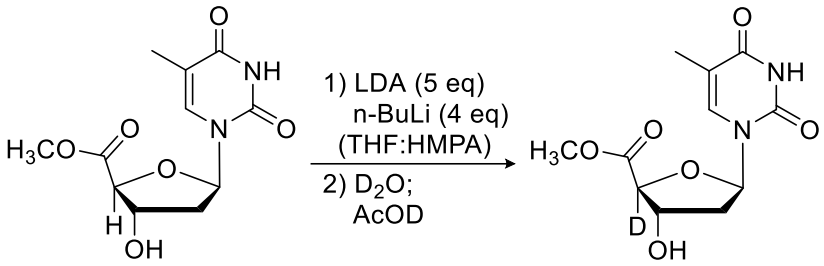

Figure 3.2. Deuterium labeling of a nucleoside by basic deprotonation and quenching with D_2O.*

One key constraint with methodologies like the one presented above is to use conditions that are compatible with the functional groups in the substrate. In what follows, deuteration strategies for various classes of compounds are examined in more detail.

3.3 H/D Exchange of Acidic Hydrogen Atoms

Alcohols, amines, carboxylic acids and many other organic functional groups contain hydrogen atoms with substantial partial positive charge. These acidic hydrogen atoms are often easily exchanged with solvent molecules. Upon exposure to solvents with exchangeable deuterium atoms, *e.g.* D_2O or CD_3OD, these labile hydrogen atoms are readily replaced with deuterium owing to the overwhelming majority of solvent molecules, Figure 3.3a.

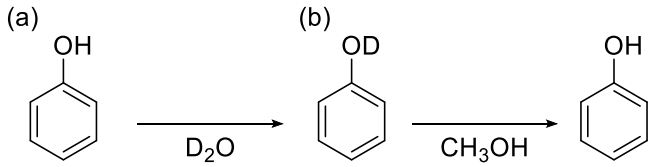

Figure 3.3. (a) Deuteration of phenol in D_2O. (b) Deuterium removal upon contact with CH_3OH.

* The authors report that using fewer equivalents of strong base gave back the starting material following the quenching step. They note that they have not found a good rationale for the necessity of 9 equivalents of strong base.

In a sense, this form of H/D exchange represents the most straightforward form of deuterium labeling. Unfortunately, the same labile character that enables this instantaneous H/D exchange means that the process is readily reversed in the presence of moisture or protic solvents, Figure 3.3b, severely limiting the range of applications for this method.

Due to the temporary and often inconsequential nature of this type of H/D exchange, the rest of this chapter only depicts the ^{1}H-containing form of acidic moieties (*i.e.* X–H versus X–D, X = N, O) even where these groups are expected to be deuterated.

3.4 H/D Exchange of α-Hydrogen Atoms in Carbonyl Compounds

Keto-enol tautomerism in carbonyl compounds allows hydrogen atoms at the α position to be exchanged with solvent. In the presence of deuterated solvent, this can lead to deuterium exchange at the α position, as demonstrated in Figure 3.4.

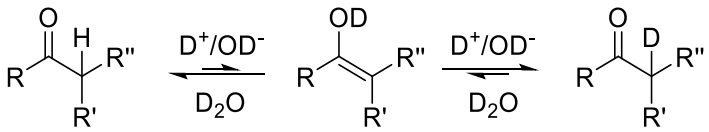

Figure 3.4. Acid or base-catalyzed H/D exchange of a ketone at the α position in D_2O through keto-enol tautomerism.

While the use of acid or base catalyst is often necessary for keto-enol tautomerism, the above process gives a cost-effective route to deuterated carbonyl compounds and is used, for instance, in the preparation of acetone-d_6 for use as NMR solvent.

3.5 H/D Exchange of Aromatic Hydrogen Atoms

The C–H bond in benzene is strong (D_0 = 113 kcal/mol for benzene versus 96–105 kcal/mol for alkanes) thanks to the sp^2 hybridization of the ring carbon atoms.[115] In addition, none of $C_6H_5^{\bullet}$, $C_6H_5^{+}$, or $C_6H_5^{-}$ are particularly stable. This might give the impression that exchanging hydrogen

atoms attached to aromatic rings, also known as aromatic or nuclear hydrogen atoms, must be difficult. Nevertheless, various methods have been developed to bring about this class of reaction.

3.5.1 Acid/Base-Catalyzed Aromatic H/D Exchange

As with other electrophiles, electrophilic deuterium atoms can react with activated aromatic rings in an electrophilic aromatic substitution reaction, effectively giving H/D exchange. This phenomenon was first investigated using gravimetric methods by Small and Wolfenden in 1938,[116] Figure 3.5a.

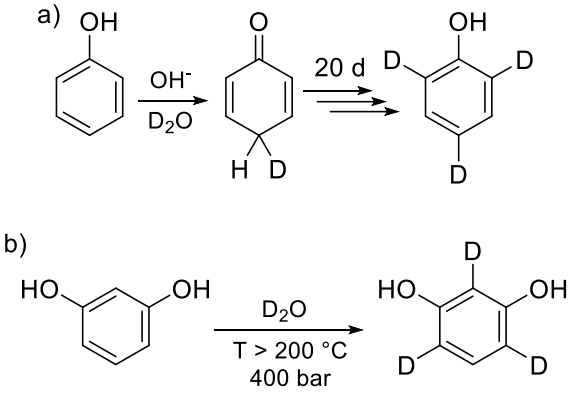

Figure 3.5. Literature examples of aromatic H/D exchange.

Exclusive ortho/para H/D exchange and the acid/base catalyzed nature of this reaction supports an electrophilic mechanism. Equilibration under neutral or acid-catalyzed conditions D_2O at high temperature (> 200 °C, 400 bar, Figure 3.5b) has been used to similar effect.[117–119]

3.5.2 Aromatic H/D Exchange using Aryl Carbonions

While not commonly used, slow deprotonation of aromatic rings by NH_2^- and reaction of the resulting Ar^- anions with D_2O can effect H/D exchange.[120] Supercritical water (250–400 °C, 0.5–16 h) with catalytic NaOH has recently been shown to give similar results with benzene.[121]

It is possible to metallate aromatic rings and quench the resulting aryl metal compounds with D_2O. The rate of deprotonation has been observed to depend critically on the acidity of the

removed hydrogen atom, which is largely determined by the inductive effect of nearby ring substituents.[122] Thus, good selectivity for a specific site in the molecule has been demonstrated in the case of 1,3-dimethoxybenzene, Figure 3.6.

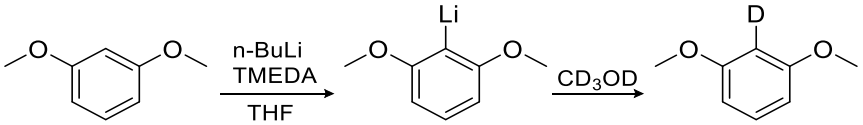

Figure 3.6. Acid or base-catalyzed H/D exchange of a ketone at the α position in D_2O through keto-enol tautomerism.

3.5.3 Transition Metal-Catalyzed Aromatic H/D Exchange

Many recent developments in aromatic H/D exchange use transition metal catalysis to lower the activation barrier.[123–126] Common examples are ruthenium (Figure 3.7a)[127] and iridium complexes,[124,125] Pt/C,[123,128] group 5 and 6 chlorides (Figure 3.7b),[129] using various deuterium sources (*e.g.* D_2, D_2O, or C_6D_6).

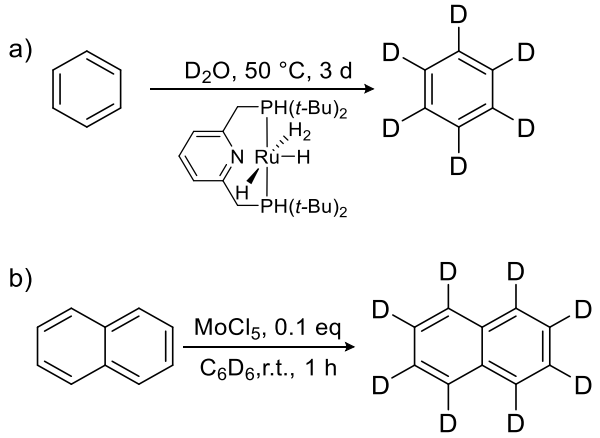

Figure 3.7. (a) Total H/D exchange of benzene using D_2O as deuterium source and a ruthenium catalyst. (b) H/D exchange between naphthalene and benzene catalyzed by $MoCl_5$.

As the examples show, transition metal-catalyzed H/D exchange generally gives superior reactivity, but poor selectivity for different aromatic positions in the molecule.

3.6 Serendipitous Discovery of H/D Exchange in a Schiff Base Macrocycle

Our first encounter with H/D exchange under ambient conditions was in the course of characterizing macrocycle **3.1**, Figure 3.8. PhD student Jian Jiang working in the MacLachlan lab noticed that the ^{1}H NMR resonances corresponding to the H^a protons in **3.1** gradually lose their intensity when exposed to CD_3OD.[51]

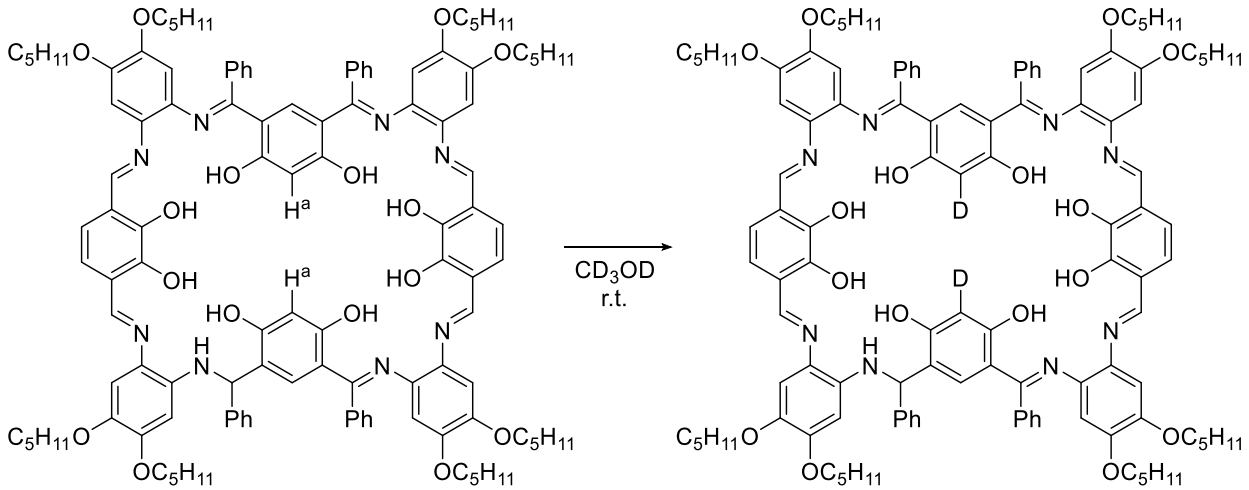

Figure 3.8. H/D exchange of the H^a position in macrocycle m in CD_3OH under ambient conditions.

While aromatic H/D exchange in resorcinols is hardly new — we found that the base-catalyzed H/D exchange of the 2,4, and 6 positions of resorcinol is essentially complete in 24 h, Figure 3.9 — the phenomenon had never been observed without the use of catalyst and in CD_3OD.

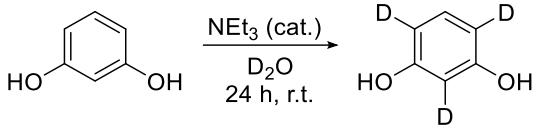

Figure 3.9. Base catalyzed H/D exchange of resorcinol.

3.7 Design and Preparation of Model Compounds

The host environment inside the cavity of a macrocycle is known to bring about changes to the reactivity of guest molecules. Therefore, one possible explanation for the abnormal H/D exchange in **3.1**. might be the enhancement of CD_3OD acidity inside the macrocycle cavity. We set out to test this hypothesis by preparing Schiff base **3.2**, Figure 3.10, a non-macrocyclic analogue of **3.1**, from the direct solvent-free condensation of 4,6-dibenzoylresorcinol and ethanolamine (ethanolamine was chosen in order to improve solubility in CD_3OD). When stored in CD_3OD, **3.2** showed similar loss of NMR signal for the H^b proton over a week while the other aromatic resonances were unaffected. This means that H/D exchange in **3.1** arises not because of a macrocycle-specific effect, but due to the properties of the individual Schiff base units.

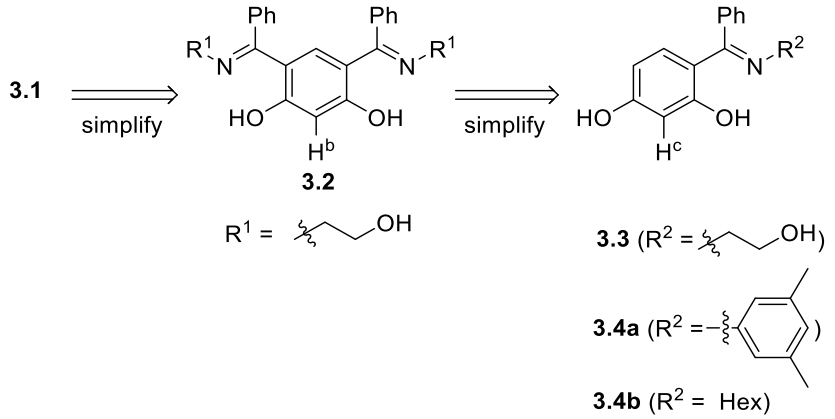

Figure 3.10. Progressive simplification of macrocycle **3.1** to smaller model compounds.

To further simplify our model system, we chose to remove one of the ketimine sidechains of **3.2**, arriving at compound **3.3**, which can be prepared in a similar fashion to **3.2**. Encouragingly, **3.3** underwent deuterium exchange of H^c faster than both **3.2** and **3.1**. The ethanolamine OH group is not essential to facile H/D exchange; Schiff bases **3.4a** and **3.4b** also undergo H/D exchange under similar conditions ($t_{1/2}$ = 303, 4.2 h, respectively). Given its reactivity, high solubility in CD_3OD, and simple structure, **3.3** was used as our principal model for the remainder of this study.

3.8 Detecting and Monitoring H/D Exchange

Mass spectrometry and ^{1}H NMR spectroscopy were used to confirm and monitor the exchange of aromatic protons. Here we describe the protocol used for each technique in detail.

3.9 Monitoring H/D Exchange by ^{1}H NMR

H/D exchange is most easily monitored using ^{1}H NMR in CD_3OD, where the signals due to exchanging protons disappear over time. Figure 3.11 shows the ^{1}H NMR spectrum of **3.3** taken at various time intervals. The exchange of proton H^c is evidenced by the disappearance of its resonance around 6.15 ppm as well as any couplings to nearby protons, owing to J^n_{H-D} being much smaller than J^n_{H-H} at comparable separation. The reverse reaction (D/H exchange) can be ignored due to the large excess of deuterated solvent relative to substrate.

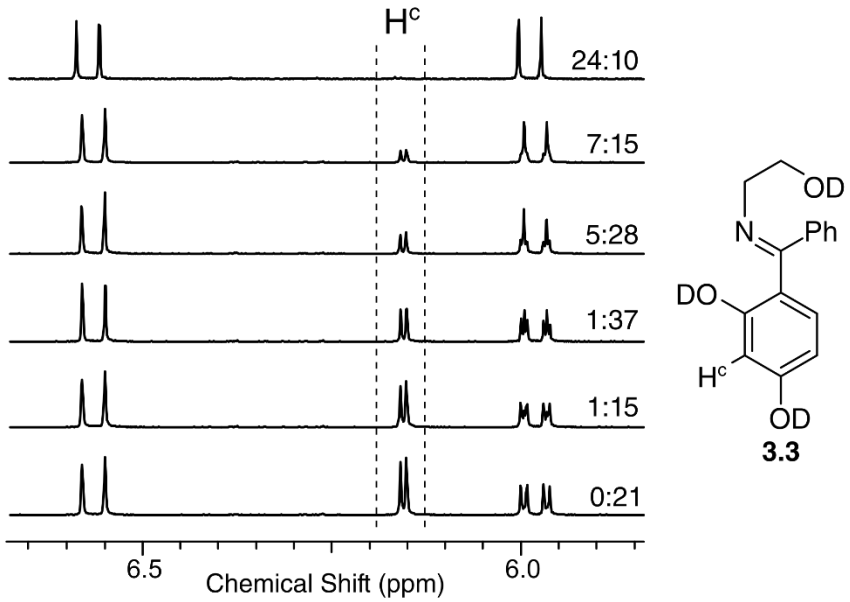

Figure 3.11. Deuterium exchange of H^c in **3.3** monitored by ^{1}H NMR (CD_3OD, hr:min).

Integration of the peak due to H^a can indicate the fraction of unexchanged substrate. In this case, getting accurate peak integration values requires that an adequate delay be added between

successive acquisitions. Termed *recycle delay* (`d1` in the Bruker terminology), integration errors within 5% are possible if this values is to 10 × T_1 or longer (T_1 being the longest longitudinal relaxation time constant for the protons in the molecule). In turn, T_1 for different resonances in a molecule can be calculated using the *inversion recovery* NMR experiment. We verified that for **3.3**, the longest T_1 < 1.5 s and therefore used `d1 =` 15 s during acquisition. These settings were used for all other compounds studied, since T_1 was assumed to be shorter than 1.5 s for them as well.

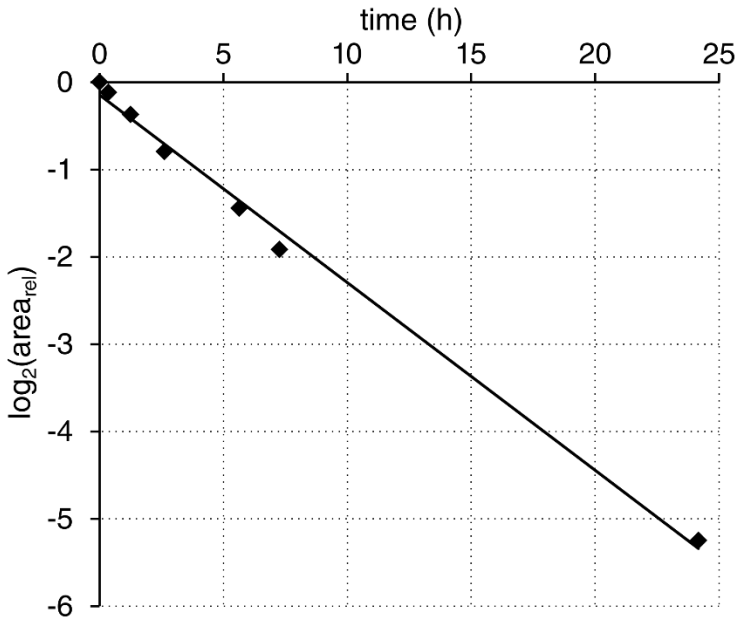

Figure 3.12. Plot of the relative area of the H^c peak in **3.3** versus time (*log_2* vertical axis). Half-life ($t_{1/2}$) = 4.0 h.

Figure 3.12 shows the area of the H^c peak (relative to any of the other aromatic peaks in Figure 3.11) over time. A linear plot results when a logarithmic vertical axis is used, indicating first-order kinetics with respect to substrate. Table 3.1 summarizes kinetic data obtained for **3.2**, **3.3**, **3.4a**, and **3.4b**.

Table 3.1. Kinetic data for H/D exchange of **3.2**–**3.4**.

	Compound 3.2 (CD_3OD)				**Compound 3.3 (CD_3OD)**				**Compound 3.4a (CD_3OD)**		**Compound 3.4b (CD_3OD)**	
	experiment #1		**experiment #2**		**experiment #1**		**experiment #2**					
	t (h)	A_{rel}	t (h)	A_{rel}	t (h)	A_{rel}	t (h)	A_{rel}	t (h)	A_{rel}	t (h)	A_{rel}
	1.5	0.97	0.4	0.91	0.35	0.92	0.42	0.94	143	0.70	0.25	0.95
	5.2	0.94	24	0.77	1.2	0.77	5.7	0.85	262	0.53	0.97	0.83
	21	0.84	70	0.54	2.6	0.58	30	0.43	282	0.51	1.9	0.71
	27	0.83	145	0.39	5.6	0.37	81	0.10	306	0.47	4.7	0.46
	53	0.70	172	0.36	7.2	0.26			331	0.45	7.7	0.28
	101	0.58			24	0.026			357	0.44		
									430	0.37		
									475	0.32		
$t_{1/2}$	134 h		128 h		4.0 h*		128 h		303 h		4.2 h	

3.10 Detection of H/D Exchange by Mass Spectrometry

One oversimplification committed in the previous sections is that of disregarding H/D exchange at the phenolic positions. Indeed, due to the labile nature of the phenolic hydrogen atoms, aromatic H/D exchange is always preceded by deuteration of these functional groups, *i.e.* the OD form results instead of OH, Figure 3.13. Naturally, these deuterated positions are not visible in ^{1}H NMR spectra and will quickly be restored to their OH form in the presence of, *e.g.*, H_2O or CH_3OH.

* Early samples of **3.3** were isolated as a 1:1 complex of **3.3** and ethanolamine, the basic properties of which lead to significantly shorter half-life in this replicate relative to replicate #2. Replicate #2 and other samples used throughout this study do not contain detectable (by ^{1}H NMR) contamination of the parent amine used in Schiff base preparation.

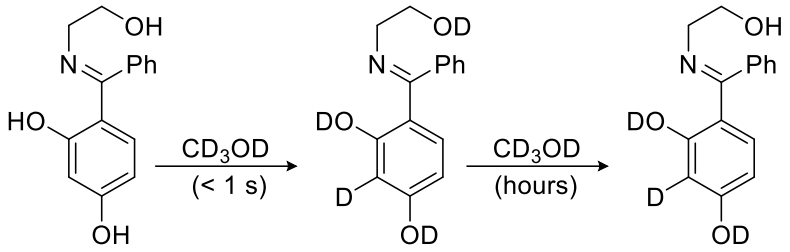

Figure 3.13. Timescale comparison for deuteration of phenolic and aromatic positions.

Mass spectrometric detection of H/D exchange follows the protocol outlined in Figure 3.14. Compound **3.3** was stored in CD_3OD for a week to allow the aromatic position of interest to fully exchange. Next, CD_3OD was evaporated under high vacuum and the residue of **3.3**-*d*$_4$ dissolved in CH_3OH, immediately restoring the phenol moieties to their original protiated (^{1}H-containing) form, **3.3**-*d*. At this point, the high-resolution ESI spectrum of the resulting solution needs to be measured before the reverse exchange of the aromatic position can take place. Alternatively, CH_3OH can be evaporated before sample submission to stop the reverse process.

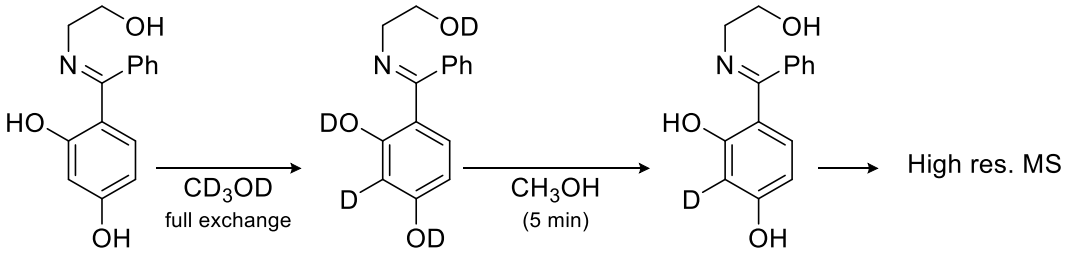

3.3
m/z
257.1052 (100.0%)
258.1085 (16.2%)
259.1119 (1.2%)

3.3-*d*$_4$

3.3-*d*
m/z
258.1121 (37%)
259.1084 (100%)
260.1214 (20%)

Figure 3.14. Example procedure for detection of H/D exchange by mass spectrometry.

The resulting high-resolution electrospray ionization mass spectrum (HRMS) shows ions at 258.1121 (37%), 259.1084 (100%), 260.1214 (20%) m/z. Considering the natural distribution of isotopologues of pristine **3.3** due to ^{13}C (Figure 3.14), one can calculate the contributions of [**3.3** + H]$^+$ and [**3.3**-*d* + H]$^+$, and [**3.3**-*d*$_2$ + H]$^+$ at 25%, 73%, and 2%, respectively.

3.11 Initial Hypothesis and Control Experiments

As mentioned in Section 3.5.1, H/D exchange of phenols in water is an electrophilic aromatic substitution, the first step of which involves combining the aromatic compound and incoming electrophile to form an unstable Wheland intermediate, Figure 3.15. The instability of this intermediate is attributed to the presence of an sp^3-hybridized ring carbon, causing disruption of aromaticity.

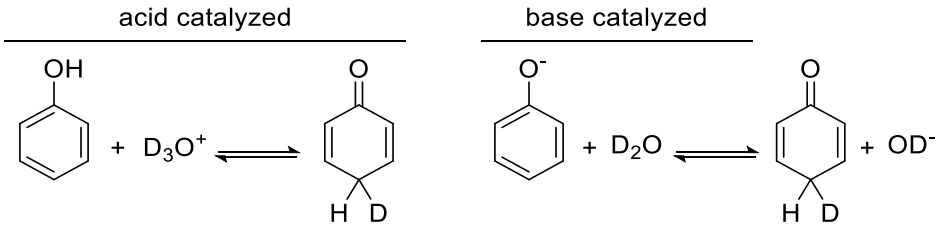

Figure 3.15. Formation of Wheland intermediate during the H/D exchange reaction of phenols.

We hypothesized that facile H/D exchange in **3.3** follows a similar mechanism, but one where the energetic cost of forming the Wheland intermediate has been mitigated by the salicylketimine moiety. In particular, we were inspired by the dearomatization of the central ring in keto-enamine TSANs, as discussed in Chapter 2. Could a similar keto-enamine tautomer weaken aromaticity and allow the Wheland intermediate to form more readily?

If this hypothesis were true, facile H/D exchange in **3.3** would depend on tautomerization of both salicylketimine and 4-hydroxy moieties. As such, we expected the process to hinge on the labile character of the salicylketimine proton, the proton affinity of the nitrogen atom, and the ability of the 4-hydroxyl moiety to undergo keto-enol tautomerism.

As an initial test of our hypothesis, we prepared a number of derivatives of **3.3** each of which targeted one of the above three factors, Figure 3.16. Thus, methyl protection of the 4-hydroxyl

group in **3.5** prevents its keto-enol tautomerism while replacement of the salicylketimine H atom with a non-labile methyl group in **3.6** disables keto-enamine/enol-imine tautomerism. In addition, we looked at the parent ketone **3.7**, expecting that the low basicity of the carbonyl oxygen would highly disfavor the keto-enamine equivalent tautomer **3.7k**. All three compounds were left intact after a week of storage in CD_3OD. This indicates that the factors outlined above are indeed essential to facile H/D exchange.

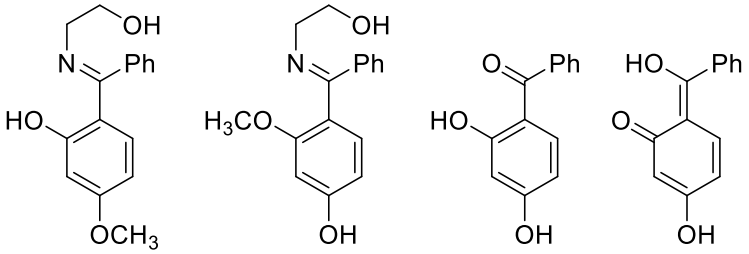

3.5 **3.6** **3.7** **3.7k**

Figure 3.16. H/D exchange substrates used in control experiments.

3.12 Effect of Solvent and pH

Given the H/D exchange activity seen in CD_3OD, we were curious whether other deuterated solvents could be used as source of deuterium. This would make the method applicable to compounds insoluble in methanol, for instance. It is necessary that the donated D atoms come from a labile position in the molecule. This criterion leaves D_2O and CD_3OD as the only viable options, since they are the only readily available NMR solvents with rapidly exchangeable deuterium atoms. Although D_2O is less expensive, it is a poor solvent for most organic compounds. To overcome this limitation, **3.4b** was dissolved in $CDCl_3$ and the resulting solution shaken with a few drops of D_2O. To our surprise, aromatic H/D exchange proceeded at a much higher rate under these conditions than in CD_3OD.

As mentioned earlier, both acid and base catalysis are known to facilitate aromatic H/D exchange. Indeed, the data in Table 3.1 shows that an equimolar mixture of **3.3** and base (ethanolamine, in this case) undergoes H/D exchange some 30 times faster than pure **3.3**. This raises the question of whether the fast exchange observed in mixed $CDCl_3$–D_2O medium might be due to the presence of fortuitous acid contamination, which is commonly seen in chloroform. Comparing the rate of exchange when unbuffered D_2O is used with that in D_2O buffer at pD = 5.6, 6.6, and 7.2 shows no significant change in H/D exchange half-life (4–5 min ± 30 s). Thus, it is safe to assume that substrate protonation (*e.g.* due to acid contamination) or deprotonation (*e.g.* by base contamination or due to the acidity of the phenolic protons) is nonessential to rapid H/D exchange. Appendix B describes the experimental protocol, obtained data, and further control experiments related to this observation.

The fast H/D exchange seen under these conditions suggests two possible explanations. Since no H/D exchange is seen in the absence of D_2O, the mechanism must include some form of substrate interaction with D_2O. Still, one can envision an intramolecular mechanism where phenolic OD deuterium (arising from the instantaneous H/D exchange of the phenolic OH with D_2O) would migrate to the 3 position in an intramolecular fashion, Figure 3.17a. Alternatively, the small amount of D_2O dissolved in $CDCl_3$ could form hydrogen bonded networks around (*i.e.*, solvate) substrate molecules, allowing solvent-mediated deuterium transfer to C3, Figure 3.17b.

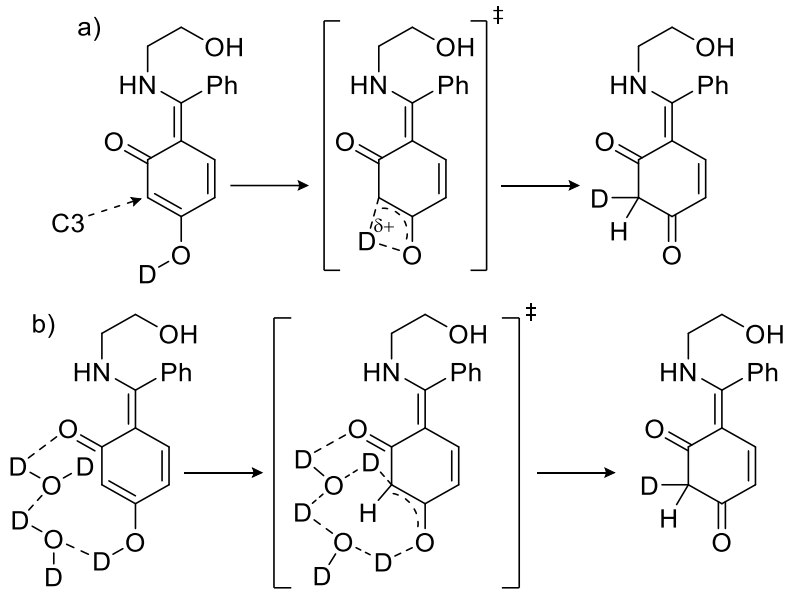

Figure 3.17. Putative intramolecular (a) and solvent-mediated (b) mechanisms for protonation of C3.

Note that Figure 3.17 shows the substrate in its keto-enamine tautomeric form based on our hypothesis that this tautomeric state forms Wheland-like intermediates more easily due to its compromised aromaticity. We shall validate this assumption in the next section. Further, Section 3.21 compares the viability of the two pathways laid out in Figure 3.16 by calculating their respective activation energies.

3.13 Initial Ab Initio Studies

Having formed a rough hypothesis regarding the mechanism of H/D exchange, we started a collaboration with Dr. Francesco Lelj to use *ab initio* techniques to probe and validate our proposed mechanism. This was done in two steps. In the first part, possible intermediates involved in the exchange reaction were screened based on their energy relative to the resting state of the system. The second part, presented in Section 3.21, involves constructing the transition states that connect these plausible intermediates. We also verified that these transition states give experimentally sound rates for the overall reaction.

3.13.1 Kinetic Verification of Mechanisms

The observed first-order rate constant *k* can be used to derive the effective activation energy for the rate-determining step in the reaction, presumably involving the transfer of deuterium to the aromatic position. The Eyring–Polanyi equation gives the following expression for the rate constant, *k*.

$$k = \frac{ln\,2}{t_{\frac{1}{2}}} = \frac{k_B T}{h} e^{-\frac{\Delta G^{\ddagger}}{RT}}$$

Based on the half-life observed for H/D exchange of **3.3** (4.6 h), $\Delta G^{\ddagger}$ is calculated to be 24 kcal/mol. This gives an upper limit to the $\Delta E^{\ddagger}$ of the reaction, since $\Delta E^{\ddagger} \approx \Delta H^{\ddagger} = \Delta G^{\ddagger} + T\Delta S^{\ddagger}$ and, as we will see, $\Delta S^{\ddagger}$ is almost certainly negative.* Therefore, in what follows, our aim will be to find a pathway with $\Delta E^{\ddagger} < 24$ kcal/mol.

3.14 Ab Initio Techniques Used

Second- and fourth-order Møller–Plesset perturbation theory using a variety of substitutions (MP2, MP4SDQ)[130,131] as well as density-functional theory (DFT) using a range of exchange-correlation functionals were evaluated. The functionals included were the popular Lee-Yang-Parr variation of the three-parameter Becke hybrid functional (B3LYP),[132–134] the Minnesota 06 functional by Truhlar and coworkers,[135] and the double hybrid mPW2PLYP functional by Schwabe and Grimme.[136] This latter functional incorporates, in addition to exact Hartree-Fock exchange, non-local correlation effects from MP2. Bulk solvent was modeled as a polarizable dielectric cavity using the polarizable continuum model (PCM).[137,138]

*This can be definitively established using variable-temperature kinetic data and the Eyring plot if desired.

Finally, it is worth mentioning that for the purposes of our calculations, we have disregarded the chemical differences between ^{1}H and ^{2}D, effectively investigating the exchange of aromatic hydrogen atoms in the substrate with labile hydrogen atoms from solvent. While the two nuclei are chemically distinct due to differing zero-point energies for C–H and C–D bonds, we feel our simplification is justified here since, as we shall see, this difference is small compared to the energetic impact of the assumptions we will have to make to model solvation, especially in Section 3.21.

3.15 Ab Initio Notation

Before we dive into details of our calculations, it is helpful to review the following notation used in the literature to indicate the methods associated with various *ab initio* results. Describing a calculation at the B3LYP/6-31G/DCM level indicates that geometry optimization (if any) as well as calculation of any properties of the final structure (also known as single-point calculations) were performed using the B3LYP functional and the 6-31G basis set, using a PCM model of solvent with the dielectric constant of dichloromethane. Further, MP4(DQ)/6-311G(d,p)//B3LYP/6-31G denotes a single-point MP4(DQ)/6-311G(d,p) calculation on geometry optimized at the B3LYP/6-31G level, which is less computationally intensive.

3.16 Preliminary Ab Initio Results

As a first step, we decide to examine the tautomerization of **3.9**, a simplified version of **3.3**, to its keto-enamine form, Figure 3.18. We expected this to be a straightforward calculation, but were surprised by the large dependence of the resulting ΔE and $\Delta E^{\ddagger}$ values on the computational technique used. For instance, depending on the theory used, values between 0.3–6.6 kcal/mol are calculated for ΔE. Cursory inspection of these figures reveals a divide between DFT and MP

results, with the Minnesota 06 and double hybrid mPW2PLYP giving values in between. For this particular calculation, we also calculated the energies at an even higher level using coupled cluster theory, CCSD(T)/Def2TZV PP/DCM[*] — to provide a reference.[†]

The computational cost of MP4 and CCSD is prohibitive for geometry optimizations (including finding transition states). Thankfully, in spite of the differences in reaction ΔE, the various techniques evaluated gave very similar energy-optimized atomic coordinates, *i.e.* very similar energies are obtained when a given technique is used to carry out a single-point calculation on a structure optimized at various other levels of theory. This allowed us to use M06 and mPW2PLYP (which has similar computational complexity as MP2) for geometry optimization and transition state search and reserve higher orders of theory for more accurate single-point calculations.

[*] Def2TZVPP refers to the high-quality density-fitted double-polarized triple-zeta basis set by Weigend and Ahlrichs.[95]

[†] Note that MP techniques are susceptible to non-convergent oscillatory behavior at higher orders. Thus, MP4 might perform worse than MP2 or DFT in pathological cases.[224,225]

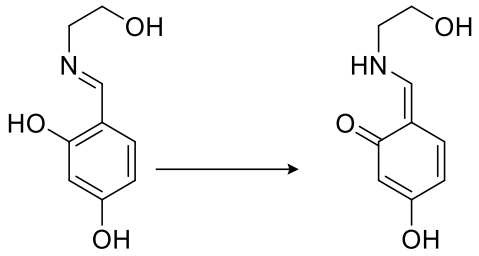

3.9

	ΔE (kcal/mol)	$\Delta E^{\ddagger}$ (kcal/mol)
B3LYP:	0.3	3.9
PB0:	0.8	3.2
M06:	1.7	6.0
mPW2PLYP:	1.8	4.9
MP2:	6.3	6.9
MP4(DQ):	6.6	9.4
MP4(SDTQ):	4.6	6.2
CCSD(T)/Def2TZVPP:	3.6	8.1

Figure 3.18. Comparison of ΔE and $\Delta E^{\ddagger}$ for tautomeric interconversion of **3.9** according to various *ab initio* techniques. DCM solvent (PCM) and the 6-311G(d,p) used unless otherwise indicated.

3.17 Intermediate Screening

The search for reasonable intermediates is straightforward and involves subjecting a number of chemically plausible candidate structures to *ab initio* energy optimization. In this case, at the M06/6-311G(d,p)/DCM level, we were able to obtain five chemically relevant energy minima for **3.9**, **3.9a**–**3.9e** (Figure 3.19). Of these, **3.9a** represents the resting state of the molecule and, as expected, has the lowest energy. The stability of **3.9b**–**3.9e** was therefore gauged based on their energy relative to that of **3.9a**.

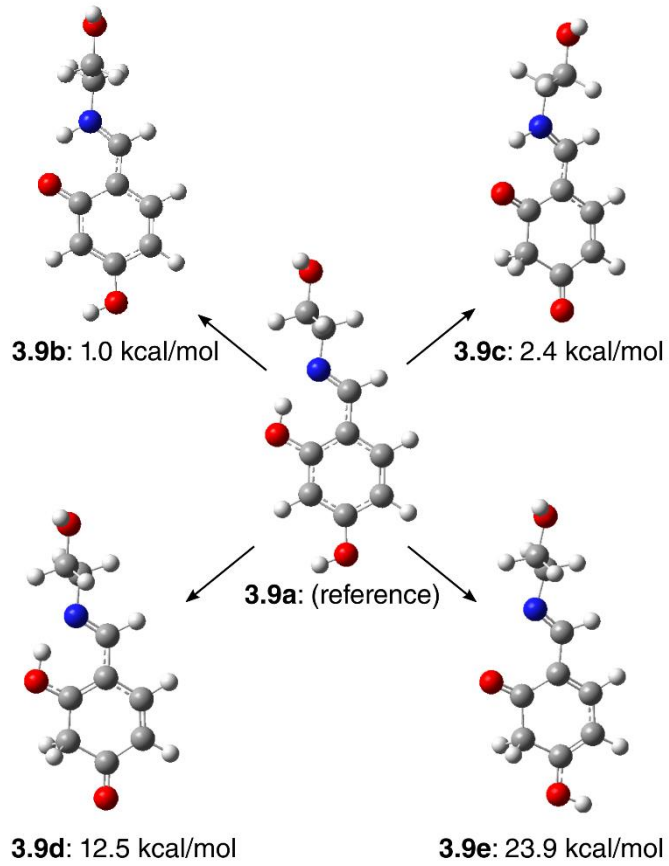

Figure 3.19. Calculated optimized energies of possible intermediates for the H/D exchange of **3.9**.

As Figure 3.19 shows, conversion of **3.9a** to its keto-enamine tautomer **3.9b** has a very low energetic cost of only 1.0 kcal/mol. Likewise, the ring-protonated double-keto structure **3.9c** is only 2.4 kcal/mol above the **3.9a** in spite of having an sp^3 hybridized carbon atom at the 3 position. This supports the hypothesis that both compounds are involved in facile H/D exchange in **3.9**.

To control for other possible pathways, structures **3.9d** and **3.9e** were used represent direct keto-enol tautomerization of the phenols at the 2 and 4 positions, respectively. Both were calculated to be far less stable than **3.9a**–**3.9c**, demonstrating the synergy between keto-enamine/enol-imine and keto-enol tautomerization in this system

3.18 H/D Exchange in Hydroxysalicylaldimines

As a natural extension of the chemistry explored so far with **3.3**, and encouraged by our early *ab initio* results, we expected that its aldimine analogue, **3.9**, would also show facile H/D exchange in experiment. Here, an important distinction between aldimines and ketimines is the former's ability to form reversibly under ambient conditions. Consequently, catalytic amounts of amine should be able to bring about H/D exchange in a larger pool of aldehyde.

Monitoring the ^{1}H NMR spectrum of 2,4-dihydroxybenzaldehyde, **3.8**, and 0.25 eq ethanolamine solution shows this to be the case indeed. H/D exchange at the 3 position proceeds in CD_3OD with a half-life of 49 hours. We suspect that this catalytic action is brought about by the reversible *in situ* formation and hydrolysis of the aldimine, as shown in Figure 3.20. It is worth noting that **3.8** by itself does not undergo H/D exchange over a period of 2 weeks (r.t., CD_3OD).

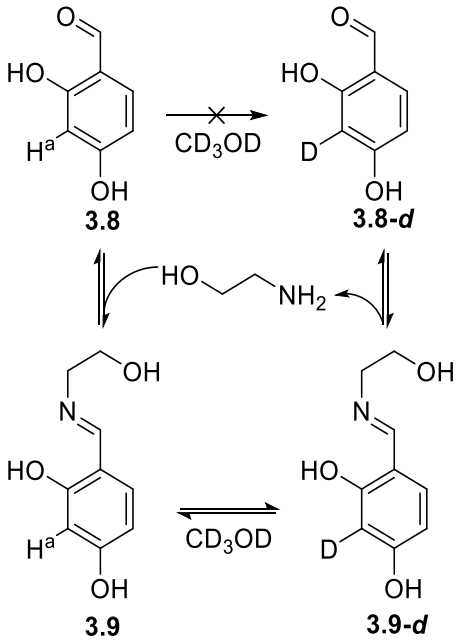

Figure 3.20. Proposed mechanism for facilitation of H/D exchange of **3.8** in the presence of catalytic ethanolamine.

3.19 Influence of Hydroxyl Group Position on H/D Exchange Activity

While the proposed mechanism for facile H/D exchange does require the presence of a salicylimine moiety, the position of the "free" second hydroxyl group is not constrained in principle. Figure 3.21 shows **3.9** along with 3-, 5-, and 6-hydroxy analogues **3.10**, **3.11**, and **3.12**. Like **3.9**, **3.12** underwent facile H/D exchange in CD_3OD, while **3.10** and **3.11** were recovered intact. Double deuteration in **3.12** can be explained by noting that the imine functionality can hydrogen bond with either hydroxyl group, allowing the 3 and 5 position to undergo exchange.

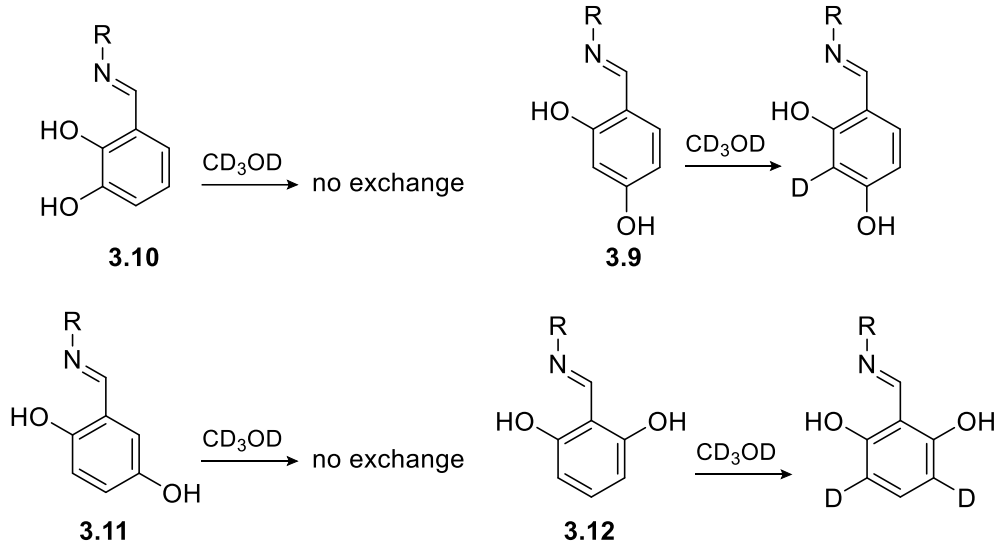

Figure 3.21. Various hydroxy substitutions of a salicylimine and the experimental outcome of deuterium exchange in each case (R = $(CH_2)_2OH$).

3.20 Ab Initio Explanation

In order to explain the relative reactivities of **3.9**-**3.12**, we first noted that the position of the second hydroxyl group should not strongly affect the enol-imine/keto-enamine equilibrium. Indeed, for the simplified computational analogues of these compounds, **3.13**–**3.16** (Figure 3.22), the first tautomerization step hardly incurs any energetic cost. In contrast, ring protonation produces intermediates with a wide range of stabilities. The outcome of the H/D exchange

experiment for each compound seems to be reflected by the stability of these intermediates. For instance, with **3.13**, all ring-protonated intermediates are at least 13.0 kcal/mol higher in energy than the starting Schiff base, consistent with its lack of reactivity. Similarly, the site of H/D exchange in **3.14** and **3.16** is correctly predicted by the most stable intermediate. Only in the case of **3.15** do the results seem inconsistent with experiment — it appears that protonation of C6 for this compound generates an intermediate that is more stable than both **3.15** and **3.15**$_{\mathbf{K\text{-}E}}$.

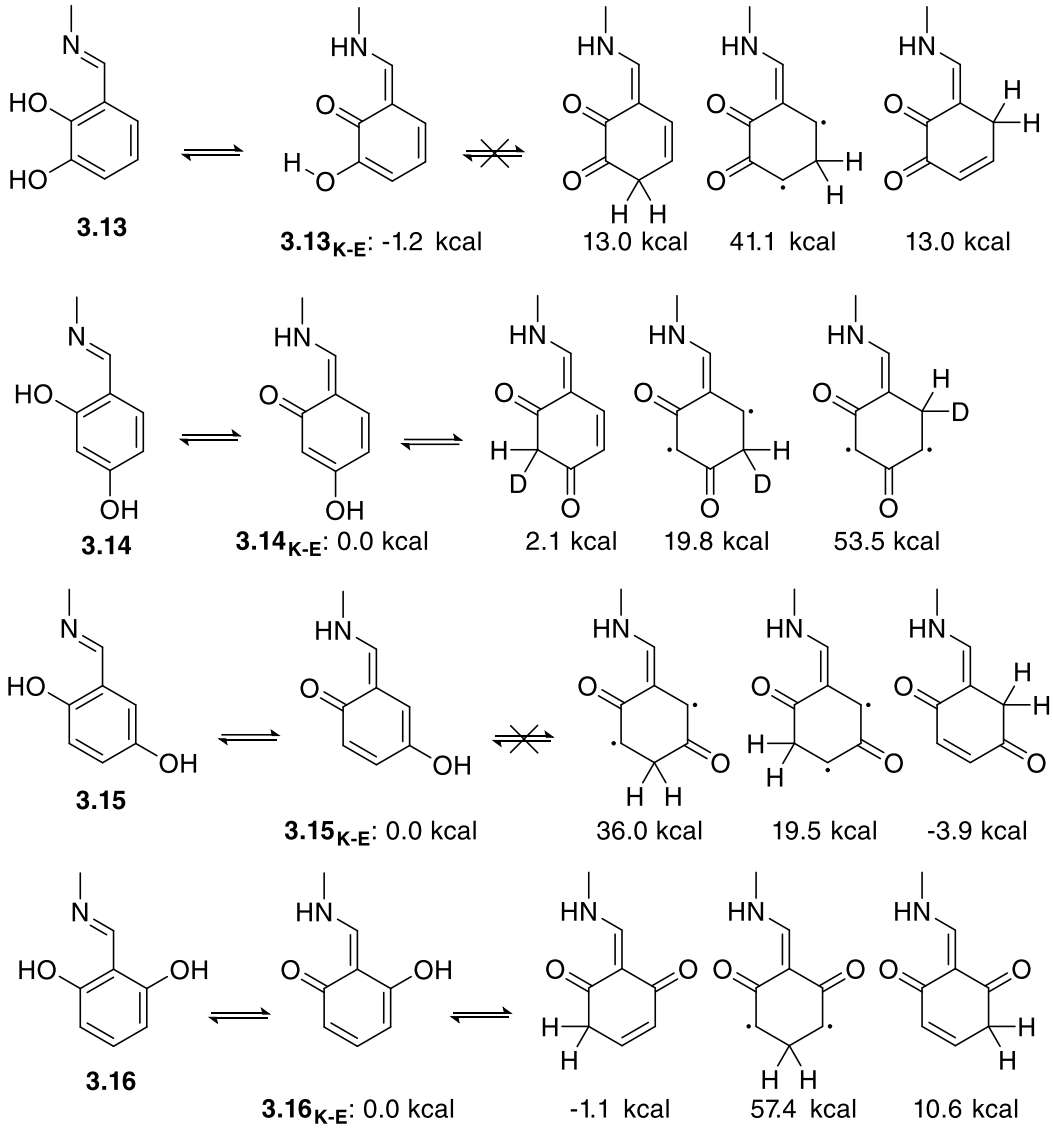

Figure 3.22. Calculated energies for geometry optimized computational analogues of **3.13**–**3.16** and their ring-protonated intermediates at the 6-311G(d,p)/M06/DCM level (all energies reported per mole and referenced to the enol-imine tautomer of each compound).

Differences in the nucleophilicity of ring carbons can be invoked as another explanation of the observed reactivities. Figure 3.23 shows the calculated Mulliken charges for ring carbons in the conjugate base of each of **3.13**$_{\text{K-E}}$–**3.16**$_{\text{K-E}}$ at the 6-311G(d,p)/M06/DCM level of theory. One must exercise care when interpreting these results, given the well-known theoretical shortcomings associated with Mulliken charges.[87,90] That said, the distribution of negative charge can be seen to

agree well with the experimental site of deuteration in **3.14** and **3.16** as well as the expected site of deuteration suggested by simple arrow pushing for all four compounds. Further, **3.13**'s lack of reactivity agrees with the relatively small negative charge found on the ring carbons in [**3.13** – H]$^-$

.

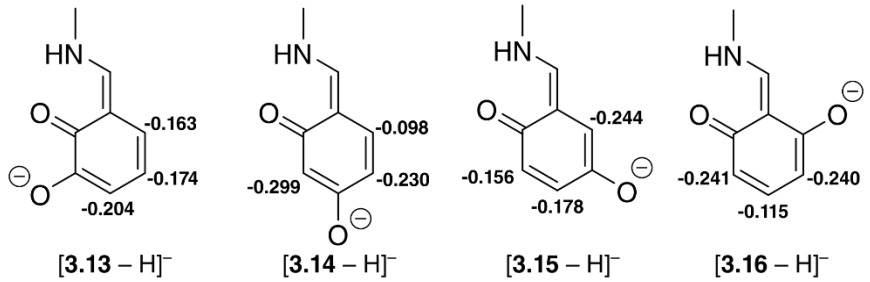

Figure 3.23. Calculated Mulliken charges for ring carbon atoms in the deprotonated form of **3.13**$_{\mathbf{K\text{-}E}}$–**3.16**$_{\mathbf{K\text{-}E}}$.

Here, as with the previous discussion of intermediate stabilities (Figure 3.22), the absence of H/D exchange in **3.15** is surprising given the large negative charge at the C6 position of [**3.15** – H]$^-$. Needless to say, one cannot rule out kinetic factors, such as the difficulty of constructing a solvent cage around **3.15**$_{\mathbf{K\text{-}E}}$, which we will revisit in the next Section.

3.21 Ab Initio Investigation of the Ring Protonation Step

With the most stable ring-protonated intermediate established for each of **3.13**–**3.16**, we turned our attention to the pathway for proton transfer to the carbon at position 3 (C3). As mentioned in Section 3.12, the simplest possible mechanism for protonation of C3 would involve intramolecular movement of a proton from the phenolic position. As Figure 3.24 shows, a transition state can be calculated for this pathway, but at more than 50 kcal/mol, the corresponding activation energy is more than twice the ~ 24 kcal/mol expected for this reaction.

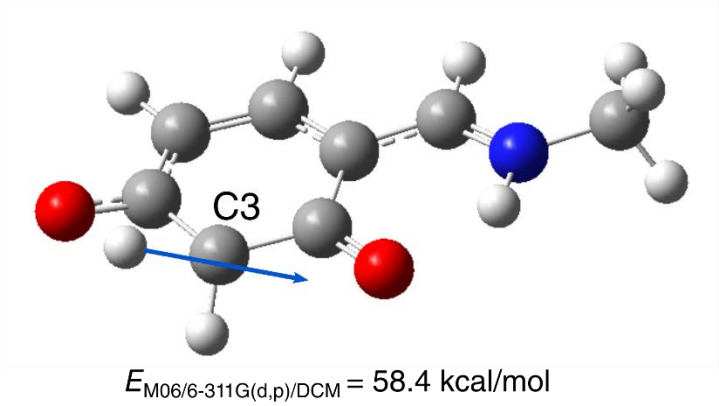

Figure 3.24. Calculated transition state for intramolecular proton transfer to C3 in **3.14**. The blue arrow shows the direction of movement associated with the imaginary frequency. Energy is reported relative to the resting state of **3.14**.

Inspired by the accelerating effect of water presented in Section 3.12, we turned our attention to solvent-mediated proton transfer. Similar water mediated proton transfer has been invoked for the study of keto-enol tautomerism in pyruvate anion and acetylacetone.[139] Here the main difficulty lies in the fact that proton transfer from substrate to a single water molecule (or vice versa) inevitably produces charge separation, yielding a very unstable intermediate. In reality, the energetic cost of this charge separation step is largely mitigated by the solvation of the resulting ion pair. While this phenomenon can (at least in principle) still be modeled by *ab initio* techniques, the increased size and degrees of freedom of the resulting substrate + solvent system greatly increases the computational burden of this type of calculation.

Figure 3.25b shows the simplest arrangement for solvent-assisted transfer of the 4-OH proton to the ring. Compared to the ground state of the complex (Figure 3.25a) the transition state for ring protonation lies at 33.9 kcal/mol (M06/6-311G(d,p)/DCM), Figure 3.25b. While it is difficult to attribute this instability to a particular part of the complex, we suspect that it is due to the concentration of positive charge on the water molecule (the H^2 and H^3 atoms in particular), as the electrostatic potential (ESP) surface of Figure 3.25c shows. Indeed, partitioning of the electronic

wavefunction into atomic basins using the theory of atoms in molecules (AIM) and comparing the energy contribution for H^1, H^2, and H^3, E_{IQA}, shows H^2, with the largest concentration of partial positive charge, to contribute most to the energy of the transition state.

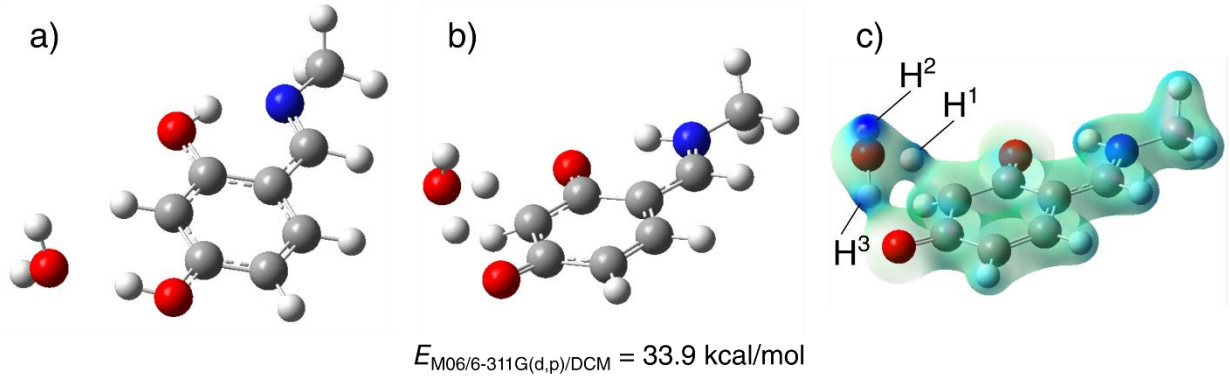

Figure 3.25. Substrate + H_2O complex: resting state (a), transition state for ring protonation (b), electrostatic potential surface of transition state (c).

Table 3.2. Contribution of H^1–H^3 to total energy of the transition state in Figure 3.25.

	H^1	H^2	H^3
E_{IQA} **(a.u.)**	-0.4548	-0.4441	-0.4472
E_{IQA} **(rel., a.u.)**	0	0.0107	0.0076
E_{IQA} **(rel., kcal/mol)**	0	6.71	4.8

Although simplistic, this basic formulation of the transition state can provide valuable insight into the roots of facile H/D exchange. For instance, the ESP map in Figure 3.25c shows remarkable stabilization of negative charge by equal delocalization over the ring oxygen atoms. This might explain the superior reactivity of **3.14** compared to, **3.15**, where such delocalization is not possible, Figure 3.26.

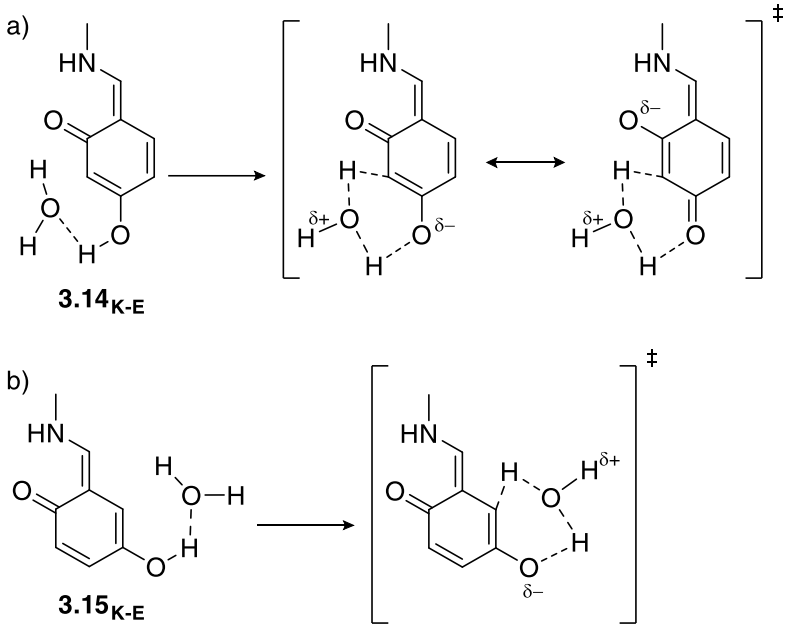

Figure 3.26. Comparison of delocalization of separated charge in the transitions states for the ring protonation of **3.14** (a) versus **3.15** (b).

Guided by the localization of positive charge on the water molecule in Figure 3.25c, we attempted to construct transition states with more solvent molecules in an attempt to further stabilize the transition state through charge dispersion. To more realistically model the process, we decided to surround model compound **3.14** with a hydrogen bonded network of water molecules, presumably clustered around the oxygen atoms in the substrate (which act as hydrogen bond acceptors). Thus, the chain of proton transfer ultimately leading to protonation of C3 was envisioned to start with deprotonation of the acidic phenol moiety and propagate by proton transfers between water molecules in the network. Experimenting with the number of water molecules, we found that a network of five water molecules could accomplish this reasonably at manageable computational cost. This network molecules was initially roughly constructed using chemical intuition and was refined by geometry optimization to a local energy minimum. Reassuringly, the resulting geometry retains the hydrogen bonded network initially envisioned. A

relaxed geometry scan corresponding to the approach of the phenolic proton and its hydrogen bonding partner then led to an initial guess for the transition state.

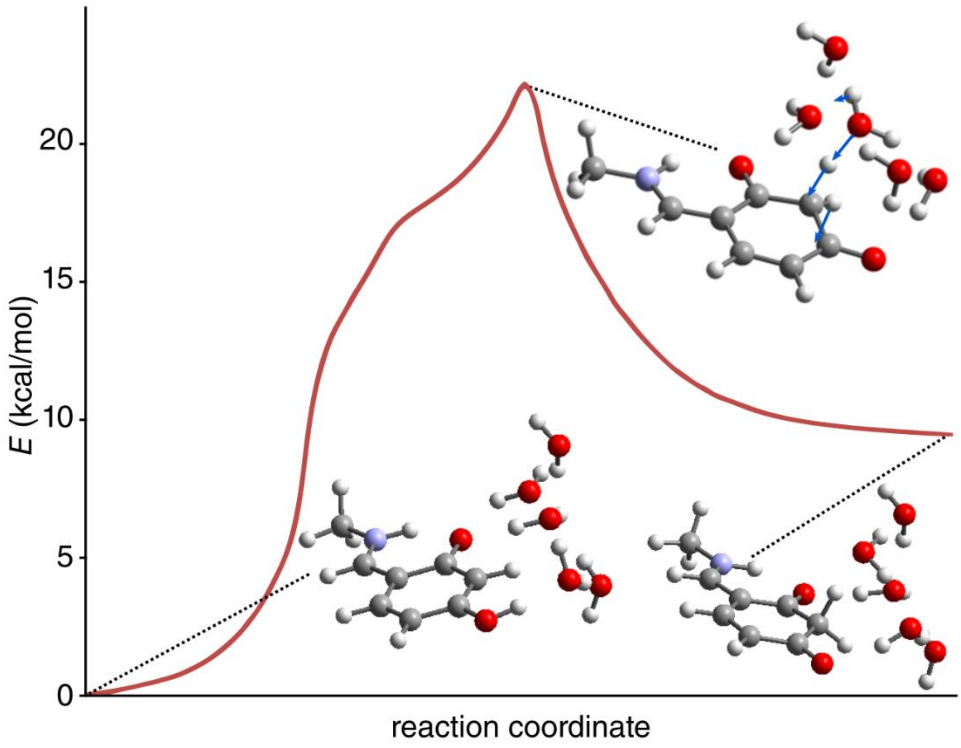

Figure 3.27. Internal reaction coordinate (IRC) diagram for water-mediated ring protonation of **3.14** (mPW2PLYP/DCM)/6-311G(d,p)/DCM): Optimized **3.14** + 5 H_2O complex (reference, left), transition state (middle), C3-protonated product (right). Blue arrows show direction and amplitude of atomic motion associated with the imaginary frequency in the transition state. (Adapted with permission from *J. Org. Chem.*, 2015, 80 (10), 5144–5150 Copyright (2015) American Chemical Society).

In this fashion, we were able to construct (at the mPW2PLY/6-311G(d,p)/DCM level) a transition state for this solvent-mediated protonation that is only 20.2 kcal/mol above the resting state of the system (**3.14** + 5H_2O). Contrary to our expectation of a step-wise proton transfer pathway with distinct intermediates at each stage, the calculated internal reaction coordinate diagram (Figure 3.27) shows a continuous rise in potential energy to reach the transition state, with

small shoulders along the way representing each proton "hop". As with previous structures, the results do vary based on the computational method used. For instance, the activation energy calculated using MP4(DQ)/6-311G(d,p)/DCM//mPW2PLYP/6-311G(d,p)/DCM is higher at 27.3 kcal/mol. Appendix C outlines the general procedure used to construct the IRC diagrams in Figure 3.27 and Figure 3.28.

The same strategy can be applied to proton transfer to C5 in **3.16**. Using a network of five water molecules clustered around phenolic OH at the 6 position, a similar pathway can be calculated for **3.16** with the corresponding $\Delta E^{\ddagger}$ = 23.7 kcal/mol (mPW2PLY/6-311G(d,p)/DCM, referenced to **3.16**), Figure 3.28.

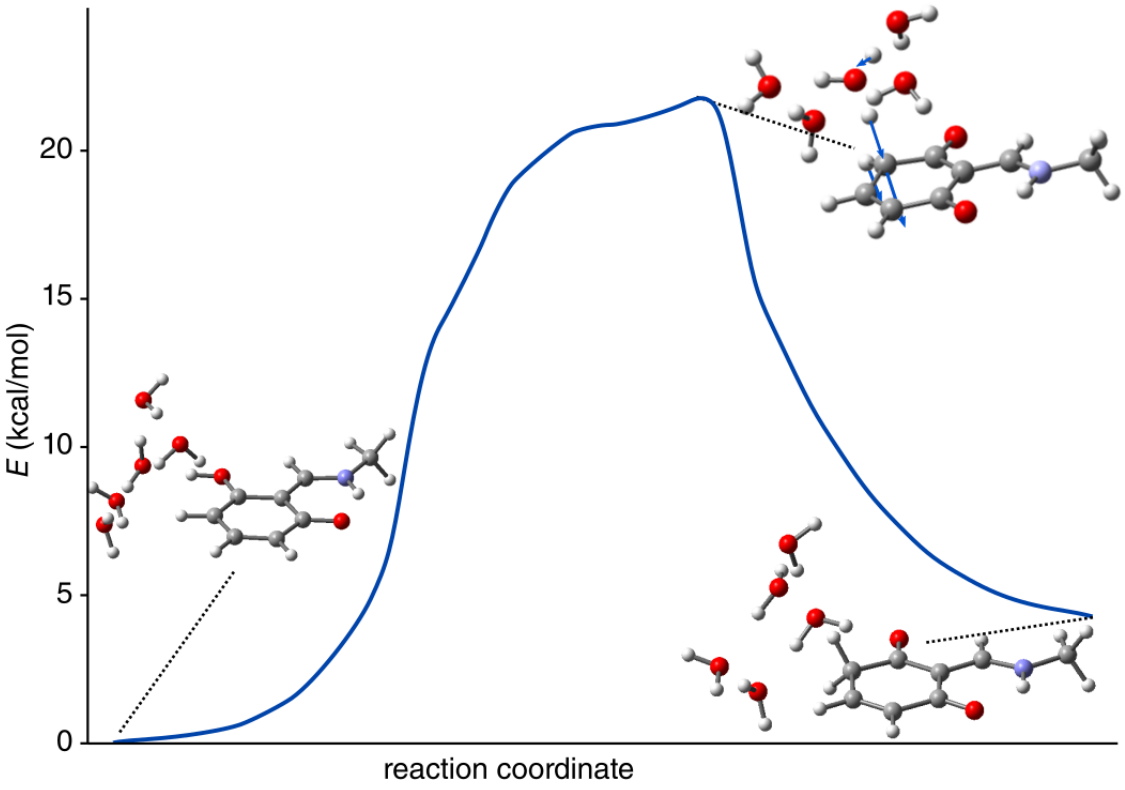

Figure 3.28. Internal reaction coordinate diagram for water-mediated ring protonation of **3.16** (6-311G(d,p)/mPW2PLYP/DCM): Optimized **3.16** + 5 H_2O complex (reference, left), transition state (middle), C5-protonated product (right). Blue arrows show direction and amplitude of atomic motion associated with the imaginary frequency in the transition state. (Adapted with

permission from *J. Org. Chem.*, 2015, 80 (10), 5144–5150 Copyright (2015) American Chemical Society).

From here, the reverse process — removal of an H atom from C3 (in **3.13**) or C5 (in **3.16**) by solvent, reprotonation of the transient phenoxide intermediate, and tautomerization back to the enol-imine form — can be expected to complete the cycle, effectively bringing about aromatic deuteration of substrate.

In summary, our computational study confirms the hypothesis that the initial tautomeric conversion to the keto-enamine form is responsible for room-temperature uncatalyzed H/D exchange, the principal contribution being the stabilization of the Wheland-type intermediate formed upon ring protonation. Further, the accelerating effect of water was justified by elucidation of its role as proton (deuterium) transfer mediator.

3.22 Conclusions and Future Work

To sum up our findings, it appears that tautomeric interconversion of salicylimines to their keto-enamine form can compromise aromaticity to the point that reactivity very atypical of aromatic compounds can arise. Indeed, this is a clear affirmation of the material presented in Chapter 2 regarding the interplay between tautomerism and aromaticity. While the range of compounds exhibiting facile H/D exchange of the type discussed in this chapter is admittedly limited, we are excited to have uncovered the principle and are looking at future extensions to it, some of which are briefly discussed below.

An immediate extension of the chemistry presented in this chapter is to use electrophiles other than deuterium. In this fashion, we can take advantage of the tautomeric amplification effect

introduced in this chapter to accelerate general electrophilic aromatic substitution reactions. For instance, using acrolein, one might hope to access the Michael addition product in Figure 3.29.

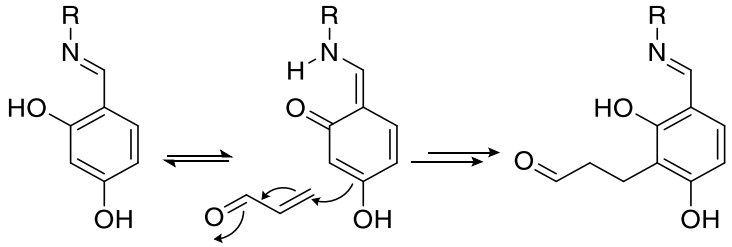

Figure 3.29. Hypothetical uncatalyzed Michael addition of a keto-enamine enol to acrolein.

The ability of tautomeric interconversion to localize the aromatic π cloud can be envisioned to apply to other classes of reactions as well. For instance, if the keto-enamine form can be stabilized sufficiently, the aromatic ring can be expected to react as a diene in a Diels–Alder reaction, Figure 3.30a. Alternatively, diradical character can develop if the molecule is designed to house two keto-enamine moieties in a 1,2,4,5 arrangement, as shown in Figure 3.30b. Work is ongoing on methods to detect/capture the localized electronic character of these compounds.

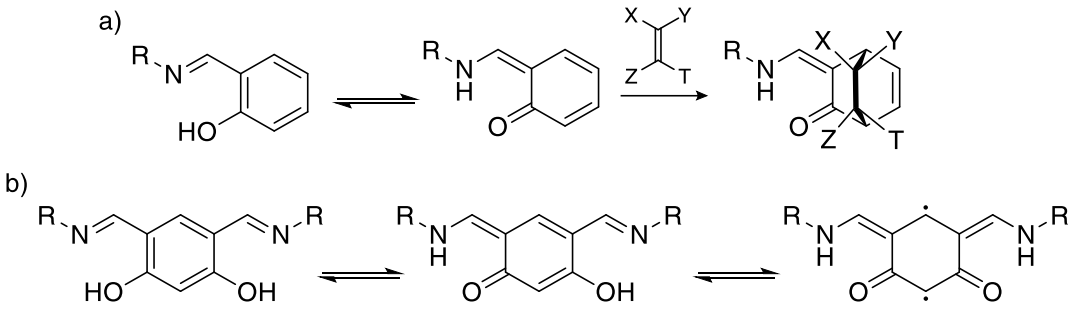

Figure 3.30. Activation of an aromatic compound towards Diels–Alder attack by a dienophile (a). Diradical character through conversion to double keto-enamine form.

3.23 Experimental

3.23.1 General

^{1}H NMR spectra were collected on 400 and 300 MHz Bruker Avance spectrometers configured with inverse probes. All kinetic experiments were carried out on the 400 MHz spectrometer. ^{13}C spectra were collected using a power-gated proton-decoupled pulse sequence, ^{13}C{^{1}H}, on a 400 MHz Bruker Avance spectrometer equipped with a direct probe and a 600 MHz Bruker Avance spectrometer with an inverse cryoprobe. In some cases, the ^{13}C UDEFT pulse sequence as described by Piotto and coworkers[140] was used to improve sensitivity for quaternary carbons. Indirect measurement using two-dimensional heteronuclear multiple-bond correlation (HMBC {^{1}H,^{13}C}) spectroscopy was used for structure verification in such cases.

High-resolution ESI mass spectra were obtained on a Waters/Micromass LCT time-of-flight (TOF) mass spectrometer.

3.23.2 Procedures and Characterization Data

General Method for the Preparation of Ketimines

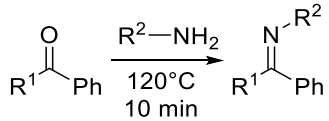

Figure 3.31. Solvent-free synthesis of ketimines.

All ketimines were prepared by the high-temperature, solvent-free reaction of amine (ethanolamine or 3,5-dimethylaniline) with the appropriate ketone, Figure 3.31. In a typical procedure, the ketone and a tenfold excess of amine were combined in a small Schlenk tube, which was purged three times with nitrogen before heating at 120 °C for 10 min to complete the conversion. Depending on the substrate used, most or all of the excess amine could be removed by

heating the flask for 12 h at 80 °C under high vacuum. When the product is a glaze, amine removal is much quicker if the glaze is thinned with methanol or toluene.

Aldimines formed *in situ* were not isolated.

4,6-Dibenzoylresorcinol ethanolamine Schiff base (3.2)

The product was further purified by recrystallizing from a mixture of water and methanol, yielding **3.2** as a yellow solid in 89% (114 mg from 101 mg 4,6-dibenzoylresorcinol) yield. Melts with decomposition. ^{1}H NMR (400 MHz, CD_3OD) δ 7.36 (m, 6H; Ar), 7.13 (d, $^{3}J_{HH}$ = 7.4 Hz, 4H; Ar), 6.38 (s, 1H; Ar), 5.97 (s, 1H; Ar), 3.70 (t, $^{3}J_{HH}$ = 5.2 Hz, 4H; CH_2), 3.41 (t, $^{3}J_{HH}$ = 5.2 Hz, 4H; CH_2). $^{13}C\{^{1}H\}$ NMR (100 MHz, DMSO-d_6) δ 173.7, 171.5, 139.0, 131.5, 128.9, 128.2, 127.4, 110.9, 104.9, 60.3, 51.6. UV-Vis (MeOH) λ_{max} (ε) = 393 (1.6×10^4), 317 (2.5×10^4) nm ($cm^{-1}\,mol^{-1}\,L$). IR (neat) ν = 2900 (br), 1556, 1435, 1301, 1250, 1143, 1080, 938, 919, 840, 782, 756, 705, 669, 591, 566, 467 cm^{-1}. HRMS (ESI/TOF-Q) *m/z*: [**3.2** + H]$^+$ Calcd for $C_{24}H_{25}N_2O_4$ 405.1814; Found 405.1812.

2,4-Dihydroxybenzophenone ethanolamine Schiff base (3.3)

All traces of leftover amine were removed by flash column chromatography of the product using 1:9 methanol:dichloromethane. The yellow first fraction was evaporated to give **3.3** in 85% (102 mg from 100 mg 2,4-dihydroxybenzophenone) yield. mp 186–191 °C. ^{1}H NMR (300 MHz, CD_3OD) δ 7.58 (m, 3H; Ar) , 7.36 (m, 2H; Ar), 6.55 (d, $^{3}J_{HH}$ = 9.0 Hz, 1H; Ar), 6.14 (d, $^{3}J_{HH}$ = 2.4 Hz, 1H; Ar), 5.96 (dd, $^{3}J_{HH}$ = 9.0, 2.4 Hz, 1H; Ar), 3.71 (t, $^{3}J_{HH}$ = 5.4 Hz, 2H; CH_2), 3.40 (t, $^{3}J_{HH}$ = 5.4 Hz, 2H; CH_2). $^{13}C\{^{1}H\}$ NMR (100 MHz, CD_3OD) δ 177.3, 175.9, 166.3, 135.7, 133.0, 131.0, 129.9, 129.1, 112.0, 107.6, 105.8, 61.6, 50.4. UV-Vis (MeOH) λ_{max} (ε) = 384 (8.2×10^3), 309 (1.5×10^4) nm ($cm^{-1}\,mol^{-1}\,L$). IR (neat) ν = 1591, 1573, 1556, 1496, 1471, 1384, 1335, 1260,

1235, 1175, 1118, 1059, 980, 851, 806, 778, 717, 631, 563, 439 cm^{-1}. HRMS (ESI/TOF-Q) *m/z*: [**3.3** + H]$^+$ Calcd for $C_{15}H_{16}NO_3$ 258.1130; Found 258.1122.

2,4-Dihydroxybenzophenone 3,5-dimethylaniline Schiff base (3.4a)

A yellow-orange solid was obtained in 87% (387 mg from 300 mg 2,4-dihydroxybenzophenone) yield from the methanol solution by the addition of water. mp 203–205 °C. ^{1}H NMR (600 MHz, $CDCl_3$) δ 7.36 (m, 3H; Ar), 7.19 (m, 2H; Ar), 6.93 (d, $^3J_{HH}$ = 8.9 Hz, 1H; Ar), 6.64 (bs, 1H; Ar), 6.55 (d, $^3J_{HH}$ = 2.5 Hz, 1H; Ar), 6.39 (bs, 2H; Ar), 6.25 (dd, $^3J_{HH}$ = 8.9, 2.5 Hz, Ar), 2.14 (s, 6H; CH_3). $^{13}C\{^1H\}$ (150 MHz, $CDCl_3$) δ 171.9, 167.9, 161.5, 144.7, 138.2, 134.3, 133.9, 129.1, 128.9, 128.3, 126.6, 121.0, 113.4, 106.9, 104.4, 21.3. UV-Vis (MeOH) λ_{max} (ε) = 403 (shoulder, 3.6×10^3), 332 (1.3×10^4), 287 (1.2×10^4), 240 (shoulder, 1.5×10^3) nm (cm^{-1} mol^{-1} L). IR (neat) *v* = 3351, 2922, 1582, 1442, 1339, 1192, 1112, 1020, 962, 908, 852, 816, 774, 701, 670, 561, 542, 525, 459 cm^{-1}. HRMS (ESI/TOF-Q) *m/z*: [**3.4a** + H]$^+$ Calcd for $C_{21}H_{20}NO_2$ 318.1490; Found 318.1494.

2,4-Dihydroxybenzophenone hexylamine Schiff base (3.4b)

Yellow-orange crystals (270 mg, 84% from 250 mg 2,4-dihydroxybenzophenone) yield from the cold methanol-water solution. mp 141–147 °C. ^{1}H NMR (400 MHz, $CDCl_3$) δ 7.51 (m, 3H; Ar), 7.26 (m, 2H; Ar), 6.55 (d, $^3J_{HH}$ = 9.2 Hz, 1H; Ar), 6.50 (d, $^3J_{HH}$ = 2.6 Hz, 1H; Ar), 6.07 (dd, $^3J_{HH}$ = 9.2, 2.6 Hz, 1H; Ar), 3.21 (t, $^3J_{HH}$ = 7.0 Hz, 2H; CH_2), 1.60 (q, $^3J_{HH}$ = 7.4 Hz, 2H; CH_2), 1.34-1.16 (m, 6H; CH_2), 0.83 (t, $^3J_{HH}$ = 7.0 Hz, 3H; CH_3). $^{13}C\{^1H\}$ (75 MHz, $CDCl_3$) δ 174.8, 173.3, 164.5, 134.0, 132.1, 129.5, 128.6, 127.7, 110.8, 106.9, 105.7, 47.2, 31.3, 30.1, 26.5, 22.4, 14.0. UV-Vis (MeOH) λ_{max} (ε) = 337 (7.3×10^3), 305 (1.2×10^4), 211 (1.3×10^3) nm (cm^{-1} mol^{-1} L). IR (neat) *v* = 2954, 2927, 2856, 2550 (br), 1574, 1531, 1488, 1453, 1393, 1340, 1238, 1175,

1113, 1074, 1026, 979, 924, 851, 800, 771, 698, 634, 553 cm^{-1}. HRMS (ESI/TOF-Q) *m/z*: [**3.4b** + H]$^+$ Calcd for $C_{19}H_{24}NO_2$ 298.1807; Found 298.1807.

2-Hydroxy-4-methoxybenzophenone ethanolamine Schiff base (3.5)

A sticky orange-brown solid was obtained in 94% (254 mg from 204 mg 2-hydroxy-4-methoxybenzophenone) yield that is pure by ^{1}H NMR spectroscopy. Samples suitable for optical characterization were obtained by passing the product through a short column of silica gel using ethyl acetate as eluent (R_f = 0.3) followed by the evaporation of solvent under vacuum. A fluorescent waxy yellow solid was thus obtained in 79% overall yield. ^{1}H NMR (400 MHz, CD_3OD) δ 7.58 (m, 3H; Ar), 7.35 (m, 2H; Ar), 6.58 (d, $^3J_{HH}$ = 9.2 Hz, 1H; Ar), 6.23 (d, $^3J_{HH}$ = 2.6 Hz, 1H; Ar), 6.04 (dd, $^3J_{HH}$ = 9.2, 2.6 Hz, Ar), 3.77 (s, 3H; CH_3), 3.71 (t, $^3J_{HH}$ = 5.5 Hz, 2H; CH_2), 3.40 (t, $^3J_{HH}$ = 5.5 Hz, 2H; CH_2). ^{13}C{^{1}H} NMR (100 MHz, acetone-d_6) δ 175.1, 168.3, 164.5, 134.9, 133.5, 129.9, 129.6, 128.6, 114.3, 105.8, 102.4, 62.6, 55.7, 54.0. UV-Vis (MeOH) λ_{max} (ε) = 387 (2.2×10^4), 305 (3.2×10^3) nm (cm^{-1} mol^{-1} L). IR (neat) *v* = 3152, 2951, 2834, 1582, 1538, 1440, 1340, 1221, 1075, 1022, 833, 799, 769, 702, 545, 493 cm^{-1}. HRMS (ESI/TOF-Q) *m/z*: [**3.5** + H]$^+$ Calcd for $C_{16}H_{18}NO_3$ 272.1287; Found 272.1282.

4-Hydroxy-2-methoxybenzophenone ethanolamine Schiff base (3.6)

The product was obtained in 93% (136 mg from 122 mg 4-hydroxy-2-methoxybenzophenone) yield as a red glaze. Passing the product through a pad of silica gel using 1:9 methanol/dichloromethane as eluent can yield a bright yellow product, R_f = 0.1, suitable for optical characterization, albeit at a lower yield of 45%. ^{1}H NMR (300 MHz, acetone-d_6) δ 7.64 (m, 2H; Ar), 7.32 (m, 3H; Ar), 6.82 (d, $^3J_{HH}$ = 8.1 Hz, 1H; Ar), 6.62 (d, $^3J_{HH}$ = 2.2 Hz, Ar), 6.56 (dd, $^3J_{HH}$ = 8.1 Hz, 2.2 Hz, Ar), 3.77 (t, $^3J_{HH}$ = 6.1 Hz, 2H; CH_2), 3.40 (t, $^3J_{HH}$ = 6.1 Hz, 2H; CH_2). ^{13}C{^{1}H}

NMR (100 MHz, acetone-d_6) δ 166.9, 160.2, 158.5, 141.2, 130.01, 129.98, 128.4, 128.3, 117.5, 108.1, 99.7, 63.1, 57.1, 55.7. UV-Vis (MeOH) λ_{max} (ε) = 374 (1.6×10^4), 238 (9.3×10^3) nm (cm^{-1} mol^{-1} L). IR (neat) ν = 2930 (br), 1563, 1504, 1366, 1294, 1253, 1200, 1123, 1060, 1027, 958, 836, 774, 697, 590, 548, 511, 456 cm^{-1}. HRMS (ESI/TOF-Q) *m/z*: [**3.6** + H]$^+$ Calcd for $C_{16}H_{18}NO_3$ 272.1287; Found 272.1292. Note: Regardless of the purification method used, solutions in acetone-d_6 yield clean ^{1}H NMR spectra whereas in $CDCl_3$ and methanol-d_4 there appears to be a pair of similar compounds. We suspect this to be due to geometrical isomerism about the C=N double bond.

Chapter 4

Peripheral Electron Delocalization in a Strained Heteroradialene

4.1 Introduction

This chapter is concerned with a molecule whose discovery was inspired by the properties of TSANs. Specifically, we exploit the idea that keto-enamine connectivity in TSANs can compromise aromaticity to synthesize a compound that clearly lacks aromaticity but displays other interesting modes of electron delocalization.

4.2 Radialenes and Heteroradialenes

The family of *n*-membered cyclic compounds with exocyclic double bonds on each ring atom is termed *[n]radialenes*. The first preparation of a radialene is due to Hopff who, in 1961, synthesized a substituted [6]radialene from the reaction of hexakis(α-chloroethyl)benzene and magnesium in methanol,[141] Figure 4.1.[142,143] Radialenes with heteroatoms at the exocyclic positions are termed *Heteroradialenes*.

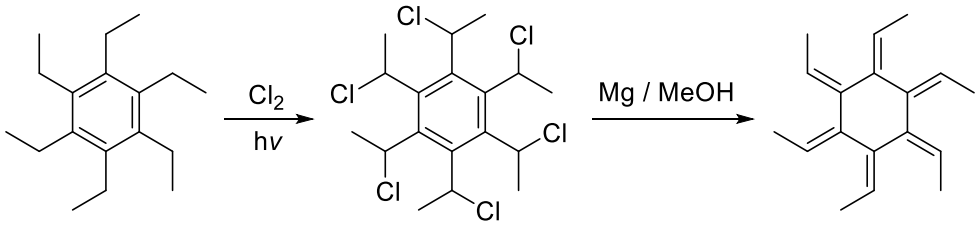

Figure 4.1. Early example of a radialene, prepared via an elimination reaction.*

* Magnesium in methanol (Mg/MeOH) is a versatile reagent used in organic chemistry for a variety of reduction reactions. Mg/MeOH can reduce vicinal dihalides to olefins through single electron transfer.[226] Since hexakis(α-chloroethyl)benzene is structurally equivalent to three extended *vic*-dichlorides, it is not surprising that the product is a radialene.

Radialenes and heteroradialenes are very similar structurally. Although all ring atoms are sp^2-hybridized and coplanar, these compounds lack the properties often associated with aromatic molecules. In fact, calculations show that radialenes have virtually no aromatic ring current.[144] Other research has shown that the relatively independent nature of the exocyclic double bonds translates to unique magnetic properties in heteroradialene compounds. For instance, the strong spin-polarization transmission between *m*-phenylene positions in aromatic compounds is absent in heteroradialenes, causing the corresponding multinuclear metal complexes to show very weak ferromagnetic (or weakly antiferromagnetic) coupling when heteroradialenes are used as chelating bridges.[145,146]

Examples of isolated unsubstituted radialenes are sparse in the literature, partly due to the instability of the parent [n]radialenes. For instance, the parent [6]radialene hydrocarbon **4.1** has been prepared at -85 °C but is only stable at room temperature as its adduct with a dihalocarbene formed *in situ*, Figure 4.2.[147]

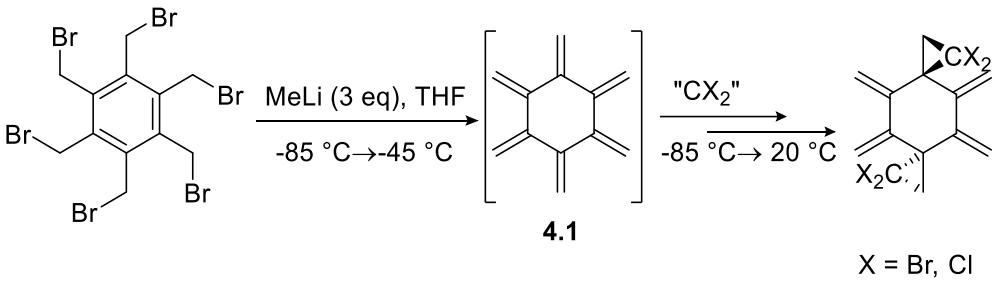

Figure 4.2. Preparation and trapping of the parent [6]radialene, **4.1**.

Compared to radialenes, there are even fewer examples of heteroradialenes. In fact, most known heteroradialenes are keto-enamine Schiff bases of 2,4,6-triformylphloroglucinol (TFP), visited in Chapter 2, which are in equilibrium with their aromatic enol-imine form, Figure 4.3.

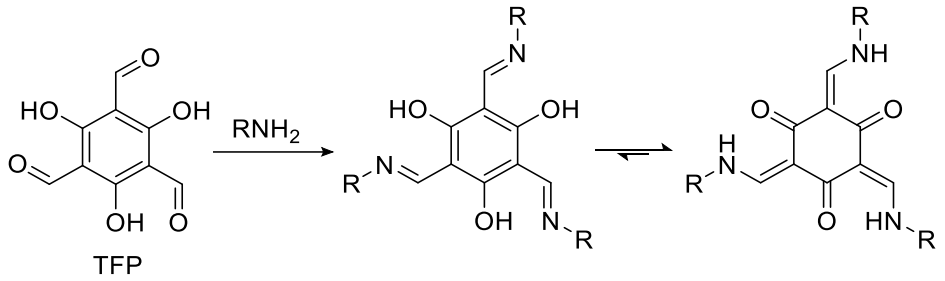

Figure 4.3. Rapid heteroradialene/aromatic interconversion of TFP Schiff bases.

In a similar vein, revisiting the mechanism for H/D exchange from Chapter 3, it is worth remembering that partial migration of double bonds to exocyclic positions (*e.g.* in **4.2**) coincided with extraordinary reactivity toward H/D exchange, Figure 4.4.

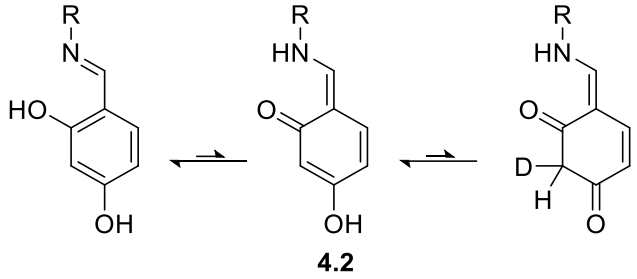

Figure 4.4. H/D exchange facilitated by formation of keto-enamine intermediate **4.2**.

4.3 Inspiration and Design

Both keto-enamine compounds discussed above exist only transiently owing to easy interconversion to the aromatic enol-imine form. Intrigued by the electronic structure of heteroradialenes, we were inspired to prepare a stable, permanent TSAN heteroradialene. The idea is to lock the molecule in the more interesting keto-enamine form by replacing the labile hydrogen atom with an immobile group, disabling the tautomeric equilibrium, *e.g.* Figure 4.5.

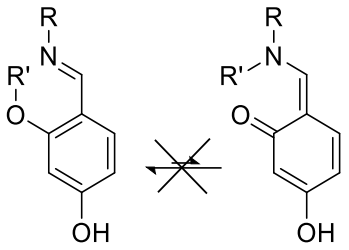

Figure 4.5. Inhibited equilibration in a **4.2** analogue with non-labile R′.

As one might expect, reacting a simple salicylaldehyde with a secondary amine will not lead to Schiff base formation. The product of such a reaction, can have keto-enamine or zwitterionic resonance contributors, Figure 4.6a, neither of which stabilize it: keto-enamine character would imply the disruption of aromaticity while zwitterionic character would require significant charge localization in the imine and phenoxy moieties. We therefore decided to amortize the cost of disrupting aromaticity by repeating the keto-enamine motif three times around the ring, Figure 4.6b.

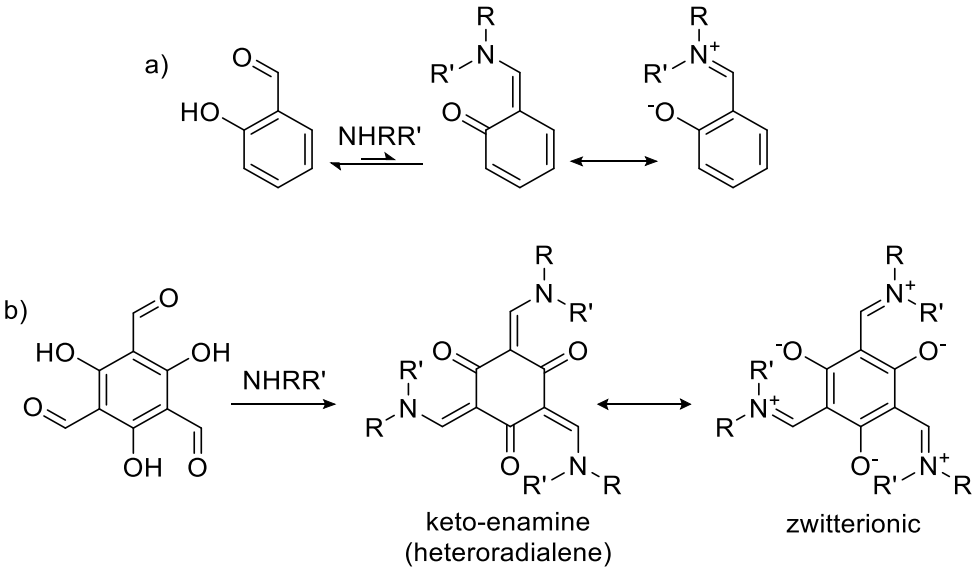

Figure 4.6. (a) Unstable condensation product of salicylaldehyde and a secondary amine. (b) Proposed preparation of a keto-enamine heteroradialene by condensation of TFP and a secondary amine.

The keto-enamine (heteroradialene) and zwitterionic resonance contributors above closely parallel the keto-enamine/enol-imine interconversion of TSANs in Figure 4.3, only with chemical equilibrium replaced with resonance due to the fixed position of R′ in Figure 4.6b.

4.4 Preparation

The only variable in our heteroradialene design above is the secondary amine, *i.e.* the choice of R and R′. Early attempts using TFP and dibenzylamine (R, R′ = CH_2Ph) were unsuccessful, giving an intractable red oil that failed to crystallize. When the procedure was repeated by reacting a methanol suspension of TFP with excess dimethylamine, however, TFP quickly dissolved to give an orange solution, Figure 4.7. This solution takes on a more reddish hue upon standing in air and a crimson mass starts to precipitate. If this red solid is dissolved in a 1:1 mixture of dichloromethane and heptane, a sticky red glaze separates first, followed by large pale yellow needles.

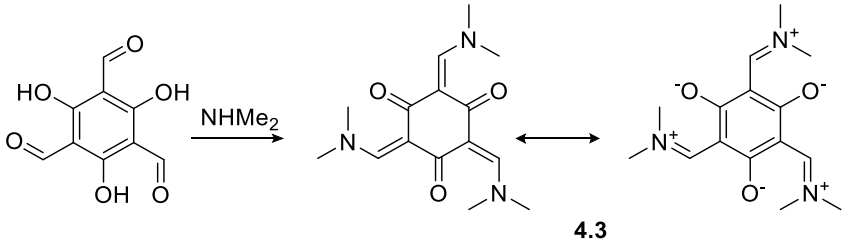

Figure 4.7. Preparation of heteroradialene/zwitterionic Schiff base **4.3**.

Single crystal X-ray diffraction (SCXRD) data for these needles shows the structure in Figure 4.8, confirming the formation of **4.3**.

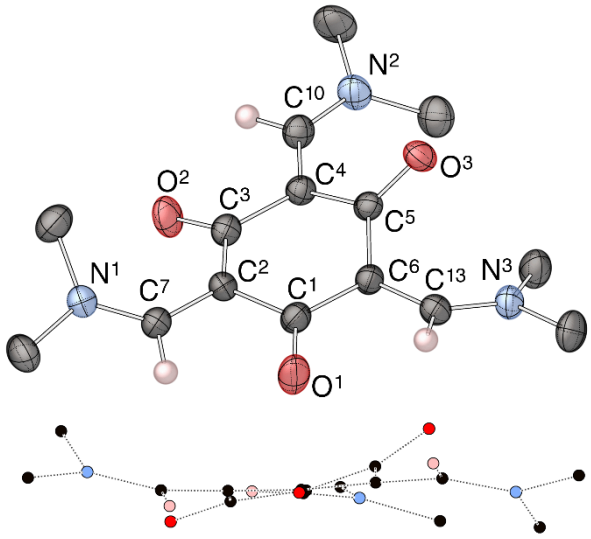

Figure 4.8. Thermal ellipsoid diagram for **4.3** (peripheral hydrogen atoms not shown, side projection at bottom).

This structure has several striking features. The molecule is asymmetric and chiral, owing to the asymmetric orientation of the $CHN(CH_3)_2$ arms and its non-planar shape. Asymmetric TFP Schiff bases have been observed spectroscopically by NMR spectroscopy, but to the best of our knowledge, this is the first example of an asymmetric heteroradialene selectively crystallizing out of solution. The departure from planarity in **4.3** is especially interesting. The oxygen atoms are displaced from the mean plane of the central ring by various amounts. Visually, and judging by their mean dihedral angles with the ring carbons (*e.g.* O^3: $O^3C^5C^4C^3 = 148.4°$, $O^3C^5C^6C^1 = 151.8°$), O^3 protrudes the most (30°, 7.5° and 10.4° for O^3, O^1 and O^2, respectively). Similarly, the $CH(CH_3)_2$ arms show large displacements, stemming from steric repulsion between the oxygen atoms and methyl groups. The space-filling diagram of **4.3** illustrates the close contact between the O and CH_3 moieties, Figure 4.9.

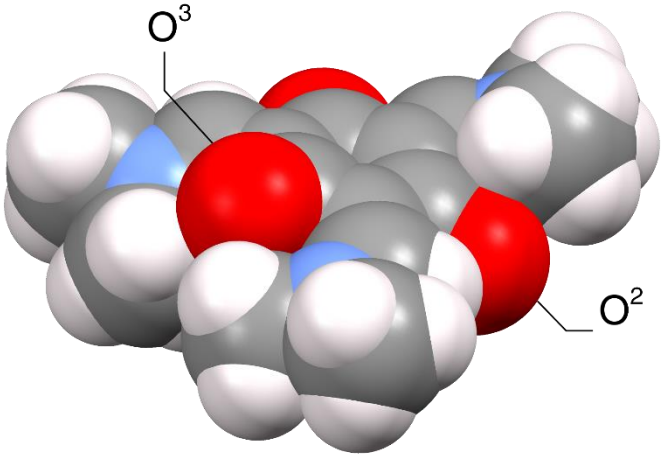

Figure 4.9. Spacefilling diagram of **4.3**. (Adapted with permission from *Org. Lett.*, 2016, 18 (8), 1840–1843, Copyright (2016) American Chemical Society).

4.5 Ab Initio Examination of Structural Strain

Since atomic coordinates in the solid state are influenced by interactions in the crystal lattice, the unusual shape of **4.3** could be attributed to crystal packing. To find out the extent of this influence, we used the atomic coordinates of **4.3** obtained from SCXRD in an *ab initio* geometry optimization calculation. This type of calculation produces the local energy minimum closest to a given initial geometry assuming no interactions outside the molecule, as one would find in the gas phase. In a separate series of calculations, we also attempted to predict the geometry of **4.3** in the solution state by modelling its interaction with bulk solvent using the polarizable continuum model (PCM).[137] A number of exchange-correlation functionals were used, including B3LYP, mPW2PLY[136], and Minnesota 06 (M06)[135] in conjunction with the 6-311G(d,p) and Dunning-type polarized triple-zeta correlation-consistent (cc-pVTZ) basis sets[148–150].* Regardless of the functional and basis set used and whether or not solvation was included, geometry optimization generally allowed the molecule to slightly relax toward planarity. For instance, the $O^3C^5C^4C^3$

* Chapter 3 includes a more detailed explanation of the various computational techniques and the related notation.

dihedral angle is relaxed from its initial 148.4° to 160.2° using M06/cc-pVTZ in DCM solvent (PCM) and 152.1° using B3LYP/6-311G(d,p) in vacuum. Thus, while crystal packing might somewhat contribute to ring contortion in **4.3**, the distorted shape of the molecule appears to be a genuine property of the discrete molecule.

Interatomic distances in the crystal structure of **4.3** can provide insight into its electronic structure. For example, keto-enamine character would be expected to lead to short exocyclic C–CH and C–O bonds and long CH–N and ring C–C bonds. Table 4.1 compares the bond lengths in **4.3** to those of a TSAN from Chapter 2 (specifically, the one with the strongest known keto-enamine character), a simple enol-imine salicylaldimine, and DMF. DMF was included since it can be regarded as a truncated analogue of **4.3** with predominantly keto-enamine character.

Table 4.1. Bond lengths in **4.3** and keto-enamine/enol-imine model compounds. (Adapted with permission from *Org. Lett.*, 2016, 18 (8), 1840–1843, Copyright (2016) American Chemical Society).

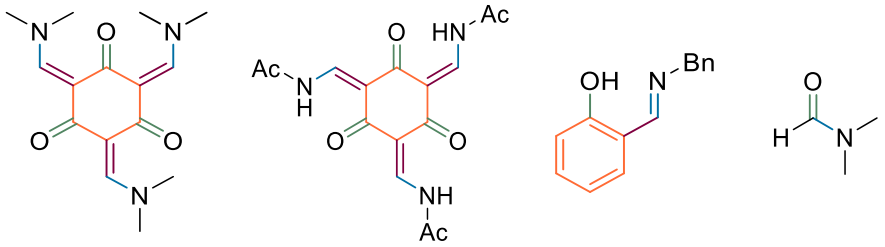

C–CH ●	1.398	1.364	1.460[a]	–
CH–N ●	1.320	1.343	1.276	1.341
C–O ●	1.253	1.248	1.357	1.231
C–C ●	1.462	1.466[b]	1.386	–

(a) Representative enol-imine from the literature.[151]

(b) Molecular average — alternating long (1.475 Å) and short (1.457 Å) bonds actually found.

The bond lengths in Table 4.1 suggest strong keto-enamine character in **4.3** (stronger than most typical keto-enamine TSANs, in fact), approaching that of **2.7** and DMF.

4.6 Solution Characterization by 1H NMR Spectroscopy

Crystals of **4.3** are readily soluble in common organic solvents. Taking advantage of this, we carried out ^{1}H NMR spectroscopy measurements in $CDCl_3$, CD_2Cl_2, CD_3OD, DMSO-d_6, and DMF-d_7. The obtained spectra are essentially the same in all solvents. Figure 4.10 shows one such spectrum in CD_3OD. There are only three resonances, which can be unambiguously assigned based on their integrations. Thus, two distinct CH_3 signals are visible around 3.2 ppm, along with a single imine/enamine resonance at 8.10 ppm.

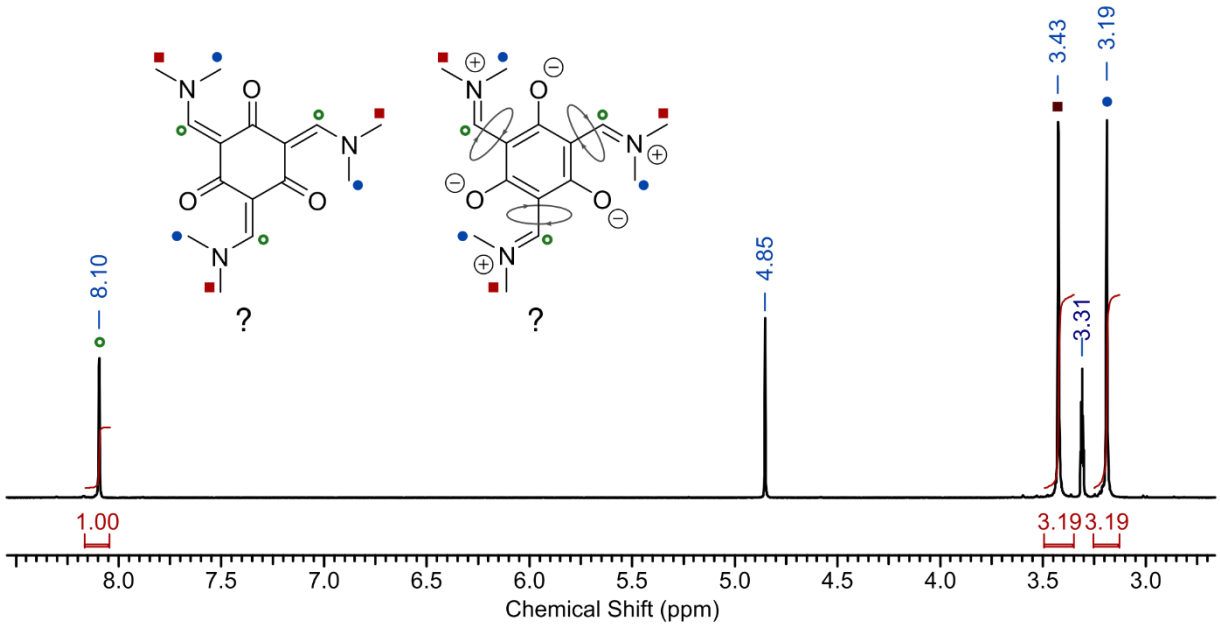

Figure 4.10. ^{1}H NMR spectrum of **4.3** (400 MHz, r.t., CD_3OD), showing two possible structures consistent with the spectrum.

The ^{1}H NMR spectrum of **4.3** can be interpreted as belonging to a compound with zwitterionic character, where C–CHN bonds rotate on a shorter timescale than CH–NMe_2 bonds do. Alternatively, it is consistent with a rigid, symmetric structure. The complete absence of the asymmetric form makes this an unlikely assignment, of course.

To find out whether the simple ^{1}H NMR spectrum of **4.3** results from a rigid, symmetric structure or fast rotation of the –CHNMe$_2$ arms, we undertook a series of variable-temperature NMR experiments. This was done in a number of solvents to control for solvent-dependent behaviour as well. Figure 4.11 shows the ^{1}H NMR spectra in toluene-d_8. The room temperature pair of CH_3 signals resolves into eight distinct resonances at low temperatures. Likewise, the single CH peak is broken up into four separate signals, three of which are the same amplitude and larger than the fourth. This is clear evidence that rapid rotation of the –CHNMe$_2$ sidechains gives rise to the simple room-temperature ^{1}H NMR spectrum of **4.3**. Consistent with selective crystallization of asymmetric **4.3** form, the major species in solution is the asymmetric form (at least at low temperatures), which contributes six CH_3 and three CH signals. The remaining two CH_3 and single CH signal can be attributed to a C_3 symmetric molecule. Based on the integration of symmetric and asymmetric signals, about 15% of the sample exists in the symmetric form at -89 °C. This fraction appears to be largest in toluene-d_8 among the solvents used in our study.

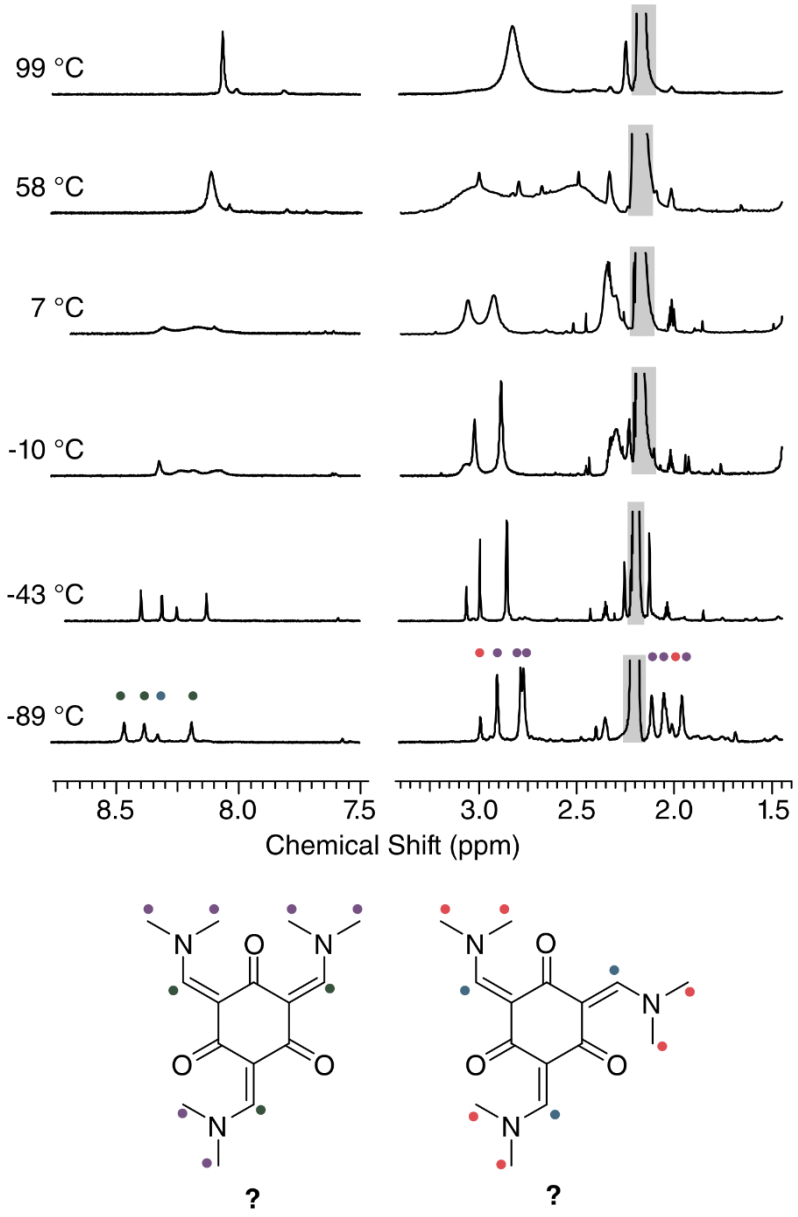

Figure 4.11. VT ^{1}H NMR spectra for **4.3** (400 MHz, r.t., toluene-d_8).

Repeating the experiment in other NMR solvents reveals some interesting trends. For instance, rotation of the $CHNMe_2$ arms (C–CH bonds) seems to be very fast in CD_3OD, Figure 4.12, where even at -89 °C the C*H*N resonances are not fully resolved. Rotation about the CH–N bonds, in contrast, appears to be slower in methanol than toluene at the same temperature.

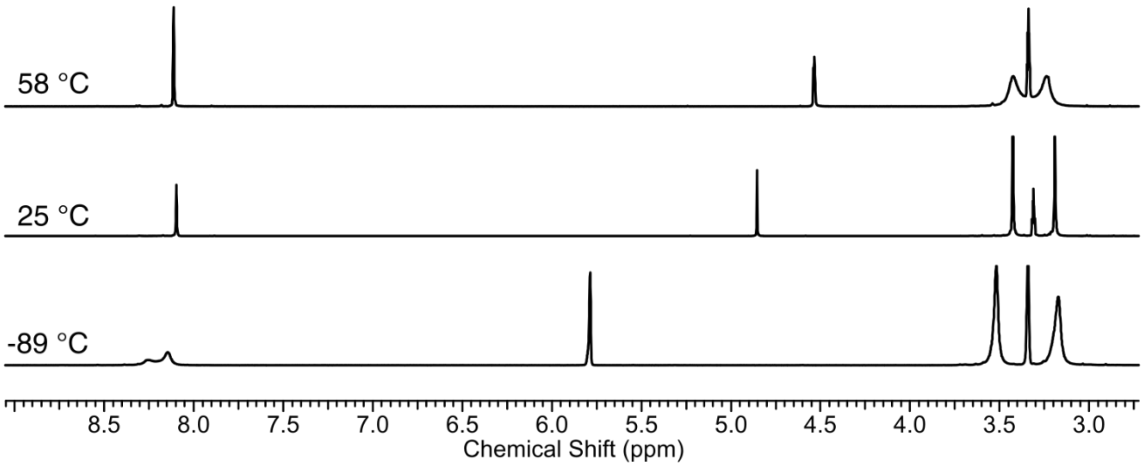

Figure 4.12. VT ^{1}H NMR experiment on **4.3** (400 MHz, r.t., CD_3OD).

The opposing trends for the rate of C–CH and CH–N bond rotation in different solvents dismiss the hypothesis that certain solvents generally facilitate rotation about all bonds (*e.g.* through stabilization of partial charges generated during the process). Further, when the same experiment was repeated in DMF-d_7, results intermediate between CD_3OD and toluene-d_8 were obtained, Table 4.2. We suspect that higher dielectric constant (and hydrogen bonding in the case of methanol) contribute to larger zwitterionic character in CD_3OD and DMF, leading to faster C–CH and slower CH–N rotation in these solvents.

Table 4.2. Coalescene temperatures and free energies of activation for bond rotation in various solvents.

Solvent	C–CH rotation			CH–N rotation		
	T_c (°C)	$\Delta\nu$ (Hz)	$\Delta G^{\ddagger}_{rot}$ (kJ/mol)	T_c (°C)	$\Delta\nu$ (Hz)	$\Delta G^{\ddagger}_{rot}$ (kJ/mol)
Toluene-d_8	7	122	57	60	250	64
DMF-d_7	-3	75	54	45	188	62
Methanol-d_4	< -89	47	< 37	> 58	138	> 65

Table 4.2 gives an estimation of the free energy barrier for rotation about the C–CH and CH–N bonds. These $\Delta G^{\ddagger}_{\text{rot}}$ values have been calculated from peak coalescence temperatures and frequency separations ($\Delta\nu$) using the Eyring equation $k_{\text{ex}} = \frac{k_B T}{h} e^{\frac{-\Delta G^{\ddagger}_{\text{rot}}}{RT}}$ (k_{ex} is the exchange rate constant) and the condition for peak coalescence, namely that at coalescene temperature $k_{\text{ex}} = \frac{\pi \Delta \nu}{\sqrt{2}}$. *

4.7 Labeling Experiments with ^{15}N

For compounds that contain nitrogen atoms, ^{15}N labeling can be used as a versatile method to better understand these compounds'electronic structures.[152,153] For instance, the acute sensitivity of ^{15}N shielding to electronic environment has been exploited in NMR experiments to distinguish between imines and enamines.[154,155] Similarly, the vibrational redshift resulting from ^{14}N→^{15}N substitution, though not as large as that for ^{1}H→^{2}D substitution, can be used to distinguish vibration of bonds involving nitrogen atoms in infrared spectra. Since ^{15}N-labeled dimethylamine hydrochloride is commercially available, we decided to used it as a precursor to ^{15}N-labeled **4.3**, **4.3-^{15}N$_3$**, Figure 4.13.

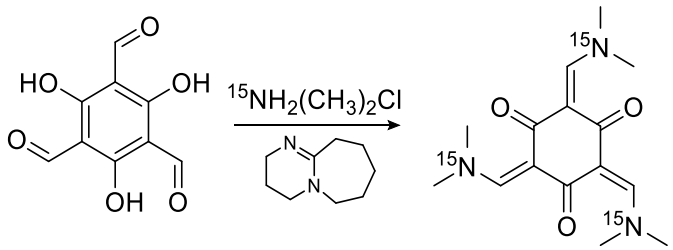

Figure 4.13. Preparation of the ^{15}N-labelled analogue of **4.3**, **4.3-^{15}N$_3$**.

* Combining the two, we have $\Delta G^{\ddagger}_{\text{rot}} = -RT_c \ln \frac{\pi h \Delta \nu}{\sqrt{2} k_B T_c}$.

To convert the hydrochloride to free amine, 1,8-diazabicyclo(5.4.0)undec-7-ene (DBU) was used as a strong, non-volatile base. Thus, heating $^{15}NH_2Me_2 \cdot HCl$ with DBU releases $^{15}NHMe_2$ gas, which is carried to the TFP solution by nitrogen gas, Figure 4.14.

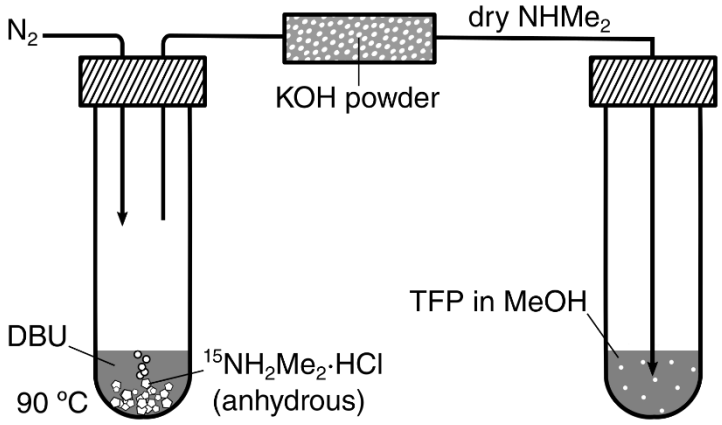

Figure 4.14. Preparation of **4.3-$^{15}N_3$**.

4.7.1 ^{15}N NMR Spectroscopy

The ^{14}N nucleus has medium NMR sensitivity (0.001 compared to ^{1}H)[156] but gives impractically broad peaks due to its large quadrupole moment. Its stable isotope, ^{15}N, while of low natural abundance (0.37%), gives narrow lineshapes and can be observed directly or through ^{1}H in heteronuclear correlation experiments (*e.g.* HSQC). The IUPAC recommendation for ^{15}N chemical shift standard is neat nitromethane but liquid ammonia appears to be more popular with researchers and instrument manufacturers. In what follows, all ^{15}N chemical shift data are referenced to liquid ammonia at 0 ppm.

As with ^{13}C NMR, acquisition of ^{15}N NMR spectra can be challenging due to the long longitudinal relaxation time constant T_1. In this case, paramagnetic relaxation agents like $Cr(acac)_3$ can be used to accelerate longitudinal relaxation, allowing ^{15}N experiments with shorter recycle delays. Driven-equilibrium adiabatic pulse sequences such as UDEFT[140] refocus and rotate

transverse magnetization in order to restore longitudinal magnetization and can be used to similar effect.

The ^{15}N nucleus has a negative gyromagnetic ratio, γ, which means that unlike with ^{13}C NMR, ^{1}H decoupling will decrease ^{15}N magnetization. For this reason, it is common to use an inverse-gated proton-decoupled pulse sequence (or no ^{1}H decoupling at all) for ^{15}N.

In CD_2Cl_2 solvent, the ^{15}N NMR spectrum of **4.3-^{15}N$_3$** showed very broad lineshapes regardless of pulse sequence and whether or not decoupling or relaxation agent was used. Naturally, these spectra were noisy due to the NMR signal being spread out over a very large chemical shift range. Thus, overnight acquisition (4096 transients) using the inverse-gated ^{15}N{^{1}H} pulse sequence gave the spectrum in Figure 4.15. Impurity peaks can be seen at 127.2 and 134.9 ppm presumably originating from trace hydrolysis of one of the enamine sidechains in **4.3-^{15}N$_3$**. These peaks, which are not present in the ^{1}H NMR spectrum of the same sample, are only visible by virtue of the extreme broadening of the main **4.3-^{15}N$_3$** peak (113–119 ppm).

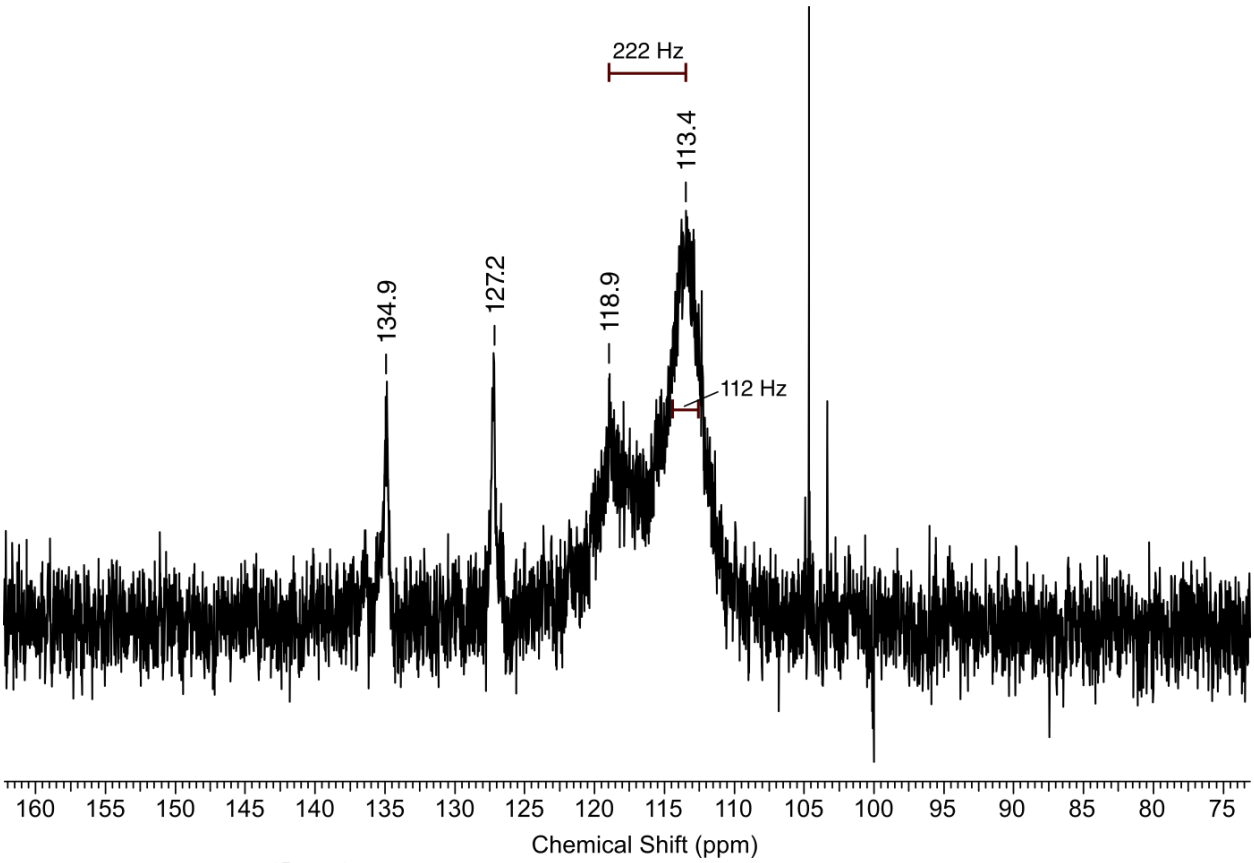

Figure 4.15. ^{15}N {^{1}H} spectrum of **4.3-^{15}N$_3$** (inverse gated, 40 MHz, CD_2Cl_2, r.t.).

The broad lineshape seen in CD_2Cl_2 indicates that the inequivalent ^{15}N sites in the asymmetric structure of **4.3** are interconverting on an intermediate timescale. Based on an estimated peak width at half-hight ($\Delta\nu_{1/2}$) of 112 Hz, the exchange rate is calculated at $k = 2\pi\left(\frac{\Delta\nu 1}{2}\right) \approx 700\ \mathrm{s}^{-1}$.

As expected, faster isomerization/conformation change in CD_3OD leads to a unique ^{15}N resonance at room temperature, giving a single, sharp resonance at 130.2 ppm, Figure 4.16. Acquisition is complete in a much shorter time in this case (32 transients), since the narrow lineshape of the peak allows it to be easily detected.

Previous work has established an acute dependence of ^{15}N chemical shift on imine versus enamine structure. Thus, whereas imines have large downfield chemical shifts of more than 200 ppm, much lower values (50–80 ppm) are obtained with enamines.[154,155,157,158] The

intermediate ^{15}N chemical shift value of compound **4.3** indicates intermediate imine/enamine bonding. Furthermore, the downfield shift in ^{15}N resonance in methanol compared to CD_2Cl_2 (130 vs ~ 115 ppm) can be interpreted as being due to larger zwitterionic contribution in methanol, similar to the case of ^{1}H VT NMR in Section 4.6.

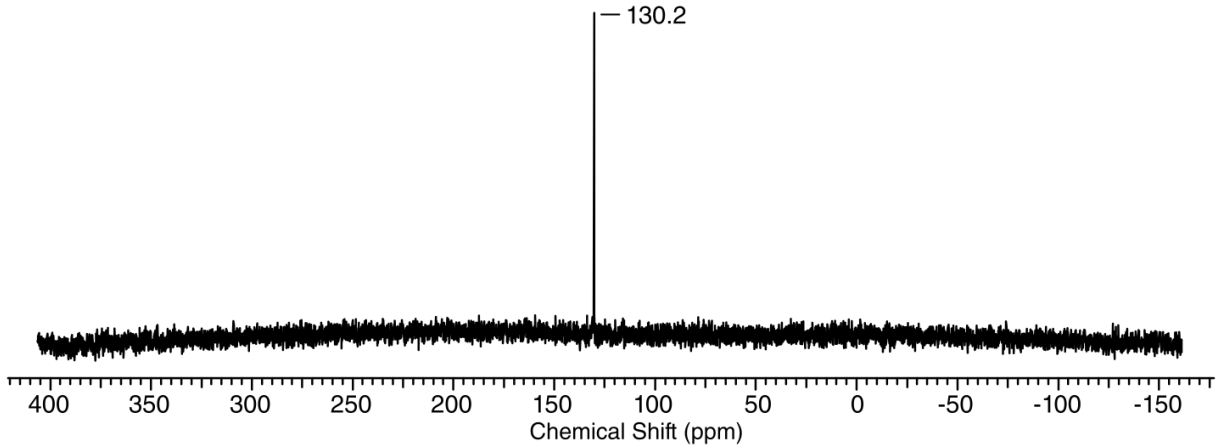

Figure 4.16. ^{15}N {^{1}H} NMR spectrum of **4.3-^{15}N$_3$** (inverse gated, 40 MHz, CD_3OD, r.t.).

Indirect proton-observed heteronuclear correlation methods such as HSQC (Heteronuclear Single Quantum Correlation) and HMBC (Heteronuclear Multiple Bond Correlation) provide a more powerful alternative to direct observation of ^{15}N. Here, we take advantage of the much larger (*ca.* 10 times) gyromagnetic ratio, γ, of the proton relative to the ^{15}N nucleus by transferring the much larger magnetization of the former to the latter. This gives ^{15}N chemical shifts and ^{15}N–^{1}H connectivity in a single experiment.

In most cases, HSQC is used to reveal direct (1 bond) H–X connectivity, inapplicable to **4.3** as there are no direct H–^{15}N bonds. However, by reducing the expected J_{H-X} coupling constant (CNST2 in Bruker terminology), longer range *J* couplings can be observed. For instance, typical default values for J_{H-X} are 145 Hz for HSQC {^{1}H, ^{13}C} and 90 Hz for HSQC {^{1}H, ^{15}N}. With some trial and error, we found that CNST2= 12 Hz was optimal for observation of $^2J_{H-N}$ in **4.3**.

One advantage of using HSQC is the short time required to collect a spectrum. Taking advantage of this, we carried out the experiment at a range of temperatures in CD_2Cl_2. Figure 4.17 shows the resulting spectrum at -84 °C. Slow bond rotation at this temperature allows individual CH_3, CH, and ^{15}N resonances in the molecule to be resolved.

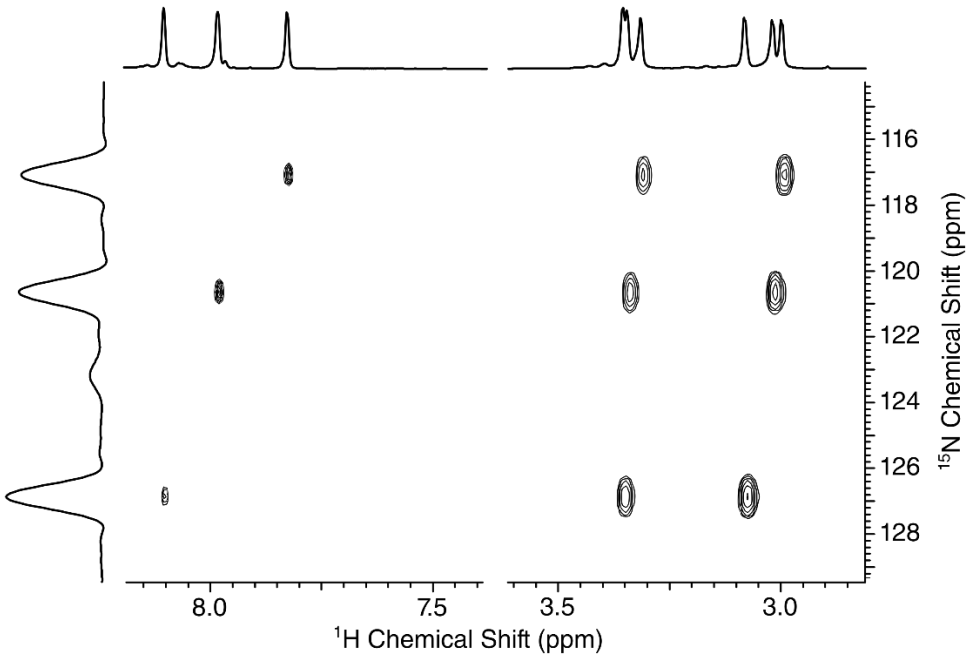

Figure 4.17. ^{1}H–^{15}N HSQC spectrum of **4.3-$^{15}N_3$** (CD_2Cl_2, -84 °C, ^{1}H: 400 MHz).

The lack of symmetry suggested by this HSQC experiment is reminescent of the strained, asymmetric arrangement of atoms in the crystal lattice of **4.3**. Indeed, *ab initio* calculations (B3LYP/Def2TZVPP/GIAO, gas phase) using atomic coordinates from the crystal structure of **4.3**, give ^{15}N shieldings that are similarly spaced, Figure 4.18.

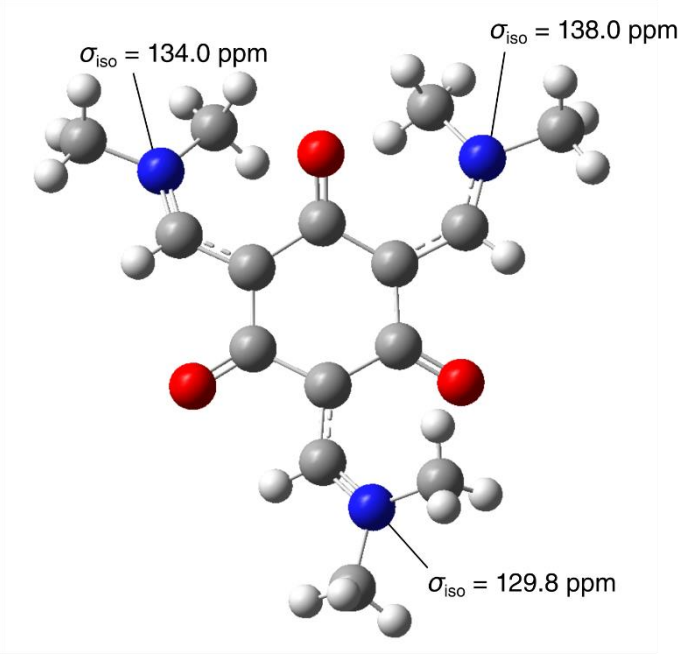

Figure 4.18. Calculated gas phase ^{15}N isotropic magnetic shieldings using GIAO (B3LYP/Def2TZVPP//B3LYP/6-311G(d,p)).

4.7.2 Isotopic Shift

One useful aspect of isotope labeling is that it allows vibrational bands to be assigned with certainty. This is commonly done with deuterium-labelled compounds,[159] owing both to the availability of low-cost deuterated precursors as well as the large ^{2}D/^{1}H mass ratio of *ca.* 2, which results in dramatic red shifts upon deuterium substitution. Although the ^{15}N/^{14}N mass ratio is not nearly as large, an appreciable isotope shift can still be observed.

The extent to which the infrared spectrum is red-shifted as a result of ^{14}N/^{15}N is straightforward to calculate using the simple harmonic oscillator as model. The natural frequency of the harmonic oscillator between atoms of mass m_1 and m_2 is given by $\nu = \sqrt{\frac{k}{\mu}}$, where μ is the reduced mass $\frac{m_1 m_2}{m_1 + m_2}$ and for a C–N bond $m_1 \approx 12$.

$$\frac{\nu(^{12}C\ -^{14}\ N)}{\nu(^{12}C\ -^{15}\ N)} = \sqrt{\frac{\mu_{15}}{\mu_{14}}} = \sqrt{\frac{12 \cdot 15\ (12+14)}{12 \cdot 14(12+15)}} = 1.016 = \ 1.6\%^{*}$$

Since the C–N stretch is expected to lie in the 1400-1600 cm^{-1} range, a red shift of 22–25 cm^{-1} is expected upon isotope labelling with ^{15}N.

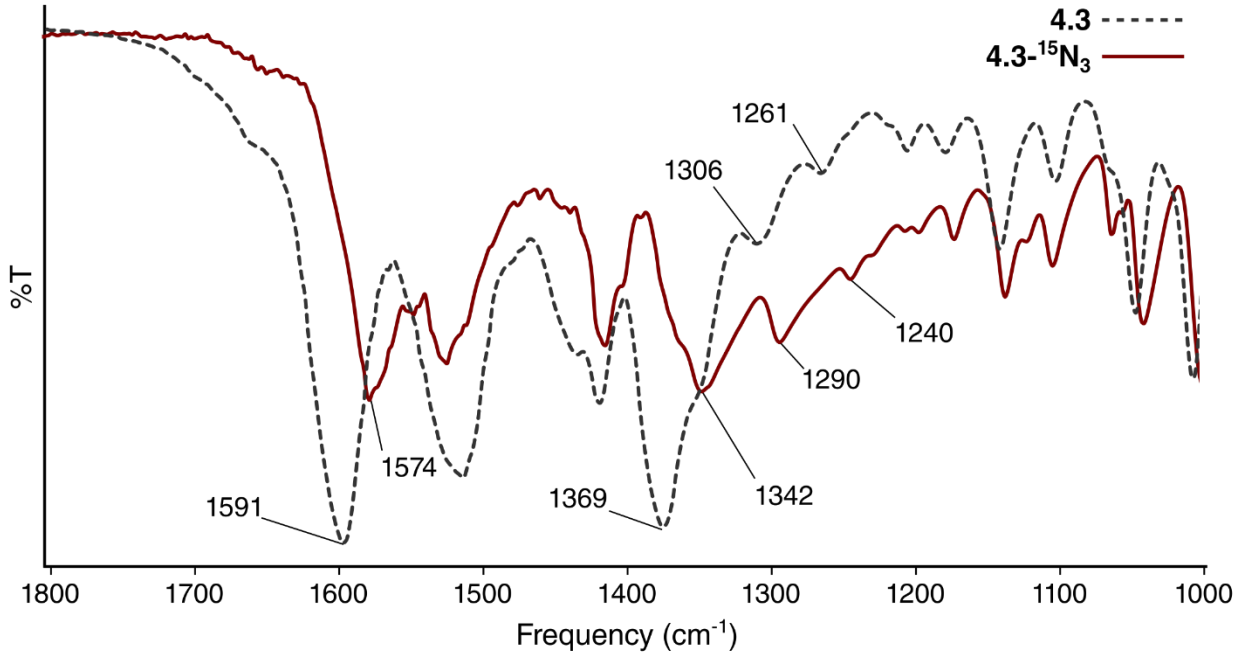

Figure 4.19. Infrared spectrum of **4.3** (dashed), and **4.3-^{15}N$_3$** (red).

Figure 4.19 compares the IR spectra of **4.3** and **4.3-^{15}N$_3$**, where the affected peaks show a redshift of 15–27 cm^{-1}. To account for the intermediate redshifts of certain peaks, we used gas phase computational modelling of the compound and calculated the vibration frequencies for both **4.3** and **4.3-^{15}N$_3$**. Examining the results reveals that C–N and C–O stretches are strongly coupled for the vibrations with the largest transition dipoles. Figure 4.20 shows the displacement extrema of the O and N atoms for the most intense absorption (ν = 1630 (^{14}N), 1621 (^{15}N) cm^{-1}) When

* Assuming equivalent bond strength for ^{12}C–^{14}N and ^{12}C–^{15}N.

compared between **4.3** and **4.3-$^{15}N_3$**, the calculated frequencies for these modes show redshifts of 9–20 cm^{-1}, consistent with experiment. In summary, vibrational analysis does not attribute simple single/double bond character to the C–N bond, instead showing combined C–N/C–O vibrations due to strong coupling.

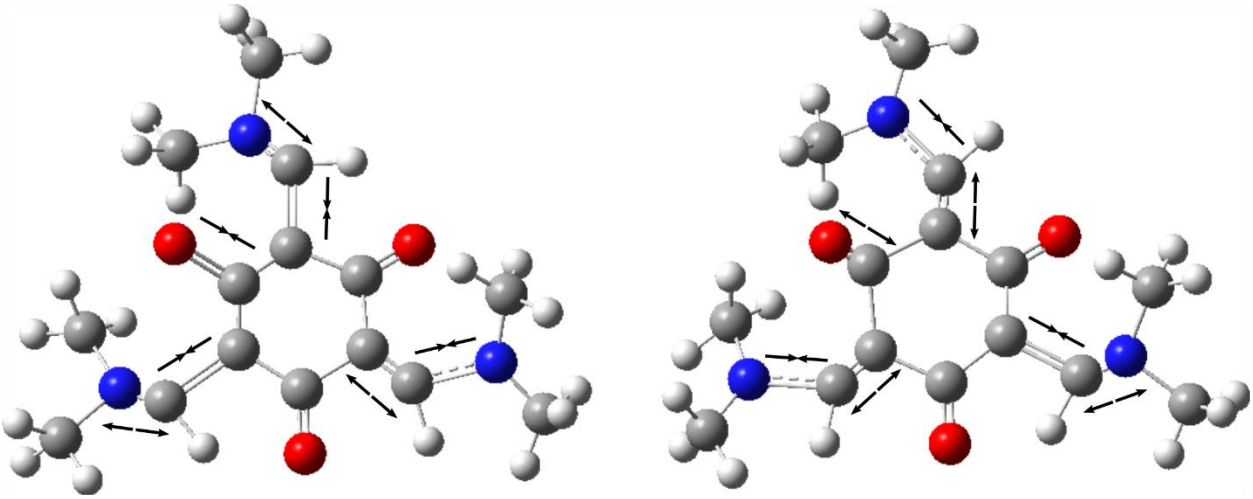

Figure 4.20. Extrema of atomic movement for the most intense infrared absorption of **4.3**, showing strong coupling of the C–O and C–N stretch in this normal mode.

4.8 Analogues with Longer Alkyl Chains

As one might expect, steric crowding in **4.3** has a destabilizing effect on the molecule. To demonstrate this, we prepared analogues of **4.3** with longer alkyl chains, Figure 4.21

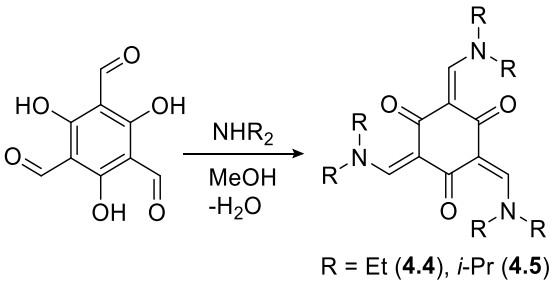

Figure 4.21. Preparation of **4.3** analogues with R = Et (**4.4**) and i-Pr (**4.5**).

Compounds **4.4** is slow to form and full conversion happens only when a suspension of TFP in methanol is reacted with a tenfold excess of diethylamine overnight. This large excess of diethylamine is necessary not only to accelerated the formation of **4.4** but also to drive the equilibrium in its favour. In fact, even when fully formed, the reaction in Figure 4.21 is readily reversed by traces of water if diethylamine is allowed to slowly evaporate under vacuum.

As expected, the diisopropylamine analogue, **4.5**, is even less stable: a 10-fold excess of amine (30 eq) and heating at 55 °C overnight did not bring about the formation of **4.5**. Indeed, the ^{1}H NMR spectrum of the reaction mixture shows a roughly equal mix of aldehyde and enamine/imine CH peaks.

4.9 Cyclic Voltametry

The unusual structure of **4.3** naturally leads one to inquire about its redox properties. Compound **4.3** visibly decomposes in solution when exposed to air but is stable in the absence of air and moisture. Whereas TSANs are prized for their electrochemical robustness,[160,161] the introduction of strain and removal of intramolecular hydrogen bonds in heteroradialene **4.3** can be seen as a method of electrochemical activation. We were therefore interested to measure how readily this heteroradialene undergoes oxidation.

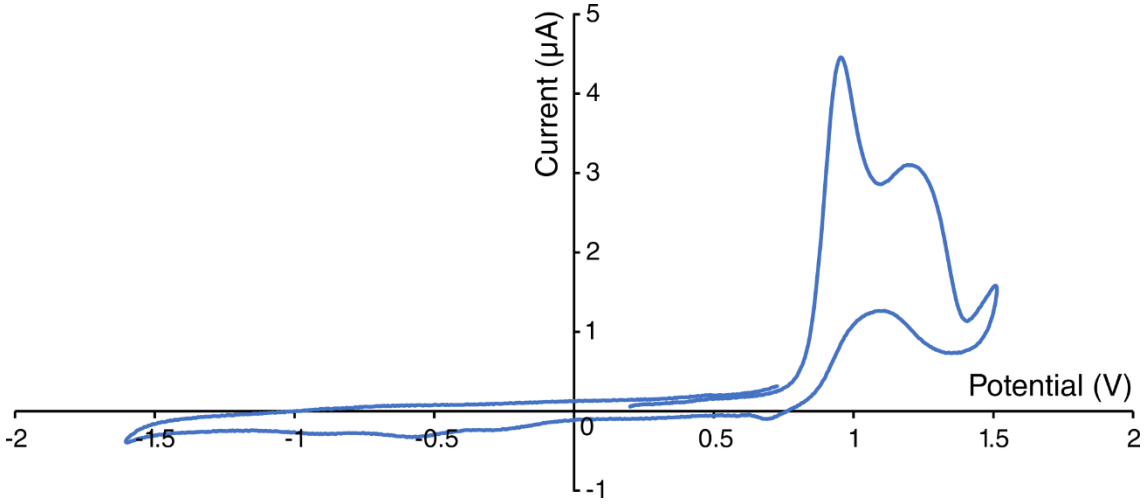

Figure 4.22. Cyclic voltammogram of **4.3** showing two oxidation events.

The cyclic voltammogram of **4.3** in DCM (Figure 4.22, NBu_4PF_6 electrolyte, ferrocene reference) does show two irreversible oxidation events at 0.95 and 1.19 V, respectively. No reduction events were observed within the potential window permitted by solvent.

4.10 Conclusions and Future Work

The unique twisted geometry of heteroradialene **4.3** and its stability in spite of its lack of aromaticity demonstrate the importance of electron delocalization along the periphery of the molecule. The preparation and characterization of this molecule serve as proof of the concept that competing modes of electron delocalization in a molecule can act as driving forces toward unconventional reactivity. An example application is outlined below.

As pointed out in Section 4.9, compound **4.3** is oxidized relatively easily. One interesting experiment would be to introduce groups that compete with the central heteroradialene carbonyl groups for the electron density formally originating from the nitrogen lone pairs. Figure 4.23 shows two proposed examples, where phenyl and acetyl groups are have been added as extra centres for

electron delocalization. In addition to better stability toward oxidation, we expect to see a stronger keto-enamine like heteroradialene and lower zwitterionic character in these new compounds.

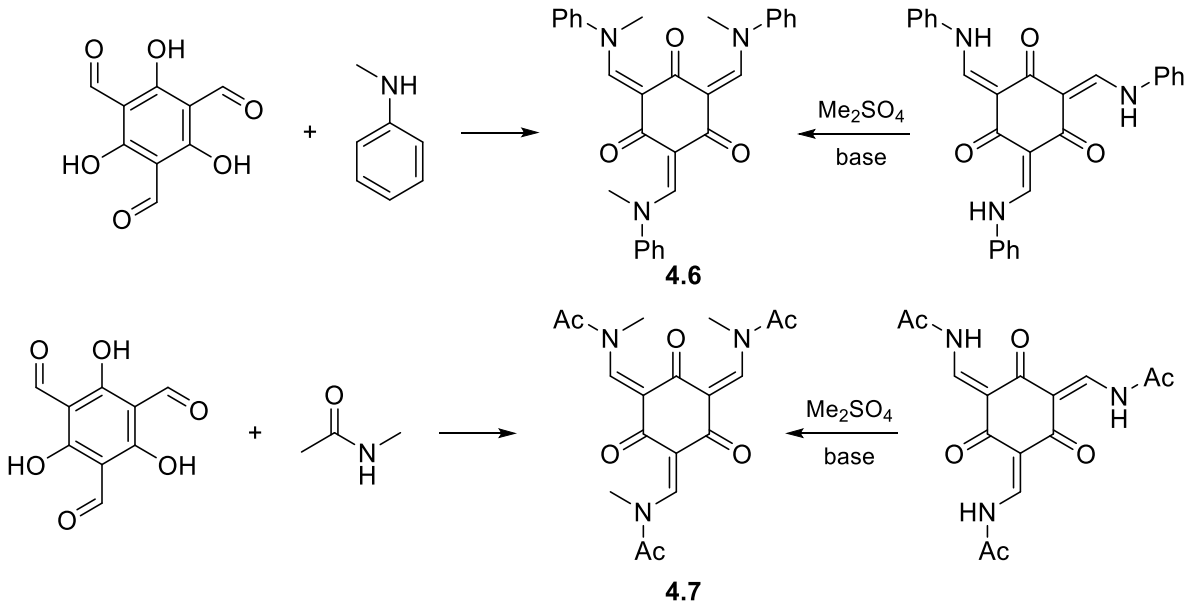

Figure 4.23. Proposed preparation of two **4.3** analogues with competing electron-withdrawing groups.

Preliminary experiments on the direct preparation of **4.6** from TFP and N-methylaniline did not give a crystalline product. An alternative preparation of both **4.6** and **4.7** is through base-promoted methylation. Due to the weaker conjugation between the nitrogen atoms and the central ring, both **4.6** and **4.7** are expected to have groups protruding from the plane of the molecule. If stable enough, these compounds might pave the way to new self-assembled structures that are three dimensional by nature, such as the capsule shown in Figure 4.24. Simple TSAN analogues of such capsules have been reported, but strong intramolecular hydrogen bonding in TSANs is often at odds with the three dimensional structure imposed by the cage/capsule geometry.[62,162] In comparison, compounds based on **4.6** and **4.7** have the advantage of naturally adopting a non-planar shape.

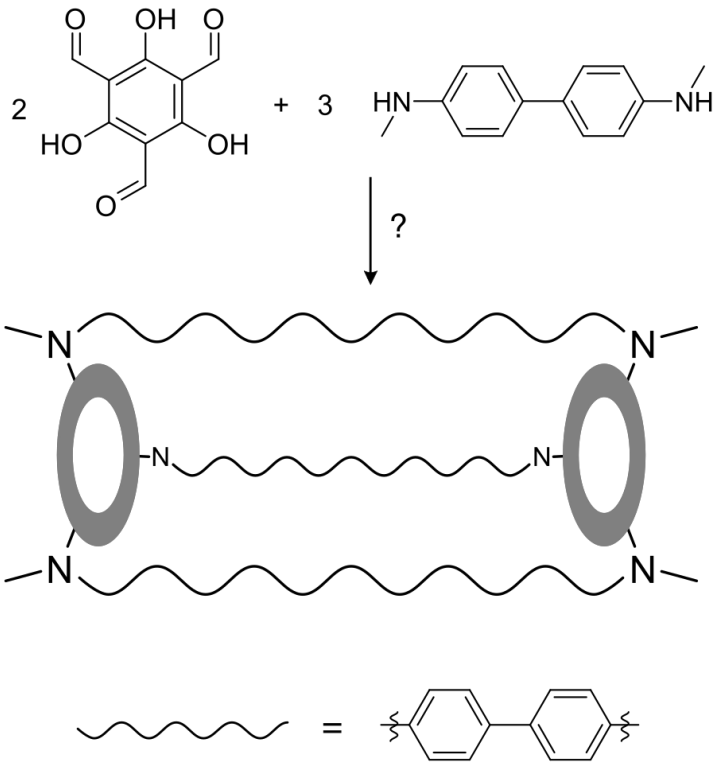

Figure 4.24. Tentative design for a heteroradialene capsule.

4.11 Experimental Section

4.11.1 Cyclic Voltammetry

Cyclic voltammetry experiments were carried out on a Pine Instruments AFCBP1 potentiostat. The setup comprised dichloromethane as solvent, tetrabutylammonium hexafluorophosphate as electrolyte, a platinum mesh counter electrode, a glassy carbon working electrode, silver wire used as pseudoreference, and ferrocene (added after the measurement) as reference.

4.11.2 Procedures and Data

Preparation of 4.3: Triformylphloroglucinol (TFP, 10.0 mg, 0.0476 mmol, 1 equiv) was added to a septum-capped NMR tube containing 0.6 mL of $CDCl_3$ and dispersed by sonicating for 5 min. A septum-capped Schlenk flask was charged with 50 mg (0.61 mmol, 13 equiv) of anhydrous dimethylamine hydrochloride and 0.100 mL (101 mg, 0.67 mmol, 14 equiv) of 1,8-

diazabicycloundec-7-ene (DBU) under nitrogen and sonicated until a viscous, white suspension was obtained. Dimethylamine was carried from the headspace of the Schlenk flask by nitrogen gas introduced through the sidearm and, using a steel canula, bubbled into the NMR solvent. After 1 min, the Schlenk flask was brought in contact with a heating bath at 95 °C, causing bubbles of dimethylamine gas to form in the suspension. During the following 20 min, the suspension of TFP in $CDCl_3$ underwent a change of colour from the initial pale yellow to brilliant fluorescent yellow-green, to a bright orange. At this point, the cannula was removed and the progress of the reaction was monitored by ^{1}H NMR spectroscopy. The reaction was complete after about 1 h, judging by the disappearance of the aldehyde peak. Evaporation of NMR solvent under high vacuum left 13.7 mg (0.0471 mmol, 99%) of an orange powder.

Data for 4.3: ^{1}H NMR (400 MHz, CD_3OD) δ 8.10 (s, 3H; CH), 3.43 (s, 9H; CH_3), 3.19 (s, 9H; CH_3). ^{13}C {^{1}H} NMR (100 MHz, $CDCl_3$) δ 182.7 (CO, br), 159.5 (CH–N), 107.4 (*C*–CHN, br), 48.2 (CH_3), 44.4 (CH_3). ^{15}N NMR (**4.3-^{15}N$_3$**, 40 MHz, CD_3OD) δ 130.2. UV-Vis (CH_2Cl_2) λ_{max} (ε) = 363 (5.3×10^4), 308 (4.1×10^4), 257 (1.3×10^4) nm ($cm^{-1}\,mol^{-1}\,L$). IR (neat) ν = 2918 (br), 2806, 1582, 1525, 1414, 1339, 1293, 1135, 1042, 998, 967, 944, 809, 733, 625, 588, 463 cm^{-1}. HRMS (ESI/TOF-Q) *m/z*: [**4.3** + H]$^+$ Calcd for $C_{15}H_{22}N_3O_3$ 292.1661; Found 292.1663.

Preparation of 4.3-^{15}N$_3$: The preparation of **4.3-^{15}N$_3$** was carried out identically to that of **4.3** except using ^{15}N-labelled anhydrous dimethylamine hydrochloride instead of anhydrous dimethylamine hydrochloride. IR (neat) ν = 2917 (br), 2806, 1574, 1520, 1411, 1344, 1290, 1134, 1038, 997, 945, 810, 733, 624, 586, 461 cm^{-1}. HRMS (ESI/TOF-Q) *m/z*: [**4.3-^{15}N$_3$** + H]$^+$ Calcd for $C_{15}H_{22}{}^{15}N_3O_3$ 295.1572; Found 295.1567 (base peak); Calcd for $C_{15}H_{22}{}^{15}N_2{}^{14}NO_3$ 294.1602; Found 294.1581 (6.5%).

Preparation of 4.4: Triformylphloroglucinol (TFP, 10.0 mg, 0.0476 mmol, 1 equiv) was introduced into a septum-capped NMR tube containing 0.6 mL of CD_3OD; the contents were degassed with N_2. Diethylamine (0.10 mL, 71 mg, 0.97 mmol, 20 equiv) was injected into a Schlenk flask and the flask warmed up to 40 °C to accelerate the evaporation of the amine while the gaseous diethylamine was bubbled into the NMR solvent through a canula. During the next 15 min the suspended TFP dissolved to give a yellow-orange solution. Following this, the canula was removed and the NMR tube stored at room temperature for 16 h. The ^{1}H NMR spectrum of the resulting orange-red solution shows virtually complete conversion of TFP to **4.4**, along with a large excess of diethylamine. Solvent and excess diethylamine were then removed at room temperature under high vacuum, leaving a dark crimson semi-solid. When dissolved in benzene, a light orange supernatant and small amounts of a sticky dark solid resulted. Evaporation of the supernatant under high vacuum gave a thick orange oil (17.7 mg, 0.0467 mmol, 98%) which is pure **4.4** by ^{1}H NMR spectroscopy.

Data for 4.4: ^{1}H NMR (400 MHz, $CDCl_3$) δ 8.10 (s, 3H; CH), 3.88 (q, br, $^3J_{HH}$ = 7.04 Hz, 6H; CH_2), 3.52 (q, br, $^3J_{HH}$ = 7.04 Hz, 6H; CH_2), 1.33 (t, br, $^3J_{HH}$ = 7.04 Hz, 9H; CH_3), 1.16 (t, br, $^3J_{HH}$ = 7.04 Hz, 9H; CH_3). ^{13}C {^{1}H} NMR (100 MHz, $CDCl_3$) δ 183.1 (CO), 157.2 (CH–N), 107.4 (*C*–CHN), 53.5 (CH_2), 47.8 (CH_2), 15.2 (CH_3), 12.7 (CH_3). UV-Vis (CH_2Cl_2) λ_{max} (ε) = 365 (3.6×10^4), 308 (3.5×10^4), 273 (3.0×10^4) nm ($cm^{-1}\,mol^{-1}\,L$). IR (neat) *v* = 2926 (br), 1591, 1508, 1414, 1371, 1138, 1043, 1003, 947, 810, 627, 590, 469 cm^{-1}. IR (neat glaze) *v* = 2973, 2934, 2873, 1573, 1515, 1442, 1389, 1346, 1301, 1259, 1178, 1138, 1049, 1020, 938, 924, 807, 619, 591, 529, 476 cm^{-1}. HRMS (ESI/TOF-Q) *m/z*: [**4.4** + H]$^+$ Calcd for $C_{21}H_{34}N_3O_3$ 376.2600; Found 376.2595.

Chapter 5

Mild and Efficient Formylation of Phenols using Formamidine Acetate

5.1 Introduction

Much of the rich tautomeric behaviour discussed in previous chapters is due to the properties of the salicylaldimine moiety. In this chapter, we address the challenges of preparing the parent salicylaldehydes used in the synthesis of these Schiff bases. Specifically, we develop a convenient route to salicylaldehydes such as 2,4,6-triformylphloroglucinol (TFP), **5.1**, 2,3-dihydroxy-5,6-dimethylterephthalaldehyde, **5.2**, and 2,3-dihydroxynaphthalene-1,4-dicarbaldehyde, **5.3** (Figure 5.1) that is substantially more efficient than state-of-the-art methods.

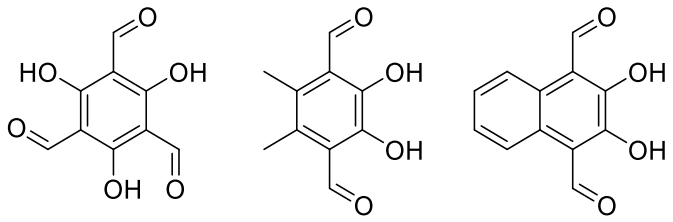

5.1 **5.2** **5.3**

Figure 5.1. Common aldehydes used in salicylaldimine Schiff base preparations.

Even though they are simple, symmetric compounds, the existing preparations of **5.1**–**5.3** are far from satisfactory. In principle, **5.1**–**5.3** can be obtained by formylation of the parent phenols, **(**Figure 5.2); however, as discussed below, common methods of formylation perform poorly when applied to these electron-rich phenolic substrates.

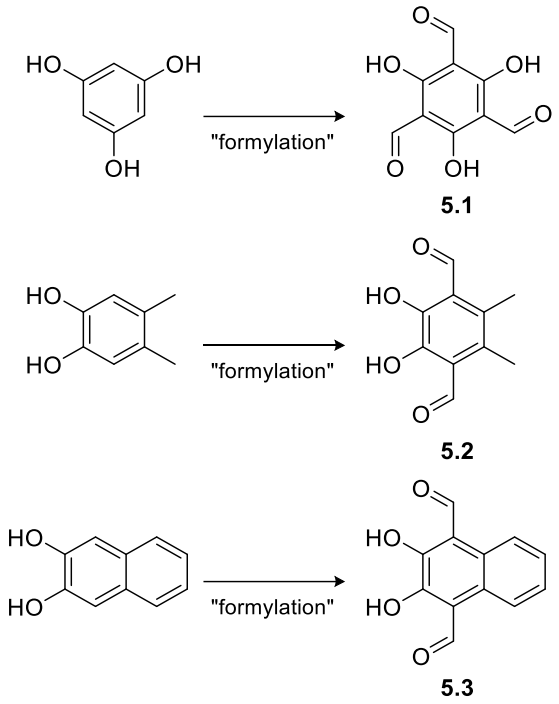

Figure 5.2. Preparation of **5.1**–**5.3** by formylation of their phenolic precursors.

5.2 Methods of Formylation

Owing to the versatility of aromatic aldehydes, a variety of methods has been developed for adding aldehyde functions to aromatic compounds. In what follows, we review the state of the art in this area. Given our interest in electron-rich phenols as substrates, we focus on syntheses based on electrophilic addition of the aldehyde carbon to the aromatic ring.

5.2.1 Formylation versus Acylation Reactions

Since well established and robust reactions exist for acylation of aromatic compounds, it is worthwhile to contrast them against the closely-related formylation reactions, especially when applied to electron-rich substrates. The highly activated aromatic rings found in phenols are especially easy to functionalize with acyl groups using variations of the Friedel-Crafts method. For instance, owing to its high reactivity, acetic anhydride (in the presence of $ZnCl_2$) can be used

to diacetylate resorcinol, Figure 5.3a.[163] Classic Friedel-Crafts conditions are also commonly used to prepare acyl phenols, Figure 5.3b,c.[164,165]

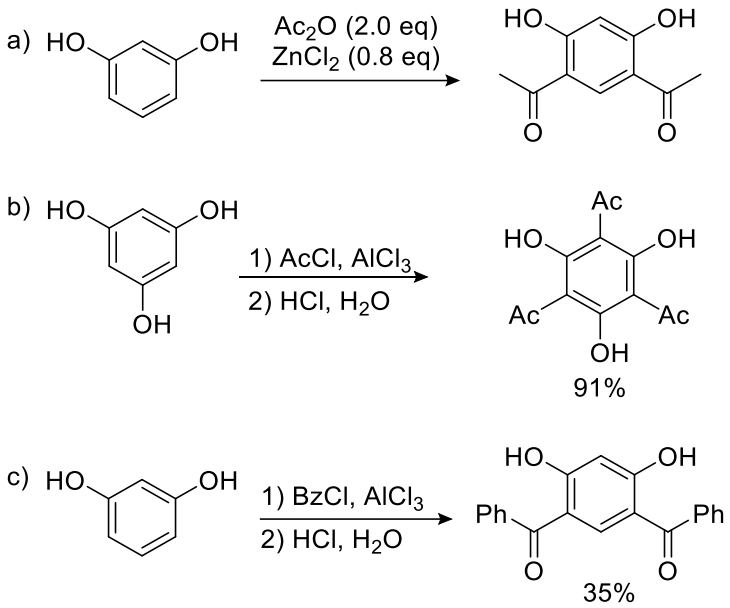

Figure 5.3. (a) Mild acetylation of resorcinol using acetic anhydride and $ZnCl_2$. (b,c) Acylation of phenols using acyl chloride and $AlCl_3$.

Unfortunately, Friedel-Crafts conditions cannot be directly applied to formylation reactions due to the fact that formic anhydride as well as formyl chloride and bromide are unstable and decompose with the release of carbon monoxide.[166] Formyl fluoride is more stable in comparison (though it still decomposes to HF and CO near room temperature) and can be used in conjunction with BF_3 catalyst to mono-formylate relatively inactive aromatic substrates, Figure 5.4.[167] Further adoption of this method is impeded by the relatively unstable nature of formyl fluoride and its hazardous decomposition products.

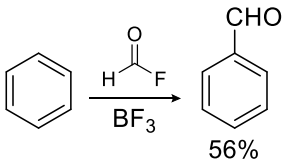

Figure 5.4. Formylation of benzene under Friedel-Crafts-like conditions using formyl fluoride and BF_3.[167]

More generally, we found that electrophilic formylation reactions in the literature can be categorized into two groups based on the oxidation state of the electrophilic carbon atom in the reagent. The remainder of this section presents various examples and explores the connection between mechanism and the advantages or shortcomings of reactions in each category.

5.2.2 Formylation Reactions using Carbon (II) Electrophiles

Like formyl halides, the formyl cation (CHO^+) is unstable and is readily deprotonated to form carbon monoxide. Most common formylation methods thus rely on stable equivalents of the formyl cation, *i.e.* reagents with an electrophilic carbon atom in oxidation state +2. These methods include the Vilsmeier–Haack,[168] Gattermann,[73] and Gattermann–Koch[169] reactions. Among these, the Vilsmeier–Haack reaction stands out as the most practical, hence its widespread usage in preparatory organic synthesis, *e.g.* Figure 5.5.[170]

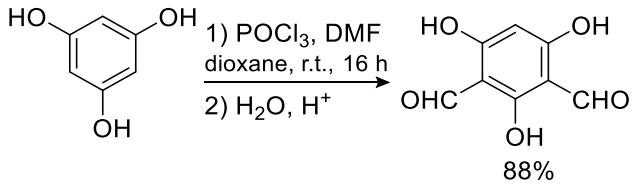

Figure 5.5. Vilsmeier–Haack diformylation of phloroglucinol.

The mechanism of the Vilsmeier–Hack reaction[171,172] involves a chloroiminium species as the active formylating agent. This electrophilic cation is attacked by the substrate in an electrophilic substitution reaction, giving an aryl *N*,*N*-dimethyliminium intermediate, Figure 5.6.

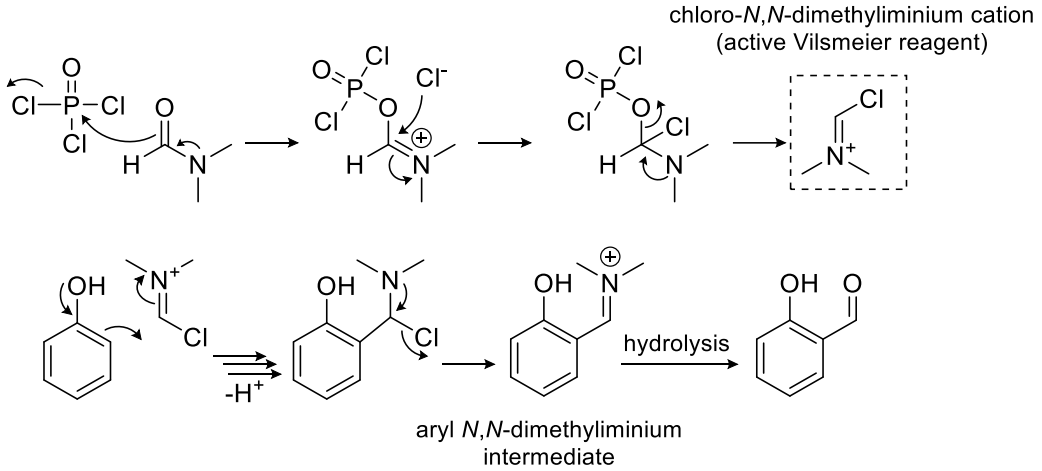

Figure 5.6. Mechanism of the Vilsmeier–Haack reaction.

The major drawback encountered with this methodology is deactivation of the substrate by the addition of *N*,*N*-dimethyliminium groups. This is problematic if multiple formyl groups need to be added, since the dimethyliminium moiety is strongly deactivating and has the additional disadvantage of encouraging side-reactions, particularly nucleophilic aromatic substitutions. The Vilsmeier formylation of phloroglucinol is especially illustrative in this context: mono- and diformylation of phloroglucinol proceed smoothly at room temperature (Figure 5.5),[170] but triformylation requires the application of heat and invariably leads to chlorine substitution at the phenolic positions, Figure 5.7.

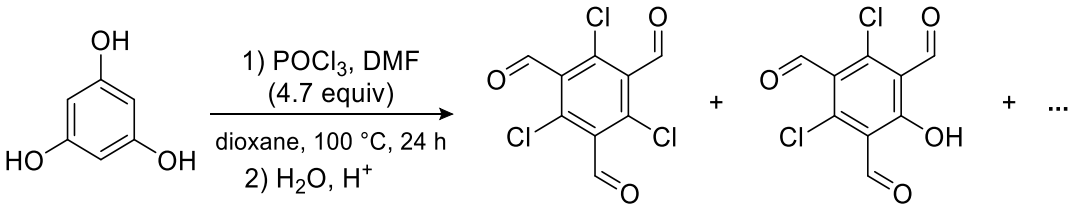

Figure 5.7. Outcome of Vilsmeier–Haack formylation under harsh conditions.

5.2.3 Formylation Reactions using Carbon (0) Electrophiles

A second category of formylation reactions relies on the relatively facile installation of hydroxymethyl or equivalent -CH_2X (X = OH, NR_2) groups using a reagent that contains an

electrophilic carbon atom in the 0 oxidation state. This adduct is then oxidized, often by hydride transfer to another equivalent of the same electrophile (CH_2X^+), Figure 5.8.

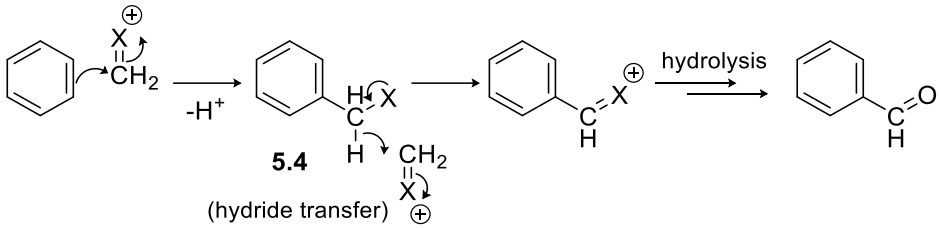

Figure 5.8. Formylation by electrophilic addition and hydride transfer.

Here, the main advantage compared to direct addition of a formyl equivalent (as seen in Section 5.2.2) is the intermediacy of compound **5.4**, whose CH_2X group does not have a deactivating effect. Thus, further equivalents of the electrophile CH_2X^+ can be readily added. This is beneficial in situations where multiple formyl groups need to be installed.

Well-known examples in this category are the Duff[71] and Skattebøl[173–176] reactions, Figure 5.9.[177] The Skattebøl reaction (X = O) provides a mild, inexpensive route to salicylaldehydes. The Duff reaction (X = NR_2), on the other hand, works best when the substrate is reacted with hexamethylenetetramine (HMTA) and a large excess of the more expensive trifluoroacetic acid (TFA) is used. Despite this, it is invaluable as the only practical method for the preparation of a number of aldehydes, including **5.1** and **5.2**.

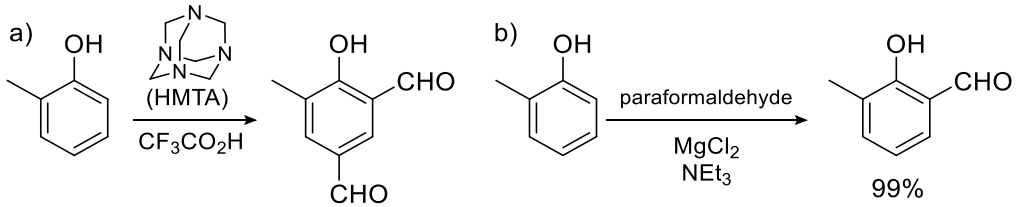

Figure 5.9. Modern forms of the Duff reaction (a) and the Skattebøl reaction (b). HMTA = hexamethylenetetramine.

While ideal for monoformylation of phenols to salicylaldehydes, the Skattebøl conditions are ineffective with deactivated substrates. Furthermore, there have been no reports of di- or triformylation using the Skattebøl protocol. The Duff reaction does not suffer from the same drawbacks, since it involves a more reactive iminium electrophile formed *in situ*, Figure 5.10a. However, yields tend to be low in many cases, especially when di- or triformylation is desired, *e.g.* Figure 5.10b.[178] Direct formylation of phloroglucinol using the Duff reaction similarly has a poor yield of *ca.* 15%.[49]

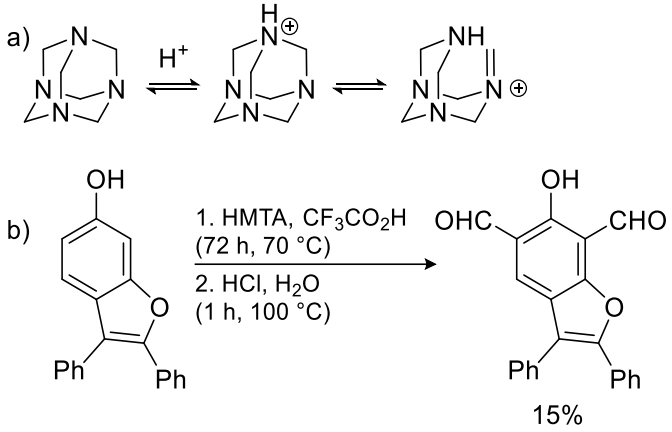

Figure 5.10. (a) Electrophilic iminium ion formed *in situ* in the Duff reaction. (b) Example Duff diformylation.

5.3 Attempts at an Improved Multiple Formylation Protocol

The following describes a number of avenues toward multiply-formylated phenols that we explored during our search for an improved method. The triformylation of phloroglucinol to **5.1** was used throughout as a benchmark. Although none of the methods presented in this section proved to be satisfactory for our purposes (often very little or no **5.1** formed), they are still briefly discussed here as they may serve as a starting point for future work to improve upon our work or successfully adapt it to formylation of other substrates.

5.3.1 Isolated Vilsmeier Reagents

As described before, substrate deactivation during successive Vilsmeier formylations of compounds like phloroglucinol can lead to the formation of chlorinated products, presumably through nucleophilic attack on a deactivated [chloro]phosphate ester, Figure 5.11.

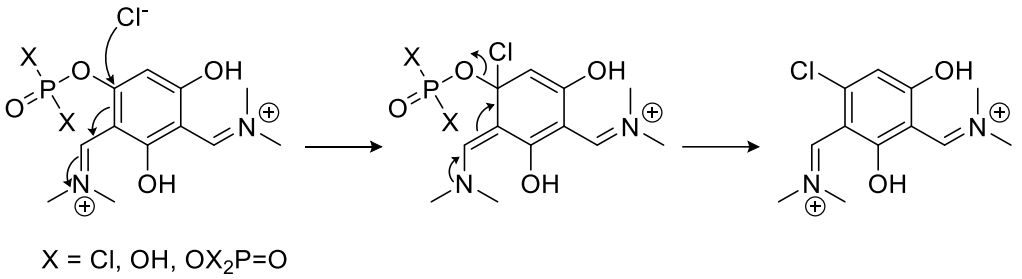

Figure 5.11. Possible pathway for formation of chlorinated side products in the Vilsmeier–Haack triformylation of phloroglucinol.

In light of our discovery of the zwitterionic/keto-enamine Schiff base described in Chapter 4, another possible pathway for the formation of these side products is direct chloride attack at the keto position of **4.3** under acidic conditions, Figure 5.12.

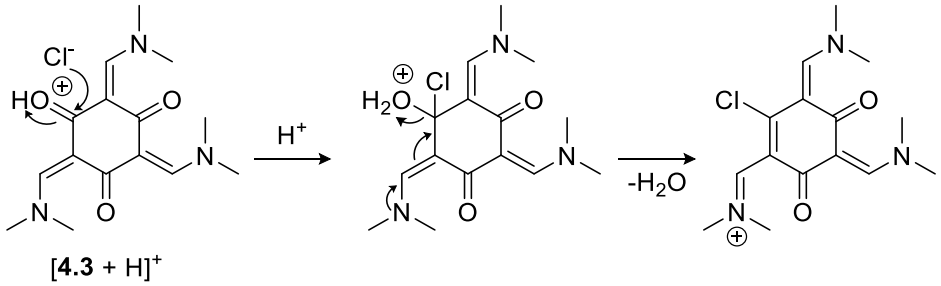

Figure 5.12. Alternative pathway for formation of chlorinated side products in the Vilsmeier–Haack triformylation of phloroglucinol.

Assuming that chlorinated side products are formed through the pathway shown in Figure 5.11, chlorination can be avoided if no aromatic phosphate esters are formed during the reaction. Thus, one can imagine that a pre-formed “pure” Vilsmeier reagent would lead to clean formylated product.

With this idea in mind, we attempted to synthesize the pure Vilsmeier reagent by reacting thionyl chloride ($SOCl_2$), instead of $POCl_3$, with DMF. Thionyl chloride has a lower boiling point of *ca.* 75 °C, allowing any excess $SOCl_2$ to be evaporated under reduced pressure. Other than the Vilsmeier iminium salt, volatile SO_2 is the only by-product of this alternative preparation, Figure 5.13.

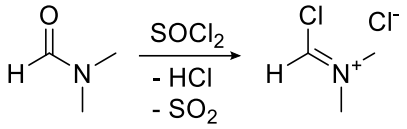

Figure 5.13. Isolation of pure Vilsmeier reagent through the reaction of DMF and $SOCl_2$.

In practice, combining DMF with $SOCl_2$ gives a thick yellow liquid that turns into a lumpy off-white powder when gently heated under high vaccum. When reacted with phloroglucinol in 1,4-dioxane, this moisture-sensitive chloroiminium salt is indeed capable of formylating all three positions, albeit unfortunately with the formation of copious amounts of chlorinated side products.

5.3.2 N,N-Dimethylmethaniminium Salts as Formylating Agents

The Duff reaction is often the method of choice for adding multiple formyl groups to aromatic substrates. Even so, the reaction involves the multifunctional hexamethylenetetramine (HMTA) molecule, which we suspected of lowering product yield by producing polymeric side-products.

Given this premise, we attempted formylations using *N*,*N*-dimethylmethaniminium salts as simplified monomeric analogues of the active Duff reagent, Figure 5.14. Iminium salts of this type, commonly known as Eschenmoser's salts when the counterion X^- is iodide,[179] are ordinarily used as reactive pre-formed Mannich reagents.[180,181]

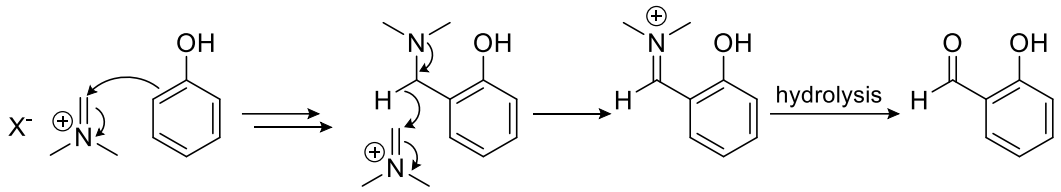

Figure 5.14. Putative mechanism for formylation using *N*,*N*-dimethyliminium ions.

In order to avoid substitution at the phenolic position, as encountered in the Vilsmeier reaction above, we chose to use trifluoroacetate as counterion (X^-), since it is a very weak nucleophile. Following the scheme shown in Figure 5.15, we prepared *N*,*N*-dimethylmethaniminium trifluoroacetate **5.5**.[180,182,183]

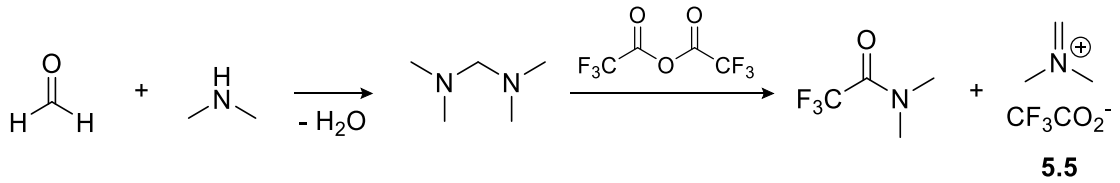

Figure 5.15. Preparation of *N*,*N*-dimethylmethaniminium trifluoroacetate.

Reacting **5.5** (10 eq.) with phloroglucinol gave the desired triformyl product **5.1**, albeit in very low yield. Based on the disappearance of the phloroglucinol CH signals in the ^{1}H spectrum of the reaction mixture, we suspect that the low yield is owing to slow oxidation of the Mannich adduct formed in the first step of the reaction, Figure 5.16.

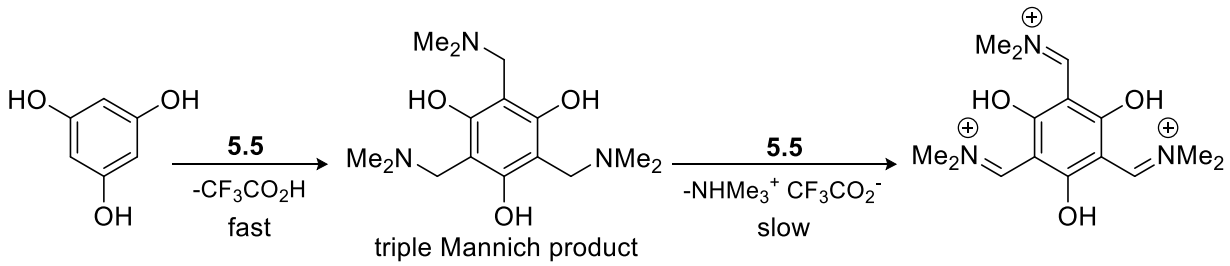

Figure 5.16. Hypothetical course of reaction between phloroglucinol and **5.5**.

5.4 Formylation by Fries Rearrangement of Aryl Formates

The Fries rearrangement has been used to preparare of many acyl phenols from the corresponding esters, *e.g.* 2,4,6-triacetylphloroglucinol from phloroglucinol triacetate, Figure 5.17a.[184] There is also a small body of work on the Fries rearrangement of aromatic formyl esters, Figure 5.17b,[185] begging the question of whether or not Fries rearrangement of aromatic formates can act as a general route to salicylaldehydes like **5.1**–**5.3**.

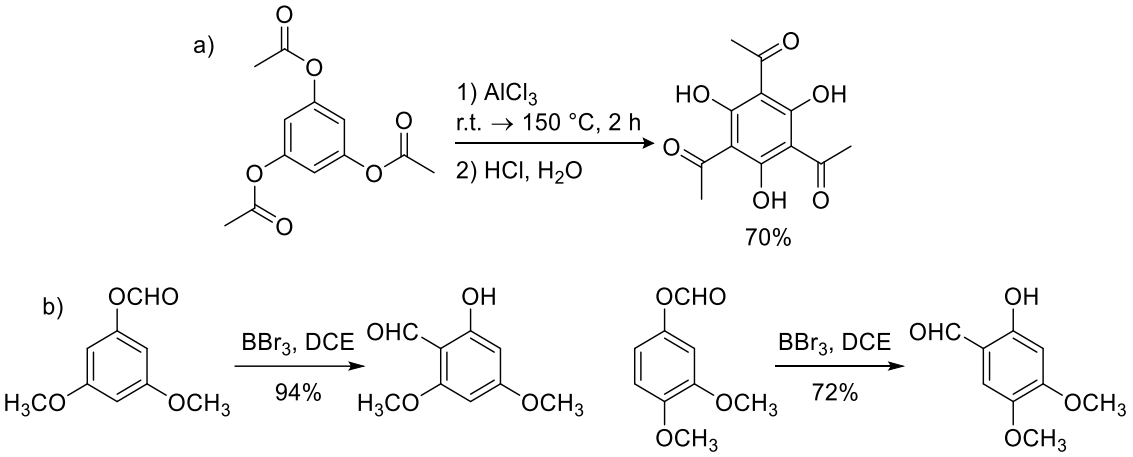

Figure 5.17. Conversion of phloroglucinol triacetate to 2,4,6-triacetylphloroglucinol under Fries conditions (a). Examples of aromatic formylation by Fries rearrangement of formate esters (b).

The aromatic formates used in the above reaction can be prepared through the base-promoted reaction of phenols with formyl acetate, a stable formic anhydride substitute, which can in turn be obtained through the reaction of sodium formate and acetyl chloride, Figure 5.18a (or from the reaction of formic acid with ketene[186]). This gives a straightforward route to formate esters of our phenolic substrates, *e.g.* phloroglucinol triformate (Figure 5.18b).

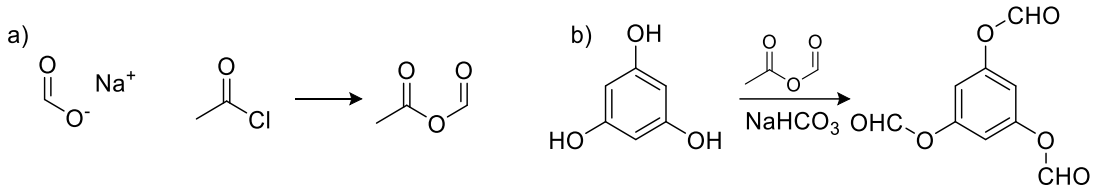

Figure 5.18. Laboratory preparation of formyl acetate (a). Synthesis of phloroglucinol triformate from phloroglucinol and formyl acetate (b).

Unfortunately, attempts at BBr_3-catalyzed rearrangement of phloroglucinol triformate to **5.1** were unsuccessful.

5.5 Criteria for Efficient Formylation of Activated Aromatic Substrates

At this point it is appropriate to relate some of the insight gained as a result of our unsuccessful attempts described above. First and foremost, the excellent reactivity of aldehydes towards nucleophiles must be carefully considered in order to avoid side reactions. For instance, if a hypothetical set of conditions is imagined that can bring about the *para*-formylation of phenol, one can anticipate that a cascade of condensation reactions can lead to oligomeric products in the presence of acid, Figure 5.19. A similar cascade can be envisioned in strongly basic media.

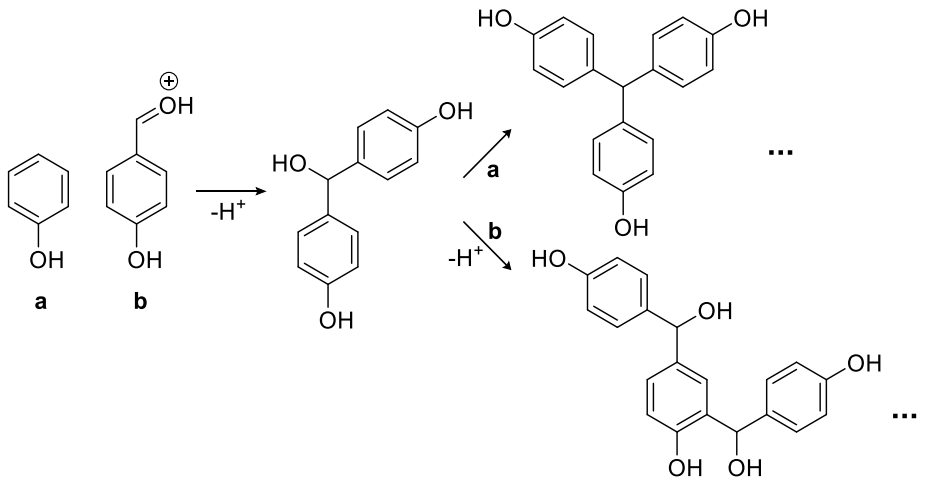

Figure 5.19. Example pathway of side-product formation starting with substrate (**a**) attack on protonated aldehyde product **b** in acidic medium.

This type of undesirable side reaction is especially likely given the unhindered nature of aromatic aldehydes. Therefore, a key criterion for a successful formylation — and one that is not as relevant with acylations — is that the conditions employed should not encourage nucleophilic attack by neighbouring substrate molecules on intermediate or product molecules.

A further criterion is that of avoiding the deactivating effect of –C=X (X = O, NR_2) substituents in intermediates, like one would encounter in the Vilsmeier–Haack reaction. The rationale is to allow multiple formyl groups to be added under similar conditions (*e.g.*, harsher conditions would not be required for triformylation versus diformylation). This has the additional benefit of preventing nucleophilic substitution reactions caused by ring deactivation.

5.6 Formamidine Acetate: A Mild and Effective Formylating Agent for Phenols

During our search for alternative methods of formylation, we happened upon a 1983 patent by Petersen for formylation of anilines using formamidine acetate and acetic anhydride.[187] According to the patent, the product of the reaction is a bis(N-acetamido) species, which is hydrolyzed to give the aldehyde product, Figure 5.20.

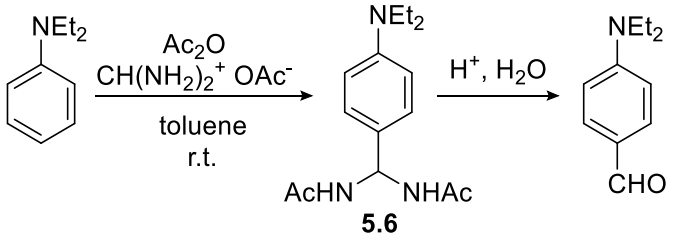

Figure 5.20. Formylation of diethylaniline with formamidine acetate and acetic anhydride.

In this case, intermediate **5.6** is described as a stable fluffy solid that melts at 220–222 °C, isolated thanks to the use of non-polar solvent (toluene in this case). Petersen identifies the ideal

conditions for the formylation reactions of this type as 25–40 °C in non-polar solvents (toluene, xylene, chlorobenzene), since these conditions allow the bis(N-acetamido) intermediates like **5.6** to precipitate, protecting it against any side reactions. Indeed, polar aprotic solvents like DMF, were found to allow **5.6** to react with aniline starting material, which is not desirable.

Formamidine acetate itself is commercially available (~$30/100 g) and can be readily prepared from triethyl orthoformate, acetic acid, and ammonia, Figure 5.21.[188,189] From a mechanistic point of view, formamidine acetate is uniquely suited to multiple formylations of electron rich aromatic systems. Due to the absence of resonance contributors that withdraw electron density from the ring, phenolic analogues of intermediate **5.6** would not experience significant deactivation. Furthermore, unlike the Duff and Sommelet methods,[72*] subsequent redox reactions are not necessary — intermediate **5.6** is simply converted to the desired aldehyde product by hydrolysis.

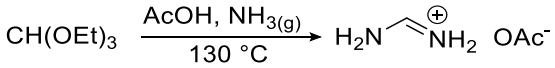

Figure 5.21. Laboratory preparation of formamidine acetate from ethyl orthoformate.

5.7 Optimization of Reaction Conditions

To adapt the methodology described above to phenols, we set out to optimize the reaction conditions for triple formylation of phloroglucinol. Phloroglucinol was chosen because its triformyl derivative (TFP, **5.1**) is useful, yet difficult to prepare in good yield. In addition, TFP is stable and simple to characterize, and has poor solubility in many common solvents, simplifying its isolation during work up.

[*] The Sommelet reaction is an older analogue of the Duff reaction that relies on the reaction between a benzyl halide and HMTA to form the initial benzylamine species.

The progress of the reaction can be monitored by the disappearance of the phloroglucinol CH protons. Initial attempts in refluxing toluene, chloroform, and dichloroethane were hampered by the poor solubility of formamidine acetate in these solvents and its tendency to form an insoluble sticky solid during the early stages of the reaction. Subsequent acidic workup did yield the desired TFP product, albeit in very poor yield. Better results were obtained in THF, in which formamidine acetate is much more soluble. Thus, when phloroglucinol is stirred overnight in THF at 45 °C with 5 equiv formamidine acetate and 10 equiv acetic anhydride, a light rose coloured homogenous, but cloudy, solution forms. THF and leftover acetic acid/anhydride can be evaporated under reduced pressure, leaving the triple bis(N-acetamido)methyl intermediate **5.7**, Figure 5.22.

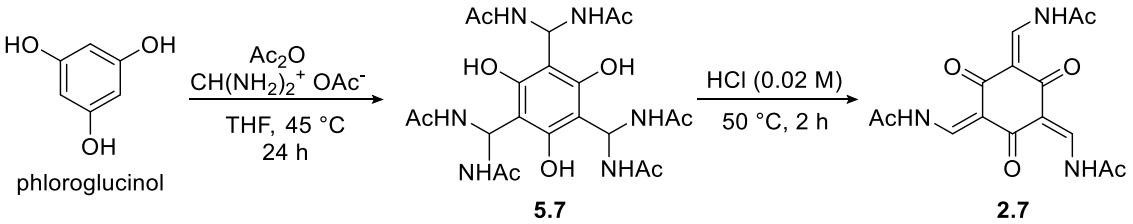

Figure 5.22. Formylation of phloroglucinol with formamidine acetate and acetic anhydride.

Intermediate **5.7** is readily hydrolyzed to keto-enamine **2.7**, which was isolated as a light salmon-coloured powder. The stability and keto-enamine structure of **2.7** was explored in Chapter 2, where it serves as an important example of surprising tautomeric behaviour in TSANs.

A cursory look at the structure of **2.7** might suggest that its hydrolysis to aldehyde product **5.1** would occur readily. In practice, this step is complicated by the counterintuitive reactivity of this TSAN. Instead of giving TFP as expected, stirring **2.7** in HCl (2 M, 90 °C, 30 min) led to the formation of a light yellow powder that is insoluble in common organic solvents, Figure 5.23. In retrospect, it is easy to recognize the product as the ammonia Schiff base of TFP, **2.1** (the symmetric form, specifically), which we know from Chapter 2 to strongly aggregate through

hydrogen-bonding. This smallest member of the TSAN family is surprisingly stable toward acidic hydrolysis and can survives boiling 9 M H_2SO_4.

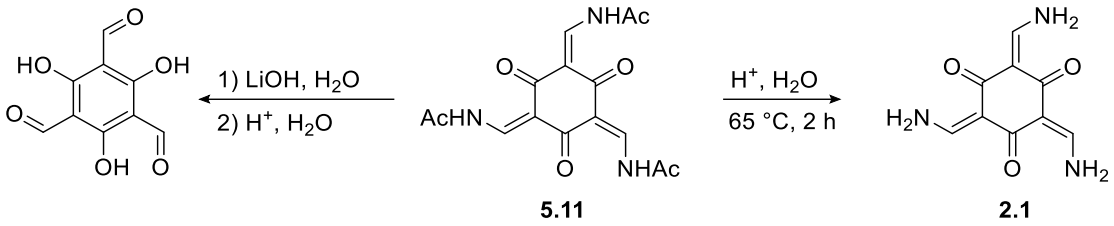

Figure 5.23. Hydrolysis of **5.11** under acidic and basic conditions.

Eventually, we were able to bring about the desired hydrolysis reaction by treating **5.11** with dilute LiOH solution. Reacidification then causes pure TFP to precipitate as an off-white powder in 50% yield. We find this one-pot protocol more convenient and the result more consistent than with the current best route to TFP (published by us in 2016),[190] where phloroglucinol is diformylated using the Vilsmeier–Haack reaction before installing the third formyl group using the Duff reaction, Figure 5.24.

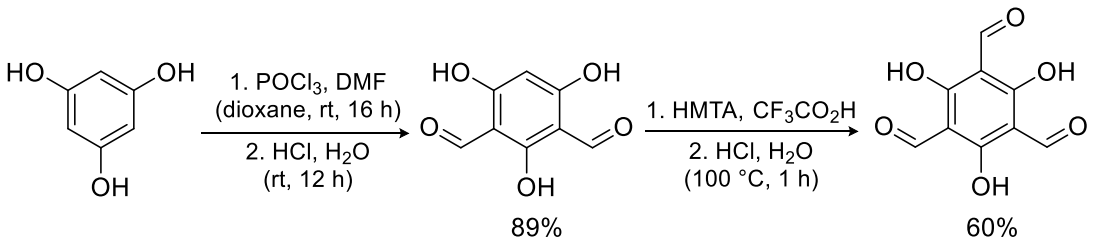

Figure 5.24. Two-step state-of-the-art preparation of TFP (**5.1**).

5.7.1 Extension to Other Phenolic Substrates

Once the ideal conditions for formylation of phloroglucinol had been found, it was fairly straightforward to adapt the procedure to a variety of other phenolic substrates. Figure 5.25 shows the range of substrates used in our study. Our search was driven by the desire to find substrates for which no convenient method of multiple formylation existed in the literature. Based on this

criterion, we found that by adjusting solvent, reaction temperature, and reaction time, compounds **5.8**–**5.12** could be prepared easily and in good yield.

With three hydroxyl groups all positioned to direct electrophilic attack to the three equivalent positions, phloroglucinol was the most reactive formylation substrate used in our studies. Other substrates, having lower reactivity, required temperatures above the normal boiling point of THF for formylation. In some instances, the reaction could still be carried out in THF but slightly above atmospheric pressure, in which case a glass bomb was used. Some substrates were only fully formylated at temperatures above 90 ºC. In the interest of safety, we used 1,4-dioxane (b.p. = 101 ºC) as solvent for these reactions, although it is not hard to imagine using THF under 2–3 atm pressure in a proper reactor.

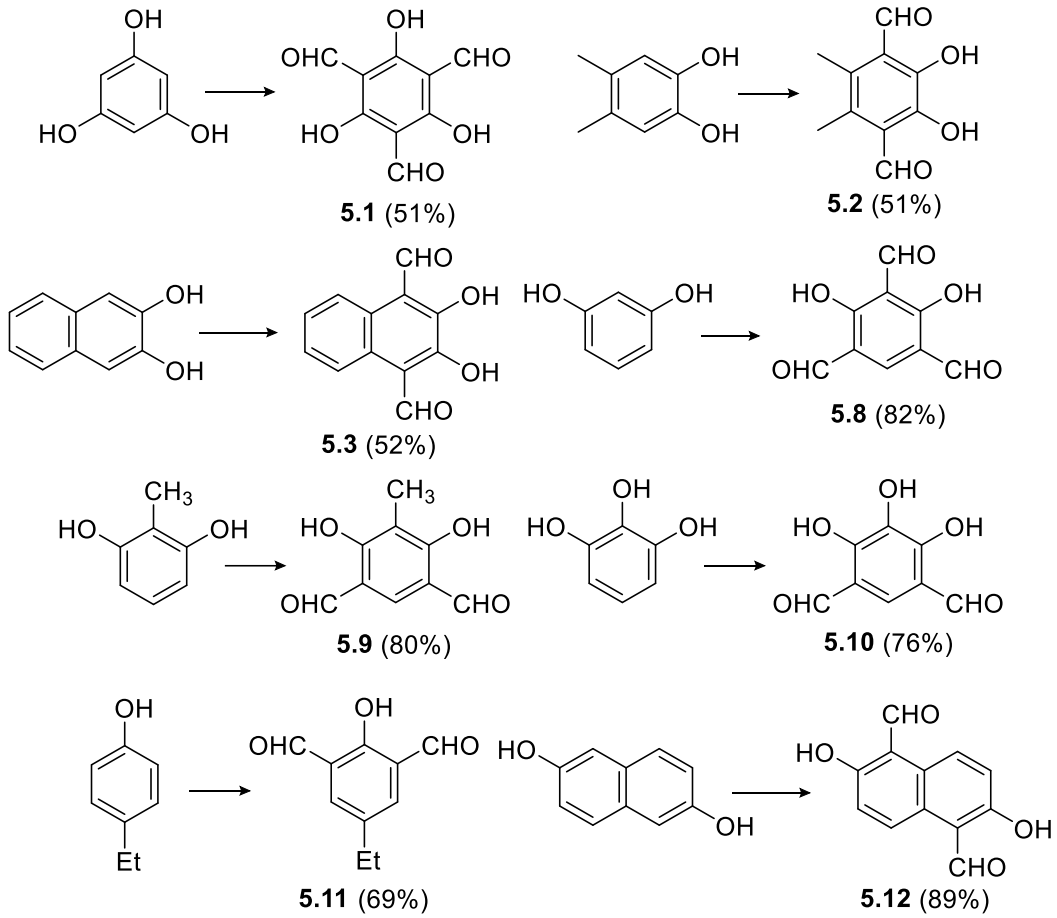

Figure 5.25. Formylation of various phenolic substrates using formamidine acetate and acetic anhydride.

In terms of regioselectivity, we found that only positions ortho to hydroxyl groups were formylated. This type of selectivity for the ortho position is not unprecedented. For instance, Skattebøl formylation of phenols is also known to yield salicylaldehydes exclusively, as explained by the mechanism in Figure 5.26.[173–175]

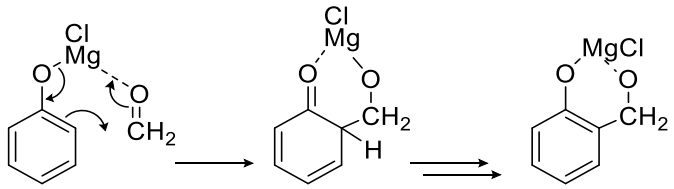

Figure 5.26. Part of the mechanism for the Skattebøl reaction showing the *ortho*-directing effect of magnesium chloride.

One last obstacle encountered when using 1,4-dioxane as solvent was the formation of a thick gel when the reactants were brought together, which slowed down the reaction dramatically. A simple workaround is to allow formamidine acetate to fully dissolve in hot dioxane before introducing the acetic anhydride and substrate.

Table 5.1 summarizes the optimized conditions found for formylation of a number of substrates. These molecules were chosen on the basis of their difficult formylation using existing methods and the potential utility of the product salicylaldehydes. For instance, compound **5.2**, a valuable precursor to self-assembled Schiff base macrocycles, was only accessible through a lengthy synthesis comprising five reactions, Figure 5.27.[191] Similarly, compound **5.3**, which has been used in the preparation of a [3 + 3] Schiff base macrocycles with a unique keto-enamine interior, was previously prepared through a similar five-step processes.[50] Glaser and coworkers have published a protocol for the synthesis of compound **5.12** based on metalation;[192] the authors note, however that other synthesis techniques (Duff, Vilsmeier, hydroxymethylation, etc.) were ineffective.

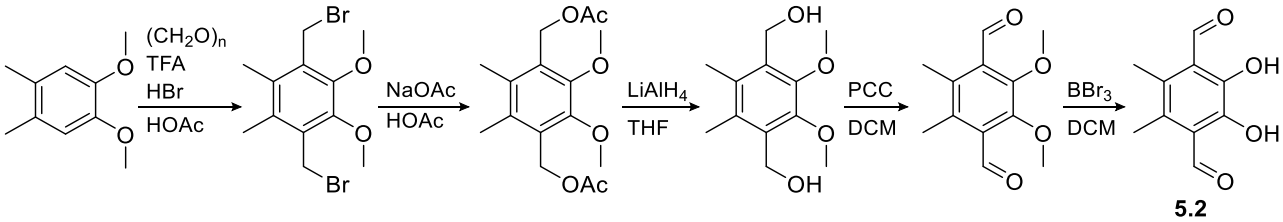

Figure 5.27. State-of-the-art preparation of compound **5.15**.

Table 5.1. Conditions used for the formylations in Figure 5.25.

Product	F.A.[a] equiv.	Ac_2O equiv.	Solvent	Temperature	Duration	Yield (%)
5.1	5	10	THF	45 °C	24 h	51
5.2	5	10	Dioxane[b]	95 °C	72 h	51
5.3	8	16	Dioxane[b]	95 °C	48 h	52
5.8	4	8	THF	85 °C[c]	24 h	82
5.9[d]	4	8	THF	55 °C	24 h	80
5.10	4	8	Dioxane[b]	95 °C	48 h	76
5.11	8	16	Dioxane[b]	100 °C	48 h	69
5.12	8	16	Dioxane[b]	95 °C	48 h	89

[a] Formamidine acetate [b] 1,4-dioxane [c] Reaction carried out above boiling point of solvent in a bomb. [d] Yield of **5.9** using the Duff procedure is 44%.[178]

5.8 Conclusions and Future Work

Formylation reactions using formamidine acetate and acetic anhydride provide an efficient route to salicylaldehydes using inexpensive reagents and reaction conditions that are far milder than those of other known routes. Since the adoption of these salicylaldehydes has been contingent on convenient methods of synthesis (as in the case of TFP), we expect researchers to tap into the unexplored properties of these less-known aromatic aldehydes as well.

One approach that was not explored much in this chapter is formylation using formyl acetate in the presence of a Lewis acid of moderate strength, such as Zn^{2+}. As Figure 5.3 demonstrates, zinc catalysis is highly effective for acetylation of these compounds. Given the lower steric requirements of the formyl versus acetyl group, we expect that Lewis acid activation of formyl acetate would lead to rapid formylation of our electron-rich substrates. Needless to say,

temperature and the nature of the Lewis acid used are critical factors to consider, since high temperatures and strong Lewis acids can cause the anhydride to decompose with the release of carbon monoxide, Figure 5.28a.

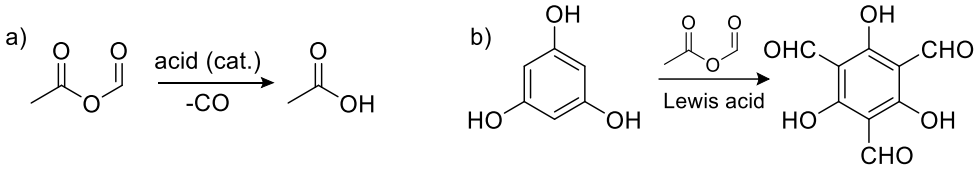

Figure 5.28. (a) Acid decomposition of formyl acetate to carbon monoxide and acetic acid. (b) Example formylation reaction using formyl acetate and Lewis acid catalyst.

One advantage of this approach is the substantially simpler workup step. Unlike formamidine acetate formylations, the aldehyde is formed directly without an extra hydrolysis steps, Figure 5.28b. Formyl acetate can be prepared very inexpensively, as described in Section 5.4.

Naturally, this method has the downside of adding the formyl group directly and, consequently, deactivating the substrate at each formylation step. It remains to be seen whether this deactivation is severe enough to prevent triple formylation of compounds like phloroglucinol and resorcinol, but we anticipate it to be milder than that seen in the Vilsmeier iminium intermediates.

Another natural avenue for improvement comes from examining the mechanism of the Duff reaction which, as pointed out in Section 5.2.3, consists of distinct addition and redox (hydride transfer) steps.[177] This reaction is low-yielding in the case of phloroglucinol, but the product, recovered by extraction into DCM, is surprisingly pure. This leads to the hypothesis that the remaining aqueous by-products are the result of inefficient hydride transfer from aminomethyl intermediates like those shown in Figure 5.29. Unlike the final imine product **5.13**, these intermediates stay in the acidic aqueous layer during workup and does not show up in the final product.

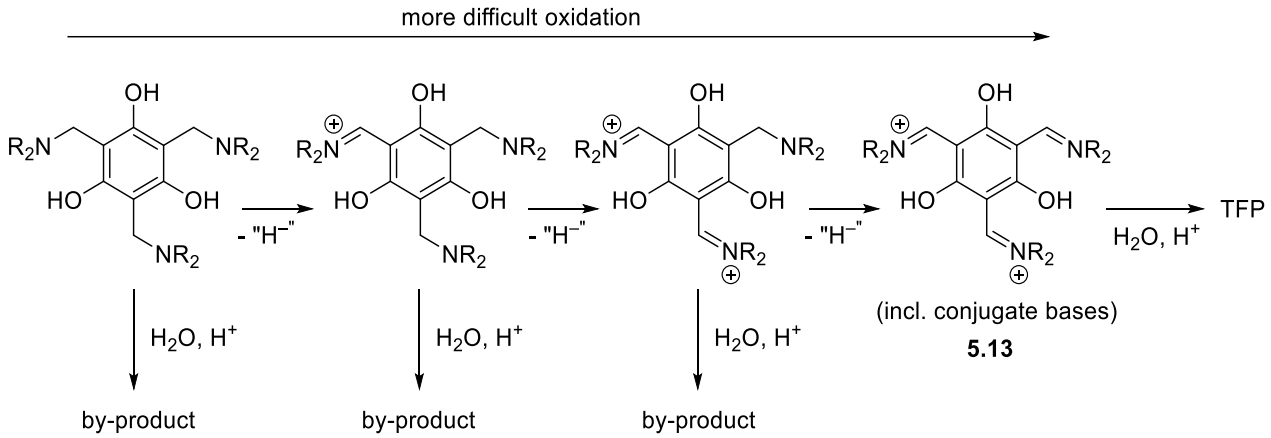

Figure 5.29. Successive oxidation of the tris(aminomethyl) intermediate.

Naturally, facilitating the oxidation of these aminomethyl intermediates should improve yields of the aldehyde product. This must be done with caution since, as stated before, the desired **5.13** is the triple conjugate acid of a compound similar to the fragile heteroradialene compound in Chapter 4 (**4.3**), which we know is fairly prone to oxidation. One promising oxidant in this regard is paraformaldehyde, which has already been shown to accelerate the Duff reaction when used alongside HMTA.[193,194]

5.9 Experimental

5.9.1 General

Formamidine acetate (F.A. in reaction schemes) was prepared from triethyl orthoformate using the literature procedure.[188] Unless otherwise stated, all NMR experiments were carried out on a 400 MHz Bruker Avance spectrometer equipped with a SmartProbe™. Power-gated ^{1}H-decoupled and driven-equilibrium adiabatic UDEFT[140] pulse sequences were used for acquisition of ^{13}C spectra.

5.9.2 Procedures and Characterization Data

Preparation of triformylphloroglucinol (2,4,6-trihydroxybenzene-1,3,5-tricarbaldehyde, 5.1)

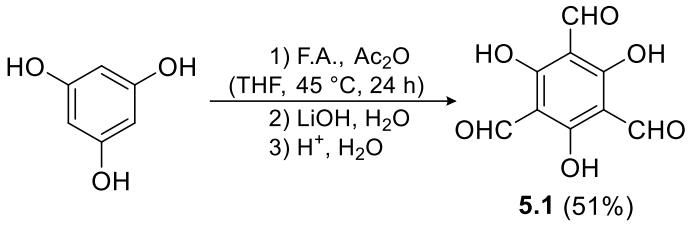

5.1 (51%)

Formamidine acetate (8.25 g, 79.4 mmol, 5.0 equiv) and phloroglucinol (2.00 g, 15.9 mmol, 1.0 equiv) were combined in THF (200 mL) at 45 °C, in a round-bottom flask. After stirring for 15 min, acetic anhydride (14.7 mL, 159 mmol, 10.0 equiv) was added, the flask was subsequently capped and the reaction allowed to proceed for 1 d. The reaction was worked up by evaporating THF solvent and leftover acetic anhydride and acetic acid under reduced pressure at 50 °C, followed by stirring in water (200 mL) at 40 °C for 2 h. Aqueous LiOH (2 M, 600.0 mL, 1200 mmol, 75.6 eq) was added slowly, then stirring continued for 18 h. Aqueous hydrochloric acid (2 M, 300 mL, 600 mmol, 37.8 equiv) was added next to re-acidify the solution, causing a very pale salmon-coloured powder to precipitate. The product was extracted into dichloromethane (4 × 60 mL), which was dried over Na_2SO_4 and evaporated to give pure **5.1** as an off-white powder (1.71 g, 8.14 mmol, 51%).

^{1}H NMR (400 MHz, DMSO-*d*$_6$) δ 9.36 (s, 3H; CHO), 5.39 ppm (s, 3H; OH). ^{13}C {^{1}H} NMR (100 MHz, DMSO-*d*$_6$) δ 191.4 (CHO), 173.3 (COH), 103.2 ppm (*C*CHO). UV-Vis (CH_2Cl_2) λ_{max} (ε) = 264 (5.3×10^4), 289 (2.6×10^4) nm ($cm^{-1}\,mol^{-1}\,L$). IR (neat) *ν* = 2888 (br), 1635, 1585, 1427, 1389, 1246, 1189, 1104, 964, 868, 806, 781, 602, 543 cm^{-1}. HRMS (ESI/TOF-Q) *m/z*: [**5.1** - H]$^-$ Calcd for $C_9H_5O_6$ 209.0086; Found 209.0080.

Preparation of 2,3-dihydroxy-5,6-dimethylterephthalaldehyde (5.2)

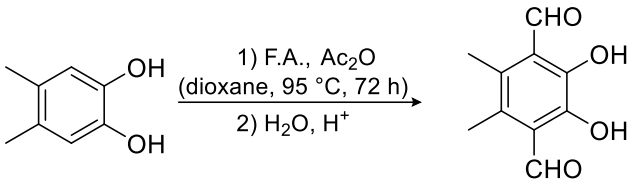

5.2 (51%)

Formamidine acetate (2.81 g, 27.0 mmol, 5.0 equiv) and acetic anhydride (5.1 mL, 54 mmol, 10 equiv) were stirred in dioxane (150 mL) at 95 °C in a round-bottom flask. Once the formamidine acetate was fully dissolved (typically after 30 min), 4,5-dimethylcatechol (745 mg, 5.40 mmol, 1.0 equiv) was added in one portion. The flask was subsequently capped and the reaction allowed to proceed for 3 d. The reaction was worked up by evaporating dioxane solvent and leftover acetic anhydride and acetic acid under reduced pressure at 50 °C followed by stirring in water (80 mL) at 60 °C for 2 h. Aqueous hydrochloric acid (1 M, 80 mL, 80 mmol, 14.9 equiv) was added next and stirring continued for 18 h. The product was extracted into dichloromethane (5 × 20 mL), which was dried over Na_2SO_4 and evaporated to give the crude product as a brown solid. Crude product was purified by column chromatography using diethyl ether:hexanes (20:80) as eluent. Evaporation of the second fraction (R_f = 0.2) gave pure **5.2** as orange powder (533 mg, 2.75 mmol, 51%).

^{1}H NMR (400 MHz, $CDCl_3$) δ 11.91 (s, 2H; OH), 10.48 (s, 2H; CHO), 2.51 ppm (s, 6H; CH_3). ^{13}C {^{1}H} NMR (100 MHz, $CDCl_3$) δ 196.9 (CHO), 151.1 (COH), 128.1 (*C*CHO), 121.9 (*C*CH_3), 13.5 ppm (CH_3). UV-Vis (CH_2Cl_2) λ_{max} (ε) = 218 (1.9×10^4), 295 (1.9×10^4), 424 (3.2×10^3) nm (cm^{-1} mol^{-1} L). IR (neat) ν = 3045, 2924 (br), 1641, 1611, 1556, 1487, 1439, 1380, 1316, 1275, 1244, 1099, 1028, 924, 743, 706, 664, 596, 516 cm^{-1}. HRMS (ESI/TOF-Q) *m/z*: [**5.2** - H]$^-$ Calcd for $C_{10}H_9O_4$ 193.0501; Found 193.0493.

Preparation of 2,3-dihydroxynaphthalene-1,4-dicarbaldehyde (5.3)

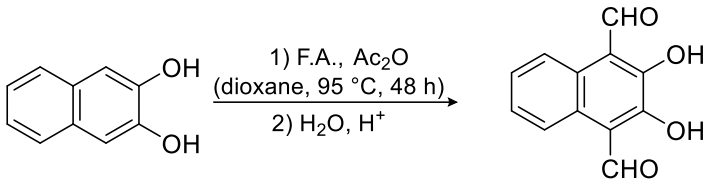

5.3 (52%)

Formamidine acetate (520 mg, 5.00 mmol, 8.0 equiv) and acetic anhydride (0.95 mL, 10 mmol, 16.0 equiv) were stirred in dioxane (15 mL) at 95 °C in a round-bottom flask. Once the formamidine acetate was fully dissolved (typically after 30 min), 2,3-naphthalenediol (100 mg, 0.625 mmol, 1.0 equiv) was added in one portion. The flask was subsequently capped and the reaction allowed to proceed for 2 d. The reaction was worked up by evaporating dioxane solvent and leftover acetic anhydride and acetic acid under reduced pressure at 50 °C, followed by stirring in water (15 mL) at 60 °C for 2 h. Aqueous hydrochloric acid (1 M, 15 mL, 15 mmol, 24 equiv) was added next and stirring continued for 18 h. During the hydrolysis step the product precipitated as yellow-brownish powder and was isolated by filtration and washing with hexanes. Crude **5.3** was purified by column chromatography using dichloromethane as eluent. Evaporation of the first fraction (R_f = 0.25) gave pure product as a yellow powder (70 mg, 0.32 mmol, 52%).

^{1}H NMR (400 MHz, $CDCl_3$) δ 13.00 (s, 2H; OH), 10.92 (s, 2H; CHO), 8.40 (dd, $^3J_{HH}$=6.38 Hz, $^4J_{HH}$=3.08 Hz, 2H; Ar), 7.62 (dd, $^3J_{HH}$=6.38 Hz, $^4J_{HH}$=3.08 Hz, 2H; Ar) ppm. ^{13}C {^{1}H} NMR (100 MHz, DMSO-d_6) δ 194.2 (CHO), 154.3 (COH), 126.8 (Ar), 126.3 (Ar), 122.3 (Ar), 117.0 (*C*CHO) ppm. UV-Vis (CH_2Cl_2) λ_{max} (ε) = 225 (5.2×10^4), 372 (1.1×10^4) nm ($cm^{-1}\,mol^{-1}\,L$). IR (neat) ν = 3152, 2919 (br), 1672, 1635, 1608, 1549, 1520, 1450, 1402, 1373, 1304, 1258, 1240, 1213, 1120, 1050, 1001, 965, 916, 853, 798, 738, 698, 663, 597, 568, 505 cm^{-1}. HRMS (ESI/TOF-Q) *m/z*: [**5.3** - H]$^-$ Calcd for $C_{12}H_7O_4$ 215.0344; Found 215.0353.

Preparation of 2,4-dihydroxybenzene-1,3,5-tricarbaldehyde (5.8)

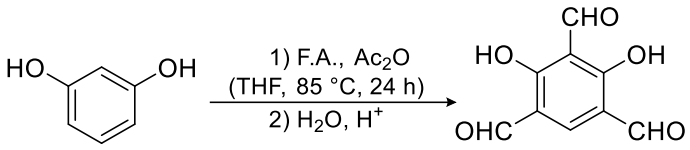

5.8 (82%)

Formamidine acetate (374 mg, 3.63 mmol, 4.0 equiv), acetic anhydride (0.72 mL, 7.3 mmol, 8.0 equiv) and resorcinol (100 mg, 0.909 mmol, 1.0 equiv) were combined in THF (15 mL) in an autoclave. The reaction was heated to 85 °C and allowed to proceed for 1 d.

The reaction was worked up by evaporating THF solvent and leftover acetic anhydride and acetic acid under reduced pressure at 50 °C, followed by stirring in a solution of ethanol (2 mL) in water (5 mL) at r.t. for 2 h. Aqueous hydrochloric acid (1 M, 10 mL, 10 mmol, 11.0 equiv) was added next and stirring continued for 18 h.

During the hydrolysis step the product precipitated as a salmon-coloured powder and was isolated by filtration and washing with water. This step gave pure **5.8** as a salmon-coloured powder (144 mg, 0.742 mmol, 82%).

^{1}H NMR (400 MHz, DMSO-d_6) δ 10.24 (s, 1H; CHO), 10.09 (s, 2H; CHO), 8.37 ppm (s, 1H; Ar). ^{13}C {^{1}H} NMR (100 MHz, DMSO-d_6) δ 193.9 (CHO), 190.0 (CHO), 170.0 (COH), 140.6 (CH), 115.8 (*C*CHO), 110.0 ppm (*C*CHO). UV-Vis (CH_2Cl_2) λ_{max} (ε) = 248 (4.6×10^4), 344 (7.5×10^3) nm (cm^{-1} mol^{-1} L). IR (neat) *v* = 1640, 1591, 1436, 1366, 1322, 1273, 1247, 1218, 1147, 987, 864, 938, 805, 775, 748, 602 cm^{-1}. HRMS (ESI/TOF-Q) *m/z*: [**5.8** - H]$^-$ Calcd for $C_9H_5O_5$ 193.0137; Found 193.0128.

Preparation of 4,6-dihydroxy-5-methylisophthalaldehyde (5.9)

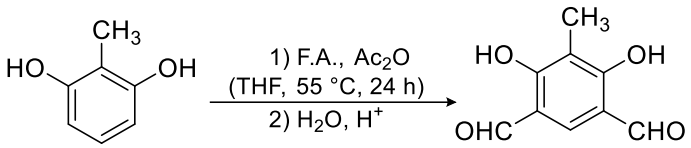

5.9 (80%)

Formamidine acetate (335 mg, 3.23 mmol, 4.0 equiv) and 2-methylresorcinol (100 mg, 0.806 mmol, 1.0 equiv) were combined in THF (15 mL) at 55 °C in a round-bottom flask. After 10 min, acetic anhydride (0.61 mL, 6.45 mmol, 8.0 equiv) was added, the flask was capped and the reaction was allowed to proceed for 1 d at 55 °C. Worked up involved evaporating THF solvent and leftover acetic anhydride and acetic acid under reduced pressure at 50 °C, followed by stirring in water (10 mL) at r.t. for 2 h. Aqueous hydrochloric acid (1 M, 10 mL, 10 mmol, 12.4 equiv) was added next and stirring continued for 18 h. During the hydrolysis step the product precipitated as salmon coloured powder and was isolated by filtration and washing with water first and then with hexanes. This step gave pure **5.9** as a salmon-coloured powder (116 mg, 0.644 mmol, 80%).

^{1}H NMR (400 MHz, DMSO-d_6) δ 11.94 (s, 2H; OH), 9.94 (s, 2H; CHO), 8.20 (s, 1H; Ar), 2.05 ppm (s, 3H; CH_3). ^{13}C {^{1}H} NMR (100 MHz, DMSO-d_6) δ 195.1 (CHO), 164.8 (COH), 139.3 (CH), 115.3 (*C*CHO), 111.7 (*C*CH_3), 6.9 ppm (CH_3). UV-Vis (CH_2Cl_2) λ_{max} (ε) = 207 (1.3×10^4), 259 (4.9×10^4) nm ($cm^{-1}\,mol^{-1}\,L$). IR (neat) ν = 3038, 2931, 2865, 1633, 1607, 1508, 1468, 1446, 1375, 1337, 1303, 1223, 1007, 905, 891, 864, 775, 764, 724, 646, 532, 510 cm^{-1}. HRMS (ESI/TOF-Q) *m/z*: [**5.9** - H]$^-$ Calcd for $C_9H_7O_4$ 179.0344; Found 179.0342.

Preparation of 4,5,6-trihydroxyisophthalaldehyde (5.10)

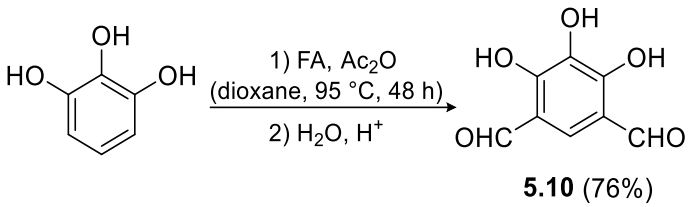

5.10 (76%)

Formamidine acetate (330 mg, 3.17 mmol, 4.0 equiv) and acetic anhydride (0.59 mL, 6.3 mmol, 16.0 equiv) were stirred in dioxane (15 mL) at 95 °C, in a round-bottom flask. Once the formamidine acetate was fully dissolved (typically after 30 min), pyrogallol (100 mg, 0.79 mmol, 1.0 equiv) was added in one portion. The flask was subsequently capped and the reaction allowed to proceed for 2 d. The reaction was worked up by evaporating dioxane solvent and leftover acetic anhydride and acetic acid under reduced pressure at 50 °C, followed by stirring in water (20 mL) at 40 °C for 2 h. Aqueous hydrochloric acid (0.5 M, 10 mL, 5 mmol, 6.3 equiv) was added next and stirring continued for 18 h. The product was extracted into dichloromethane (5 × 5 mL) and the combined extractions dried over Na_2SO_4 to give a light orange solid upon evaporation. This solid was stirred in MeOH (with one drop of trifluoroacetic acid added) at 60 °C for 18 h. The salmon-coloured residue left after solvent evaporation was washed with 1 mL $CHCl_3$, leaving pure **5.10** (109 mg, 0.600 mmol, 76%).

^{1}H NMR (400 MHz, DMSO-d_6) δ 11.20 (br s, 2H; OH), 10.02 (s, 2H; CHO), 7.75 ppm (s, 1H; Ar).^{13}C {^{1}H} NMR (100 MHz, DMSO-d_6) δ 192.3 (CHO), 155.2 (COH), 132.5 (COH), 126.9 (CH), 116.3 (*C*CHO) ppm. UV-Vis (MeOH) λ_{max} (ε) = 267 (6.1×10^4), 203 (1.7×10^4) nm (cm^{-1} mol^{-1} L). IR (neat) ν = 3254 (br), 2859, 1639, 1620, 1488, 1456, 1380, 1239, 1197, 1144, 1061, 915, 885, 916, 885, 794, 777, 737, 663, 643, 543, 512 cm^{-1}. HRMS (ESI/TOF-Q) *m/z*: [**5.10** - H]$^-$ Calcd for $C_8H_5O_5$ 181.0137; Found 181.0138.

Preparation of 5-ethyl-2-hydroxyisophthalaldehyde (5.11)

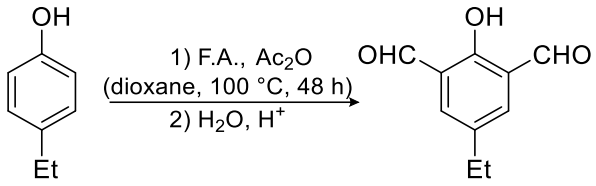

5.11 (69%)

Formamidine acetate (681 mg, 6.56 mmol, 8.0 equiv) and acetic anhydride (1.23 mL, 13.1 mmol, 16.0 equiv) were stirred in dioxane (15 mL) at 100 °C, in a round-bottom flask. Once the formamidine acetate was fully dissolved (typically after 30 min), 4-ethylphenol (100 mg, 0.820 mmol, 1.0 equiv) was added in one portion. The flask was subsequently capped and the reaction allowed to proceed for 2 d. The reaction was worked up by evaporating dioxane solvent and leftover acetic anhydride and acetic acid under reduced pressure at 50 °C, followed by stirring in water (15 mL) at 60 °C for 2 h. Aqueous hydrochloric acid (1 M, 15 mL, 15 mmol, 18.3 equiv) was added next and stirring continued for 18 h. The product was extracted into dichloromethane (5 × 5 mL), which was dried over Na_2SO_4 and evaporated to give **5.11** as a yellow oil. Crude **5.11** was purified by column chromatography using CH_2Cl_2 (100%) as eluent. Evaporation of the second fraction (R_f = 0.6) gave pure product of **5.11** as yellow crystals (100 mg, 0.562 mmol, 69%).

^{1}H NMR (400 MHz, $CDCl_3$) δ 11.47 (s, 1H; OH), 10.23 (s, 2H; CHO), 7.80 (s, 2H; Ar), 2.68 (q, $^3J_{HH}$ = 7.70 Hz, 2H; CH_2), 1.27 ppm (t, $^3J_{HH}$ = 7.70 Hz, 3H, CH_3). ^{13}C {^{1}H} NMR (100 MHz, CD_3CN) δ 193.9 (CO), 162.4 (COH), 138.0 (CH), 137.2 (*C*CH_2), 124.0 (*C*CHO), 28.1 (CH_2), 15.8 ppm (CH_3). UV-Vis (CH_2Cl_2) λ_{max} (ε) = 206 (3.7×10^4), 236 (5.8×10^4), 354 (1.36×10^4) nm (cm^{-1} mol^{-1} L). IR (neat) *v* = 3138 (br), 2965, 2930, 2872, 2776, 1660, 1596, 1455, 1443, 1402, 1377, 1325, 1296, 1267, 1200, 1065, 1002, 971, 938, 927, 907, 789, 742, 649, 630, 609, 541, 486 cm^{-1}.

HRMS (ESI/TOF-Q) *m/z*: [**5.11** - H]$^-$ Calcd for $C_{10}H_9O_3$ 177.0552; Found 177.0555.

Preparation of 2,6-dihydroxynaphthalene-1,5-dicarbaldehyde (5.12)

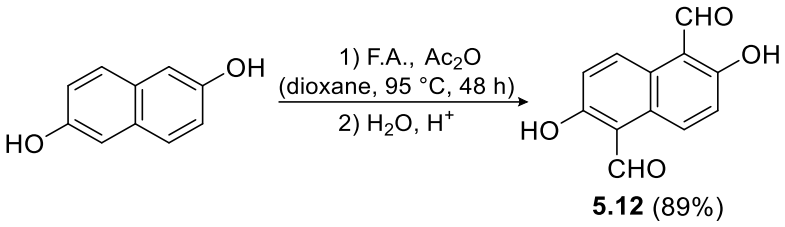

5.12 (89%)

Formamidine acetate (520 mg, 5.00 mmol, 8.0 equiv) and acetic anhydride (0.95 mL, 10 mmol, 16.0 equiv) were stirred in dioxane (15 mL) at 95 °C, in a round-bottom flask. Once the formamidine acetate was fully dissolved (typically after 30 min), 2,6-naphthalenediol (100 mg, 0.625 mmol, 1.0 equiv) was added in one portion. The flask was subsequently capped and the reaction allowed to proceed for 2 d. The reaction was worked up by evaporating dioxane solvent and leftover acetic anhydride and acetic acid under reduced pressure at 50 °C, followed by stirring in water (15 mL) at 60 °C for 2 h. Aqueous hydrochloric acid (1 M, 15 mL, 15 mmol, 24 equiv) was added next and stirring continued for 18 h. The product was extracted into dichloromethane (5 × 5 mL), which was dried over Na_2SO_4 and evaporated to give **5.12** as orange-brownish solid. Crude **5.12** was purified by column chromatography using dichloromethane:hexanes (50%:50%) as eluent. Evaporation of the second fraction (R_f = 0.25) gave pure product as a yellow powder (120 mg, 0.556 mmol, 89%).

^{1}H NMR (400 MHz, DMSO-d_6) δ 11.59 (s, 2H; OH), 10.77 (s, 2H; CHO), 9.16 (d, $^3J_{HH}$=9.36 Hz, 2H; Ar), 7.37 (d, $^3J_{HH}$=9.36 Hz, 2H; Ar) ppm. ^{13}C {^{1}H} NMR (100 MHz, DMSO-d_6) δ 192.7 (CHO), 161.6 (COH), 132.4 (CH), 125.9 (Ar), 121.4 (CH), 113.3 (*C*CHO) ppm. UV-Vis (CH_2Cl_2) λ_{max} (ε) = 400 (6.6 × 10^3), 385 (1.1 × 10^4), 314 (1.2 × 10^4), 302 (1.2 × 10^4) nm (cm^{-1} mol^{-1} L). IR (neat) *v* = 2917 (br), 1633, 1584, 1502, 1409, 1359, 1262, 1212, 1163, 1039, 836, 776, 731, 703,

653, 483, 450 cm^{-1}. HRMS (ESI/TOF-Q) *m/z*: [**5.12** - H]$^-$ Calcd for $C_{12}H_7O_4$ 215.0344; Found 215.0342.

Chapter 6

Conclusions

The process of discovery can start with an unusual observation and develop into a hypothesis backed by careful experiments. Alternatively, science can be born of necessity and making tools to scratch an itch. With the material in the previous chapters, the hope was to connect the beginnings of each project to these roots and expose the process such that the reader could join in our sense of adventure and deep satisfaction that came with each step.

The core ideas presented in this thesis are remarkably basic and require little beyond undergraduate chemistry in order to be fully understood. Namely, all chapters begin with intuitive pen-and-paper designs inspired by parallels to familiar natural or synthetic systems and realized with help from spectroscopic characterization techniques and *ab initio* computational simulations.

Chapter 2 lays the foundation for subsequent chapters by addressing a question that many researchers working with salicylimines have pondered: "If aromaticity has such a large stabilizing effect, then why do some salicylimines prefer the apparently keto-enamine tautomeric form?[*]" We sought the answer in some of the more obvious places, *e.g.* stronger N–H versus O–H bonds or stronger NH···O versus OH···N hydrogen bonds, but found that a more comprehensive model was needed to account for the trends we observed in keto-enamine versus enol-imine tautomeric preference, Figure 6.1. Experimental evidence for enol-imine TSANs, unknown at the time of our investigations, has recently been published including, notably, the molecular structure (from SCXRD data) of **2.3b**, which was published in early 2017 by Premužić and coworkers.[81,82] Nevertheless, we believe that the contribution of this work to the understanding of tautomerism

[*] Or, more fundamentally, to what degree is aromaticity disturbed in the keto-enamine tautomeric form.

and electron delocalization in TSANs still stands. From the point of view of physical chemistry, the actual answer to the question posed above depends on the partition of total molecular energy into atomic and bond contributions. Thus, while the theory of atoms in molecules (AIM) might predict that certain atoms have a larger contribution to total energy, *i.e.* are less "stable" in a given tautomer, other interpretations attribute the instability to a different atom. A more practical approach is taken here, where we focus on delineating which structural factors lead to stronger preference for one or the other tautomeric form.

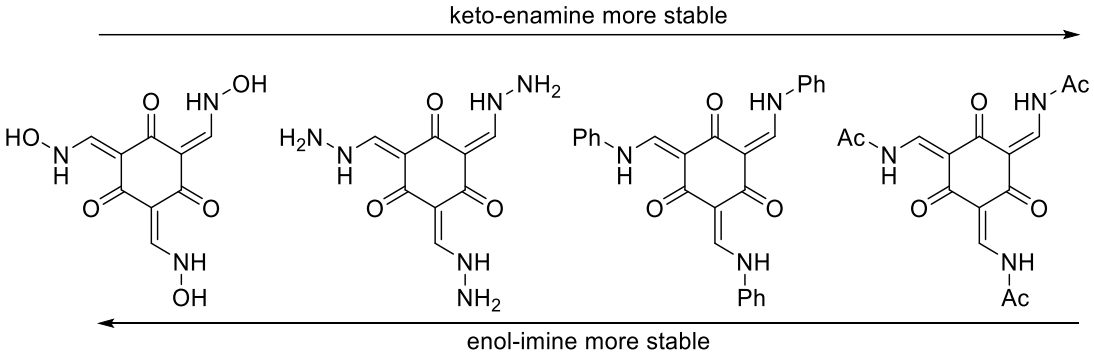

Figure 6.1. Trends in the relative stability of keto-enamine and enol-imine TSANs/TSAN analogues.

Ideally, the theory laid out in Chapter 2 would help create "designer tautomers": TSANs where the relative stability of the keto-enamine and enol-imine tautomers can be tuned to the application at hand. This is especially important in light of the contrasting behaviour of the two tautomeric forms in terms of geometry (presence or lack of geometrical isomerism) and aromaticity.

The chemistry introduced in Chapter 2 naturally leads to the phenomenon of facile aromatic H/D exchange of hydroxysalicylimines in Chapter 3. The observation of this phenomenon in CD_3OD solvent at neutral pH (the first of its kind, to the best of our knowledge) is remarkable, since the apparent ease of forming the sp^3-hybridized Wheland complex **6.1** seems contradictory to our understanding of the aromatic stabilization energy (ASE), Figure 6.2a. We were able to

determine that a much more stable intermediate, **6.2**, can be accessed if the molecule is allowed to tautomerize to its keto-enamine form prior to the electrophilic addition of the deuterium atom, Figure 6.2b.

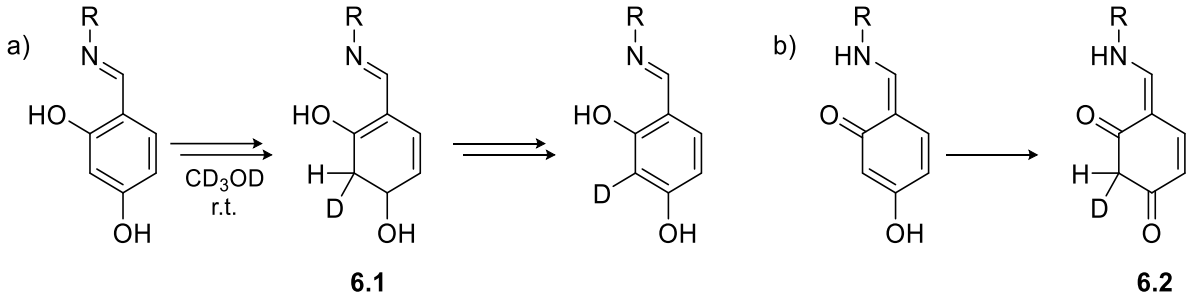

Figure 6.2. (a) Naïve mechanism for aromatic H/D exchange in a 4-hydroxysalicylimine. (b) Formation of Wheland intermediate facilitated in keto-enamine form of substrate.

Conceptually, this discovery is interesting because it demonstrates that a small change on the periphery of the molecule such as the small movement of a proton can profoundly alter the reactivity of the ring. This is reminiscent of the action of pyridoxal phosphate (PLP) and its dependence on the protonation of the PLP pyridine moiety, as we saw in Chapter 1. Finally, it is reassuring that even the simple tool of Lewis structures can accurately predict the site of facile H/D exchange.

Where we demonstrate that aromaticity can be weakened by tautomeric interconversion in Chapter 3, Chapter 4 goes further to show that competing modes of electron delocalization in the periphery can completely destroy aromaticity in the central ring. Here the TSAN design from Chapter 2 is modified by replacing the small, labile protons with relatively bulky and immobile methyl groups, Figure 6.3. As a result, the molecule is "locked" into keto-enamine connectivity, replacing the tautomeric equilibrium with a pair of resonance contributors. Additionally, the steric bulk of the methyl groups is incompatible with the flat TSAN geometry due to repulsive interactions with the oxygen atoms on the ring. Surprisingly, the molecule adopts a strained central

ring geometry that still allows the enamine arms to be approximately coplanar with the ring carbonyls, thereby preserving peripheral electron delocalization at the cost of losing aromaticity.

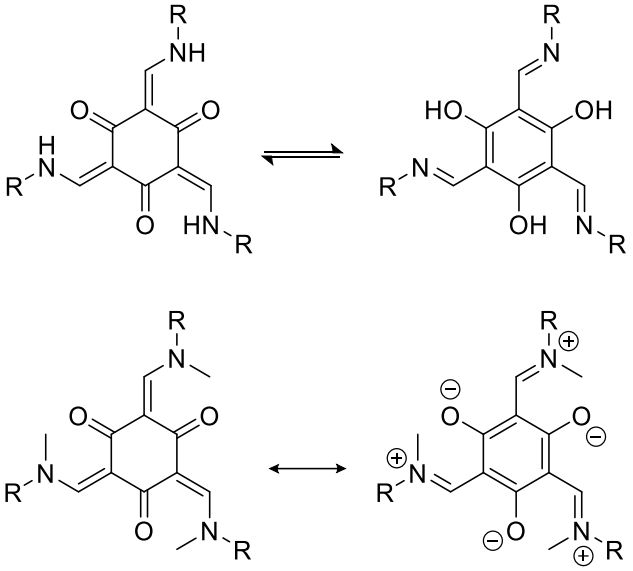

Figure 6.3. Tandem movement of protons and electrons in a TSAN (top) versus delocalization of electrons in a locked keto-enamine heteroradialene (bottom).

In Chapter 5, we close by re-visiting the preparation of the salicylaldehyde precursors to the various Schiff bases in the preceding chapters. The difficulty of efficiently synthesizing these salicylaldehydes by adding multiple formyl groups to the parent phenols is surprising both because of the simple, symmetric structure of the products and the high reactivity of phenols towards electrophilic formylation methods, such as the Vilsmeier–Haack or Duff reactions. Ultimately, what makes multiple formylations challenging is the formyl group itself: due to the highly deactivating nature of this group, mild formylation conditions fail to add more than a single formyl function, while harsh conditions lead to significant side reactions given the fragile nature of the substrates. Compounding this difficulty, the deactivating effect of the formyl group tends to cause side-reactions, most notably in the case of phloroglucinol where the Vilsmeier conditions might bring about substitution of the OH groups without proper caution.

Formylation with formamidine acetate and acetic anhydride overcomes the issue of deactivation by deferring the full realization of the electronically deactivating formyl group until the final hydrolysis step. Thus, only the mildly deactivating $–CH(NHAc)_2$ is introduced during the critical electrophilic aromatic substitution step, paving the way to multiply formylated products.

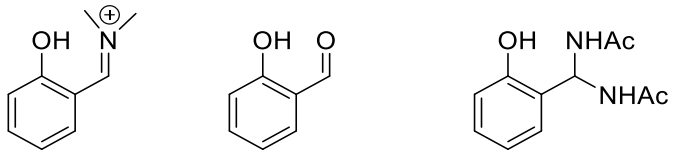

6.3 **6.4** **6.5**

Figure 6.4. Comparison of deactivated intermediates encountered with common methods of formylation, **6.3** and **6.4**, with that encountered in formylation using formamidine acetate, **6.5**.

Fortuitously, the hydrolysis of the bis(*N*-acetamido)methyl intermediates provided a chance for the material in this thesis to come full circle, as it led to the discovery of compound **2.7** and furnished a new pathway to **2.1** (through hydrolysis of **2.7**). Furthermore, the odd behaviour of **2.7** under basic hydrolysis, yielding **2.1** instead of the desired TFP product, can be understood and anticipated in light of the material in Chapter 2.

Where transition metal complexes are hailed for their versatility in catalyzing various chemical transformations, we hope to have demonstrated that a careful design of organic motifs (particularly using tautomerism and electron delocalization as tools) can lead to similar interesting reactivity in the absence of metals. Accordingly, many enzymatic processes in nature do not involve transition metals, instead relying on organic motifs whose structure and reactivity have been tuned by natural selection.

Evolutionary emergence of organic catalysts is not exclusive to nature. Indeed, recent years have seen the opening of a promising new avenue of research where manmade organic catalysts are discovered by a combinatorial approach, often using computational techniques to screen a vast

number of oligomers of natural (*e.g.* natural amino acids) or synthetic building blocks for activity.[195–199] So far, research has mostly focused on the sequence of these building blocks, rather than their individual electronic structure. Unlike nature, however, we are not limited to using a fixed pool of monomers, there is opportunity in evaluating novel building blocks with improved properties. For instance, the Schafmeister research group has devised spiroligomers, Figure 6.5, oligomers held together with double (as opposed to single in the case of amino acids) amide linkages. Compared to polypeptides, spiroligomers offer enhanced thermal stability thanks to their relatively rigid structure and robust connectivity. Computer-aided[200] design of spiroligomers has so far led to the discovery of examples with promising catalytic and biological function.[201,202]

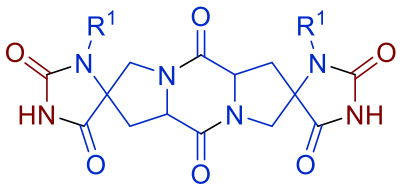

Figure 6.5. A spiroligomer with colour-coded residues. Amide linkages (three pairs) are shown in black.

Just as non-biological building blocks can be designed with the goal of building more robust oligomeric catalysts, we anticipate that the tautomeric and electron delocalization behaviour of the motifs discussed in this thesis be able to contribute to enhanced catalytic activity. Specifically, we expect them to be ideally suited to catalysis of concerted reactions, where the push-pull nature of electron delocalization can stabilize transition states with large charge separations.

Bibliography

(1) Kol, N.; Adler-Abramovich, L.; Barlam, D.; Shneck, R. Z.; Gazit, E.; Rousso, I. *Nano Lett.* **2005**, *5*, 1343–1346.

(2) Choi, M.-S.; Yamazaki, T.; Yamazaki, I.; Aida, T. *Angew. Chem. Int. Ed.* **2004**, *43*, 150–158.

(3) Lehn, J.-M. *Reports Prog. Phys.* **2004**, *67*, 249–265.

(4) Chen, X.; Li, N.; Ellington, A. D. *Chem. Biodivers.* **2007**, *4*, 633–655.

(5) Meyer, D.; Neumann, P.; Koers, E.; Sjuts, H.; Ludtke, S.; Sheldrick, G. M.; Ficner, R.; Tittmann, K. *Proc. Natl. Acad. Sci.* **2012**, *109*, 10867–10872.

(6) Smith, M. B.; March, J. *March's Advanced Organic Chemistry*, 5th ed.; Wiley-Interscience: New York, 2001.

(7) Fersner, A.; Karty, J. M.; Mo, Y. *J. Org. Chem.* **2009**, *74*, 7245–7253.

(8) Mo, Y.; Schleyer, P. von R.; Wu, W.; Lin, M.; Zhang, Q.; Gao, J. *J. Phys. Chem. A* **2003**, *107*, 10011–10018.

(9) Miessler, G. L.; Tarr, D. H. *Inorganic Chemistry*, 3rd ed.; Prentice Hall: Upper Saddle River, N.J., 2003.

(10) Pauling, L. *The Nature of the Chemical Bond*, 3rd ed.; Cornell University Press: Ithaca, NY, 1960.

(11) Hiberty, P. C.; Byrman, C. P. *J. Am. Chem. Soc.* **1995**, *117*, 9875–9880.

(12) Shaik, S.; Hiberty, P. C. *A Chemist's Guide to Valence Bond Theory*; John Wiley & Sons,

Inc.: Hoboken, NJ, 2007.

(13) Fock, V. *Zeitschrift für Phys.* **1930**, *61*, 126–148.

(14) Foster, J. M.; Boys, S. F. *Rev. Mod. Phys.* **1960**, *32*, 300–302.

(15) Edmiston, C.; Ruedenberg, K. *Rev. Mod. Phys.* **1963**, *35*, 457–464.

(16) Pipek, J.; Mezey, P. G. *J. Chem. Phys.* **1989**, *90*, 4916–4926.

(17) Reed, A. E.; Weinhold, F. *J. Chem. Phys.* **1985**, *83*, 1736–1740.

(18) Hiberty, P. C.; Shaik, S. *Theor. Chem. Accounts Theory, Comput. Model. (Theoretica Chim. Acta)* **2002**, *108*, 255–272.

(19) Thorsteinsson, T.; Cooper, D. L.; Gerratt, J.; Karadakov, P. B.; Raimondi, M. *Theor. Chim. Acta* **1996**, *93*, 343–366.

(20) G. Angyan, J. *Curr. Org. Chem.* **2011**, *15*, 3609–3618.

(21) Breslow, R. *J. Am. Chem. Soc.* **1957**, *79*, 1762–1763.

(22) Breslow, R. *J. Am. Chem. Soc.* **1958**, *80*, 3719–3726.

(23) Breslow, R.; McNelis, E. *J. Am. Chem. Soc.* **1959**, *81*, 3080–3082.

(24) Cabelli, D. E.; Bielski, B. H. J. *J. Phys. Chem.* **1983**, *87*, 1809–1812.

(25) Hu, I. F.; Kuwana, T. *Anal. Chem.* **1986**, *58*, 3235–3239.

(26) Yang, W.; Drueckhammer, D. G. *J. Am. Chem. Soc.* **2001**, *123*, 11004–11009.

(27) Ting, R.; Harwig, C. W.; Lo, J.; Li, Y.; Adam, M. J.; Ruth, T. J.; Perrin, D. M. *J. Org. Chem.* **2008**, *73*, 4662–4670.

(28) Liu, Z.; Hundal-Jabal, N.; Wong, M.; Yapp, D.; Lin, K.-S.; Bénard, F.; Perrin, D. M. *Med. Chem. Commun.* **2014**, *5*, 171–179.

(29) *IUPAC Compendium of Chemical Terminology*; Nič, M., Jirát, J., Košata, B., Jenkins, A., McNaught, A., Eds.; IUPAC: Research Triangle Park, NC, 2009.

(30) Scanlan, M. J.; Hillier, I. H. *Chem. Phys. Lett.* **1984**, *107*, 330–332.

(31) Fu, A.; Li, H.; Du, D.; Zhou, Z. *J. Phys. Chem. A* **2005**, *109*, 1468–1477.

(32) Muller, P. *Pure Appl. Chem.* **1994**, *66*.

(33) Leeladee, P.; Baglia, R. A.; Prokop, K. A.; Latifi, R.; de Visser, S. P.; Goldberg, D. P. *J. Am. Chem. Soc.* **2012**, *134*, 10397–10400.

(34) Kolsaker, P.; Arukwe, J.; Barcóczy, J.; Wiberg, A.; Fagerli, A. K.; Hammerich, O.; Søtofte, I.; Långström, B. *Acta Chem. Scand.* **1998**, *52*, 490–498.

(35) Bowden, K.; Hiscocks, S. P.; Perjéssy, A. *J. Chem. Soc. Perkin Trans. 2* **1998**, No. 2, 291–296.

(36) Lown, J. W.; Akhtar, M. H. *Tetrahedron Lett.* **1973**, *14*, 3727–3730.

(37) Sobczyk, L.; Grabowski, S. J.; Krygowski, T. M. *Chem. Rev.* **2005**, *105*, 3513–3560.

(38) Raczyńska, E. D.; Krygowski, T. M.; Zachara, J. E.; Ośmiałowski, B.; Gawinecki, R. *J. Phys. Org. Chem.* **2005**, *18*, 892–897.

(39) Krygowski, T. M.; Stępień, B. T. *Chem. Rev.* **2005**, *105*, 3482–3512.

(40) Raczyńska, E. D.; Kosińska, W.; Ośmiałowski, B.; Gawinecki, R. *Chem. Rev.* **2005**, *105*, 3561–3612.

(41) Gilli, G.; Bellucci, F.; Ferretti, V.; Bertolasi, V. *J. Am. Chem. Soc.* **1989**, *111*, 1023–1028.

(42) Bertolasi, V.; Gilli, P.; Ferretti, V.; Gilli, G. *J. Am. Chem. Soc.* **1991**, *113*, 4917–4925.

(43) Palusiak, M.; Simon, S.; Solà, M. *J. Org. Chem.* **2006**, *71*, 5241–5248.

(44) Swain, C. G.; Brown, J. F. *J. Am. Chem. Soc.* **1952**, *74*, 2534–2537.

(45) Fischer, C. B.; Steininger, H.; Stephenson, D. S.; Zipse, H. *J. Phys. Org. Chem.* **2005**, *18*, 901–907.

(46) Metzler, D. E. In *Advances in Enzymology and Related Areas of Molecular Biology, Volume 50*; Meister, A., Ed.; 2006; pp 1–40.

(47) Müller, C.; Wang, L.-H.; Zipse, H. In *Transition State Modeling for Catalysis*; Truhlar, D. G., Morokuma, K., Eds.; American Chemical Society, 1999; pp 61–73.

(48) Rony, P. R. *J. Am. Chem. Soc.* **1969**, *91*, 6090–6096.

(49) Chong, J. H.; Sauer, M.; Patrick, B. O.; MacLachlan, M. J. *Org. Lett.* **2003**, *5*, 3823–3826.

(50) Gallant, A. J.; Yun, M.; Sauer, M.; Yeung, C. S.; MacLachlan, M. J. *Org. Lett.* **2005**, *7*, 4827–4830.

(51) Jiang, J.; MacLachlan, M. J. *Chem. Commun. (Cambridge, United Kingdom)* **2009**, No. 38, 5695–5697.

(52) Elbert, S. M.; Rominger, F.; Mastalerz, M. *Chem. Eur. J.* **2014**, *20*, 16707–16720.

(53) Sauer, M.; Yeung, C.; Chong, J. H.; Patrick, B. O.; MacLachlan, M. J. *J. Org. Chem.* **2006**, *71*, 775–788.

(54) Frischmann, P. D.; Mehr, S. H. M.; Patrick, B. O.; Lelj, F.; MacLachlan, M. J. *Inorg. Chem.*

2012, *51*, 3443–3453.

(55) Villa, A. M.; Casella, L.; Fantucci, P. *Bioorg. Chem.* **1988**, *16*, 133–148.

(56) Percudani, R.; Peracchi, A. *EMBO Rep.* **2003**, *4*, 850–854.

(57) John, R. A. *Biochim. Biophys. Acta - Protein Struct. Mol. Enzymol.* **1995**, *1248*, 81–96.

(58) Ogawa, K.; Kasahara, Y.; Ohtani, Y.; Harada, J. *J. Am. Chem. Soc.* **1998**, *120*, 7107–7108.

(59) Ogawa, K.; Harada, J.; Tamura, I.; Noda, Y. *Chem. Lett.* **2000**, *29*, 528–529.

(60) Zhu, Y.; Long, H.; Zhang, W. *Chem. Mater.* **2013**, *25*, 1630–1635.

(61) Pachfule, P.; Kandmabeth, S.; Mallick, A.; Banerjee, R. *Chem. Commun.* **2015**, *51*, 11717–11720.

(62) Bera, S.; Basu, A.; Tothadi, S.; Garai, B.; Banerjee, S.; Vanka, K.; Banerjee, R. *Angew. Chem. Int. Ed.* **2017**, *56*, 2123–2126.

(63) Chandra, S.; Kundu, T.; Dey, K.; Addicoat, M.; Heine, T.; Banerjee, R. *Chem. Mater.* **2016**, *28*, 1489–1494.

(64) Mitra, S.; Kandambeth, S.; Biswal, B. P.; Khayum M., A.; Choudhury, C. K.; Mehta, M.; Kaur, G.; Banerjee, S.; Prabhune, A.; Verma, S.; Roy, S.; Kharul, U. K.; Banerjee, R. *J. Am. Chem. Soc.* **2016**, *138*, 2823–2828.

(65) Shinde, D. B.; Aiyappa, H. B.; Bhadra, M.; Biswal, B. P.; Wadge, P.; Kandambeth, S.; Garai, B.; Kundu, T.; Kurungot, S.; Banerjee, R. *J. Mater. Chem. A* **2016**, *4*, 2682–2690.

(66) Feldscher, B.; Stammler, A.; Bögge, H.; Glaser, T. *Polyhedron* **2011**, *30*, 3038–3047.

(67) Freiherr von Richthofen, C.-G.; Feldscher, B.; Lippert, K.-A.; Stammler, A.; Bögge, H.;

Glaser, T. *Zeitschrift für Naturforsch. B* **2013**, *68b*, 64–86.

(68) Reimer, K. *Ber. Dtsch. Chem. Ges.* **1876**, *9*, 423–424.

(69) Reimer, K.; Tiemann, F. *Ber. Dtsch. Chem. Ges.* **1876**, *9*, 824–828.

(70) Wittig, G. *Angew. Chemie* **1940**, *53*, 211–217.

(71) Duff, J. C. *J. Chem. Soc.* **1941**, 547–550.

(72) Angyal, S. J. *Org. React.* **2011**, *8*, 197–217.

(73) Gattermann, L.; Berchelmann, W. *Ber. Dtsch. Chem. Ges.* **1898**, *31*, 1765–1769.

(74) Himmelman, W.; Roos, E.; Sobel, J. Hardeners for photographic gelatinous layers. DE 2002063, 1971.

(75) Yang, C.-X.; Liu, C.; Cao, Y.-M.; Yan, X.-P. *Chem. Commun.* **2015**, *51*, 12254–12257.

(76) Aiyappa, H. B.; Thote, J.; Shinde, D. B.; Banerjee, R.; Kurungot, S. *Chem. Mater.* **2016**, *28*, 4375–4379.

(77) Riddle, J. A.; Lathrop, S. P.; Bollinger, J. C.; Lee, D. *J. Am. Chem. Soc.* **2006**, *128*, 10986–10987.

(78) Suresh, P.; Varghese, B.; Varadarajan, T. K.; Viswanathan, B. *Acta Crystallogr. Sect. E Struct. Reports Online* **2007**, *63*, o984–o986.

(79) Kline, M. A.; Wei, X.; Horner, I. J.; Liu, R.; Chen, S.; Chen, S.; Yung, K. Y.; Yamato, K.; Cai, Z.; Bright, F. V.; Zeng, X. C.; Gong, B. *Chem. Sci.* **2015**, *6*, 152–157.

(80) Kruszewski, J.; Krygowski, T. M. *Tetrahedron Lett.* **1972**, *13*, 3839–3842.

(81) Premužić, D.; Filarowski, A.; Hołyńska, M. *J. Mol. Struct.* **2017**, *1136*, 100–106.

(82) Foster, J. S.; Żurek, J. M.; Almeida, N. M. S.; Hendriksen, W. E.; le Sage, V. A. A.; Lakshminarayanan, V.; Thompson, A. L.; Banerjee, R.; Eelkema, R.; Mulvana, H.; Paterson, M. J.; van Esch, J. H.; Lloyd, G. O. *J. Am. Chem. Soc.* **2015**, *137*, 14236–14239.

(83) Hall, H. K. *J. Am. Chem. Soc.* **1957**, *79*, 5441–5444.

(84) Huber, W. In *Titrations in Nonaqueous Solvents*; Academic Press: New York, 1967; pp 215–229.

(85) Kokko, B. J.; Edmondson, S. D. In *Encyclopedia of Reagents for Organic Synthesis*; John Wiley & Sons, Ltd: Chichester, UK, 2008.

(86) In *CRC Handbook of Chemistry and Physics*; Lide, D. R., Ed.; CRC Press, 2001; p "8-42."

(87) Mulliken, R. S. *J. Chem. Phys.* **1955**, *23*, 1833–1840.

(88) Löwdin, P.-O. *Adv. Quantum Chem.* **1970**, *5*, 185–199.

(89) Löwdin, P. *J. Chem. Phys.* **1950**, *18*, 365–375.

(90) Reed, A. E.; Weinstock, R. B.; Weinhold, F. *J. Chem. Phys.* **1985**, *83*, 735–746.

(91) Gross, K. C.; Seybold, P. G.; Hadad, C. M. *Int. J. Quantum Chem.* **2002**, *90*, 445–458.

(92) Annibale, V. T.; Song, D. *RSC Adv.* **2013**, *3*, 11432.

(93) van der Vlugt, J. I.; Reek, J. N. H. *Angew. Chem. Int. Ed.* **2009**, *48*, 8832–8846.

(94) Ibrahim, R.; Tsuchiya, S.; Ogawa, S. *J. Am. Chem. Soc.* **2000**, *122*, 12174–12185.

(95) Weigend, F.; Ahlrichs, R. *Phys. Chem. Chem. Phys.* **2005**, *7*, 3297.

(96) Frisch, M. J.; Trucks, G. W.; Schlegel, H. B.; Scuseria, G. E.; Robb, M. A.; Cheeseman, J. R.; Scalmani, G.; Barone, V.; Mennucci, B.; Petersson, G. A.; Nakatsuji, H.; Caricato, M.; Li, X.; Hratchian, H. P.; Izmaylov, A. F.; Bloino, J.; Zheng, G.; Sonnenberg, J. L.; Hada, M.; Ehara, M.; Toyota, K.; Fukuda, R.; Hasegawa, J.; Ishida, M.; Nakajima, T.; Honda, Y.; Kitao, O.; Nakai, H.; Vreven, T.; Montgomery Jr., J. A.; Peralta, J. E.; Ogliaro, F.; Bearpark, M.; Heyd, J. J.; Brothers, E.; Kudin, K. N.; Staroverov, V. N.; Kobayashi, R.; Normand, J.; Raghavachari, K.; Rendell, A.; Burant, J. C.; Iyengar, S. S.; Tomasi, J.; Cossi, M.; Rega, N.; Millam, J. M.; Klene, M.; Knox, J. E.; Cross, J. B.; Bakken, V.; Adamo, C.; Jaramillo, J.; Gomperts, R.; Stratmann, R. E.; Yazyev, O.; Austin, A. J.; Cammi, R.; Pomelli, C.; Ochterski, J. W.; Martin, R. L.; Morokuma, K.; Zakrzewski, V. G.; Voth, G. A.; Salvador, P.; Dannenberg, J. J.; Dapprich, S.; Daniels, A. D.; Farkas, Ö.; Foresman, J. B.; Ortiz, J. V; Cioslowski, J.; Fox, D. J. Gaussian Inc.: Wallingford, CT 2009.

(97) Keith, T. A. *AIMAll Rev. 16.10*; TK Gristmill Software: Overland Park, 2016.

(98) Schleyer, P. von R.; Maerker, C.; Dransfeld, A.; Jiao, H.; Hommes, N. J. R. van E. *J. Am. Chem. Soc.* **1996**, *118*, 6317–6318.

(99) Fallah-Bagher-Shaidaei, H.; Wannere, C. S.; Corminboeuf, C.; Puchta, R.; Schleyer, P. v. R. *Org. Lett.* **2006**, *8*, 863–866.

(100) Schreckenbach, G.; Ziegler, T. *J. Phys. Chem.* **1995**, *99*, 606–611.

(101) Wolinski, K.; Hinton, J. F.; Pulay, P. *J. Am. Chem. Soc.* **1990**, *112*, 8251–8260.

(102) Bloch, K. *Science* **1965**, *150*, 19–28.

(103) Chen, T. T.; Bloch, K. *J. Biol. Chem.* **1957**, *226*, 921–930.

(104) Clayton, R. B.; Bloch, K. *J. Biol. Chem.* **1956**, *218*, 319–325.

(105) Woodward, R. B.; Bloch, K. *J. Am. Chem. Soc.* **1953**, *75*, 2023–2024.

(106) Foster, A. B. In *Advances in Drug Research*; Academic Press, 1985; Vol. 14, pp 1–40.

(107) Fernandez, H. H.; Factor, S. A.; Hauser, R. A.; Jimenez-Shahed, J.; Ondo, W. G.; Jarskog, L. F.; Meltzer, H. Y.; Woods, S. W.; Bega, D.; LeDoux, M. S.; Shprecher, D. R.; Davis, C.; Davis, M. D.; Stamler, D.; Anderson, K. E. *Neurology* **2017**, *88*, 2003–2010.

(108) Schmidt, C. *Nat. Biotechnol.* **2017**, *35*, 493–494.

(109) Miller, A. I. *Can. Nucl. Soc. Bull.* **2001**, *22*, 1–14.

(110) Hoshino, M.; Katou, H.; Hagihara, Y.; Hasegawa, K.; Naiki, H.; Goto, Y. *Nat. Struct. Mol. Biol.* **2002**, *9*, 332–336.

(111) Niimura, N. *Curr. Opin. Struct. Biol.* **1999**.

(112) Smirnovas, V.; Baron, G.; Offerdahl, D. *Nat. Struct.* **2011**.

(113) Engelman, D.; Moore, P. *Proc. Natl.* **1972**.

(114) Jung, M.; Yue, X. *Heterocycles* **1998**, *47*, 349–356.

(115) Blanksby, S. J.; Ellison, G. B. *Acc. Chem. Res.* **2003**, *36*, 255–263.

(116) Small, P. A.; Wolfenden, J. H. *J. Chem. Soc.* **1936**, 1811–1817.

(117) Bai, S.; Palmer, B. J.; Yonker, C. R. *J. Phys. Chem. A* **2000**, *104*, 53–58.

(118) Werstiuk, N. H.; Timmins, G. *Can. J. Chem.* **1989**, *67*, 1744–1747.

(119) Boix, C.; Poliakoff, M. *Tetrahedron Lett.* **1999**, *40*, 4433–4436.

(120) Elvidge, J. A.; Jones, J. R.; O'Brien, C.; Evans, E. A.; Sheppard, H. C. *Adv. Heterocycl. Chem.* **1974**, *16*, 1–31.

(121) Sadjadi, S.; Hosseinpour, M.; Mohammadnezhad, F.; Ahmadi, S. J.; Khazayi, M. A. *J. Supercrit. Fluids* **2017**.

(122) Shatenshtein, A. I. *Tetrahedron* **1962**, *18*, 95–106.

(123) Ito, N.; Esaki, H.; Maesawa, T.; Imamiya, E.; Maegawa, T.; Sajiki, H. *Bull. Chem. Soc. Jpn.* **2008**, *81*, 278–286.

(124) Iluc, V. M.; Fedorov, A.; Grubbs, R. H. *Organometallics* **2012**, *31*, 39–41.

(125) Parmentier, M.; Hartung, T.; Pfaltz, A.; Muri, D. *Chem. Eur. J.* **2014**, *20*, 11496–11504.

(126) Atzordt, J.; Derdau, V.; Fey, T.; Zimmermann, J. *Angew. Chem. Int. Ed.* **2007**, *46*, 7744–7765.

(127) Prechtl, M. H. G.; Hölscher, M.; Ben-David, Y.; Theyssen, N.; Loschen, R.; Milstein, D.; Leitner, W. *Angew. Chem. Int. Ed.* **2007**, *46*, 2269–2272.

(128) Sawama, Y.; Yamada, T.; Yabe, Y.; Morita, K.; Shibata, K.; Shigetsura, M.; Monguchi, Y.; Sajiki, H. *Adv. Synth. Catal.* **2013**, *355*, 1529–1534.

(129) Qiao-Xia, G.; Bao-Jian, S.; Hai-Qing, G.; Tamotsu, T. *Chin. J. Chem.* **2005**, *23*, 341–344.

(130) Krishnan, R.; Pople, J. A. *Int. J. Quantum Chem.* **1978**, *14*, 91–100.

(131) Krishnan, R.; Frisch, M. J.; Pople, J. A. *J. Chem. Phys.* **1980**, *72*, 4244.

(132) Becke, A. D. *J. Chem. Phys.* **1993**, *98*, 5648–5652.

(133) Lee, C.; Yang, W.; Parr, R. G. *Phys. Rev. B* **1988**, *37*, 785–789.

(134) Miehlich, B.; Savin, A.; Stoll, H.; Preuss, H. *Chem. Phys. Lett.* **1989**, *157*, 200–206.

(135) Zhao, Y.; Truhlar, D. G. *Theor. Chem. Acc.* **2008**, *120*, 215–241.

(136) Schwabe, T.; Grimme, S. *Phys. Chem. Chem. Phys.* **2006**, *8*, 4398–4401.

(137) Tomasi, J.; Mennucci, B.; Cammi, R. *Chem. Rev.* **2005**, *105*, 2999–3093.

(138) Scalmani, G.; Frisch, M. J.; Mennucci, B.; Tomasi, J.; Cammi, R.; Barone, V. *J. Chem. Phys.* **2006**, *124*, 94107.

(139) Alagona, G.; Ghio, C.; Nagy, P. I. *Phys. Chem. Chem. Phys.* **2010**, *12*, 10173.

(140) Piotto, M.; Bourdonneau, M.; Elbayed, K.; Wieruszeski, J.-M.; Lippens, G. *Magn. Reson. Chem.* **2006**, *44*, 943–947.

(141) Lee, G.; Youn, I.; Choi, E.; Lee, H.; Yon, G.; Yang, H.; Pak, C. *Curr. Org. Chem.* **2004**, *8*, 1263–1287.

(142) Hopff, H.; Wick, A. K. *Helv. Chim. Acta* **1961**, *44*, 19–24.

(143) Hopff, H. *Chimia* **1964**, *18*, 140–141.

(144) Domene, C.; Fowler, P. W.; Jenneskens, L. W.; Steiner, E. *Chem. Eur. J.* **2007**, *13*, 269–276.

(145) Freiherr Von Richthofen, C. G.; Stammler, A.; Bögge, H.; Glaser, T. *Eur. J. Inorg. Chem.* **2012**, *2012*, 5934–5952.

(146) Glaser, T. *Coord. Chem. Rev.* **2013**, *257*, 140–152.

(147) Höpfner, T.; Jones, P. G.; Ahrens, B.; Dix, I.; Ernst, L.; Hopf, H. *European J. Org. Chem.* **2003**, *2003*, 2596–2611.

(148) Dunning, T. H. *J. Chem. Phys.* **1989**, *90*, 1007.

(149) Kendall, R. A.; Dunning, T. H.; Harrison, R. J. *J. Chem. Phys.* **1992**, *96*, 6796.

(150) Davidson, E. R. *Chem. Phys. Lett.* **1996**, *260*, 514–518.

(151) Elerman, Y.; Paulus, H.; Svoboda, I.; Fuess, H. *Zeitschrift für Krist. - Cryst. Mater.* **1992**, *198*, 135–136.

(152) Schlabach, M.; Wehrle, B.; Limbach, H. H.; Bunnenberg, E.; Knierzinger, A.; Shu, A. Y. L.; Tolf, B. R.; Djerassi, C. *J. Am. Chem. Soc.* **1986**, *108*, 3856–3858.

(153) Schwotzer, W.; Von Philipsborn, W. *Helv. Chim. Acta* **1977**, *60*, 1501–1509.

(154) Laxer, A.; Major, D. T.; Gottlieb, H. E.; Fischer, B. *J. Org. Chem.* **2001**, *66*, 5463–5481.

(155) Bojarska-Olejnik, E.; Stefaniak, L.; Witanowski, M.; Webb, G. A. *Bull. Chem. Soc. Jpn.* **1986**, *59*, 3263–3265.

(156) Lambert, J. B.; Mazzola, E. P. *Nuclear Magnetic Resonance Spectroscopy: An Introduction to Principles, Applications, and Experimental Methods*, 1st ed.; Pearson/Prentice Hall: Upper Saddle River, N.J., 2003.

(157) Chan-Huot, M.; Sharif, S.; Tolstoy, P. M.; Toney, M. D.; Limbach, H.-H. *Biochemistry* **2010**, *49*, 10818–10830.

(158) Westerman, P. W.; Roberts, J. D. *J. Org. Chem.* **1977**, *42*, 2249–2252.

(159) Meić, Z.; Güsten, H. *Spectrochim. Acta Part A Mol. Spectrosc.* **1978**, *34*, 101–111.

(160) Yang, D.-H.; Yao, Z.-Q.; Wu, D.; Zhang, Y.-H.; Zhou, Z.; Bu, X.-H. *J. Mater. Chem. A* **2016**, *4*, 18621–18627.

(161) Mulzer, C. R.; Shen, L.; Bisbey, R. P.; McKone, J. R.; Zhang, N.; Abruña, H. D.; Dichtel, W. R. *ACS Cent. Sci.* **2016**, *2*, 667–673.

(162) Kieryk, P.; Janczak, J.; Panek, J.; Miklitz, M.; Lisowski, J. *Org. Lett.* **2016**, *18*, 12–15.

(163) Anjaneyulu, A. S. R.; Rama Prasad, A. V.; Sivakumar Reddy, D. *Curr. Sci.* **1979**, *48*, 300–301.

(164) Tupchiangmai, W.; Choksakulporn, S.; Tewtrakul, S.; Pianwanit, S.; Sritana-anant, Y. *Chem. Pharm. Bull.* **2014**, *62*, 754–763.

(165) Abdul-Aziz, M.; Auping, J. V.; Meador, M. A. *J. Org. Chem.* **1995**, *60*, 1303–1308.

(166) Olah, G. A.; Ohannesian, L.; Arvanaghi, M. *Chem. Rev.* **1987**, *87*, 671–686.

(167) Olah, G. A.; Kuhn, S. J. *J. Am. Chem. Soc.* **1960**, *82*, 2380–2382.

(168) Vilsmeier, A.; Haack, A. *Chem. Ber.* **1927**, *60*, 119.

(169) Gattermann, L.; Koch, J. A. *Ber. Dtsch. Chem. Ges.* **1897**, *30*, 1622–1624.

(170) Lawrence, A. L.; Adlington, R. M.; Baldwin, J. E.; Lee, V.; Kershaw, J. A.; Thompson, A. L. *Org. Lett.* **2010**, *12*, 1676–1679.

(171) Bosshard, H. H.; Zollinger, H. *Helv. Chim. Acta* **1959**, *42*, 1659–1671.

(172) Alunni, S.; Linda, P.; Marino, G.; Santini, S.; Savelli, G. *J. Chem. Soc., Perkin Trans. 2* **1972**, No. 14, 2070–2073.

(173) Hofsløkken, N. U.; Skattebøl, L. *Acta Chem. Scand.* **1999**, *53*, 258–262.

(174) Casiraghi, G.; Casnati, G.; Puglia, G.; Sartori, G.; Terenghi, G. *J. Chem. Soc. Perkin Trans. 1* **1980**, 1862.

(175) Casiraghi, G.; Casnati, G.; Cornia, M.; Pochini, A.; Puglia, G.; Sartori, G.; Ungaro, R. *J. Chem. Soc. Perkin Trans. 1* **1978**, No. 4, 318.

(176) Casnati, G.; Crisafulli, M.; Ricca, A. *Tetrahedron Lett.* **1965**, *6*, 243–245.

(177) Ogata, Y.; Kawasaki, A.; Sugiura, F. *Tetrahedron* **1968**, *24*, 5001–5010.

(178) Skonieczny, K.; Charalambidis, G.; Tasior, M.; Krzeszewski, M.; Kalkan-Burat, A.; Coutsolelos, A. G.; Gryko, D. T. *Synthesis* **2012**, *44*, 3683–3687.

(179) Schreiber, J.; Maag, H.; Hashimoto, N.; Eschenmoser, A. *Angew. Chem. Int. Ed. Engl.* **1971**, *10*, 330–331.

(180) Gaudry, M.; Jasor, Y.; Khac, T. B. *Org. Synth.* **1979**, *59*, 153.

(181) Yun, H. *Synlett* **2004**, No. 7, 1321–1322.

(182) Barl, N. M.; Sansiaume-Dagousset, E.; Monzón, G.; Wagner, A. J.; Knochel, P. *Org. Lett.* **2014**, *16*, 2422–2425.

(183) Werner, V.; Klatt, T.; Fujii, M.; Markiewicz, J.; Apeloig, Y.; Knochel, P. *Chem. Eur. J.* **2014**, *20*, 8338–8342.

(184) Seth, S. K. *J. Mol. Struct.* **2014**, *1064*, 70–75.

(185) Ziegler, G.; Kantlehner, W. *Zeitschrift für Naturforsch. B* **2001**, *56*, 1178–1187.

(186) Hurd, C. D.; Roe, A. S. *J. Am. Chem. Soc.* **1939**, *61*, 3355–3359.

(187) Petersen, W. C. Process of preparing aromatic aldehydes by reacting selected aromatic compounds with formamidine acetate and an organic acid anhydride. United States Patent 4,394,314, July 19, 1983.

(188) Taylor, E. C.; Erhart, W. A.; Kawanisi, M. *Org. Synth.* **1966**, *46*, 39.

(189) Taylor, E. C.; Ehrhart, W. A. *J. Am. Chem. Soc.* **1960**, *82*, 3138–3141.

(190) Mehr, S. H. M.; Patrick, B. O.; MacLachlan, M. J. *Org. Lett.* **2016**, *18*, 1840–1843.

(191) Shopsowitz, K. E.; Edwards, D.; Gallant, A. J.; MacLachlan, M. J. *Tetrahedron* **2009**, *65*, 8113–8119.

(192) Glaser, T.; Liratzis, I. *Synlett* **2004**, No. 4, 735–737.

(193) Dammert, W. Amidine substituted naphthalene carboxylic acid. United States Patent 3,839,434 A, 1974.

(194) Bender, T. P.; Hu, N.-X.; Goodbrand, H. B. Arylamine Processes. US 7,122,700, 2006.

(195) Schreiner, P. R. *Chem. Soc. Rev.* **2003**, *32*, 289.

(196) Kheirabadi, M.; Çelebi-Ölçüm, N.; Parker, M. F. L.; Zhao, Q.; Kiss, G.; Houk, K. N.; Schafmeister, C. E. *J. Am. Chem. Soc.* **2012**, *134*, 18345–18353.

(197) Juliá, S.; Guixer, J.; Masana, J.; Rocas, J.; Colonna, S.; Annuziata, R.; Molinari, H. *J. Chem. Soc., Perkin Trans. 1* **1982**, 1317–1324.

(198) Schlosser, K.; Li, Y. *Chem. Biol.* **2009**, *16*, 311–322.

(199) Jiang, L.; Althoff, E. A.; Clemente, F. R.; Doyle, L.; Rothlisberger, D.; Zanghellini, A.; Gallaher, J. L.; Betker, J. L.; Tanaka, F.; Barbas, C. F.; Hilvert, D.; Houk, K. N.; Stoddard, B. L.; Baker, D. *Science* **2008**, *319*, 1387–1391.

(200) Schafmeister, C. E. In *Proceedings of the 9th European Lisp Symposium on European Lisp Symposium*; European Lisp Scientific Activities Association: Kraków, 2016; p 9:75-9:82.

(201) Parker, M. F. L.; Osuna, S.; Bollot, G.; Vaddypally, S.; Zdilla, M. J.; Houk, K. N.; Schafmeister, C. E. *J. Am. Chem. Soc.* **2014**, *136*, 3817–3827.

(202) Brown, Z. Z.; Akula, K.; Arzumanyan, A.; Alleva, J.; Jackson, M.; Bichenkov, E.; Sheffield, J. B.; Feitelson, M. A.; Schafmeister, C. E. *PLoS One* **2012**, *7*, e45948.

(203) *APEX2*; Bruker AXS Inc.: Madison, Wisconsin, USA, 2007.

(204) Palatinus, L.; Chapuis, G. *J. Appl. Crystallogr.* **2007**, *40*, 786–790.

(205) Betteridge, P. W.; Carruthers, J. R.; Cooper, R. I.; Prout, K.; Watkin, D. J. *J. Appl. Crystallogr.* **2003**, *36*, 1487–1487.

(206) Cooper, R. I.; Thompson, A. L.; Watkin, D. J. *J. Appl. Crystallogr.* **2010**, *43*, 1100–1107.

(207) Krause, L.; Herbst-Irmer, R.; Sheldrick, G. M.; Stalke, D. *J. Appl. Crystallogr.* **2015**, *48*, 3–10.

(208) Sheldrick, G. M. *Acta Crystallogr. Sect. C Struct. Chem.* **2015**, *71*, 3–8.

(209) Cromer, D. T.; Waber, J. T. *International Tables for Crystallography*; The Kynoch Press: Birmingham, England, 1974.

(210) Creagh, D. C.; McAuley, W. J. *International Tables for Crystallography, Vol. C*; Wilson, A. J. C., Ed.; Kluwer Academic Publishers: Boston, 1992.

(211) Creagh, D. C.; Hubbell, J. H. *International Tables for Crystallography, Vol. C*; Wilson, A. J. C., Ed.; Kluwer Academic Publishers: Boston, 1992.

(212) Dolomanov, O. V.; Bourhis, L. J.; Gildea, R. J.; Howard, J. A. K.; Puschmann, H. *J. Appl. Crystallogr.* **2009**, *42*, 339–341.

(213) Sheldrick, G. M. *Acta Crystallogr. Sect. A Found. Adv.* **2015**, *71*, 3–8.

(214) Kawai, S. *Yakugaku Zasshi* **1966**, *86*, 1125–1132.

(215) Clover, A. M. *J. Am. Chem. Soc.* **1923**, *45*, 3133–3138.

(216) Wang, K.; Yang, E.-C.; Zhao, X.-J.; Liu, Y. *RSC Adv.* **2015**, *5*, 2640–2646.

(217) Glasoe, P. K.; Long, F. A. *J. Phys. Chem.* **1960**, *64*, 188–190.

(218) Ruzin, S. E. *Plant Microtechnique and Microscopy*; Oxford University Press, USA, 1999.

(219) Kirchnerová, J.; Cave, G. C. B. *Can. J. Chem.* **1976**, *54*, 3909–3916.

(220) Jensen, F. *Introduction to Computational Chemistry*, 2nd ed.; John Wiley & Sons, Ltd.: Chichester, UK, 2007.

(221) Gallant, A. J.; Hui, J. K.-H.; Zahariev, F. E.; Wang, Y. A.; MacLachlan, M. J. *J. Org. Chem.* **2005**, *70*, 7936–7946.

(222) Liu, M.; Mao, X.; Ye, C.; Huang, H.; Nicholson, J. K.; Lindon, J. C. *J. Magn. Reson.* **1998**, *132*, 125–129.

(223) Herrebout, W. A.; van der Veken, B. J.; Wang, A.; Durig, J. R. *J. Phys. Chem.* **1995**, *99*, 578–585.

(224) Christiansen, O.; Olsen, J.; Jørgensen, P.; Koch, H.; Malmqvist, P.-Å. *Chem. Phys. Lett.* **1996**, *261*, 369–378.

(225) Cremer, D.; He, Z. *J. Phys. Chem.* **1996**, *100*, 6173–6188.

(226) Khurana, J. M.; Gogia, A.; Bankhwal, R. K. *Synth. Commun.* **1997**, *27*, 1801–1809.

Appendix A

X-Ray Crystallography

A.1 Compound 2.2

Single crystal X-ray data were collected using graphite monochromated Mo Kα radiation (λ = 0.71073 Å). All data were collected at 90 K to a resolution of 0.70 Å. Raw frame data (including data reduction, interframe scaling, unit cell refinement and absorption corrections) for all structures were processed using APEX2.[203] Structures were solved using SUPERFLIP[204] and refined using full-matrix least-squares on F^2 within the CRYSTALS suite.[205] Hydrogen atoms were generally visible in the Fourier difference map and were initially refined with restraints on bond lengths and angles, after which the positions were used as the basis for a riding model.[206]

An initial structural determination of **2.2** compound suggested the presence of disorder of the entire structure over a major and minor position. In order to investigate this further, a high quality dataset was collected at 90 K using long exposure times and collecting to a resolution of 0.7 Å. The diffraction intensities and R_{merge} values were still reasonable for reflections at high angle (*e.g.* R_{merge} ~ 0.10 for reflections at 0.70 Å resolution).

This dataset shows that the crystal contains positional disorder over two positions (Figure A.1–A.3). The data were modelled by having two positions for every atom in the structure. Refinement of the occupancies of the two positions gave site occupancy factors of 0.9254(18) for the major position and 0.0746(18) for the minor position. A list of bond lengths for each of the two positions are provided in Table 1 – while the errors on the bond lengths for the minor position are relatively

large (as would be expected given its very low occupancy), they still allow sensible discussion of the tautomerism (*see later*).

The major occupancy position of the molecule refined smoothly, with all non-hydrogen atoms refined anisotropically and no restraints necessary. Hydrogen atoms for this position were visible in the difference map, their positions refined, and then fixed.

The minor occupancy position of the molecule was not as well-behaved, which is unsurprising given its low occupancy. It was necessary to refine these atoms isotropically. Hydrogen atoms for this position of the molecule were inserted at geometric positions. No restraints were applied to C–C, C–N, or C–O bond lengths or angles in order to give the best possible insight into which tautomer is present – as a result, there is significant variation in bond lengths and some slightly unusual bond angles. Again, given the very low occupancy of this position, it is unsurprising that the refinement is less than ideal.

Warming the crystal used for this data collection to 230 K and collecting another dataset gave lower quality data. However, it was possible to determine that the ratio of the two disorder positions was the same, within experimental error (~ 93:7 major:minor).

The major position has consistently long C–C ring bonds [1.441(2)–1.453(2) Å] bonds, consistently short C–O bonds [1.2579(16)–1.2687(15) Å], consistently short C–C bonds coming out of the ring [1.3891(18)–1.3950(17) Å], and moderately long C–N bonds [1.3068(15)–1.3169(16) Å]. All of these bond lengths are clearly consistent with this position being the ketone-enamine tautomer.

The minor position has short C–C ring bonds, with a mean length of 1.37 Å (*cf.* 1.45 Å in the major position). The C–O bonds are long, with a mean length of 1.36 Å (*cf.* 1.26 Å in the major

position) as are the C–C bonds coming out of the ring, with a mean length of 1.48 Å (*cf.* 1.39 Å in the major position). The C–N bonds are shorter in the minor position than in the major position (mean lengths: 1.28 and 1.31 Å for the minor and major position respectively). These bond lengths suggest that this minor position is the phenol-imine tautomer.

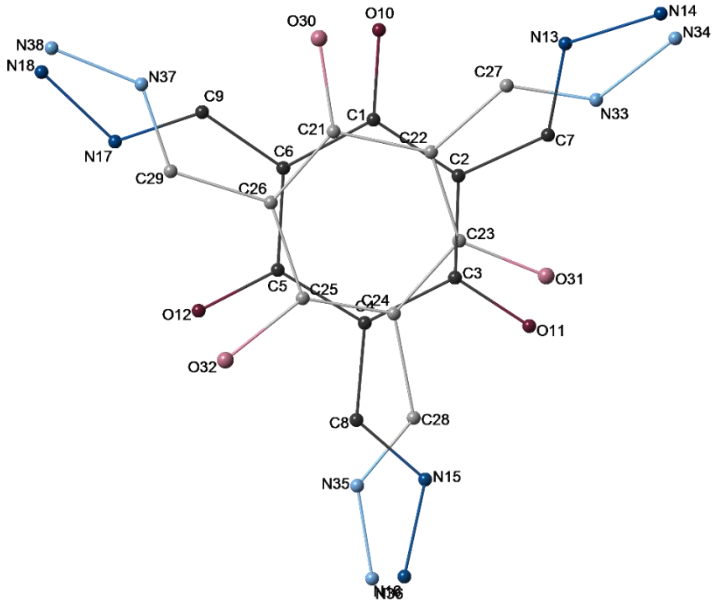

Figure A.1. Overlay plot showing two disordered tautomers in the structure of **2.2**, as well as numbering scheme. Atoms corresponding to the major tautomer are shown darker than those of the minor tautomer. Hydrogen atoms are omitted for clarity.

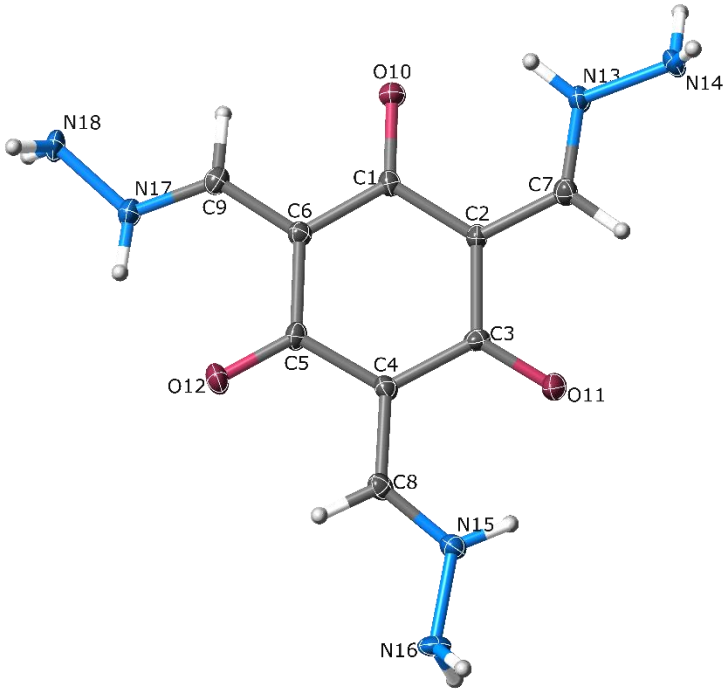

Figure A.2. Thermal ellipsoid plot of the major occupancy [s.o.f.: 0.9254 (18)] tautomer of **2.2** (ellipsoids shown at 50% probability).

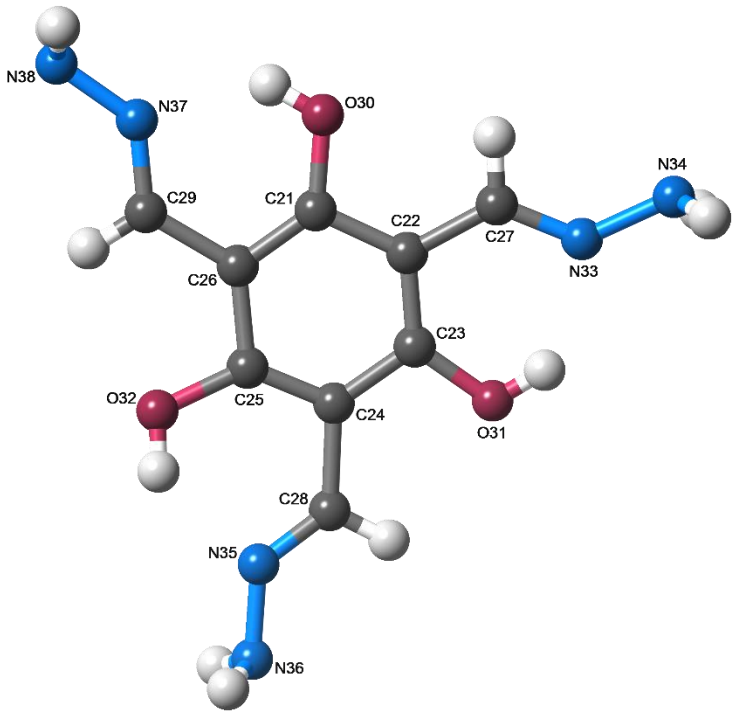

Figure A.3. Structure of the minor occupancy [s.o.f.: 0.0746(18)] tautomer of **2.2**.

Table A.1. Bond lengths for two positions of disordered structure in **2.2**. All bond lengths given in Å, with estimated standard deviations given in parentheses. Major position is numbered C1 through N18, minor position is numbered C21 through N38.

Bond	**Major position** **[site occupancy factor: 0.9254(18)]**	**Minor position** **[site occupancy factor: 0.0746(18)]**
6 × Ring C–C bonds	1.441(2), 1.446(2), 1.449(2),	1.32(3), 1.32(3), 1.34(2),
(C1–C6 and C21–C26)	1.450(2), 1.450(2), 1.453(2)	1.39(3), 1.41(3), 1.43(3)
Mean C–C ring bond	***1.45***	***1.37***
3 × C–O bonds (C1–O10, C3–O11, C5–O12 and C21–O30, C23–O31, C25–O32)	1.2579(16), 1.2605(15), 1.2687(15)	1.335(19), 1.35(2), 1.40(3)

Mean C–O bond	***1.26***	***1.36***
3 × C–C bonds (C2–C7, C4–C8, C6–C9 and C22–C27, C24–C28, C26–C29)	1.3891(18), 1.3946(16), 1.3950(17)	1.43(2), 1.49(2), 1.53(2)
Mean C–C bond	***1.39***	***1.48***
3 × C–N bonds (C7–N13, C8–N15, C9–N17 and C27–N33, C28–N35, C29–N37)	1.3068(15), 1.3102(16), 1.3169(16)	1.26(2), 1.28(2), 1.30(2)
Mean C–N bond	***1.31***	***1.28***

A.2 Compound 2.3

X-ray crystallographic data obtained for **2.3** are identical to those published by Premužić et al.[81]

A.3 Compound 2.4

A colourless needle crystal of $C_{24}H_{36}N_6O_6 \cdot 2(iPrOH)$, having approximate dimensions of 0.03 × 0.004 × 0.004 mm was mounted on a glass fiber. All measurements were made on a MAR300 CCD detector at the Canadian Light Source using 0.68879 Å synchrotron radiation.

The data were collected using Mo-Kα radiation at a temperature of 173.0 $\pm$ 2 K to a maximum 2θ value of 61.6°. Data were collected in a series of φ and ω scans in 1.0° oscillations using 30s exposures. The crystal-to-detector distance was 114.90 mm.

Of the 51133 reflections that were collected, 9383 were unique (R_{int} = 0.055); equivalent reflections were merged. Data were collected and integrated using the Bruker SAINT software package. The linear absorption coefficient, μ, for Mo-Kα radiation is 0.84 cm^{-1}. Data were corrected for absorption effects using the multi-scan technique (SADABS[207]), with minimum and maximum transmission coefficients of 0.689 and 0.9997, respectively. The data were corrected for Lorentz and polarization effects.

The structure was solved by direct methods.[208] The compound crystallizes with two molecules of solvent isopropanol in the asymmetric unit, each hydrogen bonded to a carbonyl oxygen of the main molecule. There appears to be a mixture of tautomers about the 6-membered ring. Oxygen O2 is exclusively the alcohol, O1 and O3 appear to be mixture of the two. Partially occupied hydrogen atom sites are found in sites consistent with both O—H and N—H hydrogens. All non-hydrogen atoms were refined anisotropically. All OH and NH hydrogen atoms were located in difference maps. H1, H2, H5 and H6 were refined isotropically, while H3 and H4 were refined in calculate positions. All C—H and O—H hydrogen atoms were placed in calculated positions and however were refined in calculated positions.

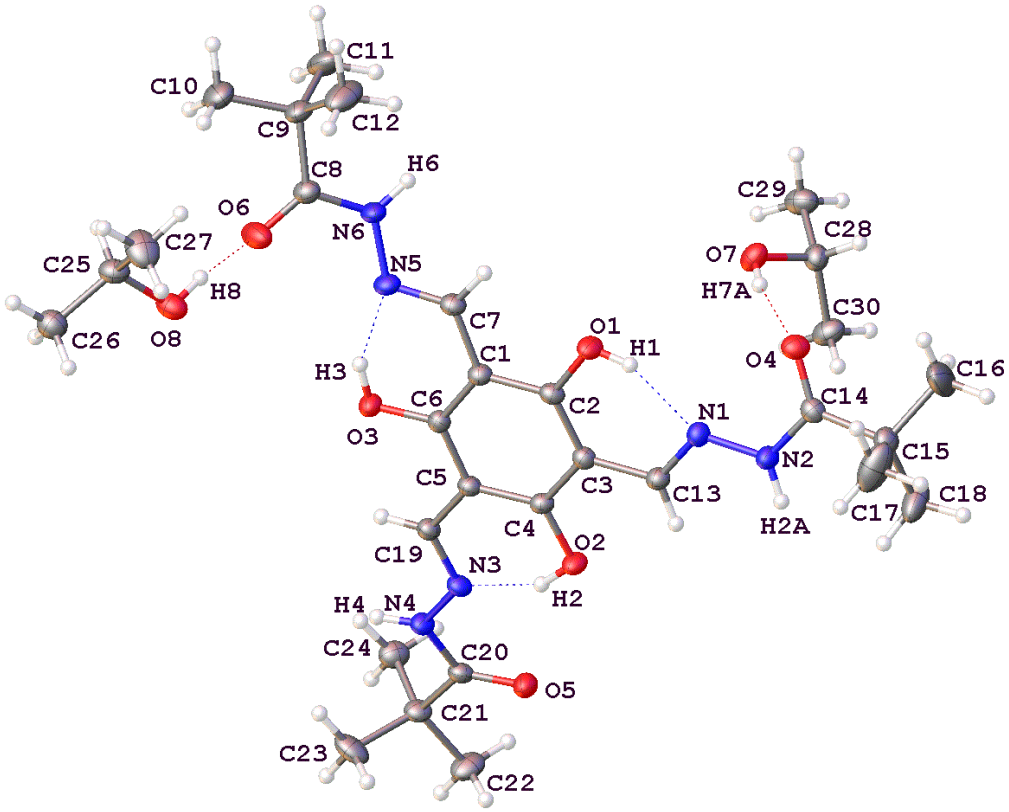

Figure A.4. Thermal ellipsoids and numbering scheme for the major positions of the SCXRD for **2.4** with solvent molecules included.

The final cycle of full-matrix least-squares refinement (least squares function minimized: $\Sigma\, w(F_o^2\text{-}F_c^2)^2$) on F2 was based on 9383 reflections and 451 variable parameters and converged (largest parameter shift was 0.00 times its esd) with unweighted and weighted agreement factors of:

$$R1 = \Sigma\, ||F_o| - |F_c|| \,/\, \Sigma\, |F_o| = 0.049$$

$$wR2 = [\, \Sigma\, (\, w(F_o^2 - F_c^2)^2\,)/\, \Sigma\, w(F_o^2)^2]^{1/2} = 0.134$$

The standard deviation of an observation of unit weight ($[\Sigma\, w(F_o^2\text{-}F_c^2)^2/(N_o\text{-}N_v)]^{1/2}$ where N_o = number of observations and N_v = number of variables) was 1.02. The weighting scheme was based

on counting statistics. The maximum and minimum peaks on the final difference Fourier map corresponded to 0.48 and -0.25 $e^-/Å^3$, respectively.

Neutral atom scattering factors were taken from Cromer and Waber.[209] Anomalous dispersion effects were included in Fcalc; the values for Δf′ and Δf″ were those of Creagh and McAuley.[210] The values for the mass attenuation coefficients are those of Creagh and Hubbell.[211] All refinements were performed using the SHELXL-2014[208] via the OLEX2 interface.[212]

Table A.2. Bond lengths for compound **2.4**. All bond lengths given in Å.

Bond	**Distances (Å)**
6 × Ring C–C bonds (C1–C6)	1.4089(19), 1.4060(17), 1.4028(18), 1.4090(17), 1.4137(18), 1.4087(17)
Mean C–C ring bond	***1.41***
3 × C–O bonds (C2–O1, C4–O2, C6–O3)	1.3414(15), 1.3397(15), 1.3459(16)
Mean C–O bond	***1.34***
3 × C–C bonds (C1–C7, C3–C13, C5–C19)	1.4429(18), 1.4519(18), 1.4506(17)
Mean C–C bond	***1.45***
3 × C–N bonds (C7–N5, C13–N1, C19–N3)	1.2845(17), 1.2879(17), 1.2853(19)
Mean C–N bond	***1.29***

A.4 Compound 2.5

Single crystal X-ray data were collected using cross-coupled multilayer optics Cu-Kα radiation (λ = 1.54158 Å). All data were collected at 90 K to a resolution of 0.80 Å. Raw frame data (including data reduction, interframe scaling, unit cell refinement and absorption corrections) for all structures were processed using APEX2.[203] Structures were solved using SUPERFLIP[204] and refined using full-matrix least-squares on F^2 within the CRYSTALS suite. C–H hydrogen atoms were generally visible in the Fourier difference map and were initially refined with restraints on bond lengths and angles, after which the positions were used as the basis for a riding model, O–H hydrogen atoms were visible in the Fourier difference map and were refined with restraints on bond lengths and angles.[206]

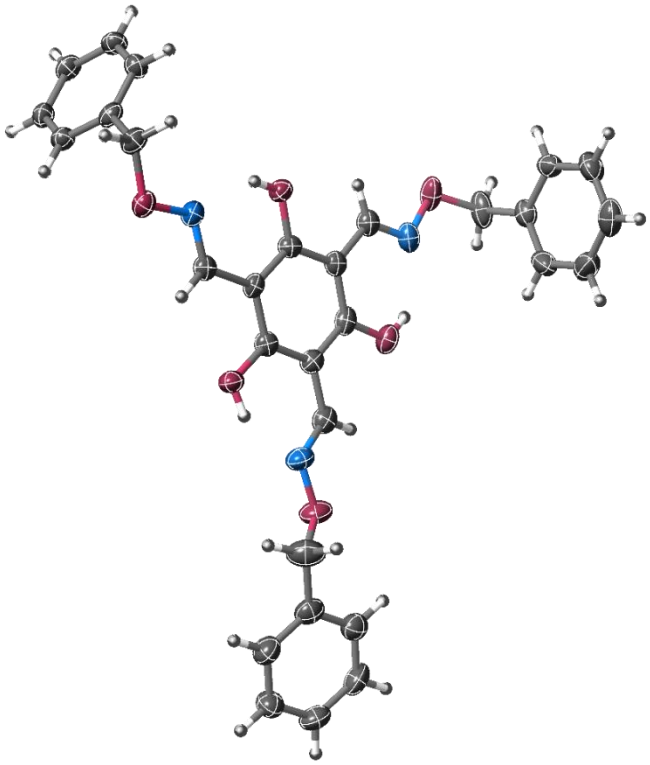

Figure A.5. Thermal ellipsoid plot of **2.5** (thermal ellipsoids are shown at 50% occupancy).

Table A.3. Bond lengths for compound **2.5**. All bond lengths given in Å.

Bond	Distances (Å)
6 × Ring C–C bonds (C1–C6)	1.399(4), 1.412(4), 1.411(4), 1.407(4), 1.402(4), 1.404(4)
Mean C–C ring bond	***1.41***
3 × C–O bonds (C2–O7, C4–O8, C6–O9)	1.337(3), 1.352(4), 1.343(4)
Mean C–O bond	***1.34***
3 × C–C bonds (C1–C10, C3–C20, C5–C30)	1.450(4), 1.451(4), 1.453(4)
Mean C–C bond	***1.45***
3 × C–N bonds (C10–N11, C20–N21, C30–N31)	1.274(4), 1.281(4), 1.286(4)
Mean C–N bond	***1.28***
R1(2964 reflections) = 0.0434, wR2(3420 reflections) = 0.1110, S = 0.957	

A.5 Compound 2.6

A yellow needle crystal of $C_{27}H_6N_3O_3F_{15}$, having approximate dimensions of 0.01 × 0.01 × 0.10 mm was mounted on a glass fiber. All measurements were made on a MAR300 CCD detector at the Canadian Light Source using 0.68873 Å synchrotron radiation.

The data were collected using Mo-Kα radiation at a temperature of 173.0 $\pm$ 2 K to a maximum 2θ value of 54.6°. Data were collected in a series of φ and ω scans in 1.5° oscillations using 60s exposures. The crystal-to-detector distance was 114.99 mm.

Of the 41628 reflections that were collected, 11208 were unique (R_{int} = 0.035); equivalent reflections were merged. Data were collected and integrated using the Bruker SAINT software package. The linear absorption coefficient, μ, for Mo-Kα radiation is 1.98 cm^{-1}. Data were corrected for absorption effects using the multi-scan technique (SADABS[207]), with minimum and maximum transmission coefficients of 0.692 and 0.998, respectively. The data were corrected for Lorentz and polarization effects.

The structure was solved by direct methods.[208] The material crystallizes with two independent molecules in the asymmetric unit. Each molecule is disordered, with each site partially occupied by both keto and enol tautomers. As the difference in bond lengths between the two forms is relatively small, no restraints or constraints were employed, beyond EADP for atoms occupying the same space. In each case the keto form is present in a roughly 4:1 ratio. All non-hydrogen atoms were refined anisotropically. All N—H hydrogen atoms were located in difference maps. H1, H2, H5 and H6 were refined isotropically, while H3 and H4 were refined in calculate positions.

All C—H and O—H hydrogen atoms were placed in calculated positions and however were refined in calculated positions.

The final cycle of full-matrix least-squares refinement (least squares function minimized: $\Sigma\, w(F_o^2\text{-}F_c^2)^2$) on F2 was based on 11208 reflections and 1102 variable parameters and converged (largest parameter shift was 0.00 times its esd) with unweighted and weighted agreement factors of:

$$R1 = \Sigma\, ||F_o| - |F_c|| \,/\, \Sigma\, |F_o| = 0.034$$

$$wR2 = [\, \Sigma\, (w(F_o^2 - F_c^2)^2\,)/\, \Sigma\, w(F_o^2)^2]^{1/2} = 0.093$$

The standard deviation of an observation of unit weight ($[\Sigma\, w(F_o^2\text{-}F_c^2)^2/(N_o\text{-}N_v)]^{1/2}$ where N_o = number of observations and N_v = number of variables) was 1.10. The weighting scheme was based on counting statistics. The maximum and minimum peaks on the final difference Fourier map corresponded to 0.26 and -0.21 $e^-/Å^3$, respectively.

Neutral atom scattering factors were taken from Cromer and Waber. Anomalous dispersion effects were included in Fcalc; the values for $\Delta f'$ and $\Delta f''$ were those of Creagh and McAuley. The values for the mass attenuation coefficients are those of Creagh and Hubbell. All refinements were performed using the SHELXL-2014 via the Olex2 interface.

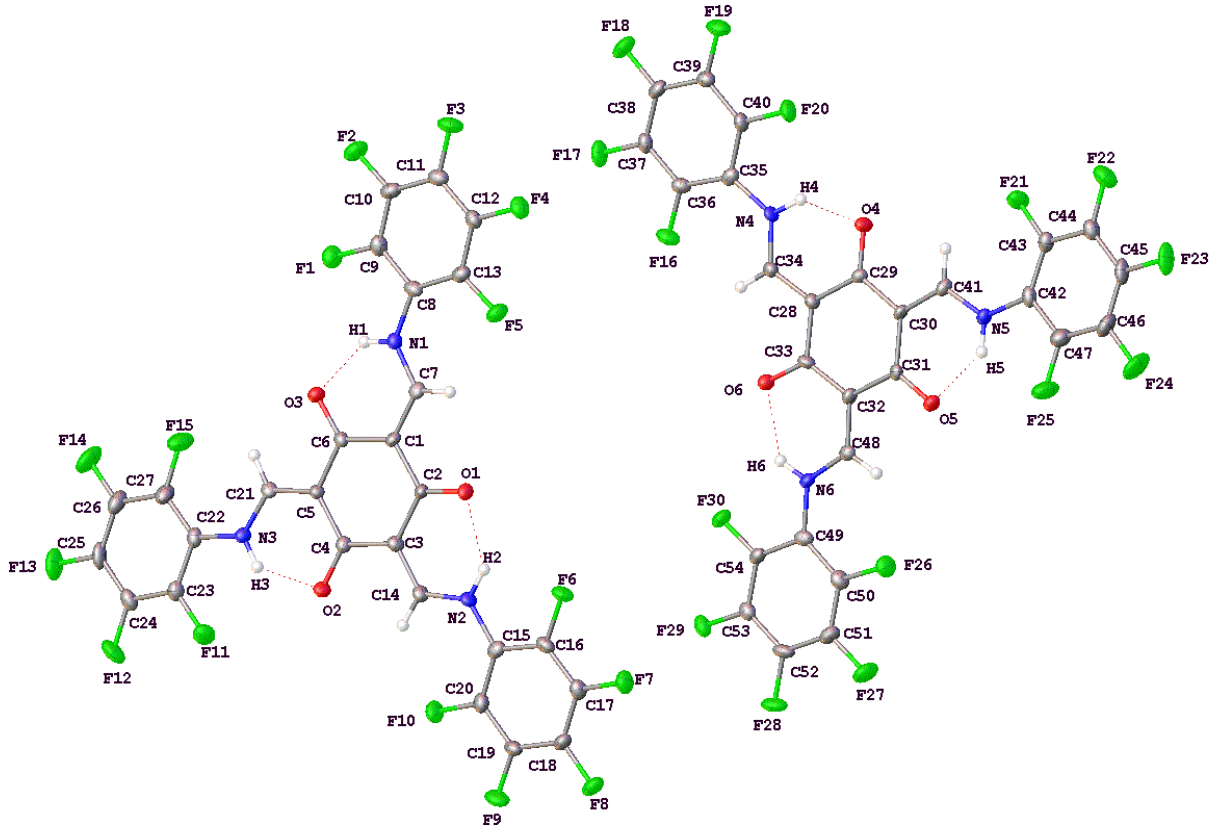

Figure A.6. Thermal ellipsoid plot for the major disorder component of **2.6** by SCXRD (thermal ellipsoids are shown at 50% occupancy).

Table A.4. Bond lengths for compound **2.6** (major disorder component). All bond lengths given in Å.

Bond	**Distances (Å)**
6 × Ring C–C bonds (C1–C6)	1.464(6), 1.455(6), 1.467(6), 1.451(7), 1.463(6), 1.450(6)
Mean C–C ring bond	***1.46***
3 × C–O bonds (C2–O1, C4–O2, C6–O3)	1.249(5), 1.257(5), 1.261(5)
Mean C–O bond	***1.26***

3 × C–C bonds (C1–C7, C3–C14, C5–C21)	1.380(5), 1.364(6), 1.375(5)
Mean C–C bond	***1.37***
3 × C–N bonds (C7–N1, C14–N2, C21–N3)	1.328(5), 1.333(5), 1.345(5)
Mean C–N bond	***1.28***

R1(9991 reflections) = 0.0344, wR2(11208 reflections) = 0.0929, S = 1.104

A.6 Compound 2.7

Single crystal X-ray data for compound **2.7** were collected using graphite monochromated Mo Kα radiation (λ = 0.71073 Å). The data were collected at 90 K to a resolution of 0.77 Å. Raw frame data (including data reduction, interframe scaling, unit cell refinement and absorption corrections) were processed using APEX2.[203] The structure was solved using SUPERFLIP[204] and refined using full-matrix least-squares on F^2 within the CRYSTALS suite.[205] Hydrogen atoms were generally visible in the Fourier difference map and were initially refined with restraints on bond lengths and angles, after which the positions were used as the basis for a riding model.[206]

The structure solved and refined in the space group P 2_1/n. One of the unit cell's angles is 90.4°, very close to 90°, but the reflections integrated poorly in an orthorhombic space group. The crystal presents pseudo-merohedral twinning, which was treated using ROTAX analysis. The structure in general does not show significant disorder and all the ellipsoids are relatively small. The only bond where it was necessary to add some thermal similarity and vibrational restraints is the C(5)-C(17) double bond.

The long C-C bond length in the ring [1.446(4)-1.478(1) Å], the relatively short C-O bond lengths [1.245(3)-1.250(7) Å], and short C-C bonds out of the ring [1.353(5)-1.372(1) Å], are consistent with the presence of the keto-enamine tautomer. In this structure only the keto-enamine tautomer is present.

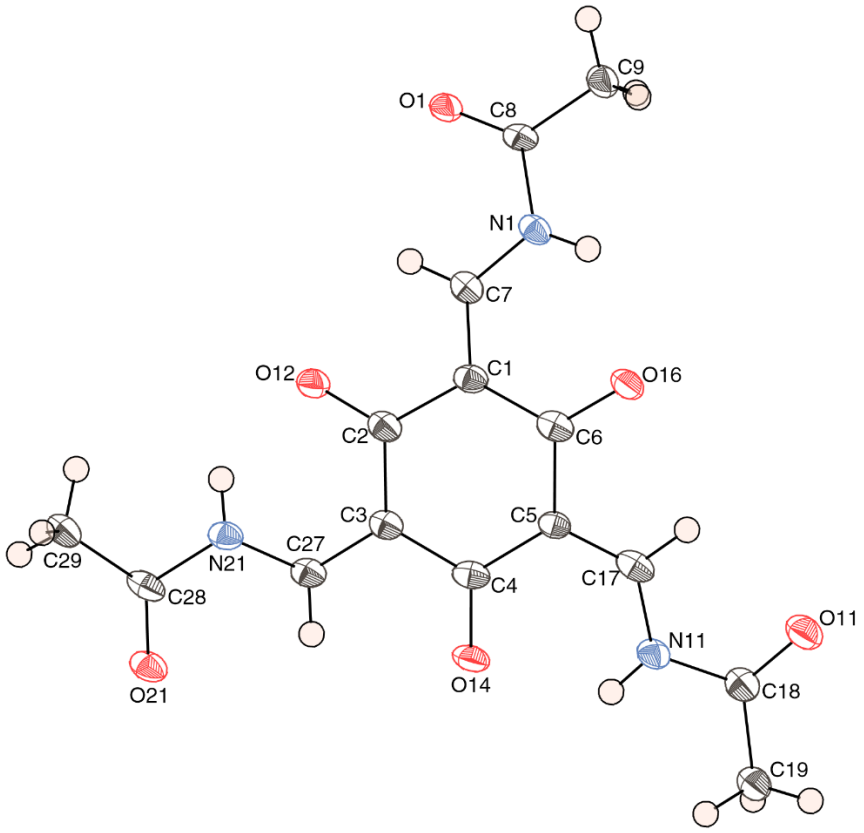

Figure A.7. Thermal ellipsoid plot of **2.7** (thermal ellipsoids are shown at 50% occupancy).

Table A.5. Bond lengths for compound **2.7**. All bond lengths given in Å.

Bond	**Distances (Å)**
6 × Ring C–C bonds (C1–C6)	1.471(7), 1.446(4), 1.470(3), 1.473(6), 1.455(2), 1.478(1)
Mean C–C ring bond	***1.47***
3 × C–O bonds (C6–O16, C2–O12, C4–O14)	1.250(7), 1.245(3), 1.249(0)
Mean C–O bond	***1.25***

3 × C–C bonds (C1–C7, C3–C27, C5–C17)	1.372(1), 1.366(8), 1.353(5)
Mean C–C bond	***1.36***
3 × C–N bonds (C7–N1, C17–N11, C27–N21)	1.334(9), 1.341(2), 1.353(5)
Mean C–N bond	***1.34***

R1(1576 reflections) = 0.0835, wR2(2043 reflections) = 0.1694, S = 0.346

A.7 Compound 4.3

All measurements were made at a temperature of -183.0 $\pm$ 0.1 °C on a Bruker APEX DUO diffractometer using graphite monochromated Mo-Kα (max 2θ = 53.0°). Data was collected in a series of ϕ and ω scans in 0.5° oscillations using 15.0-second exposures. The crystal-to-detector distance was 38.21 mm. The material crystallizes as a two-component 'split-crystal' with components one and two related by a 180º rotation about the (0.00 0.00 1.00) recirpocal axis. Data were integrated for both components, including both overlapped and non-overlapped reflections. In total 13148 reflections were integrated (2245 from component one only, 2234 from component two only, 8669 overlapped). Data were collected and integrated using the Bruker SAINT software packages. Data were corrected for absorption effects using the multi-scan technique (TWINABS), with minimum and maximum transmission coefficients of 0.851 and 0.991, respectively. The data were corrected for Lorentz and polarization effects.

The structure was solved by direct methods[213] using non-overlapped data from the major twin component. Subsequent refinements were carried out using an HKLF 5 format data set containing

complete data from component one and overlapped reflections from component two. All non-hydrogen atoms were refined anisotropically. All hydrogen atoms were placed in calculated positions. The final cycle of full-matrix least-squares refinement on F^2 was based on 2944 reflections and 197 variable parameters.

X-ray crystal data for **4.3**: $C_{15}H_{21}N_3O_3$, MW = 291.35 g mol^{-1}, colourless irregular crystal (0.10 × 0.17 × 0.28 mm^3), triclinic, space group P-1 (#2), a = 6.433(2), b = 7.542(3), c = 15.771(6) Å, α = 90.874(6)°, β = 95.675(7)°, γ = 109.593(8)°, V = 716.5(4) $Å^3$, Z = 2, ρ_{calcd} = 1.351 g cm^{-3}, F_{000} = 312.00, μ(Mo-Kα) = 0.95 cm^{-1}, λ(Mo- Kα) = 0.71073 Å, GoF = 1.05; R1, wR2 = 0.065, 0.144 (all data); 0.052, 0.137 (F^2: I > 2.00σ(I)).

Table A.6. Bond lengths for compound **4.3**. All bond lengths given in Å.

Bond	**Distances (Å)**
6 × Ring C–C bonds (C1–C6)	1.456(3), 1.460(4), 1.474(3), 1.455(3), 1.459(3), 1.468(3)
Mean C–C ring bond	***1.46***
3 × C–O bonds (C1–O1, C3–O2, C5–O3)	1.262(3), 1.250(3), 1.247(3)
Mean C–O bond	***1.25***
3 × C–C bonds (C2–C7, C4–C10, C6–C13)	1.397(4), 1.403(3), 1.394(3)
Mean C–C bond	***1.40***

3 × C–N bonds (C7–N1, C10–N2, C13–N3)	1.318(3), 1.315(3), 1.327(3)
Mean C–N bond	***1.32***

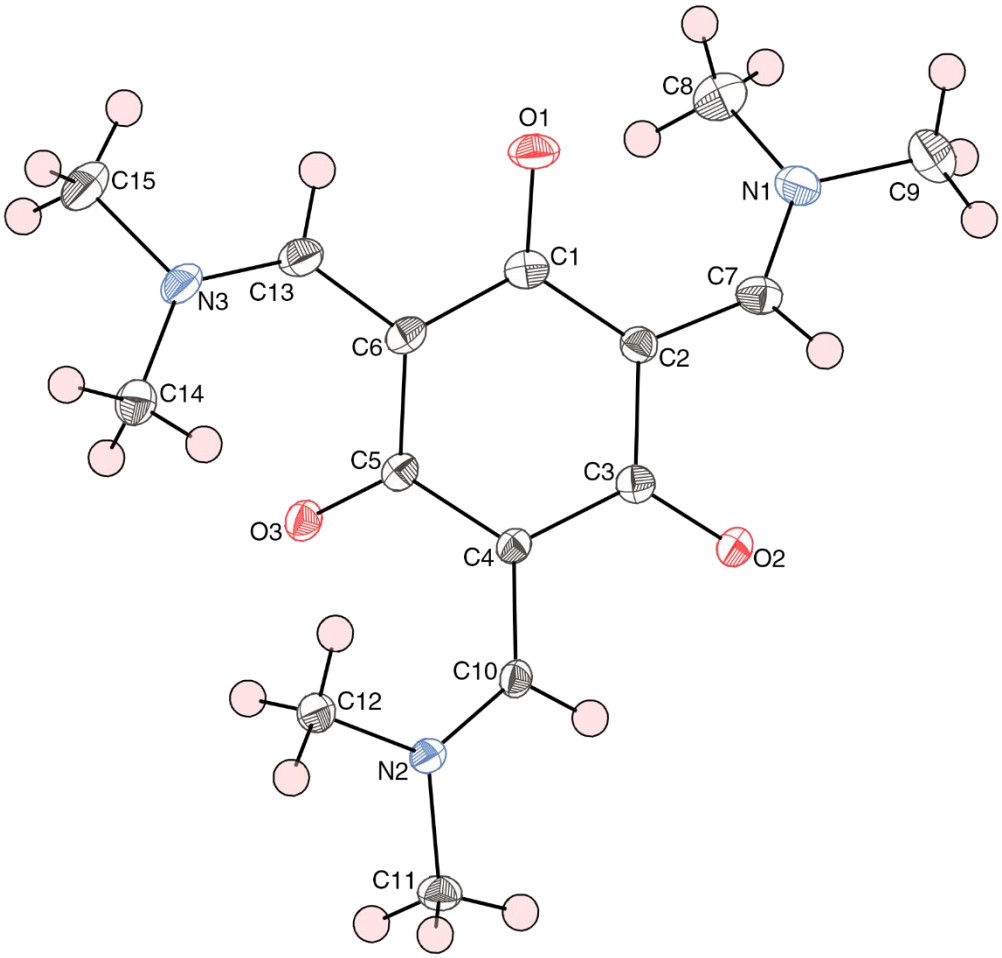

Figure A.8. Thermal ellipsoid plot of **4.3** (thermal ellipsoids are shown at 50% occupancy).

Appendix B

H/D Exchange in Mixed $CDCl_3/D_2O$ Media

As mentioned in Section 3.5.1, it is known that the presence of acid or base can greatly accelerate the H/D exchange reaction of phenols. Among commonly available NMR solvents, $CDCl_3$ is notorious for forming DCl upon exposure to oxygen and light.[214,215] It is reasonable to suspect, therefore, that the fast H/D exchange observed in mixed $CDCl_3/D_2O$ (Section 3.12) is simply be due to this trace acid. The $CDCl_3$ solvent used for this particular experiment was stored over K_2CO_3 and molecular sieves to minimize the chance of acid contamination. Nevertheless, a more careful study was carried out as described below to control for acid contaminant and in order to derive approximate half-lives used these conditions.

B.1 Procedure

$CDCl_3$ was stored over molecular sieves in an amber bottle that had been exposed to ambient light for approximately one year. Compound **3.4b** was used as H/D exchange substrate due to its high solubility in $CDCl_3$. Stock phosphate buffer solution (500 mM) in D_2O at pD = 7.2 was prepared by following the procedure published by Wang et al.,[216] which accounts for the difference in dissociation constant between H_2O and D_2O.[217] Similarly, stock cacodylate buffers at pD = 5.6 and 6.6 were prepared according to the procedure by Ruzin.[218] All buffer solutions were found to be within 1 unit of the requisite pH on VWR BDH® brand universal pH indicator (resolution = 1 pH unit). New NMR tubes were used throughout to minimize the risk of contamination.

Samples S_1 and S_2 were prepared by vigorously shaking $CDCl_3$ (800 μL) and D_2O (150 μL), discarding the aqueous layer and repeating the process once more with fresh D_2O (150 μL). Both

washes tested in the 7.0 ± 0.5 range. Subsequently S_1 and S_2 were shaken with 500 mM and 100 mM buffer solution, though the buffer layer (which also tests 7.0 ± 0.5) was not discarded in this case. Samples S_4 and S_5, similar to S_1 and S_2 except for using 800 µL CDCl3, 100 µL D2O, and 100 µL of 200 mM pD = 5.6 and 6.6 cacodylate ($(CH_3)_2AsO_2H/(CH_3)_2AsO_2Na$) buffer, respectively (resulting in *ca.* 200 µL of 100 mM cacodylate buffer in each case). For comparison, sample S_3 was prepared by simply shaking $CDCl_3$ (800 µL) and D_2O (150 µL) with no preceding washes or treatment.

The ^{1}H NMR kinetic experiment was set up in each case using the clarified $D_2O/CDCl_3$ sample prior to the addition of substrate.* The NMR tube was then ejected, **3.4b** (10 mg) added, and the tube shaken vigorously for 5 s to completely dissolve any solids. Following phase separation (which took ~ 40 s), the sample was placed back in the instrument and the resulting NMR spectrum recorded. Figure B.1 shows the ^{1}H NMR spectra 4 and 14 minutes following substrate addition.

* Experiment details: number of scans (NS) = 8; recycle delay (D1) = 10.0s; acquisition time (AQ) = 2.0s; dwell time (DW) = 69.6 µs.

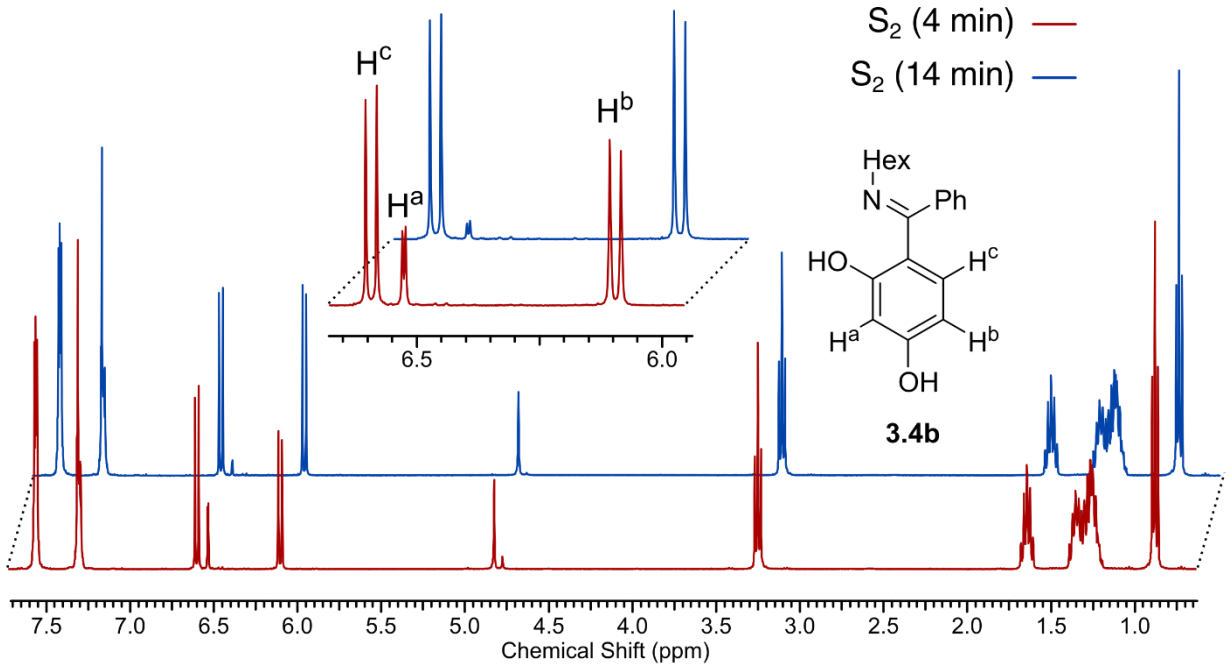

Figure B.1 ^{1}H NMR spectra of **3.4b** (sample S_2) 4 and 14 minutes after substrate addition.

B.2 Results and Discussion

Figure B.2 shows the resulting kinetics plots, where the vertical axis shows the integration value for H_a relative to H_b (logarithmic). As H_b and H_c peaks integrate to the same value (± 3%), similar results are obtained if H_c is used as reference.

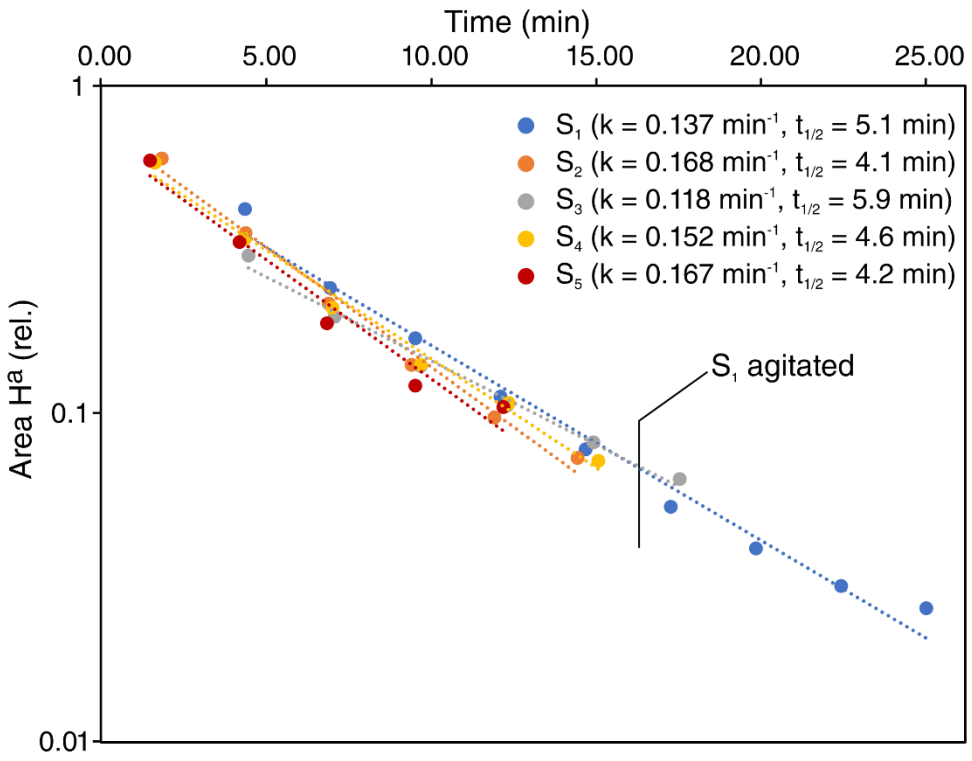

Figure B.2 Results of H/D exchange kinetic experiment.

As the traces in Figure B.2 show, the reaction is fast ($t_{1/2}$ = 4–6 min) under all three conditions. This makes it unlikely that fortuitous acid contamination in $CDCl_3$ was responsible for the fast exchange reaction in mixed $CDCl_3/D_2O$ media.

More generally, the fact that the rate of the reaction is not dramatically affected in the pD = 5.6–7.2 range lends slightly more credibility to the hypothesis that the ring protonation step, rather than happening in the two-step fashion shown in Figure B.3a, occurs in the concerted fashion depicted in Figure B.3b. Indeed, the concentration of the conjugate base, presumably involved in the rate determining step of the stepwise mechanism, would have to change by, at least, a factor of 10 across this pH range (degree of dissociation, *i.e.* $\alpha = [A^-] / ([A^-] + [HA]) = K_a / ([H^+] + K_a)$, with $K_a \approx 10^{-8}$–10^{-7})[86].

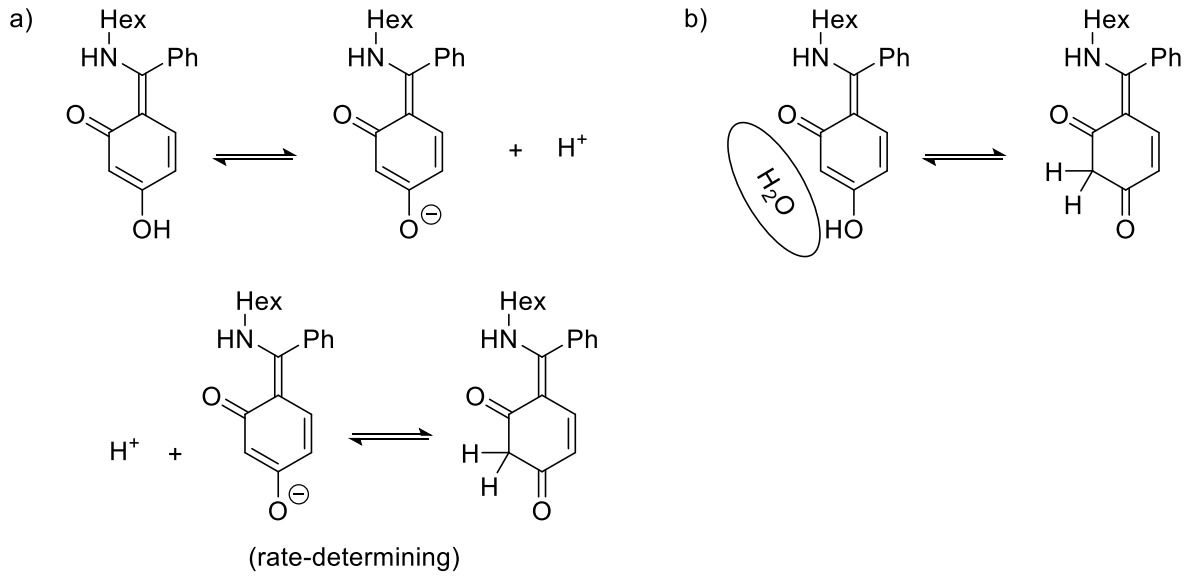

Figure B.3 Possible mechanisms for the ring protonation step of H/D exchange. (a) Protonation of an equilibrium population of the conjugate base of substrate. (b) Solvent-assisted concerted proton transfer.

It is interesting to note the D_2O content of the $CDCl_3$ solvent as well. It can be calculated that 800 μL of $CDCl_3$ at room temperature can dissolve *ca.* 58 μmol of D_2O.[219] Similarly, each NMR sample is calculated to contain about 34 μmol of substrate. Assuming that the deuterium exchange equilibrium has a K_{eq} close to unity, this amount of D_2O is not sufficient to account for the near-complete deuteration of substrate seen above. Therefore, D_2O in the bulk aqueous layer needs to be invoked to fully explain the thorough exchange reaction observed. We expect that the fast diffusion of "fresh" deuterium from bulk D_2O into the organic layer acts to replenish the supply of deuterium in the chloroform-dissolved D_2O.

As a final control experiment, sample S_1 was vigorously shaken and placed back in the spectrometer after the collection of the fifth data point, as shown in Figure B.2. Dispersion of the organic layer into small droplets in the process is expected to increase the D_2O–$CDCl_3$ contact surface by a large factor, leading to a large temporary acceleration in the following two scenarios:

1. H/D exchange occurs in the D_2O–$CDCl_3$ boundary.

2. Deuterium transport across phase boundaries is rate-limiting.

Since a noticeable acceleration was not observed, these two scenarios are deemed unlikely. Taken together, these observations motivate the mechanism proposed in Section 3.21 for water assisted proton/deuterium transfer from the phenolic moiety to the aromatic ring.

Appendix C

A Note on *Ab Initio* Methodology

The various chapters of this thesis have made use of a variety of basis sets for the calculation of energies, optimized geometries, or other molecular properties.

C.1 General Note on Interpretation of *Ab Initio* Results

The formulation of almost all *Ab initio* methods is subject to a large number of assumptions, which only hold approximately for any chemical system of interest. These simplifications range from ubiquitous ones such as the Born–Oppenheimer approximation that allows electronic and nuclear dynamics to be described independently, to the widespread neglect of dispersion and relativistic effects in routine calculations. More importantly, density functional theory, widely used due to its computational efficiency, is non-variational in nature, meaning a lower energy wavefunction does not necessarily better approximate the real electronic wavefunction. Wavefunction-based approaches suffer from other issues (*e.g.* pathological behaviour in MPn, size-inconsistency in configuration interaction).

For the above reasons, it is advisable in calculations where small energy differences are being investigated (typically a few kcal/mol) to compare the results across various *ab initio* methods (different DFT functionals, Møller–Plesset perturbation theory, etc.), basis sets, and calculation modes (*e.g.* gas phase vs. bulk solvent modeling vs. explicit solvent molecular where appropriate). Doing so gives a measure of how well the different methods agree, especially as basis set size is increased, allowing one to assess the degree of confidence and variability in the results obtained.

Any small energy differences otherwise must be interpreted with caution and are otherwise best used a semi-quantitative aid in understanding the system in question or a structural trend.

C.2 Choice of Basis Sets

The choice of basis set in each chapter was influenced by the desire to obtain quality results within a reasonable time given the computation resources at our disposal. The final stages of calculation throughout the thesis make use of the so-called *triple-zeta* basis sets (specifically, 6-311G(d,p), cc-pVTZ, and Def2TZVP/Def2TZVPP). The term triple-zeta comes from the fact that these basis sets approximate the contribution of each atom to a given one-electron wavefunction in the molecule as the combination of three *Slater-type orbitals* (also known as STOs, $\rho_n(r) = r^{n-1}e^{-\zeta r}$, n being analogous to the principal quantum number). STOs themselves often approximated as the sum of several *primitive* gaussian functions for computational efficiency.[220] Since they contain components that spread out to larger distances, triple-zeta or higher basis sets allow accurate description of phenomena like π electron delocalization or hydrogen bonding, in which atoms interact at distances that are larger than those commonly encountered in covalent interactions.

Preliminary or qualitative calculations can be performed using smaller basis sets allowing calculations to be done in a substantially shorter amount of time. This must be done judiciously, though, as smaller basis sets might be inadequate for the description of whole classes of interactions, *e.g.* ion–dipole, hydrogen bonding. In this thesis, the double zeta 6-31G(d,p) was used in the preliminary geometry optimization of many structures. Our previous experience indicates that including the d and p polarizations allows this relatively small basis set to give a reasonable qualitative description of electron delocalization in aromatic Schiff bases.[221] Final calculations (*i.e.*

full optimization, vibrational analysis, transition state search, internal reaction coordinate) were always completed in the appropriate triple zeta basis set.

Among the triple zeta basis sets, the celebrated 6-311G(d,p) basis set was used extensively in Chapter 3, making the computationally intensive calculations in this chapter (especially that of obtaining the transition state for proton transfer to the aromatic ring with an explicit network of water molecules) tractable. *Pople*-type basis sets like 6-311G(d,p) have the desirable property that the various valence orbitals (*e.g.* s, p, d, f) share a common radial component and only differ in their angular part. This reduces calculation times significantly, since fewer integrals need to be calculated and is especially useful in cases where second derivatives need to be routinely evaluated, such as internal reaction coordinate calculations or difficult cases of finding reaction transition states as encountered in Chapter 3.

The various parameters in a basis set need to be optimized for a certain criterion. Thus, while Pople basis sets have been tailored with simple Hartree-Fock calculations in mind, newer families of basis sets are often designed to give the most accurate results in combination with methods that take electron correlation into account (such as DFT, Møller–Plesset perturbation theory, or coupled cluster). In this context, the Dunning (*e.g.* cc-pVTZ) and Karlsruhe (*e.g.* Def2TZVP, Def2TZVPP) basis sets are expected to give results of similar accuracy with comparable computational effort. It must be noted that *ab initio* results in Chapters 2 and 4 have not be extensively checked for dependence on method/basis set and as such need to be treated as approximate in nature — explicit solvent interactions, zero-point energies, and entropy are not accounted for, either. This is in line with the scope of *ab initio* results in both chapters. For instance, *ab initio* energies and ring currents were used in conjunction with experimental results as part of uncovering trends governing tautomeric preference in TSANs. Similarly, geometry optimizations and NMR shielding tensor

calculations were used in Chapter 4 as a qualitative aid to better understand the experimental properties of **4.3**.